ABSTRACT

Title: DESIGN, FABRICATION, AND CHARACTERIZATION OF A ROTARY VARIABLE-CAPACITANCE MICROMOTOR SUPPORTED ON MICROBALL BEARINGS

Nima Ghalichechian, Doctor of Philosophy, 2007

Directed By: Professor Reza Ghodssi, Department of Electrical and Computer Engineering

The design, fabrication, and characterization of a rotary micromotor supported on microball bearings are reported in this dissertation. This is the first demonstration of a rotary micromachine with a robust mechanical support provided by microball-bearing technology. One key challenge in the realization of a reliable micromachine, which is successfully addressed in this work, is the development of a bearing that would result in high stability, low friction, and high resistance to wear. A six-phase, rotary, bottom-drive, variable-capacitance micromotor is designed and simulated using the finite element method. The geometry of the micromotor is optimized based on the simulation results. The development of the rotary machine is based on studies of fabrication and testing of linear micromotors. The stator and rotor are fabricated separately on silicon substrates and assembled with the stainless steel microballs. Three layers of low-k benzocyclobutene (BCB) polymer, two layers of gold, and a

silicon microball housing are fabricated on the stator. The BCB dielectric film, compared to conventional silicon dioxide insulating films, reduces the parasitic capacitance between electrodes and the stator substrate. The microball housing and salient structures (poles) are etched in the rotor and are coated with a silicon carbide film to reduce friction. A characterization methodology is developed to measure and extract the angular displacement, velocity, acceleration, torque, mechanical power, coefficient of friction, and frictional force through non-contact techniques. A top angular velocity of 517 rpm corresponding to the linear tip velocity of 324 mm/s is measured. This is 44 times higher than the velocity achieved for linear micromotors supported on microball bearings. Measurement of the transient response of the rotor indicated that the torque is 5.62±0.5 micro N-m which is comparable to finite element simulation results predicting 6.75 micro N-m. Such a robust rotary micromotor can be used in developing micropumps which are highly demanded microsystems for fuel delivery, drug delivery, cooling, and vacuum applications. Micromotors can also be employed in micro scale surgery, assembly, propulsion, and actuation.

DESIGN, FABRICATION, AND CHARACTERIZATION OF A ROTARY VARIABLE-CAPACITANCE MICROMOTOR SUPPORTED ON MICROBALL BEARINGS

By

Nima Ghalichechian

Dissertation submitted to the Faculty of the Graduate School of the
University of Maryland, College Park, in partial fulfillment
of the requirements for the degree of
Doctor of Philosophy
2007

Advisory Committee:
Professor Reza Ghodssi, Chair
Professor Christopher Cadou
Professor Isaak Mayergoyz
Professor Robert Newcomb
Professor Martin Peckerar

Dedication

This work is dedicated to my father Yousef, my mother Mansoureh, my sister Sameh, and my beloved Gulsah for their support and encouragement throughout my doctoral study years.

Acknowledgements

I would like to thank my advisor Prof. Reza Ghodssi for his guidance and support throughout the five years of my graduate studies at the University of Maryland (UMD). Thanks to my dissertation committee members Prof. Christopher Cadou, Prof. Isaak Mayergoyz, Prof. Robert Newcomb, and Prof. Martin Peckerar. Special thanks to Mr. Alireza Modafe from the MEMS Sensors and Actuators Lab (MSAL) for mentoring me during the first few years of my graduate studies; I have benefited greatly from our discussions, his insight and assistance. Thanks to Mr. Alex Frey who helped me in developing the test setup. Many thanks to all members of the MSAL for their assistance and constructive feedback, especially Stephan Koev, Matt McCarthy, Mustafa Beyaz, C. Mike Waits, Brian Morgan, and Jonathan McGee. I have significantly benefited from discussions with Prof. Isaak Mayergoyz from UMD on fundamental concepts of synchronous machines and Prof. Jeffrey Lang from MIT on motor design and testing. I am grateful to Dr. James O'Connor, Mr. Thomas Loughran, and Mr. Jonathan Hummel from the Maryland Nanocenter clean room facilities (FabLab) for their help with the fabrication. During this study, I have benefited from collaboration with Dr. Mariano Anderle at ITC-irst, Italy on polymer-metal interface study and the Army Research Laboratory (ARL), Adelphi, MD on the development of rotary micromotor. Many thanks to Prof. Inderjit Chopra from Department of Aerospace Engineering, UMD for his support. This project was generously supported by the ARL under Grant No. CA#W911NF-05-2-0026, Army Research Office under Grant No. ARMY-W911NF0410176, and the National Science Foundation under Grant No. ECS-0224361.

Table of Contents

1 Introduction

1.1 Motivation

Micromotors and microgenerators occupy a subset of microelectromechanical systems (MEMS) that convert energy between the electrical and mechanical domains. With advancements in microfabrication technologies for integrated circuits (IC) and MEMS, as well as progress in employing new materials, a reliable and efficient micromotor can be built to provide mechanical power to various microsystems. Micromotors can be used for developing microsurgery instruments [1, 2], such as endoscopes [3], cutters, and graspers, as well as developing micropumps and microvalves with numerous applications from delivery of fuel and biological samples, to cooling and analytical instruments [4-7]. Micromotors can also be employed in micro assembly [8], propulsion and actuation [9, 10]. In this dissertation the design, fabrication, and characterization a reliable rotary variable-capacitance micromotor based on microball bearing technology in silicon is reported. This micromotor is a platform for the realization of highly desirable microsystems, like micropumps and microgenerators.

1.2 Literature Review

1.2.1 Electric Machines

Electric machines are equipment for the continuous conversion of energy between the electrical and mechanical domains through rotary or linear motion. The electromechanical energy conversion takes place through an electrostatic or magnetic field. According to Trimmer and Gabriel [11], Gordon and Franklin built the first

electrostatic motors in 1750s, 100 years before the advent of magnetic motors. The replica of this motor made by the *Electret Scientific Company* is shown in Figure 1-1(a) [12]. The first capacitive electrostatic motor was developed during Edison's era in 1889 by Zipernowsky. The schematic of the motor is shown in Figure 1-1(b) [12]. Peterson was also reported [13] to be one of the pioneers in development of synchronous electrostatic motors in 1907. Nearly 50 years after Zipernowsky, Trump discussed the concept, design, and fabrication of variable-capacitance machines [14, 15]. Trump explained the regime in which the machine acts as a motor or a generator, demonstrated the average output electrical power of the generator, and discussed the insulation problems of high-voltage electrostatic generators. Bollee published a comprehensive study in 1969 on electrostatic motors in which he discussed the effects of voltage excitation waveform, stator and rotor geometry, and ohmic and frictional losses on the performance of the motor [13]. He elucidated the inherent tradeoffs in the geometry design that would result in motors with high speed or high torque. Mulcahy *et al.* demonstrate the fabrication of a macro scale 430-W vacuum-insulated generator at 24 kV and 10000 rpm with 1 mm air gap between the stator and the rotor [16].

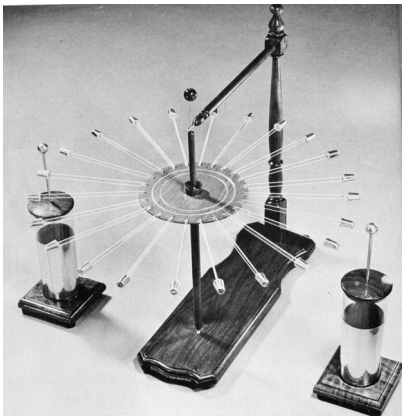

(a)

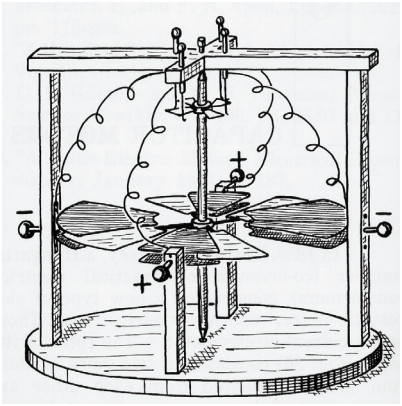

(b)

Figure 1-1: (a) Replica of the Benjamin Franklin's motor (1747), (b) schematic of the Karoly Zipernowsky's variable capacitance motor (1889). [Source: Electrostatic motors by Oleg Jefimenko, 1973].

Despite the fact that electrostatic machines were historically developed much earlier than magnetic machines, the commercialization of electrostatic machines has been very limited. In practice, all the macro scale motors, generators, and actuators are based on conversion of energy between mechanical and magnetic domains; the magnetic machines have been a dominant technology on the macro scale. This is because the macro scale electrostatic machines have low energy density compared to magnetic machines. Energy density in an electric (electrostatic) field and magnetic filed are given by $W_E = \frac{1}{2}\varepsilon E^2$ and $W_M = \frac{1}{2\mu}B^2$, respectively, where ε is the permittivity of the material, E is the magnitude of the electrostatic field, μ is the permeability of the material, and B is the magnitude of the magnetic flux density [17]. Air gap energy density is a figure of merit for evaluating the performance of electrostatic and magnetic machines [17]. The high energy density of magnetic machines (compared to electrostatic machines) has made them the dominant technology on the macro scale. Furthermore, electrostatic machines have high

operating voltage and require precise geometry fabrication (especially at the air gap) that is a disadvantage.

On the micro scale, however, the magnetic machines have several disadvantages. Magnetic machines require use of ferromagnetic materials and thick metal layers that are very challenging to fabricate and require processes that are not compatible with traditional IC fabrication. These machines are current-driven and usually require large driving currents. The current dissipates a lot of energy in the highly resistive micro scale metal windings and magnetic core of the machine [18, 19]. One of the first attempts on fabricating magnetic micromotors was reported by Dutta et al in 1970 [20].

In contrast, electrostatic machines are made of conductors and dielectrics which are commonly used in conventional IC fabrication processes. In order to increase the speed and functionality of integrated circuits the properties of conductors and dielectrics have been optimized in the last few decades; the fabrication process of the electrostatic micromachines is much easier than magnetic counterparts. Chapman and Krein [17, 21] have shown that on the micro scale (few micrometers gap size), the energy density (at the gap) of electrostatic and magnetic micromachines are comparable. Therefore, from the performance point of view, the micro scale electrostatic machines are comparable to the magnetic counterparts and in particular cases the electrostatic machines may be superior.

Several types of micromotors and microgenerators have been widely studied; permanent electret [22-25], piezo-electric [26-29], and ultrasonic [30, 31] micromachines are a few examples. Variable-capacitance and electric induction are

two major types of electrostatic micromachines[1]. Variable-reluctance and magnetic induction machines, being the magnetic equivalent of variable-capacitance and electric induction machines, together with permanent magnet machines are the main types of magnetic micromachines. Variable-capacitance micromotors that were among the first fabricated microelectromechanical devices are discussed in detail in the next section.

1.2.2 Variable-Capacitance Micromachines

The operating principle of variable-capacitance micromachines is discussed in Chapter 2. These are synchronous machines that produce torque due to spatial misalignment of electrodes on the stator and salient poles on the rotor[2]. Trimmer and Gabriel proposed the concept of linear and rotary variable-capacitance micromotors (VCM) in 1987 [11]. The first generation of VCM was simultaneously developed by two groups in the late 80's: Tai *et al.* at the University of California, Berkeley [32, 33], and Mehregany *et al.* at the Massachusetts Institute of Technology (MIT) [34]. These were synchronous motors fabricated using semi-standard IC fabrication processes known as "surface micromachining" [35]. Surface micromachining refers to a fabrication process than in one of its steps involves selective removal of a film (sacrificial layer) to release a structure. This type of micromachining, considered a major MEMS fabrication process, is adopted from an earlier work in fabricating resonant gate transistors [36]. The development of the variable-capacitance micromotors was based on initial attempts of Lober and Howe on fabricating passive

[1] Electric induction machines should not be confused with the conventional magnetic induction machines.
[2] The definition of poles in the electrostatic machines may be different than their magnetic counterparts.

polysilicon structures together with a top-drive VCM [37]. Two similar fabrication processes reported by Mehregany *et al.* were utilized for the fabrication of VCMs: center-pin and flange [38, 39]. The rotor in these types of VCMs would sit on either flanges or a center-pin. In these processes, thin films of silicon nitride and silicon dioxide were used as an electrical insulator and sacrificial layer, while a polysilicon film was used as a structural material. The design principles including the effect of different geometries on the torque of the motor, as well as the fabrication and dynamics of the machines were reported by Mehregany *et al.* [34, 39-41].

Figure 1-2 shows the schematic cross section and scanning electron micrograph of the two designs of early VCMs: side-drive and top-drive. The top-drive design was initially estimated to have lower friction (rotor elevation) and higher torque (larger active area), however, it suffers from a phenomenon known as "rotor clamping" which stops the rotor from rotating. This is due to the rotor and stator having two different potentials, causing the rotor to clamp (pull-in) to the stator due to the non-zero electric field. The result is a short circuit situation. Similarly, a potential difference between the rotor and substrate was found to cause rotor clamping to the substrate in both side-drive and top-drive designs. In the second generation of side-drive VCMs, the latter problem was addressed by electrically connecting the rotor bushing to the substrate to keep the rotor electrically grounded (instead of floating). The electrical connection was not always possible due to oxidation of the polysilicon bushing [34]. The top-drive motor shown in Figure 1-2(d) was never completely tested due to stability and clamping problems. The major problem with these

machines (both top and side-drive) was the lack of reliability, stability, and small torque.

In ordinary side-drive motors, the rotor was supported on pins (bushing). These pins are directly in contact with the stator which results in high friction, wear, and, by extension, limited lifetime. Test results showed that frictional effects play a dominant role in the dynamics of the micromotor. These motors would function well for about a week before they stopped. In addition, the active area of the motor used to produce torque was small and limited by the thickness of the polysilicon layer (side-drive design). The polysilicon thickness was limited by the constraints on fabrication processes. Since the polysilicon layers were highly stressed, the radius of the motor was limited by the maximum allowable curvature of the released rotor. Therefore, the motor torque, which directly depends on the size of the motor, was limited.

Furthermore, because of geometric tolerances in the design and fabrication, the air gap was not equal between the two sides of the motor and, as a result, the radial electrostatic forces were not balanced and the motor was not symmetric. In addition, due to the stator-rotor vertical misalignment, the rotor would elevate from its rest position, introducing instability and limiting the maximum speed. In both designs, the variation in the normal force with respect to angular position of the rotor, would cause instability in the rotor and results in the rotor crashing. The maximum speed of the Berkeley micromotors was reported to be 500 rpm and the maximum speed of the MIT micromotor was estimated[3] to be 15000 rpm [40, 42]. The torque of these machines was in the range of a few pico-Newtons meters (pN·m). A higher torque in

[3] No experimental data was found on the angular velocity measurement of up to 15000 rpm for these types of machines.

the range of micro to mili N·m with speeds of tens of thousand of rpm is generally required for pumping, actuation, or surgery.

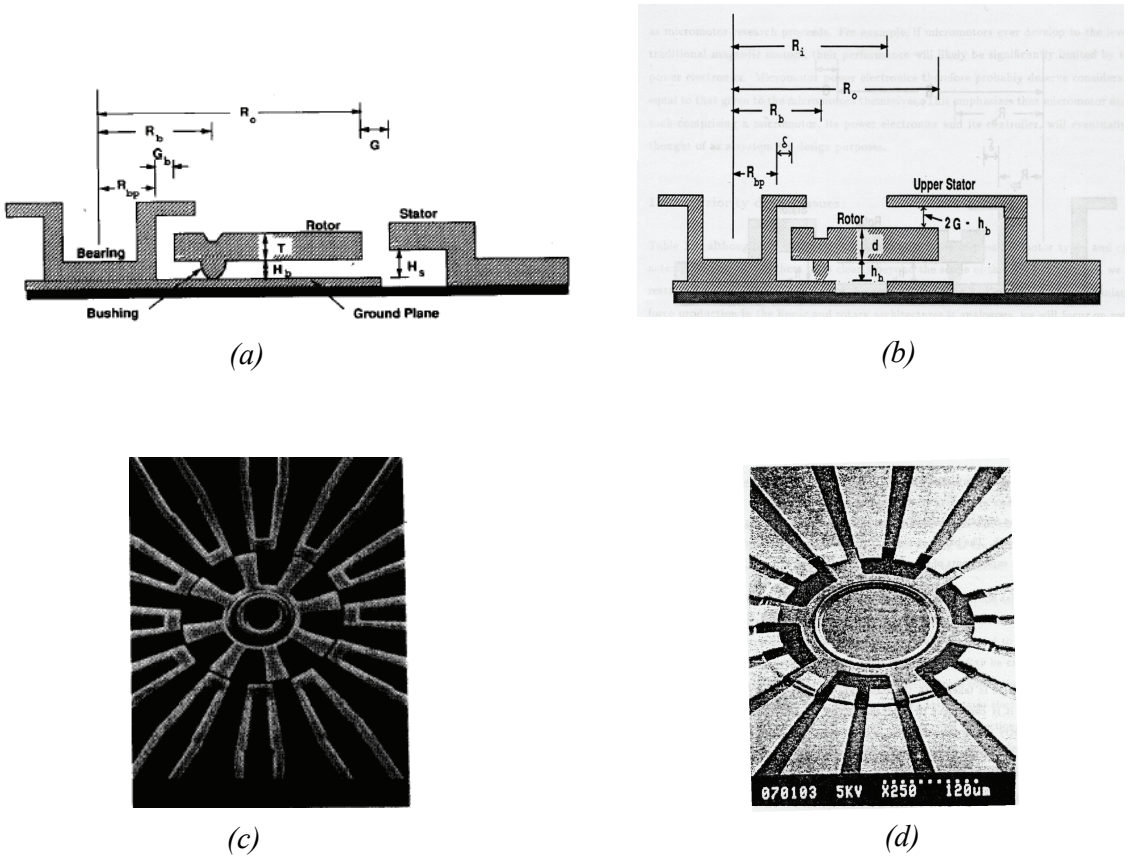

(a) *(b)*

(c) *(d)*

Figure 1-2: (a) Cross section of side-drive (radial) VCM, (b) cross section of top-drive (axial) VCM, (c) SEM of the fabricated and tested side-drive VCM, (d) SEM of fabricated top-drive VCM. The top-drive motor was never successfully tested (Mehregany et al).

In summary, side-drive VCMs discussed here have several disadvantages: (1) friction and wear due to center-pin or flange design, (2) low torque due to small size of the active area, (3) reliability and stability due to center-pin or flange design, as well as oxidation of the polysilicon, and (4) rotor stability due to imbalanced normal force resulted from electrodes design. Using a new approach, it is possible to design and fabricate a rotary micromotor to minimize these shortcomings.

Harmonic side-drive VCMs, also known as wobble VCMs, were developed in conjunction with ordinary side-drive motors by Mehregany *et al.* [34, 43, 44]. In this design, the rotor wobbles around the center shaft. The acting force between stator and rotor in this design is the normal force, whereas, in ordinary side-drive motors explained earlier, the acting force is the tangential force. The normal force could be roughly one order of magnitude larger than tangential force. Thus, these motors produce higher torque than ordinary side-drive motors. The main advantage of this design is that the torque is proportional to the motor gear ratio (the ratio of electrical excitation frequency to the mechanical frequency of rotor in center-pin design) [34, 44]. Due to friction and wear, the gear ratio would change during operation; therefore, extended operation was not possible. The wobbling motion of the rotor is another disadvantage of this type of motor and limits the applications.

The possibility of operating a wobble micromotor in a liquid environment (water or silicone) was investigated by Dhuler *et al.* [45]. The higher dielectric constant of these environments, compared to air or nitrogen, could potentially result in a larger change in the capacitance and consequently a higher gear ratio and high electromechanical torque. Using a simple parallel plate approximation, one can conclude that the rate of capacitance-change in any variable-capacitance machine is proportional to the dielectric constant at the gap. While lubricants like silicone and water may reduce the contact friction, they would introduce large viscous drag losses. Lower net torque and speed (120 rpm) were reported for the tested devices by Dhuler *et al* [45].

With advancement in the fabrication techniques and development of new materials, the new generation of VCMs was fabricated using deep reactive ion etching (DRIE) and LIGA processes[4]. Yasseen *et al.* has shown a side-drive micromotor with 200-μm-tall poles and a top-speed of 300 rpm [46, 47]. The air gap was 17 μm and the rotor was supported on a center-pin. Increasing the pole thickness while keeping the gap constant would result in increase in the active area. Similarly, a twine stator wobble VCM was fabricated using a LIGA process with 200-μm-tall poles that could potentially be used in conjunction with a closed-loop drive [48]. Surface micromachined side-drive motors using silicon carbide (SiC) as structural layer were also developed. These types of motors, suitable for operation in harsh environments, had low operating speeds of 37-317 rpm [49, 50]. Neither torque nor power for these motors was reported.

One of the major problems with the surface-micromachined micromotors is the mechanical support that holds the rotor on the stator. The support mechanism should ideally result in minimum friction, high stability, and high robustness. The center-pin design, used in conventional micromotors, results in friction, wear, fracture, stiction[5], and contamination-based failure modes [51]. Some work is currently underway to take advantage of materials with small coefficient of friction (COF), such as diamond-like-carbon (DLC), to reduce the friction in center-pin or flange designs

[4] LIGA is a German acronym for x-ray lithography, electro-deposition, and molding.
[5] Stiction refers to the permanent contact of two surfaces due to attractive forces such as electrostatic or Van der Waals.

[52]. The COF for DLC is reported to be ~0.001 compared to 0.01-0.08 reported for silicon [52-54][6].

One attempt to reduce the friction by levitating the rotor electrostatically was demonstrated by Jeon *et al.* [55]. This motor could achieve a top speed of 60 rpm with an air gap of 300 μm and applied voltage of about 500 V to the suspension electrodes. In order to reduce the operating voltage, a smaller air gap is necessary. However, maintaining stability with a smaller air gap is challenging and requires complex control schemes; therefore, to the best of my knowledge, such a motor has not been demonstrated on the micro scale. An additional drawback of this design is that some area of the motor is dedicated to the electrodes suspending the rotor and the stator. Therefore, this motor has less driving force per unit area than conventional micromotors.

Magnetic suspension of the rotor, like electrostatic suspension, can potentially result in low friction and low vibration in comparison with contact bearings. Passive and active magnets have been employed in miniature motors to levitate or guide the rotor. The implementation of magnetic levitation in a micromotor was first introduced by Shearwood et al [56, 57]. Wu et al has demonstrated the rotor levitation of 300 μm and has achieved speed of 1400 rpm for a micromotor with levitating, rotating, and stability coils fabricated on the stator [58]. Recently linear and rotary micromotors were designed and reported with magnetic levitation [59, 60]. Further test results are necessary to characterize the performance of such suspension systems.

[6] A fair comparison can only be made where different materials are tested under identical experimental conditions i.e. loading, contact surface area, and humidity.

1.2.3 Other Types of Micromachines

Another type of electrostatic machine is an electric induction micromachine. Unlike a variable-capacitance machine, this machine is an asynchronous machine. In this device, an electric potential on the stator induces image charges on the rotor. These image charges follow the traveling potential wave of the stator with some lag (motor) or lead (generator). This lag/lead time is a result of the poor conductivity of the rotor. As a result of the electric field, a force with tangential and normal components is created. Both electric induction micromotors and microgenerators have been demonstrated successfully. Livermore *et al.* reported fabrication and testing of a motor that can produce 3.5 μN·m of torque and 20 mW of power at an excitation voltage of 90 V. The machine can reach 55000 rpm at an excitation frequency of 200 kHz [61]. Similarly, an induction microgenerator was demonstrated with 108 μW electrical output power [62]. These machines were supported by gas-lubricated bearings which are inherently unstable and require complicated instrumentation for drive and control as well as complex fabrication process using a stack of 5 or more bonded wafers. The smallest imperfection in the fabrication of the bearings would result in fatal crashing of the rotor. However, the main advantage of the gas lubricated bearings is the ability to operate at angular velocities up to a few million rotation per minute.

The magnetic equivalents of the variable-capacitance and electric induction machines have also been developed. Extensive research has been performed in the last 10 years on variable-reluctance and magnetic induction micromachines. A 3.3-nN·m variable-reluctance micromotor [63, 64] and a 2.5-μN·m magnetic induction

micromotor [18, 65] are two examples of these types of machines. A complete review over design and analysis [66], fabrication and testing [67], eddy currents and nonlinear effects [68] of the magnetic induction micromachines were recently reported by Lang et al. The lack of reliable mechanical support is the major problem in all these types of micromachines. The latter and the previously mentioned motors [65], were all supported via an external shaft or a tether structure; whereas, the electric induction micromotor [61] and the microgenerator [62] were supported on gas-lubricated bearing, and the side-drive VCMs were supported on center-pin structure [33, 39, 42].

Table 1-1 summarizes the comparison between different types of rotary micromotors reported in open literature [18, 40, 47, 61, 63, 69]. The key specifications for these rotary machines including speed, torque, power, support mechanism, and size are all given in this table. The parameters that were not explicitly reported by the authors were left blank in the table (no presumption or judgment was made even in obvious cases). All the micromotors listed suffer from reliability problems associated with center-pin or gas-lubricated bearings.

Table 1-1: Comparison between existing rotary micromotors.

	1	2	3	4	5	6
Group	MIT	Georgia Tech/ MIT	Case Western	MIT	Georgia Tech	Sandia
Mechanism	Electric induction	Magnetic induction	Variable-capacitance	Variable-capacitance	Variable reluctance	Variable capacitance
Torque	3.5 μN·m	2.5 μN·m	-	12 pN·m	3.3 nN·m (predicted)	-
Max power	20 mW	-	-	-	-	-
Excitation voltage/ current	95 V_{Peak}	8 A_{Peak}	50 V	±37-150 V	0.5 A, <1 V	5 V
Number of phases	6	-	3	3	3	4
Excitation frequency	200 kHz	35 kHz	-	-	-	Pulse width: 8.7 ms
Speed	55000 rpm	0	300 rpm	<15000 rpm	500 rpm	-
Suspension	Gas-lubricated bearing	Tether	Center-pin (2-μm tall)	Center-pin	pin	Hub
Dimensions	4.2 mm dia	R_0=6, R_1=10 mm	R_0=79, R_1=500 μm	R_0=13, R_1=100 μm	R_0=100, R_1=500 μm	-
Efficiency	-	8 W per phase winding loss	-	-	-	-
Air gap	1.8 μm (calculated)	50 μm	17 μm	1.5 μm	5-10 μm	-
Power electronics	6-phase inverter	-	-	-	-	None
Stator Isolator	20-μm-thick SiO_2	-	1.5-μm-thick thermal SiO_2	3000 Å SiN	Polyimide	-
Rotor Isolator	10 μm SiO_2	-	None	None	-	-
Stator Material	TiPt, SiO_2, Si	Si, Cu, NiFe (or CoFeNi)	Si, SiO_2	Polysilicon	120-μm-thick NiFe	SiO_2, Polysilicon
Rotor Material	Si and polysilicon, (0.5 μm, B-doped)	Si, NiFe (or CoFeNi), Cu	200-μm-thick rotor and stator	Si, SiO_2, Polysilicon	40-μm-thick NiFe	SiO_2, Polysilicon
Source , year	[61], 2004	[18], 2004	[47], 1999	[40], 1990	[63], 1993	[69], 1999

Table 1-2: Comparison between existing rotary microgenerators.

	1	2	3	4	5	6
Research group	MIT	Georgia Tech/ MIT	MIT	Hitachi	University of Southampton	Georgia Tech/ MIT
Source of energy	Turbine	Spindle	Vibration	Vibration	Vibration	Spindle
Mechanism	Electro-quasi-static induction	Permanent Magnet	Variable-capacitance	Variable-capacitance	Magnetic	Permanent Magnet
Device	Rotary	Rotary	Cantilever	-	Cantilever	Rotary
Power	108 μW	1.1 W	1.8 μW	0.12 μW	157 μW	8 W
Produced voltage	30 V	-	6 V	-	< 1 V	0.8 V open voltage at 150 krpm
Speed or frequency	n_r=245 krpm	n_r=120 krpm	f_r=1.56 kHz	-	f_r=322 Hz	n_r<305 krpm
Phases	6	3	-	-	-	3
Suspension	Gas-lubricated bearing	External shaft	-	-	-	External shaft
Dimensions	15×15×2.5 mm	R_1= 3.175, R_2= 9.525 mm	-	2×2 cm^2	3.15 cm^3	R_1= 5, R_2= 10 mm
Efficiency	14 %	34 %	37.6 %	21 %	-	28 % at 300 krpm
Air gap	4.2 μm	100 μm	-	-	-	100-100 μm
Power electronics	External inductor	-	Asynchronous diode-base charge pump with flyback	-	-	Transformer and bridge
Materials	Rotor: Poly Si, SiO_2, Si Stator: Si, SiO_2, Pt	Rotor: SmCo, FeCoV Stator: NiFeMo, Cu	Steel, Mylar, Aluminum	-	NdFeB	Rotor: SmCo, FeCoV Stator: NiFeMo, Cu, Polyimide
Load	-	R_L= 21 Ω	R_L= 20 MΩ	R_L= 10 MΩ	R_L= 0.6 Ω	R_L=37Ω
Source, year	[62], 2005	[19], 2005	[70], 2005	[71], 2004	[72], 2004	[73-75], 2006

Table 1-2 provides a similar summary for microgenerators [19, 27, 62, 70-72]. Output power, speed, efficiency, size, and support mechanism are the key parameters included in Table 2. The highest electric output power reported for a magnetic induction microgenerator was 1.1 W at 120 krpm. This machine was tested using a suspended spindle. Recently, an axial flux, permanent magnet generator was reported to supply 8 W of DC power at 305 krpm [73]. Unlike an induction machine, the permanent magnetic generator was a synchronous machine. Samarium-cobalt (SmCo) rare-earth magnets were used for the rotor and Cu was used for the stator winding. The machine was tested using a suspended spindle [74, 75].

1.2.4 Test and Characterization

While a great deal of research has been conducted on the design and fabrication of micromachines, little work has been published on drive, control, and characterization of these machines. Electrostatic micromotors, in general, require multi-phase high-voltage drives. Depending on the voltage amplitude, frequency, duty cycle, phase difference, number of phases, and the type of wave-form, an in-house power electronics system is generally required. Maintaining the integrity of the wave-form delivered to the capacitive load (with stringent timing constraints) makes the circuit design challenging. One example of such a system developed by Neugebauer *et al.* is capable of operating up to 300 V and 2 MHz [76].

In some machines, the optimal driving requires instantaneous rotor position information. Therefore, a more robust and reliable control scheme for the most micromotors is a closed-loop control. This is more important in variable-capacitance motors since they are synchronous machines. With a feedback circuit, a micromotor

can be controlled to operate at a desired (steady) speed and torque. Some preliminary work has been performed for driving side-drive VCMs in a closed-loop fashion by sensing the capacitance-change of each phase using a high-frequency signal (modulated on the main drive signals) and a capacitance sensing circuit [77]. Optical position sensing can also be used; however, the integration of optical sources and detectors with a micromotor is challenging. This research is currently underway at the University of Maryland (UMD). Other approaches have been proposed to eliminate the need for capacitance sensing circuit by implementing a segmented bearing design in a wobble VCM [48]. As the rotor rolls around the segmented bearing, the gap between 2 adjacent bearing segments is bridged by the rotor and the momentary electrical short circuit can be sensed by the electronics and used to determine the position of the rotor. It was also shown that drive electronics can be monolithically integrated with the micromotor on a single chip using complementary metal-oxide-semiconductor (CMOS) processes. In this approach a surface micromachined VCM was integrated with a CMOS drive circuit containing an oscillator, a frequency divider, and double-diffused MOS transistors [78].

Characterization of the micromotors is usually performed by measuring speed, torque, and output power. Efficiency is also a key parameter determining the performance of the micromotor. Bart *et al.* has characterized the dynamic behavior of side-drive VCMs through the use of stroboscopic dynamometry [79, 80] and estimated the drive torque and friction parameters. Direct torque measurement has also been shown for wobble motors by measuring the deflection of a long cantilever beam fixed at one end and connected to the motor rotor via a surface-micromachined

gear structure at the other end [81, 82]. Non-contact torque measurement has been demonstrated in electric induction motors by removing the stator excitation and monitoring the rotor deceleration (with respect to time) with optical displacement sensors [61]. With this method, torques less than 3.5 μN·m were indirectly measured. While the output power of electrostatic motors can be estimated using similar methods, the measurement of the input power is not trivial and involves measuring currents in the range of a few pico-amps or less. An alternating current (AC) ammeter is necessary since the motor is a capacitive load. In summary, stringent driving requirements and the small size of the device makes the test and characterization of micromotors challenging.

1.3 Development of Micromachines at MSAL

Since August 2002, we have been involved in a development of a linear variable-capacitance micromotor supported on microball bearings at the MEMS Sensors and Actuators Lab (MSAL), University of Maryland. We initially demonstrated the successful operation of this device in a 3-phase configuration [83]. Figure 1-3 shows the 3D exploded view of the designed structure. Unlike the conventional VCMs that were side-drive, this micromotor has a bottom-drive design which increases the active area of the motor. Two new technologies were implemented in the development of the linear micromotor: (1) microball bearing technology in silicon as a support mechanism and (2) benzocyclobutene (BCB) low-k polymer as an insulating layer [84]. The microball bearing technology results in stable and robust mechanical support. The rolling microballs, sandwiched between rotor and stator, results in less friction and wear when compared to center-pin design and are more reliable than

unstable gas-lubricated bearings [85]. The microballs maintain a uniform air gap, which is one of the key design parameters. A conventional dielectric film of silicon dioxide (SiO_2) was replaced by a low-k (k=2.65) BCB polymer. This results in reduced parasitic capacitance and increased efficiency of the motor. BCB also exhibits less residual stress compared to SiO_2; therefore, the device has less curvature and the air gap is more uniform. A process was developed to create embedded isolated islands of BCB in silicon [86] that enabled the fabrication of the linear VCM on a thick BCB film. Chemical-mechanical planarization (CMP) of BCB films was characterized for this purpose.

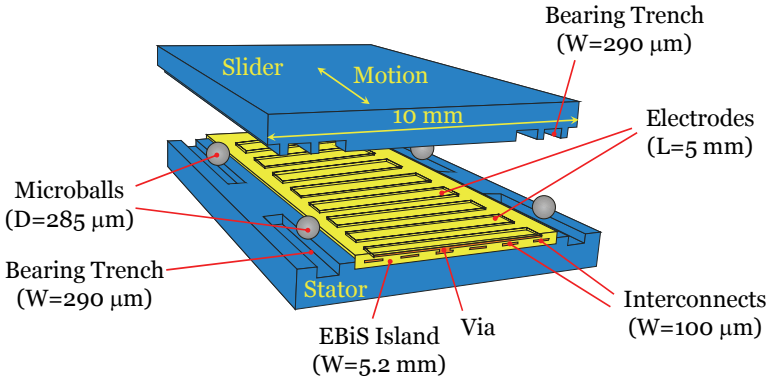

Figure 1-3: 3D view of the bottom-drive linear variable-capacitance micromotor designed at MSAL by A. Modafe [87].

The development of the linear micromotor is based on several studies of the motor core components. An *in situ* non-contact experimental system was developed to study the frictional behavior of the microballs on the micro scale regime. Static and dynamic COF of stainless steel microballs to the silicon grooves (fabricated by anisotropic silicon etching using potassium hydroxide (KOH)) were measured to be 0.01 and 0.007, respectively [88] compared to 0.01-0.08 reported for silicon-silicon structures [53, 54].

The electrical properties of the BCB and the effect of environment (e.g. humidity) on them are critical issues that affect the reliability of the micromotor. The dielectric constant and breakdown voltage of BCB were measured and the effect of humidity on these properties was studied [89]. The dielectric constant of BCB was measured to be 2.49 in dry environment. The dielectric constant was only increased by 1.2 % after a humidity stress of 85 % RH at 85 °C. The study of the I-V characteristics of BCB showed that humidity stress reduces the breakdown strength by a factor of 2-3 and increases the maximum leakage current 10 fold.

Figure 1-4 shows the top-view of the fabricated stator and slider. Initial test results estimated maximum aligning force of 0.17 mN per phase at an excitation voltage of 100 V. The average speed of the slider at frequencies of 10 and 20 Hz was measured to be 1.82 and 3.56 mm/sec, respectively [83]. The speed measurement was performed using a CCD camera and image processing software. This linear micromotor is a platform for developing the second generation device, as well as the rotary micromotor. A rotary motion, together with a bottom-drive design and microball bearing support, will enable the fabrication of a high-torque, reliable micromotor for operation as a mechanical power source in various microsystems.

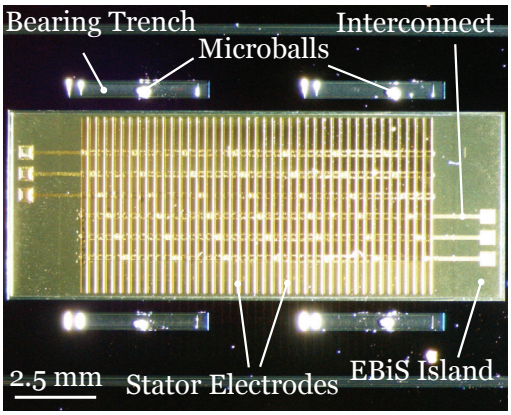

Figure 1-4 Top view of the (a) stator and (b) slider of the linear variable-capacitance micromotor fabricated at MSAL [87].

1.4 Process Integration and Interface Study

Adhesion improvement of metal films to polymers has been a major challenges in developing the first generation linear micromotor. In order to improve the adhesion a series of experiments were performed and a new fabrication process for integration of BCB and wet etching of silicon using KOH was developed [90-93]. The adhesion improvement results were used in the development of the rotary micromotor.

The advantages of BCB as a dielectric material for MEMS applications are: (1) low dielectric constant (k= 2.65), (2) easy deposition process (spin-on), (3) high level of planarization, (4) high solvent resistant, (5) low curing temperature (250 °C), (6) low residual stress (28 Mpa on silicon), (7) no outgasing during cure, and (8) ability to be deposited in thick layers. The disadvantage of this dielectric film is a low glass transition temperature [7]of 350 °C.

BCB, like other organic materials, has poor interfacial fracture resistance (adhesion) to inorganic materials. Anisotropic etching of silicon with KOH is

[7] The glass transition temperature of polymers is commonly known to be a temperature above which a polymer changes from a brittle/hard state to a rubbery/soft state.

performed in a very corrosive environment at high temperatures for a few hours. Therefore, it is essential to protect the BCB film during this process with an etch mask. It was shown that fabrication of deep silicon etched structures together with BCB dielectric films can be preformed using appropriate metal etch masks (Au/Cr) with a modified process flow to enhance the metal/BCB adhesion.

A series of experiments were performed to modify the fabrication process such that the adhesion between metal and BCB becomes strong. Adhesion improvement of BCB and Cr/Au etch mask was accomplished by partial cure of BCB prior to metallization, sputtering of the Cr/Au metal masks at 200 °C, and full curing at 250 °C. An adhesion promoter, AP3000, was proven to enhance the adhesion of these films if applied prior to metallization. Metal/BCB adhesion was tested to be very strong. Adhesion strength was experimentally verified in a qualitative manner. Deep structures (200 μm) in silicon were fabricated while the BCB film was protected by metal mask. Long exposure to KOH solution (8 h) had little or no effect on the adhesion of polymer- metal. The process was repeatable, giving the same set of results.

In order to understand the effect of soft cure and adhesion promoter prior to metallization and hard cure after metallization, the metal/BCB interface was studied. Different surface/interface techniques were used. Time-of-flight secondary ion mass spectroscopy (ToF-SIMS), Auger electron spectroscopy (AES), secondary electron spectroscopy (SEM), and atomic force microscopy (AFM) were the methods exercised along with 12 samples fabricated with different stacks of films for this study.

High lateral resolution ToF-SIMS imaging provided useful information about the surface of the Au and Cr (grain sizes) inside the Au layer. These images showed that the Cr diffusion (after curing) into Au layer was not homogeneous. Chromium-enriched grains of 2 μm or smaller were detected close to pure Au grains. The masking strength of the Au layer (against KOH) was not deteriorated by Cr diffusion. AES was used to quantify the atomic concentration of Cr diffused into Au. The Cr concentration at the Au layer was estimated to be 1 atomic percent on average. Morphology of the BCB, Cr, and Au surfaces and the effect of hard cure on their roughness were studied using AFM and SEM.

ToF-SIMS depth profiling was used for studying the interface of Au/Cr/AP3000/BCB. Concentration of different species at different depths from the surface of the wafer was measured. It was found that curing at 250 °C, together with use of adhesion promoter on partially cured BCB results in diffusion of Si and C from the BCB or AP3000 into the Cr layer. Use of cure management or adhesion promoter alone did not result in adhesion improvement. Chemical interaction of BCB and Cr at the interface, mainly in the form of oxidation of Cr, was also observed. Diffusion of Si and C from BCB or AP3000 into the Cr layer together with the formation of chromium-oxide at the Cr/BCB interface were correlated to the adhesion improvement between BCB and Cr/Au films.

This integration enabled the fabrication process development for the linear micromotor with 1 μm thick BCB film; however, if thicker BCB films are necessary in future linear micromotors, modified methods can be implemented. The results from this study were extensively used in the fabrication process of the rotary micromotor,

especially for two level metallization and three level BCB deposition steps. However, DRIE was utilized instead of KOH to fabricate rotary microball housings.

1.5 Structure of the Manuscript

In the first chapter, the history and background of micromachines were discussed. The proposed micromotor, theory of operation, microball bearing technology in silicon, and derivation of machine velocity, torque, and efficiency are presented in Chapter 2. The detailed design and finite element simulation, together with design variation and mask layouts of the micromotor are presented in Chapter 3. Chapter 4 will address the fabrication challenges and final results for the stator and rotor. The design, fabrication, and characterization of the rotary micromotor are based on prior work on optimization of the linear micromotor. The characterization results for the second-generation linear micromotor as well as the rotary machine are both reported in Chapter 5. First, the characterization methodology and system modeling for the linear micromotor are reported in Section 5.1. Second, test and characterization of the rotary device, including steady-state and transient analysis, of the motion dynamics i.e. position, velocity, acceleration, torque, and friction are discussed in Section 5.2. A summary of the dissertation, future work, and concluding remarks are discussed in Chapter 6.

2 Rotary Micromotor: Theory and Operation

2.1 Overview

The micromotor developed in this work is a six-phase, bottom-drive, rotary, variable-capacitance machine with a robust mechanical support provided by microball bearings. The device is the first demonstration of a rotary micromotor using microball bearing technology. In this chapter, a short overview of the design, fabrication, and testing of the micromotor is presented, followed by reviewing two core technologies: microball bearings and BCB. The theory of operation and the derivation of velocity, torque, and efficiency of the machine are discussed.

2.1.1 Design

The micromotor is composed of three major parts: stator, rotor, and microballs. Figure 2-1 shows the simplified 3D schematic view of the micromotor where part of the rotor is not shown for the sake of visualization. Similarly, Figure 2-2 shows salient poles of the micromotor rotor.

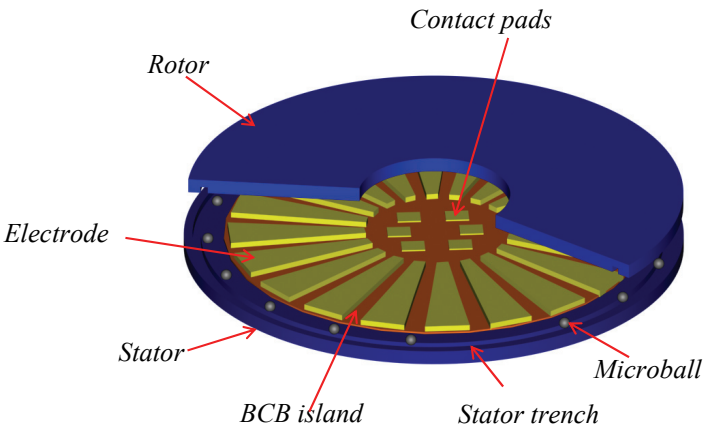

Figure 2-1: Simplified 3D schematic of the rotary micromotor (rotor on top). Dimensions are not to scale.

.

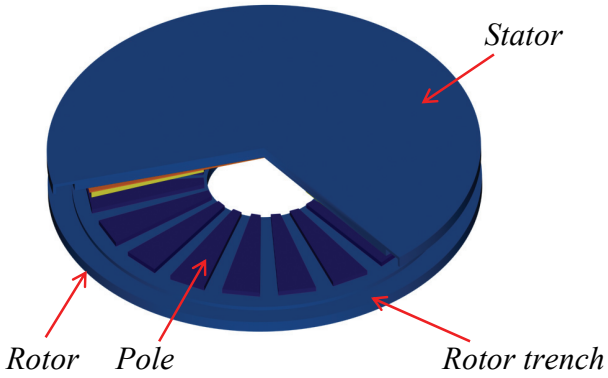

Figure 2-2: Simplified 3D schematic of the rotary micromotor (stator on top). Dimensions are not to scale.

The stator is a silicon plate that includes the active electrical components of the micromachine and microball housing. Figure 2-3 shows the cross-section schematic of the stator and rotor. Two levels of conductors on the stator form the electrode and interconnection layers. Three layers of low-dielectric-constant (k=2.65) benzocyclobutene (BCB) polymer film are used for electrical isolation of the stator electrodes, interconnections, and substrate. The low-k dielectric film, compared to silicon dioxide insulating films, reduces the parasitic capacitance between electrodes and the stator substrate; therefore, the electrical efficiency of the micromotor is increased. In addition, the residual stress of the BCB film is lower than that of silicon dioxide. This results in less wafer curvature and better gap uniformity. The stator also has a circular housing (trench) for the microballs.

The rotor is a silicon plate supported on stainless steel microballs. The rotor has fewer components than the stator and is composed of silicon salient poles and a circular microball housing. In a variable-capacitance motor, the torque is proportional to the angular gradient of the capacitance and the square of the applied voltage

amplitude[8]. Therefore, it is desirable to design the geometry of the micromachine such that at a given voltage, the angular gradient of capacitance is maximized. More details on the implementation of this approach are given in Chapter 3. The mechanical angular velocity of the rotor, when synchronized with the electrical excitation, is directly proportional to the excitation frequency and inversely proportional to the number of salient poles on the rotor. Due to the bottom-drive design, B-RVCM takes advantage of a larger active area compared to the conventional side-drive VCMs.

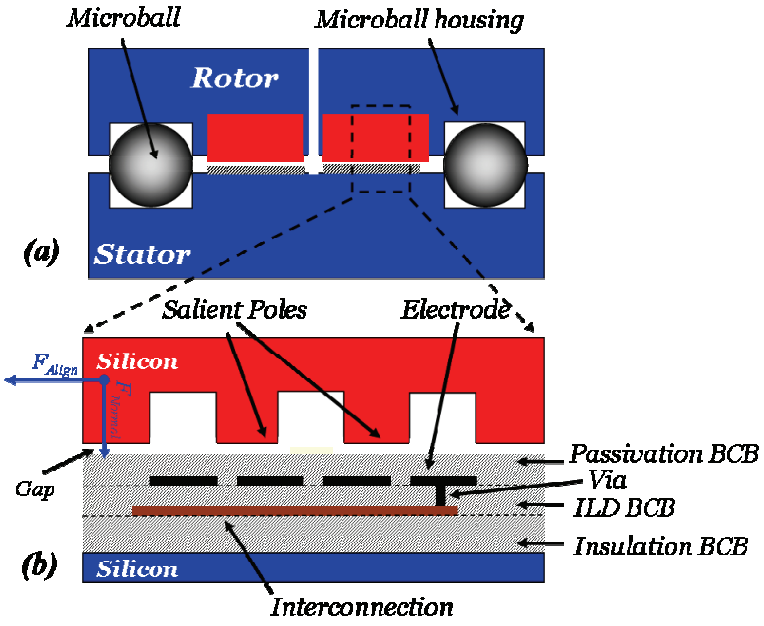

Figure 2-3: Schematic (a) radial cross section of the mechanical (bearing) and electrical (active) components of the micromachine, (b) azimuthal cross section of the stator and rotor active pars. Dimensions are not to scale.

2.1.2 Fabrication

The realization of the device requires the fabrication of the stator and rotor in separate stages, followed by manual assembly of the stator, microballs, and rotor.

[8] Analytical derivation for torque is presented at the end of Chapter 2.

As shown in Figure 2-3 the stator is composed of three layers of BCB film (dielectric) and two layers of metal film (conductor). It is important that the first metal layer be electrically insulated from the substrate. The parasitic capacitance between this layer and the substrate needs to be minimized. Two metals are electrically isolated and selectively connected to one another to form a six phase machine. Uniform dielectric deposition is necessary to avoid electric breakdown at sharp metal edges. The top electrode is passivated to reduce the chances of electric breakdown during testing. The resistance between the two metal lines should be minimal to reduce the time-constant and loss of the system. The BCB deposition is performed using spinning and curing steps. The metal deposition is performed by DC magnetron sputtering.

The mechanical support of the rotor is provided by fabrication of microball housings in both stator and rotor. The uniformity of the microball housing plays an important role in the gap uniformity. The rotor also has salient structures etched deep into the silicon using DRIE. In order to minimize the fabrication steps, the rotor housing and poles can be etched simultaneously. The rotor is released using DRIE before testing.

2.1.3 Characterization

Test and characterization of the rotary variable-capacitance micromotor require voltage excitation of 6 phases with large amplitude (~150 V), specific phase difference, frequency, and duty cycle. The motor is excited using a custom-designed power electronic system composed of a PC, LabView program, data acquisition card, and external high-voltage amplifier. The synchronization of the rotor motion with

electrical excitation of the stator is automatically accomplished due to the inherent characteristics of the machine later discussed in this Chapter. An opening in the rotor is designed such that it allows the physical contact of the 6 probe needles with stator pads. Without the presence of this opening, the fabrication process of the motor would have been significantly more complicated.

The test setup is also composed of a motion characterization component for measuring the angular position of the rotor. Two sets of measurements are performed to characterize the motion: steady state and transient. The steady state response is measured using a fiber-optic displacement sensor. These sensors are composed of a source and intensity detector that detects the position of etched marks on the rotor. The speed of the rotor is measured with this method. The transient response of the motor is measured using a high-speed, high-resolution camera system. The torque of the device, frictional forces, and the coefficient of friction are extracted from the transient response tests. In these tests, the deceleration of the rotor motion is calculated through numerical differentiation of angular position.

2.2 Microball Bearings Technology in Silicon

Mechanical support is one of the major challenges in development of microelectromechanical devices especially micromotors and microgenerators. Ideally the mechanical support would be reliable and stable with low friction and high resistance to fracture and wear. Major technologies used as a mechanical support in MEMS were reviewed in Chapter 1.

2.2.1 Mechanical Support in MEMS

The microball bearing is the core technology used in the development of the rotary micromotor. Table 2-1 summarizes a qualitative comparison between four different support mechanisms: direct contact bearings (bushing), microball bearings, gas-lubricated bearings, and magnetically or electrostatically suspended bearings. The rolling microballs have less friction and higher wear resistance than contact or sliding bearings. The fabrication of the micromachines based on this technology is significantly less complicated than gas-lubricated bearings which generally require tight fabrication tolerances for the journal and thrust bearings, as well as complex fabrication scheme using 5-6 wafer level bonding processes. Furthermore, the microball bearings are more stable than hydrostatic or hydrodynamic gas-lubricated bearings and require no control scheme; whereas, in gas lubricated bearings startup and active control are one of the many challenges.

The other important advantage of the microball bearing technology is the ability to define and sustain a uniform gap across the active area of the micromotor due to its contact nature. This property is significantly important for variable-capacitance micromachines for two obvious reasons: the air gap needs to be as small as possible and the active area of the micromotor at the gap needs to be large. Practically, the design of the machine dictates the small gap in the range of 10 μm with active areas in range of 10-100 mm^2. Microball bearings enable the design of the micromotors that have a small air gap with large active area and therefore high torque. The uncertainty in gap will be dictated by the accuracy in trench depth and ball diameter.

Table 2-1: Qualitative comparison between four different bearing technologies.

	Direct contact	Microball	Gas Lubricated	Suspended (magnetic or electrostatic)
Friction	High	Medium	Low	Low
Wear	High	Medium	Low	Low
Control	Not required	Not required	Relatively complex	Highly complex
Stability	Excellent	Excellent	Poor	Poor
Reliability	Poor	Excellent	Poor	-[9]
Fabrication	Simple	Relatively simple	Highly complex	Relatively complex

2.2.2 Stainless Steel Microballs

The Young's modulus and the hardness of the stainless steel and single crystal silicon are comparable [94][10]. Therefore, it is expected that the silicon housing and steel microballs have similar wear rates. Table 2-2 shows the properties of the stainless steel microballs. The precision in the ball manufacturing is defined with an industry index called the ball *grade*. The *grade 10* ball corresponds to the deviation from spherical form, lot diameter variation, allowable ball gage variation, and maximum surface roughness of 0.25, 0.25, 1.3, 0.025 μm, respectively. The microballs used in this study were chosen based on their tolerance, availability, and price to be 284.5 μm in the diameter. Other candidate materials are chrome-steel, silicon nitride, titanium, and tungsten carbide but were not available at small sizes during this study.

[9] Data is not available.
[10] Knoop hardness of silicon is reported to be 850-1100 kg/mm^2 .

Table 2-2: Properties of the stainless steel microballs.

Property	Value
Material	440C stainless steel
Material composition (%)	Chromium: 16-18, Carbon: 0.95-1.20, Silicon: < 1, Manganese: <1, Molybdenum <0.75, Nickel < 0.75, Copper < 0.5
Modulus of elasticity (GPa)	199
Yield strength (GPa)	1.89
Knoop hardness (kg/mm^2)	660
Density (10^3 kg/m^3)	7.6
Diameter (μm)	284.5
Tolerance (μm)	0.25
Surface roughness, Ra (nm)	25.4
Ball Grade	10
Microball mass (Kg)	9.2×10^{-8}

2.3 BCB-Based MEMS Technology

Spin-on, low dielectric constant BCB polymers [95-97] are promising candidates as insulating dielectric material in MEMS. The electrical and mechanical properties of this film are summarized in Table 2-3 [98].

Cyclotene is the commercial name of BCB produced by Dow Chemical Company (Midland, MI) and is commercially available in different types and viscosities. In this thesis the Cyclotene 3022 series was used in all the experiments. In this manuscript the terms “BCB” and “Cyclotene” are used interchangeably despite the fact that BCB refers to the chemical name of the monomer and Cyclotene carries the brand name.

Table 2-3: Summary of the physical properties of BCB.

Property	Value
Coefficient of thermal expansion, ppm/°C	52
Glass transition temperature, °C	>350
Tensile modulus, GPa	2.0±0.2
Poisson ratio	0.34
Residual stress on silicon, MPa	28
Dielectric constant (at 1 kHz)	2.65
Dissipation factor (at 1 kHz)	0.0008
Breakdown voltage (V/cm)	3.0×10^6
Volume resistivity (Ω-cm)	1×10^{19}

The main advantage of BCB over the most widely used dielectric material, silicon dioxide, is its ability to be deposited as a thick layer (up to 50 μm) with low residual stress. BCB with a dielectric constant of k=2.65 has much lower residual stress than plasma enhanced chemical vapor deposition (PECVD) SiO_2. It also has high level of planarization. These features make BCB attractive for MEMS applications. BCB is also a spin-on material which makes its deposition simpler than conventional CVD processes used for dielectrics like silicon dioxide and silicon nitride. The deposition process is completed with a cure step which is performed at a relatively low temperature (250 °C). The disadvantage of the BCB to PECVD SiO_2 is the maximum tolerable temperature. BCB has a glass temperature[11] of 350 °C which limits its use in high-temperature applications. Table 2-4 compares some relevant properties of BCB and silicon dioxide films.

[11] Glass transition temperature is defined as the temperature above which the material converts from a brittle and glassy state into ductile and rubbery state.

Table 2-4: Comparison of physical properties and deposition parameters of BCB and SiO_2.

Property/Material	BCB	SiO_2
Dielectric constant	2.65	3.9
Deposition process/method	Spin-casting, Spray-coating	PECVD and thermal
Deposition temperature	250 °C	200-1100 °C
Max. thickness	~50 μm	~20 μm
Residual stress	28 MPa, tensile	100-300 MPa, tensile or compressive
Glass transition temp	350 °C	-

BCB was primarily developed as an inter-level dielectric (ILD) and passivation coating in microelectronic interconnects [99, 100]. It has been used in multichip module (MCM) packaging [101-104], flip-chip solder bumping [105, 106], Damascene copper (Cu) interconnect [107], as a stress buffer and passivation layer [108], as an insulating dielectric in RF high-Q inductors [109] and for optical waveguides [110, 111]. Humidity sensors [112], microswitches [113], and microfilters [114] are examples of devices utilizing BCB. BCB has also been used in packaging [115] and adhesive bonding [113, 116-118].

Some preliminary studies on the mechanical, optical, and electrical properties of the film have now enabled the use of the BCB as a MEMS material. The mechanical properties of this film including fatigue effects on adhesion [119, 120], strain-stress relationship, coefficient of thermal expansion (CTE), residual stress , and adhesion to different substrate materials have been previously reported [121, 122]. The index of refraction has been measured and reported [123]. The electrical characterization of the film including dielectric constant, breakdown voltage, I-V characteristics, and the effect of moisture on these properties have been reported by our group [89]. Some MEMS devices have already been fabricated using this polymer. BCB diaphragm was demonstrated for its low thermal conductivity (0.0029 $Wcm^{-1}K^{-1}$) and mechanical

robustness in a MEMS-based infra-red detector [124]. BCB has been also used for fabricating single mode optical waveguides at 1300 nm [110]. Plane and curved waveguide mirrors, the latter acting in the same way as cylindrical lenses, are made with enhanced reflectivity by metallization of edges [111]. A red blood cell microfilter was fabricated using BCB as a channel and bonding material [114]. In this device blood cells are forced to pass through capillaries made out of BCB and glass that are slightly smaller than their diameter. Healthy cells have enough deformability to pass through the capillary. Chemical-mechanical planarization of BCB for both integrated circuits and MEMS technology has been developed in the past few years [125, 126].

In this dissertation, we have used BCB as interlayer dielectric, passivation, and insulation layer due to its low permittivity and residual stress.

2.4 Theory of Micromachine Operation

2.4.1 Physics of Operation

The rotary variable-capacitance micromotor discussed here is a synchronous[12] electrostatic machine. The stator (stationary part) is composed of a periodic structure of metal conductors (electrodes) with a fixed spacing between them. The rotor (movable part) is composed of a periodic salient silicon structure (poles), also with a fixed spacing but different from that of the electrodes. Figure 2-4 shows the simplified cross section of the device. If a potential is applied to an electrode, image charges are induced on an adjacent pole. The resulting tangential and normal forces are shown in Figure 2-4. The tangential force is the propelling force of the rotor

[12] In the synchronous machines, unlike asynchronous (induction) counterparts, the mechanical motion of the rotor and electrical excitation of the stator are in sync i.e. follow one another.

which tries to align a rotor pole to an adjacent active electrode. The normal force acts normal to the rotor and helps to keep the rotor on the stator. Continuous motion of the rotor is possible by sequential excitation of the electrodes.

Each electrode-pole pair makes a variable capacitor which has the lowest value when the pair is completely misaligned. In contrast, the capacitance value is the highest when the pair is completely aligned. The machine operates as a motor when the capacitance of each phase increases from a minimum value (complete misalignment) to a maximum value (complete alignment). The motoring behavior occurs when the derivative of capacitance is positive. Similarly, the machine is a generator when the derivative of capacitance is negative.

In an ideal lossless system, with no electrical and mechanical losses, the machine can simply be modeled as a lossless variable capacitor. The instantaneous current (i) of the variable capacitor (C) can be written as

$$i = \frac{d}{dt}(q) = \frac{d}{dt}(vC) = v\frac{dC}{dt} + C\frac{dv}{dt} \qquad \textbf{Eq. 2-1}$$

where *q, i, v*, and *C* which represent charge, current, voltage, and capacitance, respectively, and all are assumed to be time-varying *(t)* functions. The instantaneous electrical power *(p)* delivered to the system can be written as

$$p = vi = v^2\frac{dC}{dt} + Cv\frac{dv}{dt} = \frac{1}{2}v^2\frac{dC}{dt} + \frac{1}{2}v^2\frac{dC}{dt} + Cv\frac{dv}{dt} \qquad \textbf{Eq. 2-2}$$

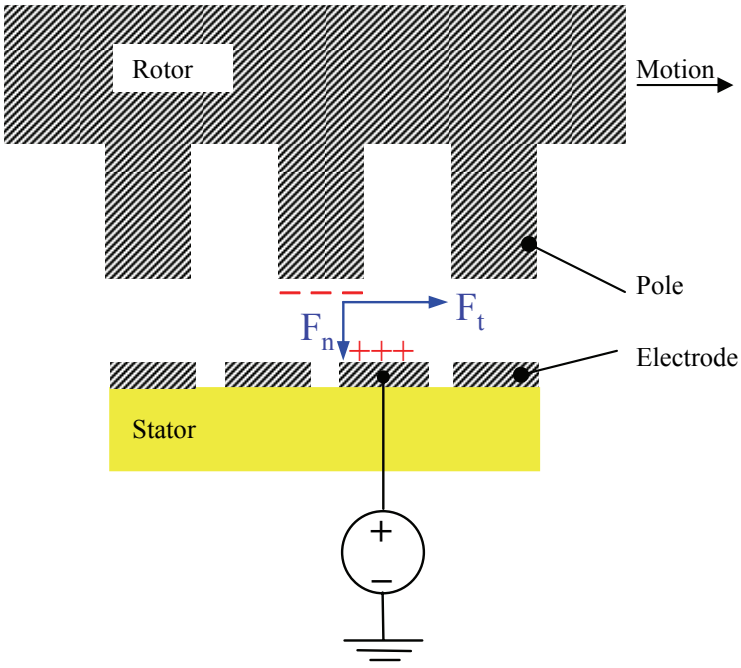

Figure 2-4: Simplified cross section of the micromotor showing tangential and normal forces produced by the electrostatic field between electrodes and poles.

The first term on the right-hand side of the above equation $\left(p_1 = \frac{1}{2} v^2 \frac{dC}{dt} \right)$ is the mechanical power. The proof for this argument is given by Bollee [13] and is rearranged here for clarity. If we rewrite the equation in differential format, the total input energy given to the system in a short time of *dt* can be written as

$$pdt = vidt = v^2 dC + Cv\, dv \qquad \textbf{Eq. 2-3}$$

Part of the input energy *(pdt)* is stored in the electric field of the capacitor. Since the instantaneous stored energy of the capacitor with voltage *v* and capacitance *C* is given by

$$W_{Stored} = \frac{1}{2} Cv^2 \qquad \textbf{Eq. 2-4}$$

the change of W_{stored} in the small time of *dt* can be calculated (by method of differentiation) to be

$$dW_{Stored} = d\left(\frac{1}{2}Cv^2\right) = \frac{1}{2}v^2 dC + Cvdv \qquad \textbf{Eq. 2-5}$$

The remaining energy that is not stored in a loss-less system can be delivered to the load as the mechanical energy,

$$pdt - dW_{Stored} = \frac{1}{2}v^2 dC \qquad \textbf{Eq. 2-6}$$

Therefore, the mechanical power delivered to the load in an ideal lossless system is

$$p_1 = \frac{1}{2}v^2 \frac{dC}{dt} \qquad \textbf{Eq. 2-7}$$

This power (p_1) is due to the mechanical work, which must be performed by or on a system at voltage v to change its capacitance at the rate of $\frac{dC}{dt}$. The second and third terms in the Eq. 2-3 are the stored power in the system. The term $p_2 = \frac{1}{2}v^2 \frac{dC}{dt}$ represents the change in the stored energy of the electric field due to change in the capacitance. The term $p_3 = Cv\frac{dv}{dt}$ represents the energy transferred from the external power source *(p)* to the electrostatic field due to the change in the voltage *(v)*.

When $p_2>0$ the electric energy is being absorbed by the system and the mechanical work is delivered. This state corresponds to a machine working as a motor. The motor behavior is also shown Figure 2-4; the opposite charges on a single electrode-pole attract each other and the rotor moves until the pair is aligned. In contrast, when $p_2<0$ the mechanical energy is being absorbed by the system and the electrical work is delivered. This state corresponds to a machine working as a generator. The sign of p_2 is the same as $\frac{dC}{dt}$. Therefore, assuming no phase difference between v^2 and (dC/dt),

one can conclude: $dC/dt > 0$ corresponds to the motor state and $(dC/dt) < 0$ corresponds to the generator state. The above inequalities for the sign of (dC/dt) are only written when an excitation voltage (v) is applied to the capacitor. Therefore, the regime in which the machine operates depends on the sign of (dC/dt) and its interaction with voltage (phase difference). For this reason, with correct excitation, the micromotor can potentially be used as a microgenerator.

2.4.2 Role of Power Angle in Operation of the Machine

As mentioned above, the regime in which the machine operates depends on the interaction of the excitation voltage and the mechanical movement (dC/dt). This characteristic is expected from any synchronous machine. In order to illustrate the effect of phase difference on the produced power, we assume that the capacitance and excitation voltage have the simple forms of

$$C(t) = C_m \sin^2(\omega_0 t) \qquad \textbf{Eq. 2-8}$$

$$v(t) = V_m \sin(\omega_0 t + \phi) \qquad \textbf{Eq. 2-9}$$

respectively; where ω_0 is the angular frequency of the applied voltage and ϕ is the phase difference between $v(t)$ and $C(t)$ (ϕ is also known as the power angle[13]). The angular frequency (ω_0) is chosen to be identical for both $v(t)$ and $C(t)$. This is a valid assumption for any synchronous machine. $C(t)$ is chosen to have a sinusoidal-squared form with minimum and maximum of 0 and C_m , respectively[14]. To identify the role

[13] The definition of power angle in other types of machines such as magnetic machines may differ from what is assumed here. No matter what definition is chosen, the result is the same.
[14] Finite element analysis (FEA), discussed in Chapter 3, has proven that the choice of the sine-squared function for the capacitance is a valid.

of phase difference *(ϕ)* on the produced electrical or mechanical power we derive *(dC/dt)* as

$$\frac{dC(t)}{dt} = 2C_m\omega_0 \sin(\omega_0 t)\cos(\omega_0 t) = C_m\omega_0 \sin(2\omega_0 t) \qquad \textbf{Eq. 2-10}$$

Figure 2-5 conceptualizes a variable-capacitance motor by plotting $v^2(t)$, $C(t)$, $dC(t)/dt$, and $p_1 = \frac{1}{2}v^2\frac{dC}{dt}$ for a case where $\phi = \frac{\pi}{4}$. The average produced mechanical power in one period, as shown in Figure 2-5, is positive; therefore, the machine operates as a motor in this region $\left(0 < \phi < \frac{\pi}{2}\right)$.

Power angle $\phi=0$ corresponds to the generalized case when the average produced mechanical power is zero. In this state, the machine is neither a motor nor a generator. This case corresponds to the transitional point between the two regimes and is shown in Figure 2-6. Similarly, when $\phi < \frac{\pi}{2} < 0$ the machine is a generator with negative mean mechanical power as shown in Figure 2-7 for $\phi = -\frac{\pi}{4}$.

The last three figures show the relationship between power, voltage, and capacitance at a three specific power angles. Thus, a more general case for the produced power for a range of power angles is shown in Figure 2-8. The maximum power in motoring mode is at $\phi=\pi/4$. Similarly, at $\phi=-\pi/4$ the maximum mechanical power is consumed (generator).

To maximize the output power of the micromachine, one might use periodic square-shape pulses (either positive or negative in amplitude) instead of the

sinusoidal waveform, however, this reduces the efficiency of the machine[15]. Square-pulse excitation, changes the interaction of power angle and produced power. During the first half of the square-pulse excitation the maximum amplitude is applied and positive power is produced. In the second half, however, the excitation is zero and no negative power is generated. Figure 2-9 shows this phenomenon. Similar to Figure 2-8, the average mechanical power can be calculated for the excitation with a half-wave square voltage. Figure 2-10 shows the average mechanical power versus power angle. Compared to the sinusoidal case, when excited with a half-wave square signal, the motor produces a peak power at $\phi=0$ instead of $\phi=\pi/4$. As shown in this figure, the machine with no load (torque) will have a power angle of $\phi = \pm\frac{\pi}{4}$. This explains the power angle adjustment of the synchronous machine at different torque conditions and plays an important role in understanding the operation of the machine.

2.5 Angular Velocity

One characteristic of any machine is the relative velocity of the rotor with respect to the stator. The velocity is defined in the forms of angular velocity *($\omega_{mech.}$)* of the mechanical motion of the rotor in rad/s, or frequency of rotor rotation *(n_r, f_r)* in rpm or Hertz. Choosing one of these notations over others could simplify a particular derivation or equation. In the following discussions all three ($\omega_{mech.}$, n_r, and f_r) are used.

[15] Efficiency is discussed at the end of this Chapter.

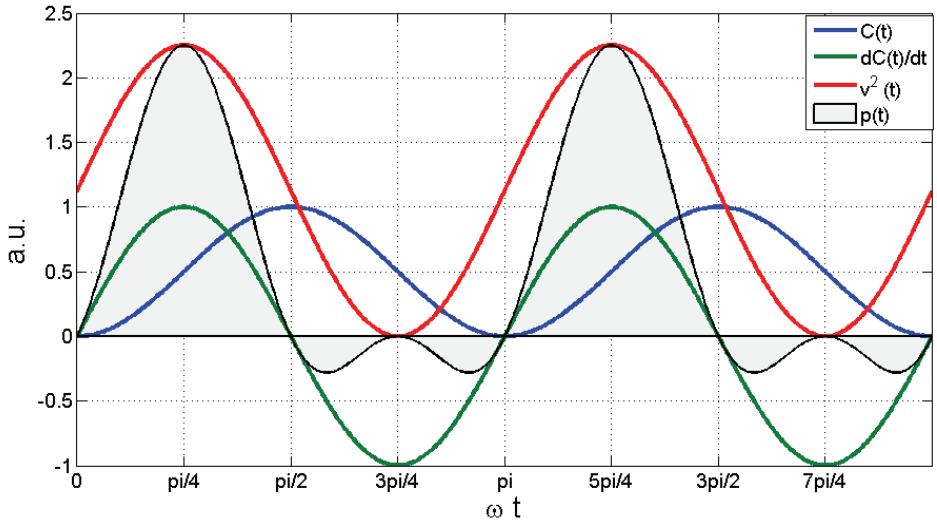

Figure 2-5: Variable-capacitance micromachine in the motor regime produces mechanical power. The four graphs are shown at a constant power angle of $\phi = \pi/4$.

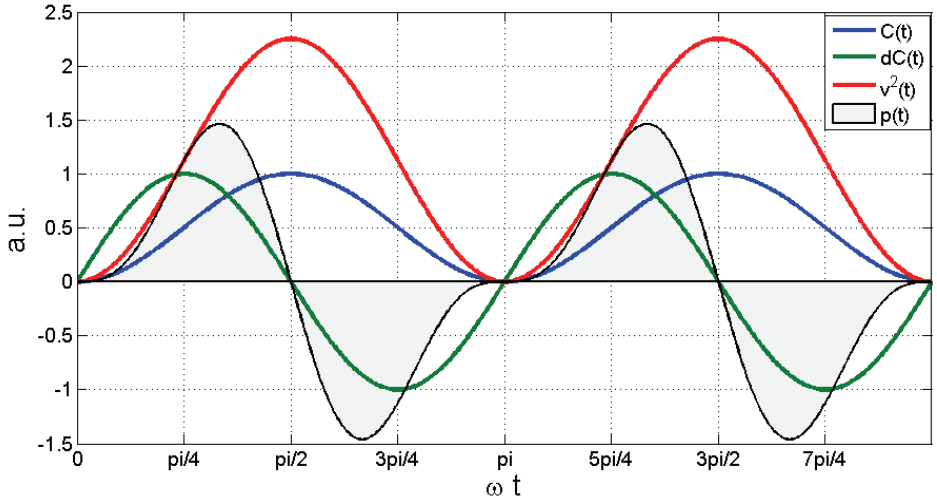

Figure 2-6: Variable-capacitance micromachine in the at a constant power angle of $\phi = 0$ *shows the transition between generator and motor regimes.*

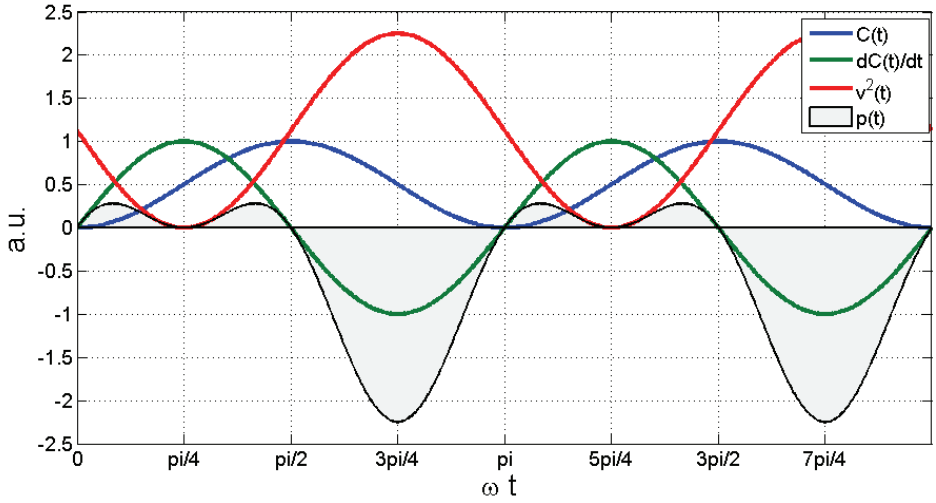

Figure 2-7: Variable-capacitance micromachine in the generator regime consumes mechanical power. The four graphs are shown at a constant power angle of $\phi = -\pi/4$.

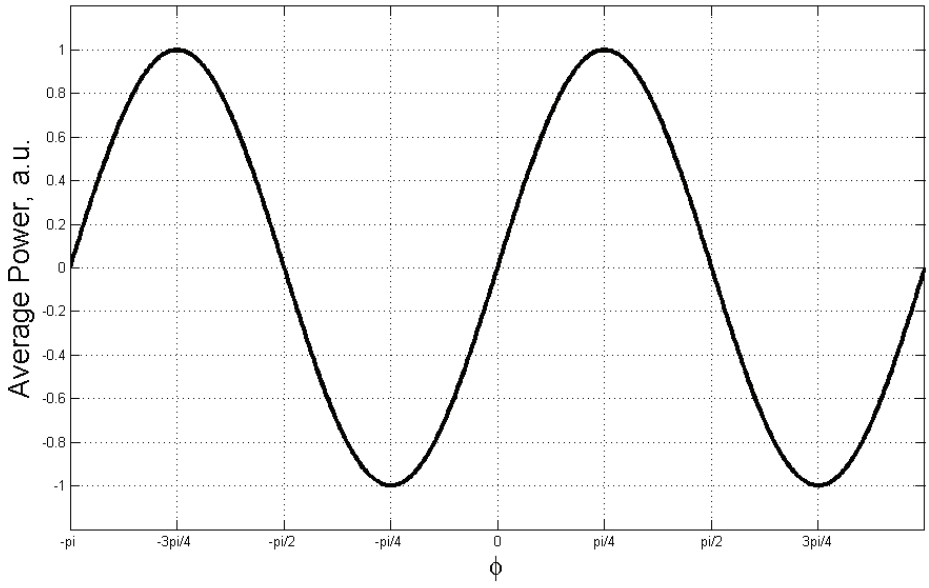

Figure 2-8: Average mechanical power of the variable-capacitance machine versus the power angle. The machine produces and consumes maxim mechanical power at π/4 and -π/4, respectively.

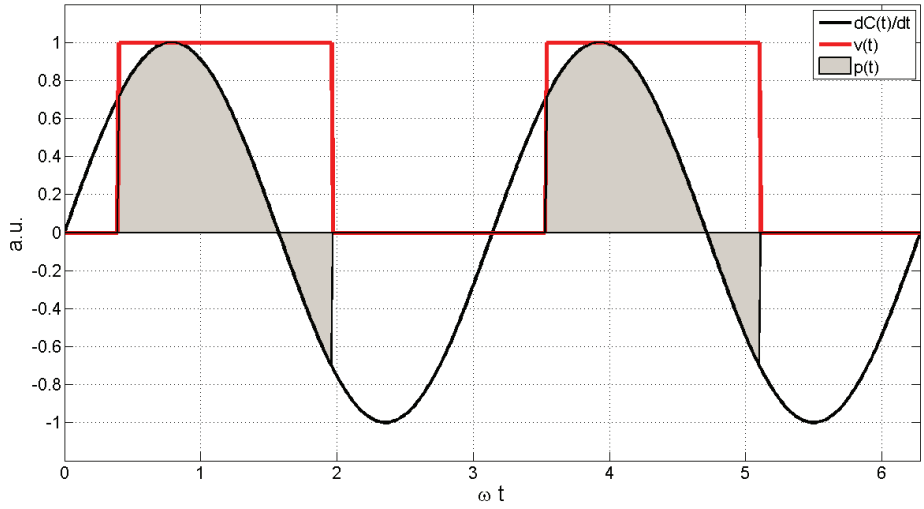

Figure 2-9: Interaction of a positive square waveform with the capacitance change results in higher produced power than conventional excitation with sinusoidal waveform.

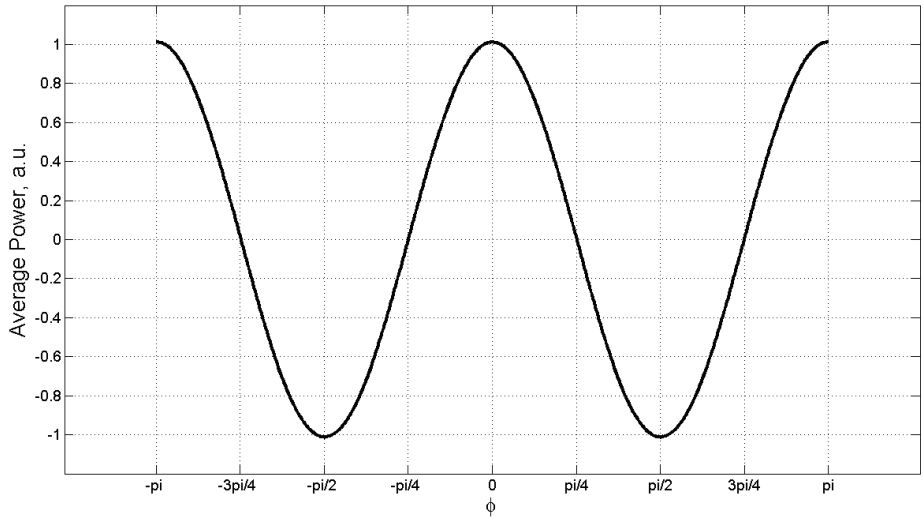

Figure 2-10: Average mechanical power of the variable-capacitance machine versus the power angle when excited with square-shape pulses as shown in the previous figure.

Three independent methods are reported here for calculation of the angular velocity of the machine. Later on in this chapter, it is discussed why these results are different from what is reported in the literature.

2.5.1 Velocity from Linear Micromotor

The linear speed of the slider[16] for a variable-capacitance machine, can be written as

$$u_r = 2Wf_{elec.} \qquad \textbf{Eq. 2-11}$$

where u_r is the linear speed of the slider in $\frac{m}{s}$, W is the width of the electrode on the stator in m, and $f_{elec.}$ is the frequency of excitation voltage applied to the stator in Hz [127]. This equation is based on the assumption that the spacing between two adjacent poles equals their width *(W)*. Assuming the period of $T_{elec.}$ for the excitation voltage $\left(T_{elec.} = 1/f_{elec.}\right)$, it is observed that if the mechanical motion of the slider is synchronous with electrical excitation, the slider would move the linear distance equal to the pole width (W) in a time equal to half of the period $\left(T_{elec.}/2\right)$. A similar formula can be applied to the rotary machine with some modifications described below.

Using the linear mechanical speed and substituting the linear velocity with equivalent angular velocity for a rotary machine results in

$$r\,\omega_{mech.} = 2Wf_{elec.} \qquad \textbf{Eq. 2-12}$$

where r is the radius of the circular rotor, and $\omega_{mech.}$ is the angular velocity of the rotor. Since *rpm* unit for speed is usually more practical, we can write $\omega_{mech.}$ as a function of n_r using

$$\omega_{mech.} = \frac{2\pi}{60} n_r \qquad \textbf{Eq. 2-13}$$

Therefore,

[16] Slider refers to the moving part of the linear micromotor which is equivalent to the rotor for the rotary device.

$$r\frac{2\pi}{60}n_r = 2Wf_{elec.} \quad \textbf{Eq. 2-14}$$

where n_r is in *rpm*. Since for a rotary machine with N_p number of poles

$$\frac{2\pi r}{N_p} = 2W \quad \textbf{Eq. 2-15}$$

We can re-write

$$r\frac{2\pi}{60}n_r = \frac{2\pi r}{N_p}f_{elec.} \quad \textbf{Eq. 2-16}$$

Therefore,

$$n_r = 60\frac{f_{elec.}}{N_p} \quad \textbf{Eq. 2-17}$$

where n_r is rotor mechanical speed in rpm, $f_{elec.}$ is frequency of the electrical excitation in *Hz*, and N_p is the number of poles of the rotor. Similar to the linear machine, the spacing between the poles of the rotary machine is assumed to be *W*. The above equation describes the synchronization of electrical excitation voltage and mechanical rotation of the rotor.

2.5.2 Velocity: Intuitive Method

It is also possible to derive the above equation without the use of linear machine relations. If one were to stand on an electrode which is excited with a constant frequency ($f_{elec.}$) and look at the poles of the machine, he/she will observe N_p complete capacitance charging cycles in each mechanical revolution. Therefore, one electrical frequency is equal to $1/N_p$ mechanical angular frequency. As a result, the mechanical angular speed ($\omega_{mech.}$) of the rotor, in synchronous with the electrical angular frequency ($\omega_{elec.}$), is

$$\omega_{mech.} = \frac{\omega_{elec.}}{N_p} \qquad \textbf{Eq. 2-18}$$

With the same argument, the electrical angle ($\theta_{elec.}$) and spatial angle ($\theta_{mech.}$) of the machine are related by the following expression

$$\theta_{elec.} = N_p \theta_{mech.} \qquad \textbf{Eq. 2-19}$$

The main characteristic of a synchronous machine is that the average mechanical speed is only a function of the excitation frequency and the geometry of the machine. Hence, with a given geometry, it is expected that a VCM operate at a constant speed independent of the mechanical load conditions, as long as the excitation frequency is kept constant.[17]

2.5.3 Velocity: Exact Method[18]

The synchronous angular velocity of the rotor also can be derived from electric field theory. Assuming that the stator is excited with a 3-phase, square waveform with a frequency of ω_0 and phase difference of $2\pi/3$, the instantaneous and position dependent traveling potential (main harmonic only) on a single stator electrode (without the presence of the rotor) is written as

$$\varphi_1^{(1)}(r,\theta,t) = C(r)\ \sin(\omega_0 t)\ \ \sin(\upsilon\theta) \qquad \textbf{Eq. 2-20}$$

The superscript and subscript of φ denotes the phase number and harmonic number, respectively, r and θ are the coordinates of the cylindrical system and υ is the number of stator segments. In this approach the traveling potential which is a function of r, θ, and t is written as a product of three functions. Each of these functions only depends

[17] Constant velocity operation mode at different torques is only possible when the applied torque is not exceeding the maximum sustainable torque.
[18] Derivation is rearranged based on the results of the personal communication with Professor Isaak Mayergoyz, University of Maryland (Dec 2006).

on one variable only. *C(r)* is the radius-dependent function, $sin\omega_0 t$ represents the 1st harmonic of the electrical excitation signal and $sin\upsilon\theta$ represents the angular dependency of the rotating potential.

Figure 2-11 shows the 2D simulation results of the electric field lines of the stator with 4 electrodes without the presence of the rotor. Because in a variable capacitance machine the gap is small and the rotor pole width is comparable to the stator width, the traveling potential corresponding to the electric field line of Figure 2-11 is perturbed with the presence of the bulky rotor. The perturbed field, shown in Figure 2-12, is now a function of the rotor position and has the position dependency of $\upsilon=N_p$ where N_p is the number of "poles" on the rotor. Therefore, the modified potential for a micromotor with presence of the rotor is

$$\varphi_1^{(1)}(r,\theta,t) = C(r)\ \sin(\omega_0 t)\ \ \sin(N_p\theta) \qquad \textbf{Eq. 2-21}$$

Consequently, the potential for the second and third phases can be respectively written as

$$\varphi_1^{(2)}(r,\theta,t) = C(r)\ \sin\left(\omega_0 t-\frac{2\pi}{3}\right)\ \ \sin\left(N_p\theta-\frac{2\pi}{3}\right) \qquad \textbf{Eq. 2-22}$$

$$\varphi_1^{(3)}(r,\theta,t) = C(r)\ \sin\left(\omega_0 t-\frac{4\pi}{3}\right)\ \ \sin\left(N_p\theta-\frac{4\pi}{3}\right) \qquad \textbf{Eq. 2-23}$$

The total instantaneous potential is simply the sum of all three potentials

$$\varphi_1(r,\theta,t) = \varphi_1^{(1)}(r,\theta,t)+\varphi_1^{(2)}(r,\theta,t)+\varphi_1^{(3)}(r,\theta,t) \qquad \textbf{Eq. 2-24}$$

$$\varphi_1(r,\theta,t) = C(r)\ \sin(\omega_0 t)\ \ \sin(N_p\theta)+\ C(r)\ \sin\left(\omega_0 t-\frac{2\pi}{3}\right)\ \ \sin\left(N_p\theta-\frac{2\pi}{3}\right)+$$
$$C(r)\ \sin\left(\omega_0 t-\frac{4\pi}{3}\right)\ \ \sin\left(N_p\theta-\frac{4\pi}{3}\right)$$

Eq. 2-25

Using the following equality

$$\sin\alpha\sin\beta = 1/2\left[\cos(\alpha-\beta)-\cos(\alpha+\beta)\right] \qquad \textbf{Eq. 2-26}$$

and adding up the three terms will results in

$$\varphi\ (r,\theta,t) = \frac{3}{2}C(r)\ Cos(\omega_0 t - N_p\theta)$$
$$+\frac{1}{2}C(r)\left[\cos(\omega_0 t + N_p\theta)+\cos\left(\omega_0 t + N_p\theta - \frac{2\pi}{3}\right)+\cos\left(\omega_0 t + N_p\theta - \frac{4\pi}{3}\right)\right]$$

Eq. 2-27

In the latter, the second term in the bracket equals zero. This can be easily seen by using the equation

$$\cos(\alpha-\beta) = \cos\alpha\cos\beta+\sin\alpha\sin\beta \qquad \textbf{Eq. 2-28}$$

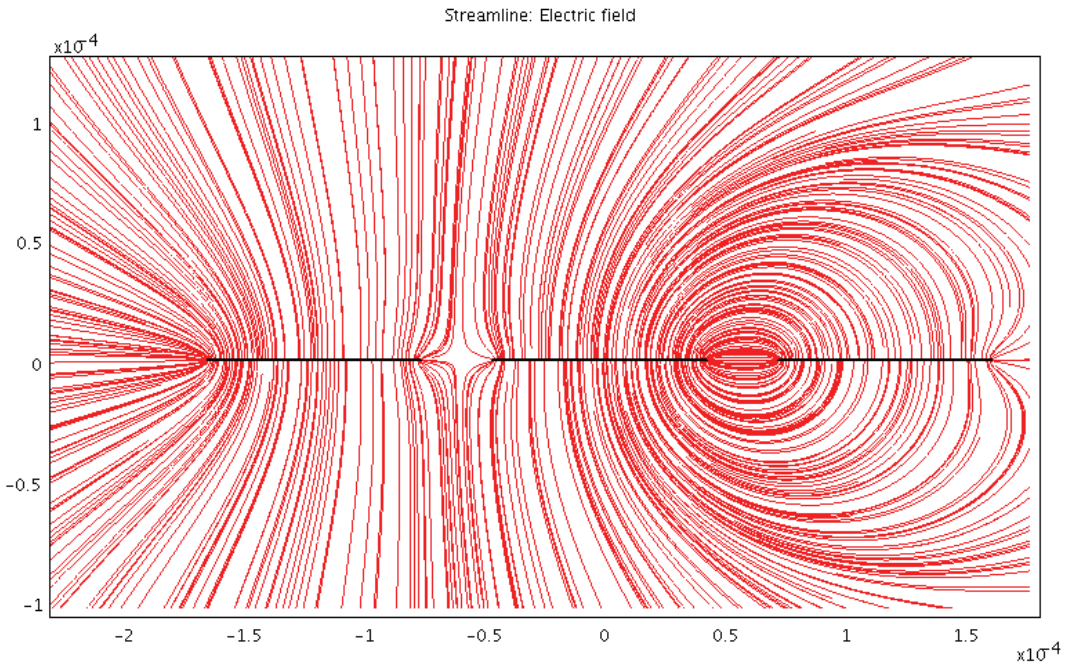

Figure 2-11: Comsol Multiphysisc (FEMLAB) simulation of electric field streamlines for three stator electrodes each 0.5 μm thick and 90 μm wide. The left two electrodes have the potential v=1 V and the right electrode is grounded.

Therefore,

$$\cos\left(\omega_0 t + N_p\theta - \frac{2\pi}{3}\right) = \cos\left(\omega_0 t + N_p\theta\right)\cos\left(\frac{2\pi}{3}\right) + \sin\left(\omega_0 t + N_p\theta\right)\sin\left(\frac{2\pi}{3}\right) \quad \textbf{Eq. 2-29}$$

$$\cos\left(\omega_0 t + N_p\theta - \frac{4\pi}{3}\right) = \cos\left(\omega_0 t + N_p\theta\right)\cos\left(\frac{4\pi}{3}\right) + \sin\left(\omega_0 t + N_p\theta\right)\sin\left(\frac{4\pi}{3}\right) \quad \textbf{Eq. 2-30}$$

Adding up the three terms in the bracket results is zero. Therefore the potential is

$$\varphi\ (r,\theta,t) = \frac{3}{2}C(r)\ \ Cos\left(\omega_0 t - N_p\theta\right) \quad \textbf{Eq. 2-31}$$

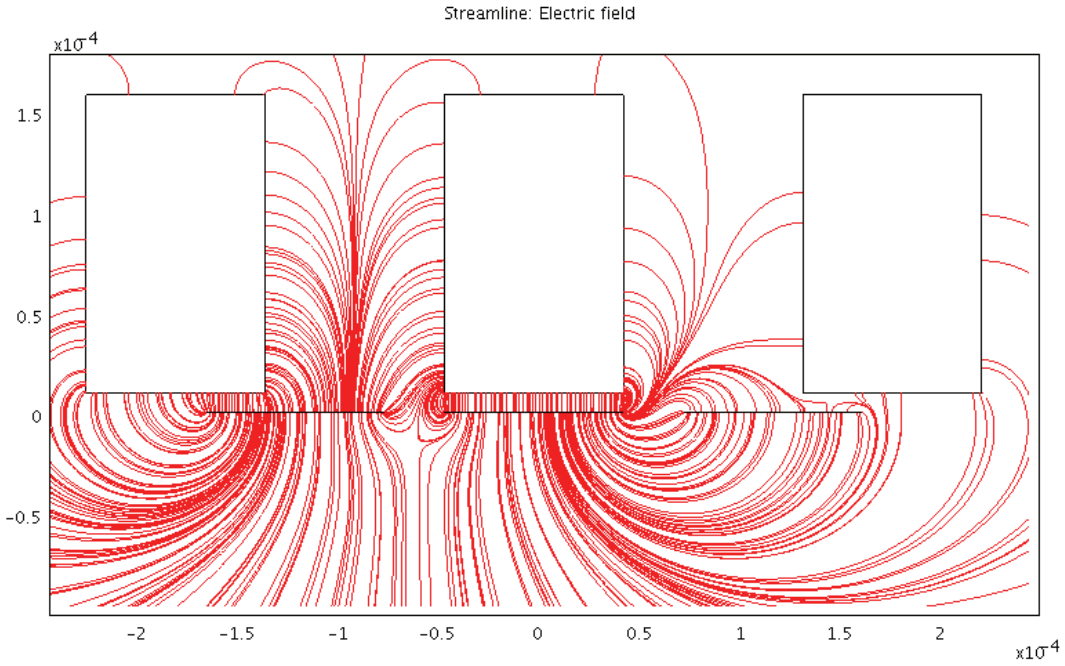

Figure 2-12: Comsol Multiphysisc (FEMLAB) simulation of electric field streamlines for three stator electrodes and three rotor poles. The poles are each 150 μm tall and 90 μm wide. The left two electrodes have the potential V=1 v and the right electrode, as well as the poles are grounded. The field lines have drastically been modified compared to the previous figure due to the existence of the rotor.

In order to satisfy the condition of synchronization, the second term in the above equation must be constant. For an observer traveling in synch with the traveling potential, there should be no change in the amplitude of potential. As long as the observer travels azimuthally with a constant radius we can write

$$Cos\left(\omega_0 t - N_p \theta(t)\right) = Const \qquad \textbf{Eq. 2-32}$$

$$\omega_0 t - N_p \theta(t) = Const \qquad \textbf{Eq. 2-33}$$

By differentiating two sides of the equation

$$\frac{d}{dt}\left(\omega_0 t - N_p \theta(t)\right) = 0 \qquad \textbf{Eq. 2-34}$$

$$\omega_0 - N_p \frac{d\theta(t)}{dt} = 0 \qquad \textbf{Eq. 2-35}$$

The value $\frac{d\theta(t)}{dt}$ is the angular velocity of the rotor. Therefore, the synchronous angular velocity $\omega_{synch.}$ can be written as

$$\omega_{synch.} = \frac{d\theta(t)}{dt} = \frac{\omega_0}{N_p} \qquad \textbf{Eq. 2-36}$$

or

$$\omega_{synch.} = \frac{2\pi f_0}{N_p} \qquad \textbf{Eq. 2-37}$$

The angular rotor velocity in rpm is

$$n_r = \frac{60 f_0}{N_p} \qquad \textbf{Eq. 2-38}$$

2.5.4 Magnetic Versus Electrostatic

The speed of a variable-capacitance machine is often mistaken from the equation describing the speed of magnetic synchronous machines (inaccurate expression is

given by Trump [14]). The discrepancy originates from the definition of a pole. In a magnetic machine, a pair of poles (*N*-*S*) makes the complete magnetic flux circuit; therefore, there are $N_p/2$ pairs in a machine. A single pole pair (*N*-*S*) is equivalent to 2π electrical radians. The electrical angle ($\theta_{elec.}$) and the spatial angle ($\theta_{mech.}$) of a magnetic machine have the following relationship

$$\theta_{elec.}\Big|_{magnetic\ \ machine} = \left(\frac{N_p}{2}\right)\theta_{mech.} \qquad \textbf{Eq. 2-39}$$

The difference between the speed of a magnetic and electrostatic machine is the factor of $\frac{1}{2}$ for N_p. The more elaborate comparison was provided in the previous section when $\upsilon=N_p$ for a variable-capacitance machine and $\upsilon=N_p/2$ for the magnetic counterparts.

2.6 Torque and Mechanical Power

Torque is a fundamental machine property that needs to be evaluated. The derivation of instantaneous and average torque of the machine is presented in this section. The body of the rotor is considered to rotate about the *z*-axis where *z* is the direction normal to the electrode surface (*r*, θ, and *z* are cylindrical coordinates). For a small angular displacement ($d\theta$) the mechanical work performed by (or on) the rotor is

$$dW^* = -T\,d\theta \qquad \textbf{Eq. 2-40}$$

where W^* is co-energy of a single capacitor and *T* is torque about the *z*-axis. The co-energy is defined as

$$W^*(v) = vq - W(q) \qquad \textbf{Eq. 2-41}$$

where q is the charge of the capacitor $C(\theta)$ in coulombs, and $W(q)$ is the stored potential energy in the capacitor in Joules. The co-energy function is given by [128]

$$W^*(v,\theta)=\frac{1}{2}C(\theta)v^2 \qquad \textbf{Eq. 2-42}$$

Torque (T) produced by a single variable-capacitor can also be written in a form of

$$T=-\frac{\partial W^*(v,\theta)}{\partial\theta}\Big|_{v=cons\tan t} \qquad \textbf{Eq. 2-43}$$

where v is the applied voltage and considered to be constant and θ is defined in counterclockwise angle from the x-axis. Therefore, the torque produced in a rotary machine with a single capacitor is

$$T(v,\theta)=-\frac{\partial W^*(v,\theta)}{\partial\theta}\bigg|_{v=cons\tan t}=-\frac{1}{2}v^2\frac{\partial C(\theta)}{\partial\theta} \qquad \textbf{Eq. 2-44}$$

or the torque produced by an electrode-pole pair with capacitance C_1

$$T_1(v,\theta)=-\frac{1}{2}v^2\frac{\partial C_1(\theta)}{\partial\theta} \qquad \textbf{Eq. 2-45}$$

Assuming that the stator electrodes of the machine are excited in a six-phase configuration where three phases are excited with positive square pulses (each $2\pi/3$ apart) and the other three are excited identical to the first except with inverse amplitude, the torque produced by each group of phases, or each "sector", consisting of $N_e/6$ electrodes will be

$$T_{sector\,1}(v,\theta)=\frac{N_e}{6}T_1(v,\theta)=-\frac{N_e}{6}\frac{1}{2}v^2\frac{\partial C_1(\theta)}{\partial\theta} \qquad \textbf{Eq. 2-46}$$

where $T_{sector\,1}(v,\theta)$ is the total torque from similar phases (e.g. *Phase A*) of the machine, N_e is number of electrodes on the stator, and C_1 is the capacitance of one particular phase. Geometrical symmetry of the machine suggests

$$\frac{\partial C_n}{\partial \theta} = \frac{\partial C_{n+3}}{\partial \theta} \quad \textbf{Eq. 2-47}$$

where n is 1, 2, or 3. Excitation voltage is also symmetric (two of six phases are excited identical with inverse amplitudes). Therefore,

$$T_{sector\,1}(v,\theta) = T_{sector\,4}(v,\theta) \quad \textbf{Eq. 2-48}$$

$$T_{sector\,2}(v,\theta) = T_{sector\,5}(v,\theta) \quad \textbf{Eq. 2-49}$$

$$T_{sector\,3}(v,\theta) = T_{sector\,6}(v,\theta) \quad \textbf{Eq. 2-50}$$

The total torque of the machine can be written as

$$T'(v,\theta) = T_{sector\,1}(v,\theta) + T_{sector\,2}(v,\theta) + T_{sector\,3}(v,\theta) + T_{sector\,4}(v,\theta) + T_{sector\,5}(v,\theta) + T_{sector\,6}(v,\theta) \quad \textbf{Eq. 2-51}$$

$$T'(v,\theta) = 2T_{sector\,1}(v,\theta) + 2T_{sector\,2}(v,\theta) + 2T_{sector\,3}(v,\theta) \quad \textbf{Eq. 2-52}$$

The above equation is based on the assumption that at each time ($t=t_1$) all the electrode-pole pairs produce torque. This is not valid for a real machine. Assuming $N_p/N_e = 4/6$ for a 6:4 machine, at $t=t_1$ either 2 or 4 pairs are active and participate in producing torque. Therefore, on average ½ of the electrode-pole pairs are not excited. Total torque of the machine can be written as

$$T(v,\theta) = \frac{1}{2}T'(v,\theta) \quad \textbf{Eq. 2-53}$$

$$T(v,\theta) = T_{sector\,1}(v,\theta) + T_{sector\,2}(v,\theta) + T_{sector\,3}(v,\theta) \quad \textbf{Eq. 2-54}$$

$$T(v,\theta) = -\left[\frac{N_e}{6}\frac{1}{2}v^2\frac{\partial C_1(\theta)}{\partial \theta} + \frac{N_e}{6}\frac{1}{2}v^2\frac{\partial C_2(\theta)}{\partial \theta} + \frac{N_e}{6}\frac{1}{2}v^2\frac{\partial C_3(\theta)}{\partial \theta}\right] \quad \textbf{Eq. 2-55}$$

$$T(v,\theta) = \frac{-1}{12}N_e v^2\left(\frac{\partial C_1(\theta)}{\partial \theta} + \frac{\partial C_2(\theta)}{\partial \theta} + \frac{\partial C_3(\theta)}{\partial \theta}\right) \quad \textbf{Eq. 2-56}$$

In above equation, v is given in volts (V), $\frac{\partial C(\theta)}{\partial(\theta)}$ in $\frac{F}{rad}$, and torque in $N.m$.

Torque can be analytically evaluated if $\frac{\partial C_n(\theta)}{\partial \theta}$ values are known. Finite element method (FEM) is used[19] to simulate $C(\theta)$ and derive $\frac{\partial C_n(\theta)}{\partial \theta}$. The average total torque for the six-phase machine can be calculated by integration:

$$\overline{T}_{total} = \frac{T_{\max}}{2\pi}\left[\int_0^{\pi}\sin(\omega t) + \int_{\frac{2\pi}{3}}^{\frac{5\pi}{3}}\sin\left(\omega t - \frac{2\pi}{3}\right) + \int_{\frac{4\pi}{3}}^{2\pi}\sin\left(\omega t + \frac{2\pi}{3}\right) + \int_0^{\frac{\pi}{3}}\sin\left(\omega t + \frac{2\pi}{3}\right)\right] \quad \textbf{Eq. 2-57}$$

where T_{max} is the amplitude of a single-phase torque. As a result,

$$\overline{T}_{total} = \frac{-T_{\max}}{2\pi}\left[(\cos\pi - \cos 0) + (\cos\pi - \cos 0) + \left(\cos\frac{2\pi}{3} - \cos 2\pi\right) + \left(\cos\pi - \cos\frac{2\pi}{3}\right)\right] \quad \textbf{Eq. 2-58}$$

$$\overline{T}_{total} = \frac{-T_{\max}}{2\pi}[-6] \quad \textbf{Eq. 2-59}$$

$$\overline{T}_{total} = \frac{3T_{\max}}{\pi} = 0.9549T_{\max} \quad \textbf{Eq. 2-60}$$

Figure 2-13 shows the theoretical toque of each phase, as well as the total instantaneous torque which is the sum of all phases.

[19] Finite element analysis of $C(\theta)$ is discussed in Chapter 3.

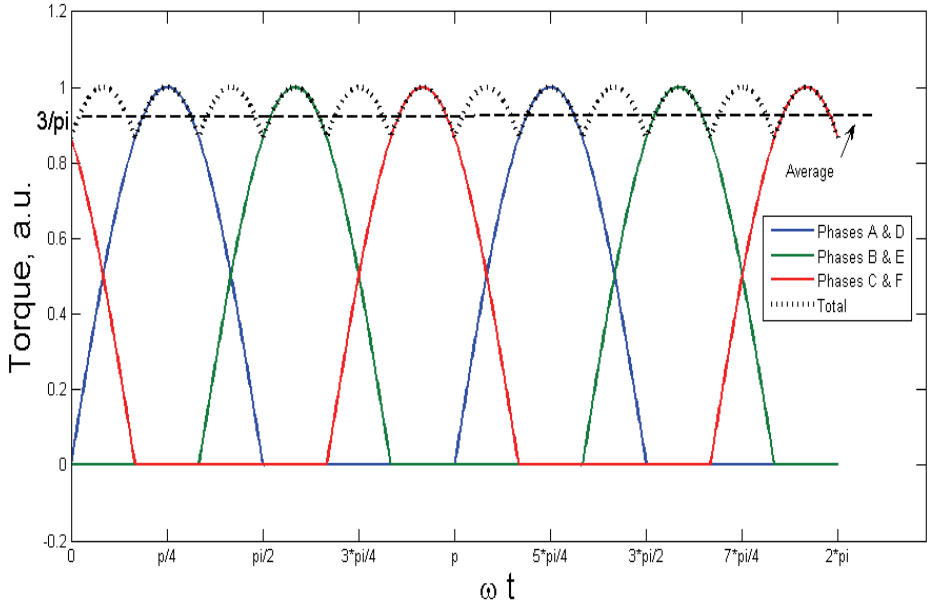

Figure 2-13: Instantaneous toque of all six phases as a function of the time, as well as the total torque and the average torque of the six-phase machine.

Several observations can be made from the velocity and torque equations: Torque is proportional to the square of excitation voltage (v^2). Unlike speed, torque is directly proportional to number of electrodes or poles (N_e or N_p). A machine with many electrodes (N_e large) has a large torque but it is slow. In contrast, a machine with small N_e is fast but incapable of producing a large torque. Torque is independent of $\omega_{elec.}$. Electromechanical torque (T) of the motor is negative. This is because $dC/dt>0$ in motor. Similarly, since $dC/dt<0$ in the generator, electromechanical torque is positive. The torque is only defined at the synchronous speed of $\omega_{mech.} = \frac{\omega_{elec.}}{N_p}$.

Unlike an induction (asynchronous) machine, a synchronous machine is not self-

starting[20]. Due to the synchronization in variable-capacitance machines, the successful starting from zero speed to the synch speed depends on the position of the rotor, as well as phase and frequency of the applied voltage. External mechanical start of the motor may be necessary in some cases. In practice $\frac{\partial C_n(\theta)}{\partial \theta}$ is not independent of N_e. In a rotary machine N_e (or N_p) is a function of the electrode (or pole) width, the spacing between them, and the radius of the machine. Changing the parameters will change N_e and $C(\theta)$. However, Increasing N_e may result in decrease in $\frac{\partial C_n(\theta)}{\partial \theta}$. Therefore, choosing large N_e for obtaining large T is not always a preferred approach. This issue is studied in Chapter 3.

Once the torque of the machine is derived, the output (input) mechanical power of the motor (generator) can be given as

$$P(v,\theta) = -\omega_{mech.}\, T(v,\theta) \qquad \textbf{Eq. 2-61}$$

Substituting mechanical angular velocity with electrical angular frequency in the above equation using $\omega_{mech.} = \frac{\omega_{elec.}}{N_p}$ results in

$$P(v,\theta) = -\frac{\omega_{elec.}}{N_p} T(v,\theta) \qquad \textbf{Eq. 2-62}$$

By substitution

$$P(v,\theta) = \frac{\omega_{elec.}}{N_p} \frac{1}{12} N_e v^2 \left(\frac{\partial C_1(\theta)}{\partial \theta} + \frac{\partial C_2(\theta)}{\partial \theta} + \frac{\partial C_3(\theta)}{\partial \theta} \right) \qquad \textbf{Eq. 2-63}$$

$$P(v,\theta) = \frac{1}{12} \frac{N_e}{N_p} \omega_{elec.} v^2 \left(\frac{\partial C_1(\theta)}{\partial \theta} + \frac{\partial C_2(\theta)}{\partial \theta} + \frac{\partial C_3(\theta)}{\partial \theta} \right) \qquad \textbf{Eq. 2-64}$$

[20] An induction machine produces non-zero torque at zero speed, maximum torque at speeds less than ω_{mech}, and zero torque at synchronous speed.

The above equation can be further simplified assuming $N_p / N_e = 4/6$,

$$P(v,\theta) = \frac{1}{12} \cdot \frac{6}{4} \omega_{elec.} v^2 \left(\frac{\partial C_1(\theta)}{\partial \theta} + \frac{\partial C_2(\theta)}{\partial \theta} + \frac{\partial C_3(\theta)}{\partial \theta} \right) \quad \textbf{Eq. 2-65}$$

$$P(v,\theta) = \frac{1}{8} \omega_{elec.} v^2 \left(\frac{\partial C_1(\theta)}{\partial \theta} + \frac{\partial C_2(\theta)}{\partial \theta} + \frac{\partial C_3(\theta)}{\partial \theta} \right) \quad \textbf{Eq. 2-66}$$

It can be seen that the mechanical power is proportional to $\omega_{elec.}$, voltage-squared, and derivative of capacitance and independent of number of electrodes.

2.7 Power Generation

In the previous sections, the velocity of the machine, electromechanical torque, and mechanical power were derived. We may consider the same device being used as a microgenerator. In this case, the electrical output of the generator is of great importance and is discussed here. The results from this discussion are insightful to the micromotor and are used for evaluating two different modes of operation of the micromotor as well as analyzing efficiency. For simplicity, the non-ideal effects like electrical and mechanical losses are neglected in this section[21]. The electric power for a lossless variable-capacitance machine can be derived from charge-voltage *(Q-V)* behavior of the machine during different work cycles. Figure 2-14 shows these work cycles for the motor and generator, respectively. A variable capacitor, $C(\theta)$, with a voltage V and charge $Q = C(\theta) V$ and maximum and minimum of C_{max} and C_{min} is considered in this case. When running a machine as a motor, path *ABCA* from Figure 2-14 is taken. Capacitor C_{min} is first charged with a voltage source to voltage V_0. The capacitor charge at point *B* is

[21] Non-ideal effects are discussed in the next section.

$$Q_B = C_{\min} V_0 \qquad \textbf{Eq. 2-67}$$

Path *AB* in Figure 2-14(a) shows this cycle. In the next cycle, the voltage at the two terminals of the capacitor is kept constant using an ideal voltage source (V_0). This is performed in synchronous with the mechanical movement of the machine which causes the change in the capacitance from C_{max} to C_{min}. Since $Q = CV_0$, the charge of the capacitor will increase due to increase in the capacitance value. The increase in the charge (ΔQ) equals

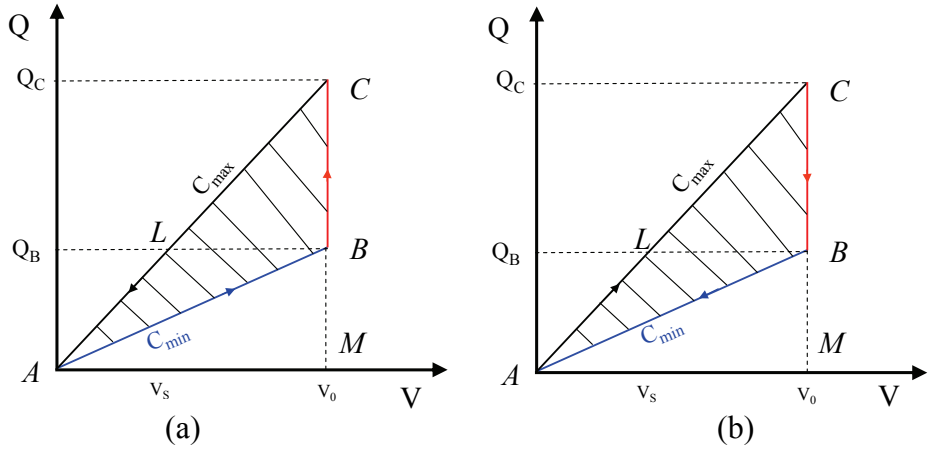

Figure 2-14: ***Charge-voltage cycles for a variable capacitance motor (a) and generator (b). While motor passes ABCA (ABLA) cycles, generator passes ACBA (ALBA) cycle in a constant voltage (constant charge) mode. The area of triangle ABC and ALB corresponds to electric energy consumed or produced in constant voltage and constant charge modes, respectively.***

$$\Delta Q = Q_C - Q_B = (C_{\max} - C_{\min}) V_0 \qquad \textbf{Eq. 2-68}$$

ΔQ is a product of the electromechanical work (path *BC*) performed by the system. The cycle ends with discharging C_{max} (path *CA*) down to the zero volts. The reverse cycle is shown in Figure 2-14(b) for the generator. In this case, C_{max} is charged following the path *AC* with voltage V_0. The charge of the capacitor at point *C* is

$$Q_C = C_{\max} V_0 \qquad \textbf{Eq. 2-69}$$

The voltage is kept constant (path *CB*) at V_0 while the capacitance drops from C_{max} to C_{min}. The new charge on the capacitor is then Q_B. This is the electromechanical work cycle where external mechanical force performs work using electric field. C_{min} is discharged into an external energy tank (reservoir) down to zero volts (path *BA*)[22].

While the motor passes path *ABCA*, the generator passes path *ACBA*. This mode of operation is called *constant voltage*, because the voltage of the variable capacitor is externally kept constant using a voltage source. This mode can be used for both motor and generator; however, due to complexity of drive circuits used for charging and discharging the capacitor in generator-mode, it is preferred to run the generator in another mode called *constant charge*. This mode can also be used for the motor; however, drive circuit for motor is not as simple as *constant voltage* mode. The *constant charge* path is shown in Figure 2-14(a) and (b) as paths of *ABLA* and *ALBA*, respectively. The fundamental difference is that *BC* (*CB*) is replaced with *BL* (*LB*). During this period, the charge of the capacitor (instead of voltage) is kept constant. This can be accomplished by opening any circuit connected to the capacitor using a switch. The advantage of this mode to the *constant voltage* mode is that there is no need for using high-voltage source (V_0) during electromechanical cycle. This simplifies the drive requirements of the system. One can use the Figure 2-14 to derive the electric energy and power. The slope of the *AC* and *AB* illustrates C_{max} and C_{min}, respectively. Therefore,

$$C_{\max} = \frac{\overline{CM}}{\overline{AM}} \qquad \textbf{Eq. 2-70}$$

[22] In practice the time constant of the mechanical cycle (C_{min} to C_{max} or reverse) is much larger than the time constant of electrical cycles i.e. chare and discharging of the capacitor.

$$C_{\min} = \frac{\overline{BM}}{\overline{AM}} \qquad \textbf{Eq. 2-71}$$

Subtracting two values results in

$$C_{\max} - C_{\min} = \frac{\overline{CM}}{\overline{AM}} - \frac{\overline{BM}}{\overline{AM}} = \frac{\overline{CB}}{\overline{AM}} \qquad \textbf{Eq. 2-72}$$

By rearranging the above equation

$$\overline{CB} = \overline{AM}\left(C_{\max} - C_{\min}\right) = V_0\left(C_{\max} - C_{\min}\right) \qquad \textbf{Eq. 2-73}$$

where $\overline{AM} = V_0$. The electrical power can be calculated using Figure 2-14. The energy stored in the system is

$$E = \int Q\, dV \qquad \textbf{Eq. 2-74}$$

where E is the electrical energy in Joules. The area of triangles *ABC* and *ABL* defines the electrical energy in *constant voltage* ($E_{voltage}$) and *constant charge* (E_{charge}) modes, respectively. These areas are equal to

$$E_{voltage} = S^{\Delta}_{ABC} = \frac{1}{2}\overline{CB}\ \overline{AM} = \frac{1}{2}\left(C_{\max} - C_{\min}\right)V_0^2 \qquad \textbf{Eq. 2-75}$$

Therefore, the energy in the *voltage constant* mode is

$$E_{voltage} = \frac{1}{2}\left(C_{\max} - C_{\min}\right)V_0^2 \qquad \textbf{Eq. 2-76}$$

Similarly, in the *constant-charge* mode we have

$$E_{charge} = S^{\Delta}_{ABL} = S^{\Delta}_{ABC} - S^{\Delta}_{BCL}\ E_{charge} = \left[\frac{1}{2}\left(C_{\max} - C_{\min}\right)V_0^2\right] - \left[\frac{1}{2}\overline{CB}\ \overline{BL}\right] \qquad \textbf{Eq. 2-77}$$

Replacing *CB* and *BL* using $\overline{CB} = V_0\left(C_{\max} - C_{\min}\right)$ and $\overline{BL} = V_0 - V_s$ results in

$$E_{charge} = \left[\frac{1}{2}\left(C_{\max} - C_{\min}\right)V_0^2\right] - \left[\frac{1}{2}\left(V_0\left(C_{\max} - C_{\min}\right)\right)\left(V_0 - V_s\right)\right] \qquad \textbf{Eq. 2-78}$$

$$E_{charge} = \frac{1}{2}\left(C_{\max} - C_{\min}\right) V_0 V_s \qquad \textbf{Eq. 2-79}$$

This equation can be further simplified. Using geometry shown in Figure 2-14 we can write

$$\frac{C_{\max}}{C_{\min}} = \frac{\dfrac{\overline{CM}}{\overline{AM}}}{\dfrac{\overline{BM}}{\overline{AM}}} = \frac{\overline{CM}}{\overline{BM}} = \frac{\overline{AC}}{\overline{AL}} = \frac{\overline{AC}}{AL}\frac{\cos\left(\hat{CAM}\right)}{\cos\left(\hat{CAM}\right)} = \frac{V_0}{V_s} \qquad \textbf{Eq. 2-80}$$

Therefore, the *charge constant* energy can be further simplified as

$$E_{charge} = \frac{1}{2}\left(C_{\max} - C_{\min}\right) V_0 V_s \qquad \textbf{Eq. 2-81}$$

$$E_{charge} = \frac{1}{2}\left(C_{\max} - C_{\min}\right) V_s \frac{C_{\max}}{C_{\min}} V_s \qquad \textbf{Eq. 2-82}$$

$$E_{charge} = \frac{1}{2}\frac{C_{\max}}{C_{\min}}\left(C_{\max} - C_{\min}\right) V_s^2 \qquad \textbf{Eq. 2-83}$$

It is clear from Figure 2-14 that the energy produced in the *constant voltage* mode is higher than the energy produced in the *constant charge* mode. The power of the machine (motor and generator) can be calculated from energy relations. Assuming the machine is rotating with mechanical frequency of $f_{mech.}(Hz)$, we can write the average electric power to be

$$\overline{P}_{elec.} = E\ f_{mech.}\ N_p\left(\frac{1}{2}N_e\right) \qquad \textbf{Eq. 2-84}$$

where $P_{elec.}$ is the average electric power in Watts and E is the energy in Joules. It was mentioned earlier that in these types of machines during ½ of the time, 4 of 6 phases are excited and during the other half only 2 of 6 phases are excited. Therefore, on average, $N_e/2$ electrodes are excited and participate in electric power production. The

N_p term in the power equation counts for the fact that in each rotation a single excited electrode passes by N_p poles. The N_e term counts for all of the electrodes that are excited in each rotation. Since

$$N_p = \frac{4}{6} N_e \qquad \textbf{Eq. 2-85}$$

the power can be written as

$$\overline{P}_{elec.} = E\ f_{mech.}\ (\frac{1}{3} N_e{}^2) \qquad \textbf{Eq. 2-86}$$

In order to write the mechanical speed in rpm units we use

$$2\pi f_{mech.} = \frac{2\pi}{60} n_r \qquad \textbf{Eq. 2-87}$$

Substituting $f_{mech.}$ with rotation frequency in rpm unit (n_r) results in

$$\overline{P}_{elec.} = E\ \frac{n_r}{60}\ (\frac{1}{3} N_e{}^2) \qquad \textbf{Eq. 2-88}$$

$$\overline{P}_{elec.} = \frac{1}{180} E\ n_r\ N_e^2 \qquad \textbf{Eq. 2-89}$$

where $P_{elec.}$ is in Watts, E in Joules, and n_r in rpm. Substituting E with E_{charge} results in

$$\overline{P}_{elec.}\Big|_{charge\ const.} = \frac{1}{180} E_{charge}\ n_r\ N_e^2 \qquad \textbf{Eq. 2-90}$$

$$\overline{P}_{elec.}\Big|_{charge\ const.} = \frac{1}{180}\frac{1}{2}\frac{C_{\max}}{C_{\min}}\left(C_{\max} - C_{\min}\right) V_s^2\ n_r\ N_e^2 \qquad \textbf{Eq. 2-91}$$

$$\overline{P}_{elec.}\Big|_{charge\ const.} = \frac{1}{360}\frac{C_{\max}}{C_{\min}}\left(C_{\max} - C_{\min}\right) V_s^2\ n_r\ N_e^2 \qquad \textbf{Eq. 2-92}$$

Electric power for *constant voltage* mode is similarly calculated to be

$$\overline{P}_{elec.}\Big|_{voltage\ const.} = \frac{1}{180} E_{voltage}\ n_r\ N_e^2 \qquad \textbf{Eq. 2-93}$$

$$\overline{P}_{elec.}\Big|_{voltage\ const.} = \frac{1}{180}\frac{1}{2}\left(C_{\max} - C_{\min}\right) V_0^2\ n_r\ N_e^2 \qquad \textbf{Eq. 2-94}$$

$$\overline{P}_{elec.}\Big|_{voltage\ const.} = \frac{1}{360}\left(C_{\max} - C_{\min}\right) V_0^2\ n_r\ N_e^2 \qquad \textbf{Eq. 2-95}$$

The two equations describing the power for two modes have two significant differences. First, the power in the *constant voltage* mode is proportional to V_0^2, whereas, the power in *constant charge* equation is proportional to V_s^2. Since $V_s < V_0$, the power of *constant charge* mode is expected to be less than *constant voltage* mode. Second, the term $\frac{C_{\max}}{C_{\min}} > 1$ does not exist in the *constant voltage* equation.

2.8 Losses and Efficiency

A micromachine converts one form of energy to another i.e. electrical to mechanical energy. This energy transduction is often accompanied with losses in the system. Two types of losses are associated with the micromotor: mechanical and electrical. Figure 2-15 shows the flow diagram of energy from the electrical input to the mechanical output. Some electrical energy is lost in the form of heat in power electronics, stator electrodes, and rotor conductors (poles). Frictional losses of rolling and sliding bearings and viscous drag loss of a rotating disk are the major sources of mechanical loss.

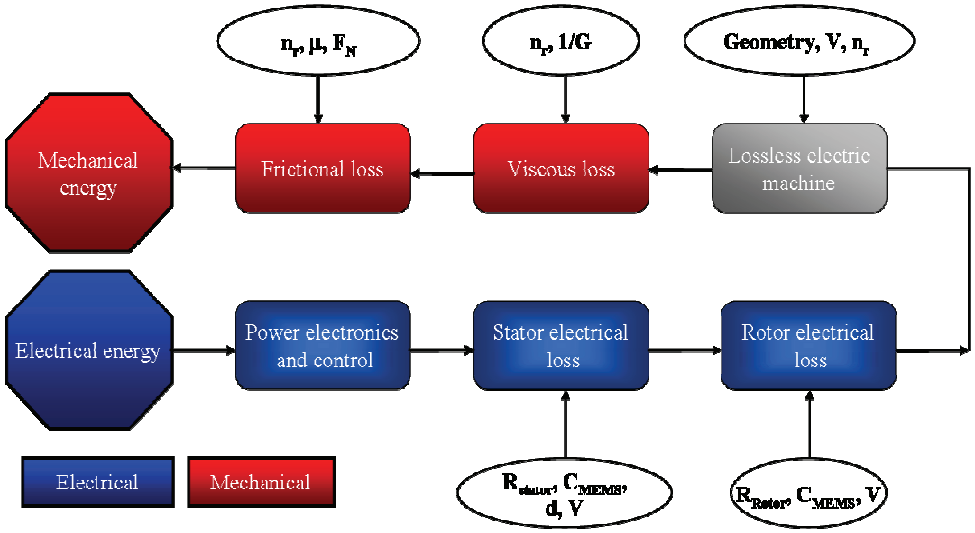

V: Applied voltage, n_r: Rotor speed, G: Air gap, d: dielectric thickness, μ: coefficient of friction, F_N: Normal force on the rotor, R: Resistance

Figure 2-15: Energy flow diagram of the micromotor showing energy losses at various stages.

The power electronics and stator electrical loss are calculated here. The system shown in Figure 2-15 can be modeled as a variable capacitor (C_{MEMS}) excited with a voltage source, $v_i(t)$,through a small source resistor, R, in series with C_{MEMS}. When the micromotor is excited with a periodic square pulse, C_{MEMS} is charged and discharged through R. The step response of such an RC system would be

$$v_o(t) = V_0\left(1 - e^{\frac{-t}{RC_{MEMS}}}\right)u(t) \qquad \textbf{Eq. 2-96}$$

where

$$v_i(t) = V_0\, u(t) \qquad \textbf{Eq. 2-97}$$

and $v_o(t)$ is the C_{MEMS} voltage, $u(t)$ is the unit step function, and V_0 is the amplitude of the step. Therefore, the current through both capacitor and resistor, $i(t)$, is

$$i(t) = \frac{v_o(t) - v_i(t)}{R} = V_0\,\frac{1 - e^{\frac{-t}{RC_{MEMS}}} - 1}{R}\,u(t) = V_0\,\frac{-e^{\frac{-t}{RC_{MEMS}}}}{R}\,u(t) \qquad \textbf{Eq. 2-98}$$

The instantaneous dissipation power, $p'(t)$, on the resistor is

$$p'(t) = R\, i^2(t) = V_0^2 \frac{e^{\frac{-2t}{RC_{MEMS}}}}{R}\ u(t) \qquad \textbf{Eq. 2-99}$$

The average power would be[23]

$$\langle p'(t) \rangle = \int_{t=0}^{\infty} V_0^2 \frac{e^{\frac{-2t}{RC_{MEMS}}}}{R}\ u(t)\, dt = V_0^2 \frac{-RC_{MEMS}}{2} \frac{1}{R}(0-1) = \frac{1}{2} V_0^2\ C_{MEMS} \qquad \textbf{Eq. 2-100}$$

Therefore, the dissipated power is independent of the resistor size. Considering a periodic square pulse, with a fixed frequency of f_0 applied to a variable capacitor $C_{Min}<C_{MEMS}<C_{Max}$, the total average dissipated power would be

$$\langle p(t)_{Loss} \rangle = \frac{1}{2} V_0^2\ C_{Min} + \frac{1}{2} V_0^2 C_{Max} = \frac{1}{2} V_0^2 (C_{Min} + C_{Max}) \qquad \textbf{Eq. 2-101}$$

The above equation is written with the assumption that the charge and discharge of the capacitor is occurred exactly when the capacitance is at minimum and maximum values, respectively (motor). As shown in the previous section, the energy produced in a *constant-voltage* cycle is

$$E_{voltage} = \frac{1}{2}(C_{\max} - C_{\min}) V_0^2 \qquad \textbf{Eq. 2-102}$$

And the average power is

$$\langle P_{Out} \rangle = \frac{1}{2}(C_{\max} - C_{\min}) V_0^2 f_0 \qquad \textbf{Eq. 2-103}$$

Finally, the theoretical efficiency of the system is

$$\eta = \frac{\langle P_{Out} \rangle}{\langle P_{In} \rangle} = \frac{\langle P_{Out} \rangle}{\langle P_{Out} \rangle + P_{Loss}} = \frac{C_{Max} - C_{Min}}{2C_{Max}} = \frac{1}{2}\left(1 - \frac{C_{Min}}{C_{Max}}\right) \qquad \textbf{Eq. 2-104}$$

The maximum theoretical system efficiency is 50% for $C_{Min}=0$.

[23] C_{MEMS} was treated as a constant when calculating the integral. This is a valid assumption since the RC time constant is orders of magnitude smaller than the period of the excitation signal.

3 Design and Simulation

3.1 Introduction

The first step in designing the micromachine is to identify the relevant parameters, i.e. input and output variables. The input design variables are geometrical features, electrical, mechanical, material properties of components, and electrical excitation schemes. The output variables are toque, angular velocity, and efficiency of the machine. The relationship between output variables and input variables were derived in Chapter 2. In this chapter, the detailed design methodology of the micromotor is reported. First, geometric, electrical, mechanical, and material considerations are discussed first. Next, finite element simulations used for modeling the effects of input variables on the output variables. Several micromotors with different geometries are the outcome of the study. Final design details are discussed and the output variables are provided for each design. Finally, a CAD tool is used for drawing the geometries. This step has been the most challenging part of the design due to the complexity of the 9-level-mask layout.

3.2 Design Considerations and Limitations

The rotary micromotor, as discussed in Chapter 2, is composed of three components: stator, rotor, and microballs. The microballs are available in a diameter of $\phi=285.4$ μm. The geometry of the stator and rotor are designed based on the factors discussed in this section.

3.2.1 Geometrical Considerations

The detailed schematic cross section of the micromotor was shown in Chapter 2. Several geometric parameters are shown in the simplified cross section schematic of Figure 3-1. These include the distance between the surface of electrode-pole pairs known as the air gap (G), the width of the electrode and pole (W)[24], the spacing between adjacent electrodes (W/a), the spacing between adjacent poles ($b \times W$), the thickness of electrode (h_e), and the pole depth (h_p). All these parameters are identified in Figure 3-1. The thickness of the dielectric layer underneath the electrodes can also be considered as a design parameter determining the parasitic capacitance of the machine.

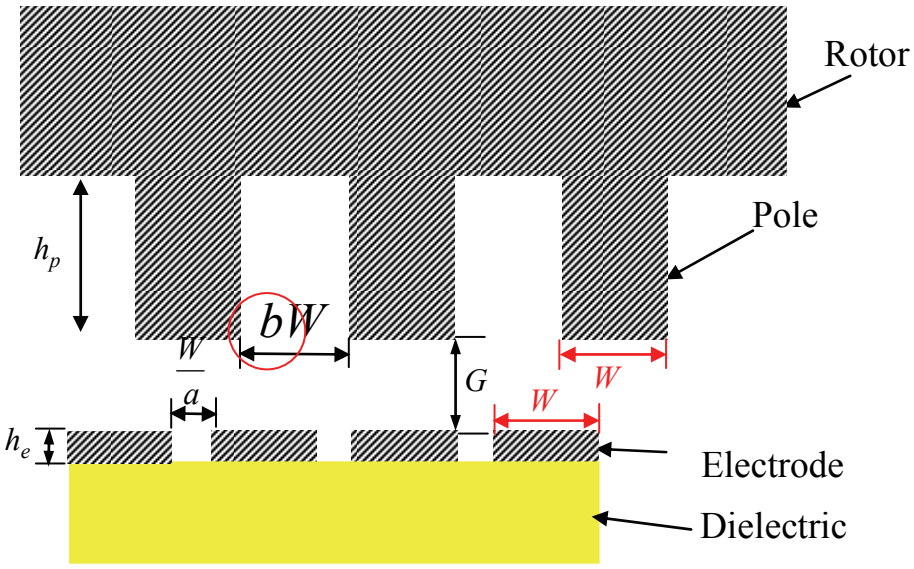

Figure 3-1: Simplified cross section schematic of the machine showing design parameters such as electrode width/height, pole width/height, gap, and distance between the electrodes and poles.

In a 6/4 machine there are for 4 poles on the rotor for each 6 electrode on the stator. Therefore, b and a are mutually dependent and are related by

[24] For simplicity of design the, width of stator electrodes and rotor poles are assumed to be identical.

$$b = \frac{1}{2}\left(1 + \frac{3}{a}\right) \qquad \textbf{Eq. 3-1}$$

The effect of *a* or *b* on the performance of the machine is studied in the next section. For simplicity, *a* is called the *packing factor* throughout this manuscript. Figure 3-1 shows an overview of finite element simulation and device geometry design. Each block will be explained in detail in this chapter.

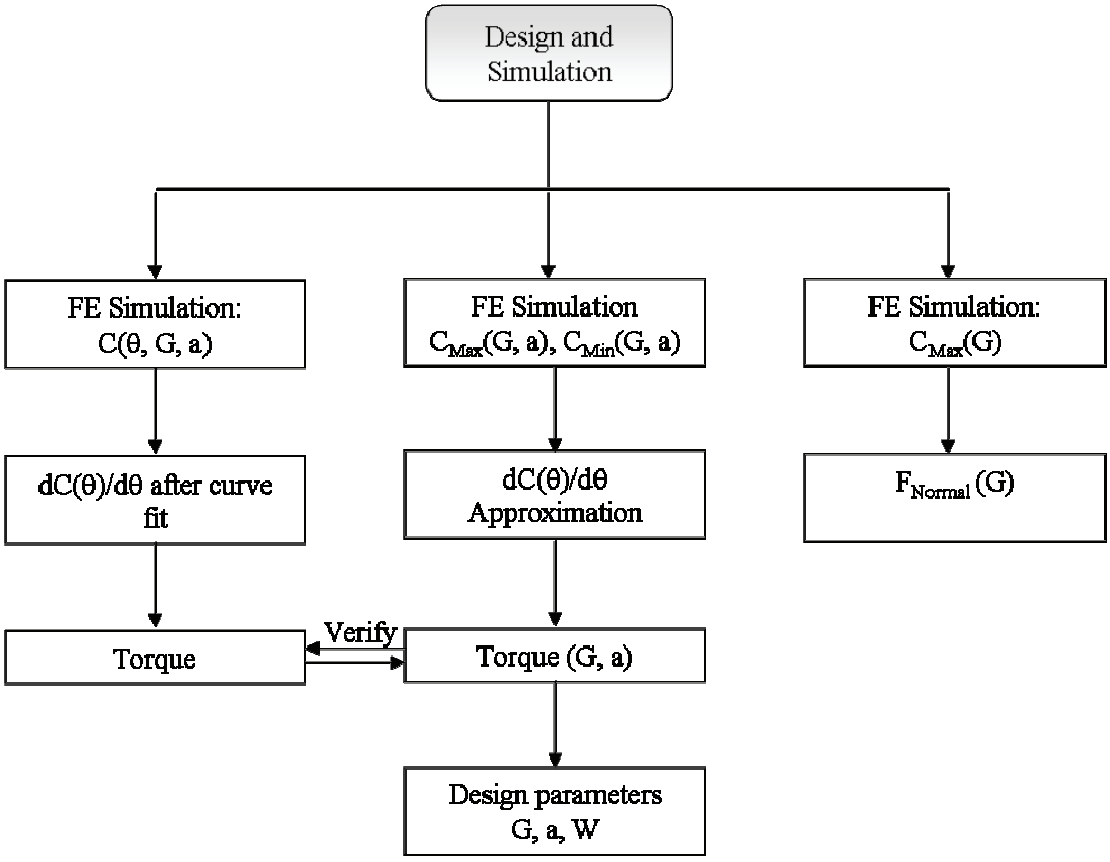

Figure 3-2: Block diagram showing overall design and simulation procedure.

The electrodes on the stator are placed radially in groups of six to form a six-phase machine. The geometry of these electrodes dictates the overall geometry of the device. Figure 3-3 illustrates the top view schematic of the stator with several electrodes, six contact pads, and a trench. The geometry of the electrodes and poles is determined through a series of FE simulations discussed in the next section. The

trench radius and device outer radius (R_3-R_4) are chosen based on the outer radius of the electrodes (R_2).

The size of the each contact pad was chosen to be 180 ×180 μm^2 so that probing with needles would be fairly convenient. A smaller pad size would make the probing difficult and time consuming. In contrast, a larger pad size would reduce the active area of the motor and the torque. As mentioned earlier, these pads are accessed through an opening in the rotor. Therefore, R_1 shown in Figure 3-3, is chosen to be 1 mm so that six probe needles pass through rotor cavity without any electrical contact to one another or the rotor.

The trench width is chosen to be 290 μm on the stator and rotor; just about 4.6 μm wider than the diameter of the ball. This assures that the balls are freely encapsulated inside the housing. The possibility of depositing thin lubricant film, as well as fabrication imperfections during lithography and DRIE steps were also considered.

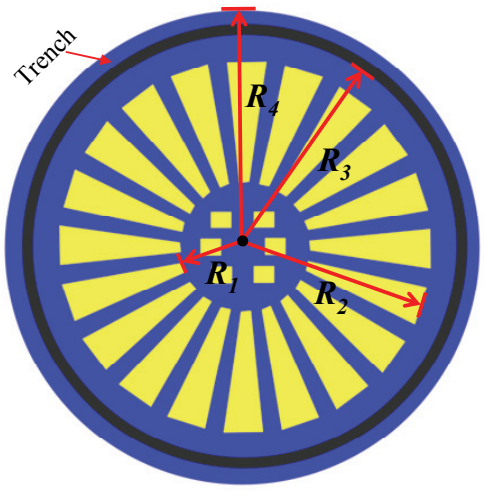

Figure 3-3: Top view schematic of the stator showing several design parameters such as electrode inner radius (R_1), electrode outer radius (R_2), microball housing radius (R_3) and width, and outer device radius (R_4).

3.2.2 Electrical, Mechanical, and Material Considerations

The rotary micromotor, as discussed in Chapter 2, is a variable-capacitance machine. As a result, the physical properties of the components are chosen to match an ideal variable capacitor. From the electrical point of view the machine requires conductors and dielectrics. Consequently, gold film was used for electrodes due to high electrical conductivity and Benzocyclobutene (BCB) polymer films were used as dielectric material due to high breakdown voltage, high volume resistance, and low relative permittivity. Other factors for choosing BCB are high level of planarization, low deposition temperature, high resistance to chemicals, low residual stress, and low moisture absorption.

The substrates on which the stator and rotor are built were chosen to be silicon because of its excellent mechanical properties needed for building the microball housing and available fabrication technologies. The substrate resistivity was chosen to be relatively low (1-10 Ω·cm) for two reasons: First, the large conductive mass ensures a uniform potential throughout the rotor. This is crucial because the rotor is not electrically grounded and could charge up during operation. Second, high conductivity is necessary for the stator to be grounded. The ground connection during the testing of the device is provided through the contact of the p-type stator substrate to an aluminum chuck. Table 3-1 shows the properties of the stator and rotor extracted from manufacturer datasheet.

Table 3-1: Properties of the stator and rotor substrates.

Material	Orientation	Type	Resistivity	Doping concentration
Silicon	<100>	P-type (Boron)	1-10 Ω·cm	~10^{15}-10^{16} (cm^{-3})

3.3 Finite Element Simulation

3.3.1 Simulation Basics

In order to obtain accurate quantitative values for the capacitance of the system through finite element method (FEM), one must consider the fundamental definition for capacitance. The argument made here is also used in defining appropriate boundary conditions for solving the problem.

For a system of n conductors, each with potential V_i and total charge Q_i, the linear functional dependence of the potential on the charge density implies that the potential of the i^{th} conductor be [129]

$$V_i = \sum_{j=1}^{n} p_{ij}\, Q_J \quad (i = 1, 2, \cdots, n) \qquad \textbf{Eq. 3-2}$$

where p_{ij} depend on the geometry of the conductors. Inverting the above equation results in

$$Q_i = \sum_{j=1}^{n} C_{ij}\, V_j \quad (i = 1, 2, \cdots, n) \qquad \textbf{Eq. 3-3}$$

In the above equation, only the C_{ii} coefficients are called *capacitance*[25]. For example in a system of two conductors,

$$Q_2 = C_{21}\, V_1 + C_{22}\, V_2 \qquad \textbf{Eq. 3-4}$$

In order to obtain the C_{22} value, V_1 is set to zero. Therefore, by definition *"the capacitance of the conductor is the total charge on the conductor when is maintained at unit potential, all other conductors being held at zero potential"* [129]. Consequently, in assigning the boundary conditions, only one electrode is set to have

[25] C_{ij}, $i \neq j$, are called coefficients of induction!

none-zero potential while the rest of the structure is set to 0 V. The potential energy of a system with *n* conductors can be written as the product of charge and potential

$$W_e = \frac{1}{2}\sum_{i=1}^{n} Q_i V_i = \frac{1}{2}\sum_{i=1}^{n}\sum_{j=1}^{n} C_{ij} V_i V_j \qquad \textbf{Eq. 3-5}$$

The Comosol Mutiphysics (FEMLAB) software was used in all the simulations discussed in this chapter. The Poisson's Equation is solved to obtain the potential V using

$$-\nabla\left(\varepsilon_0 \varepsilon_R \nabla V\right) = \rho \qquad \textbf{Eq. 3-6}$$

where ρ is the space charge density, ε_0 and ε_R are the permittivity of vacuum and relative permittivity of the medium, respectively. The energy (W_e) is then calculated by the software. With appropriate subdomain settings of V=0 and V=1 V the capacitance is simply $C=2W_e$.

3.3.2 Modeling Sequence

The FE simulation is composed of four major steps. The first step is to define a suitable geometry representing the actual structure of the micromotor. The second step is to outline sub-domain and boundary conditions such that applicable material properties, symmetric conditions, and physics of operation are represented. The third step is to mesh the structure. This is a critical step since it affects the accuracy and validity of the solution, as well as the time and complexity of numerical computation. The last step is to solve the Poisson's Equation using finite element method and compute the total energy stored in the system (W_e).

3.3.3 Sub-Domains and Boundary Conditions

Figure 3-4(a) shows the geometry used for simulating the capacitance versus angular position of the rotor. Due to the lack of symmetry, a complete sector of the machine consisting of 6 electrodes and 4 poles is simulated. Large number of high-aspect-ratio electrodes (ratio of ~10000) made this simulation extremely complex and time consuming. Simulation results for $C(\theta)$ are reported and discussed later in this chapter.

Symmetry of the micromotor at full alignment and misalignment allows further simplification of the simulated geometry to 3 electrodes and 2 poles as shown in Figure 3-4(b). The simplified structure is simulated to obtain maximum and minimum capacitance and, consequently, the torque. A sample meshed structure is shown in Figure 3-1(c) where near 300,000 elements were used. Meshing the high-aspect-ratio geometry was challenging and was performed by increasing and decreasing the number of mesh elements in the z and r directions[26], respectively. In the first case where 6 electrodes and 4 poles were simulated, about 600,000 mesh elements were used and the problem had nearly 700,000 degrees of freedom[27].

Figure 3-5 shows the boundary conditions used for the simulation of C_{Max} and C_{Min} based on the discussion in Section 3.1.1. Except one electrode, all the structure is set to be electrically grounded including the box representing the symmetrical boundary conditions. Sample simulation results for the electric energy density and potential are shown in Figure 3-6. In cases where the $C(\theta)$ is simulated a complete segment of the

[26] z and r refer to cylindrical coordinates.
[27] Generally for simplicity, 2D simulations are chosen over of 3D. However, to improve the accuracy and validity of our model a series of 3D simulations were performed in this study, despite the complexity of the problem.

machine composed of 6 electrodes and 4 poles is used due to lack of symmetry. For the torque simulation, however, the simplified geometry is used due to symmetry.

3.3.4 Effect of the Electrode Spacing and the Gap

The torque of the machine, being the most important output variable, was derived in Chapter 2 as

$$T(v,\theta)=\frac{-1}{12}N_e v^2\left(\frac{\partial C_1(\theta)}{\partial\theta}+\frac{\partial C_2(\theta)}{\partial\theta}+\frac{\partial C_3(\theta)}{\partial\theta}\right) \qquad \textbf{Eq. 3-7}$$

The above equation demonstrates that in order to design a machine with a high torque, the product of N_e and $dC/d\theta$ must be maximized. One way to change this product is to change the packing factor of the electrodes (a). First, at a fixed gap, the $dC/d\theta$ value versus packing factor is calculated. The next step is to fix the packing factor and vary the gap.

A variable capacitor with a gap of 10 μm and a packing factor of 3 was simulated. The capacitance versus the angular position of the rotor is shown in Figure 3-7. This graph is a result of 17 individual simulations with 6 electrodes and 4 rotors. The summary of the geometrical values and assumptions used in the simulation is shown in Figure 3-8. The figure shows the full cycle for each segment. As the rotor rotates, the capacitor value changes from maximum (full alignment) to minimum (full misalignment) and eventually to maximum (full alignment).

Figure 3-7 demonstrates the curve fit to the simulated data too. The capacitance values are fitted to the sine-squared function in a form of

$$C(\theta)=C_0+a_1\left[\sin\left(\frac{2\pi\theta}{a_2}+a_3\right)\right]^2 \qquad \textbf{Eq. 3-8}$$

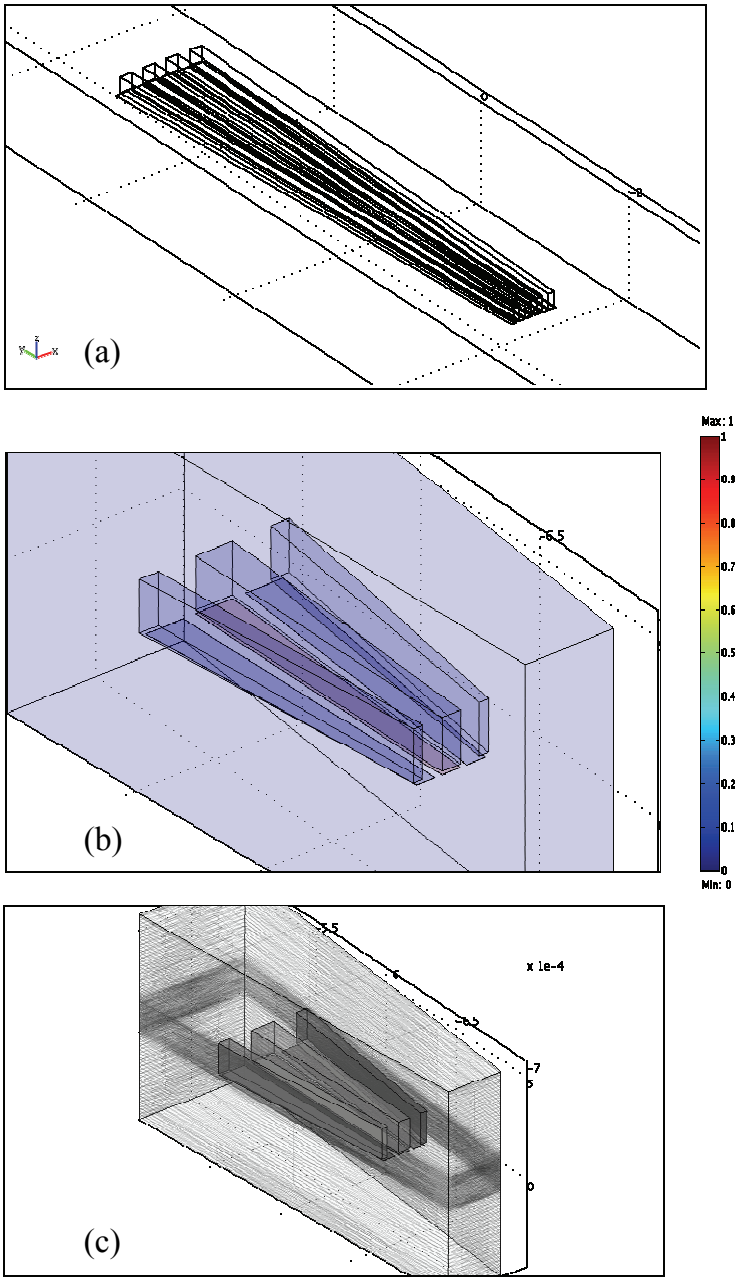

Figure 3-4: (a) Geometry of the micromotor at maximum capacitance composed of 6 electrodes on the stator and 4 poles on the rotor used for FEA, (b) boundary conditions for the simplified geometry (at full misalignment composed) of 3 electrodes, one pole, and 2 half poles; one electrode is set to V=1 V and the rest are grounded, and (c) meshed geometry of the structure consisting of up to 350,000 elements.

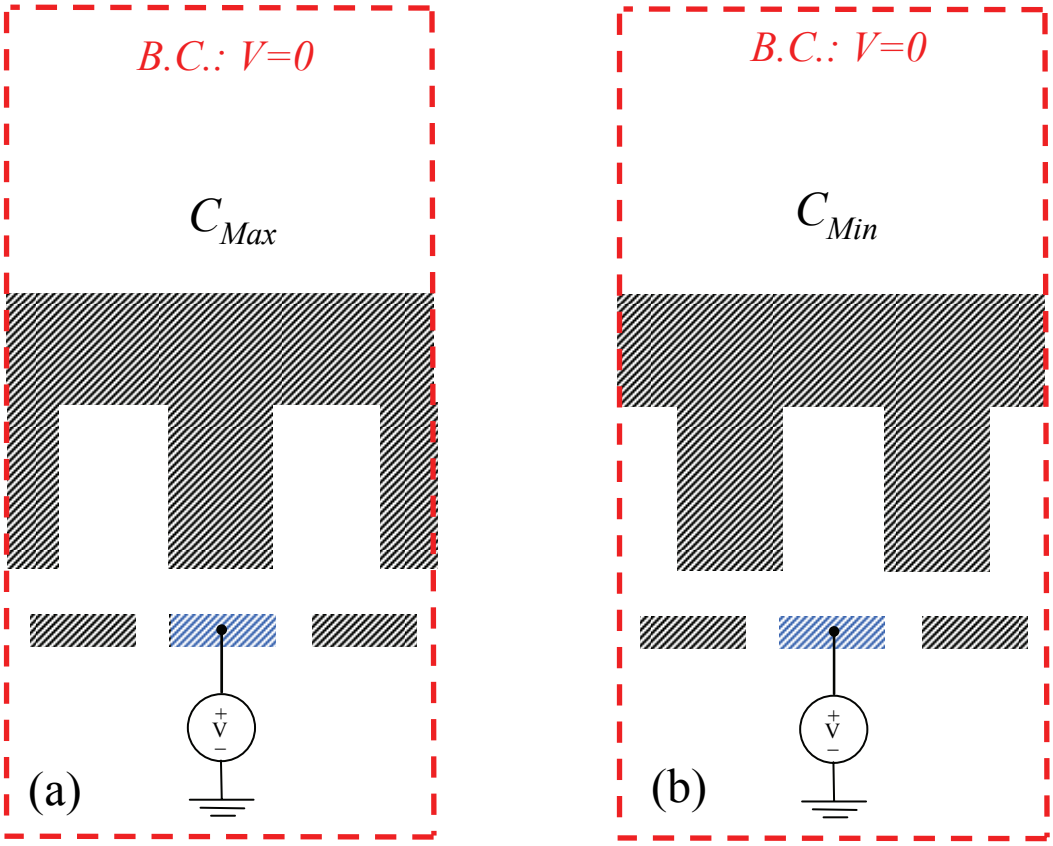

Figure 3-5: Boundary conditions used for the simulation of the simplified motor structure in two extreme cases of C_{Max} and C_{Min}. One electrode is excited while the rest of the structure is grounded. Azimuthal symmetry was used for defining the red box shown above.

The above function is fitted using SigmaPlot software to the data and the following constants were obtained: $C_0=0.33\ pF$, $a_1=0.24$, $a_2=2.87$, and $a_3=1.63$. The standard coefficient of determination (R^2), describing how well a set of data points are fitted to a curve, was calculated using SigmaPlot to be 0.9999 which shows a good agreement between the fitted curve and the simulated data.

Table 3-2: Summary of geometrical values used in the FE simulations.

Property	Inner radius	Outer radius	Electrode length	Electrode thickness (h_e)	Pole depth (h_p)
Value	1 mm	5 mm	4 mm	0.50 µm	150 µm

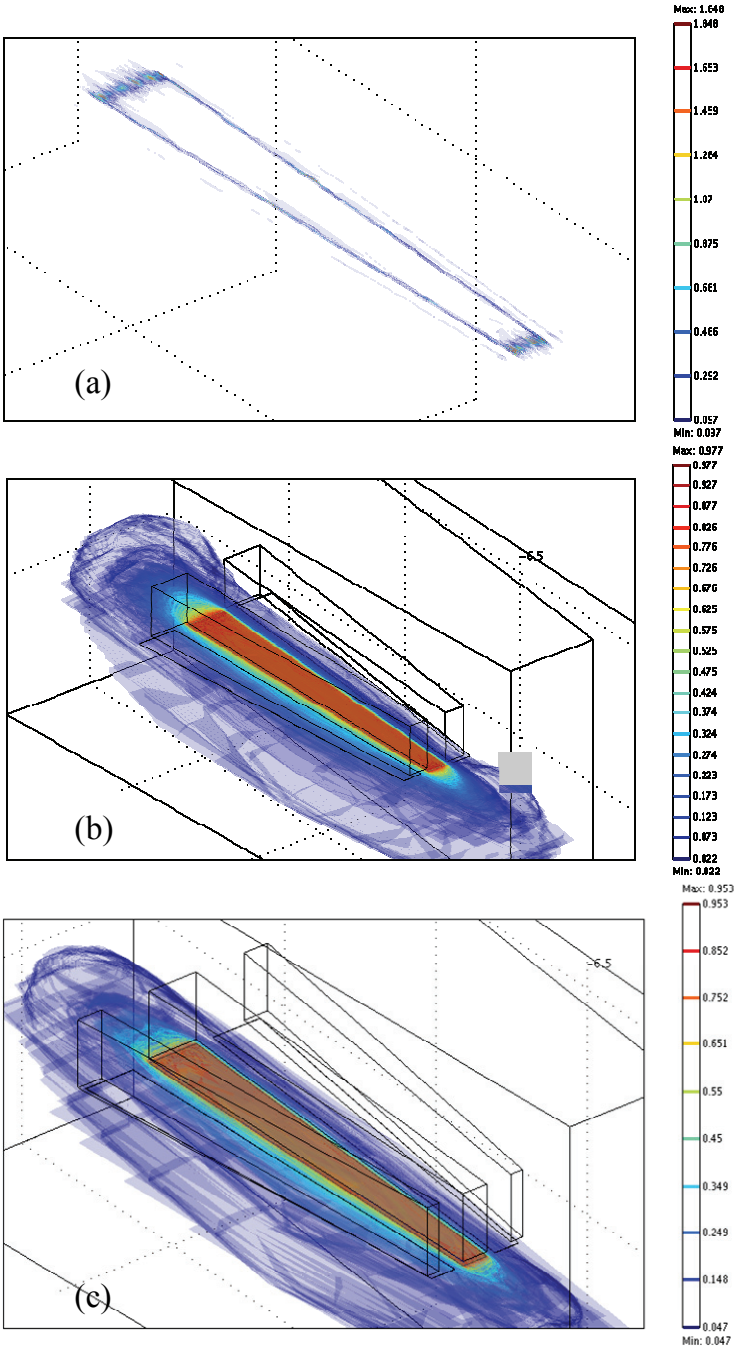

Figure 3-6 shows (a) Electric energy density (isosurface) shows maximum around the periphery (edge) of the excited electrode, (b) electric field distribution (isosurface) in full misalignment, and (c) electric field distribution (isosurface) in full alignment.

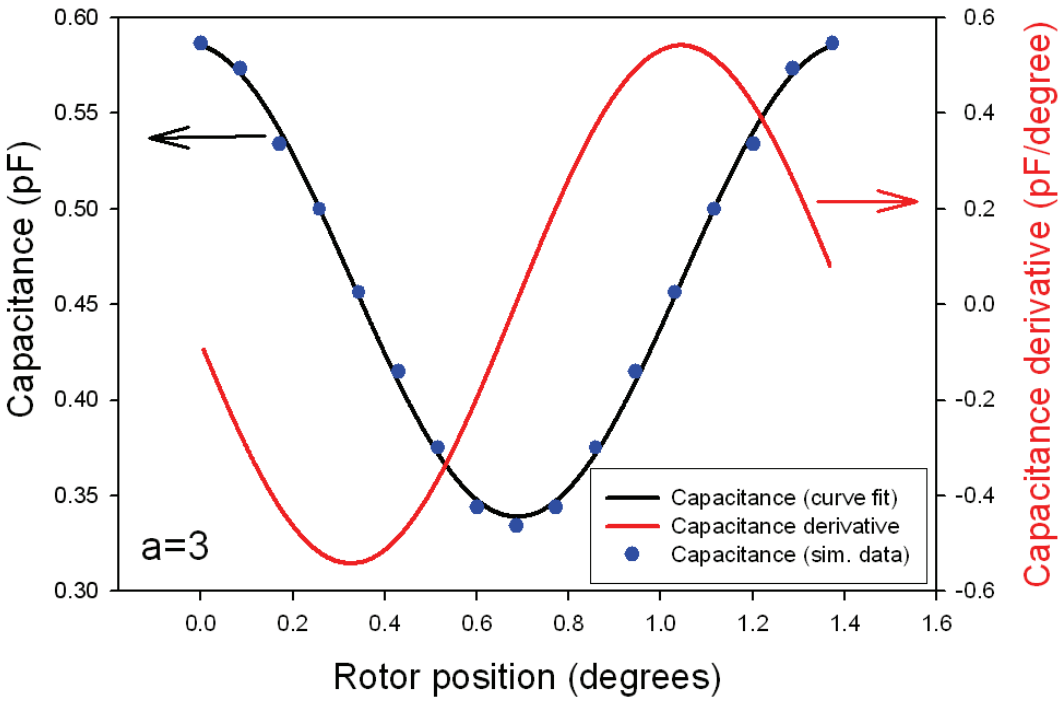

Figure 3-7: Capacitance (left axis) and derivative of the capacitance (right axis) as a function of rotor angular position when the distance between two electrodes is 1/3 of the electrode width (a=3, G=10 μm).

Using the sine-squared curve fit to the $C(\theta)$ function , the first derivative is numerically calculated. Figure 3-7 (right axis) shows the first derivative of the capacitance with respect to the angular position of the rotor. As shown in Chapter 2, the total torque of the machine is proportional to the amplitude of this graph. A similar series of simulations were performed for a machine with packing factor of a=2. The results of 23 simulation points, the fitted curve, and the calculated first derivative are shown in Figure 3-8. The values of C_0=0.26 pF, a_1=0.30, a_2=3.14, and a_3=1.59 were obtained. The amplitude of $dC(\theta)/d\theta$ in the latter is about 25% more than the previous case. However, the motor with the same active area would have a lower number of electrodes as they are loosely packed.

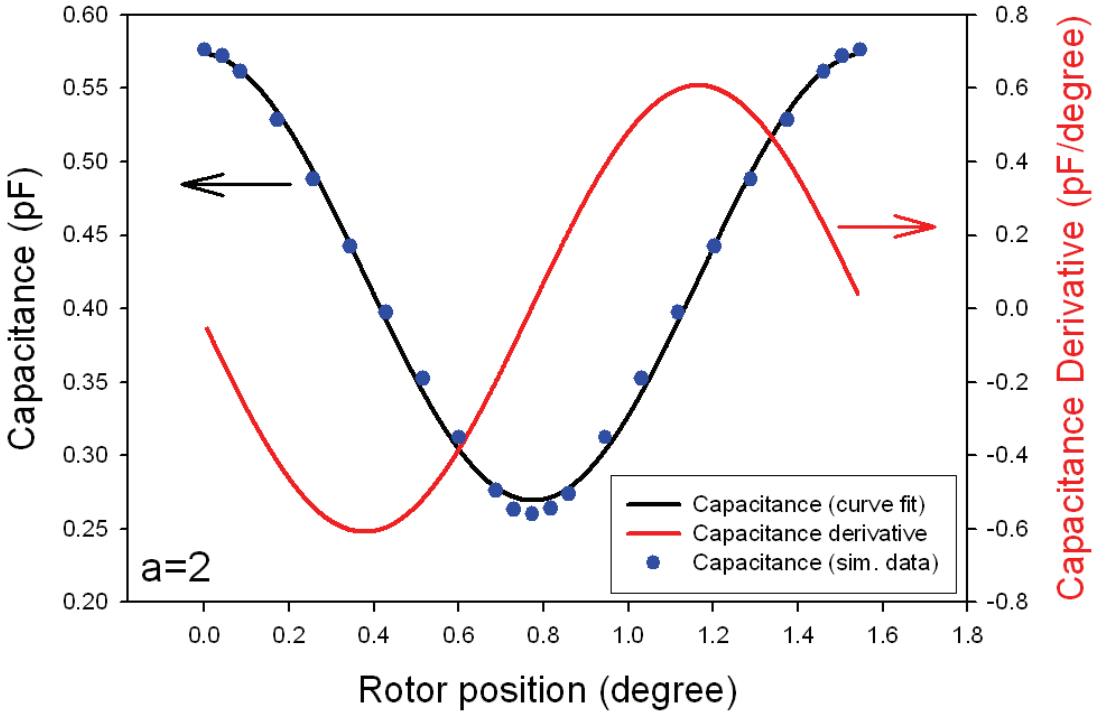

Figure 3-8: Capacitance (left axis) and derivative of the capacitance (right axis) as a function of rotor angular position when the distance between two electrodes is 1/2 of the electrode width (a=2, G=10 μm).

The torque of each machine is calculated from the simulation results shown in Figure 3-7 and Figure 3-8. Table 3-3 shows the calculated average torque using the equations derived in Chapter 2 for electrodes with the length of L=4 mm. The length of the electrode is chosen for the final designed geometry. Both of the machines produce electromechanical torque of ~3 μN·m when excited at 100 V. The linear micromotor utilized the packing factor of a=3; however, for the gap of 10 μm, the packing factor of a=2 is expected to produce the same results.

Table 3-3: Evaluation of the average torque of the six-phase machine for two different packing factors (G=10 μm, L=4 mm). The maximum and minimum values of capacitance are given per phase.

Packing Factor	N_e	C_{min} [pF]	C_{max} [pF]	$\left.\frac{\partial C}{\partial \theta}\right\|_{\max}$ [pF/rad]	Average electromechanical torque [μN·m] @ $V=100$ V
2	156	6.29	12.01	24.8	3.08
3	138	4.64	10.46	27.8	3.06

To further analyze the effect of the packing factor and the gap size on the torque of the machine, a total of 24 simulations were performed at three different gap sizes and four different packing factors. For simplicity, only C_{Max} and C_{Min} were calculated using the geometries shown in Figure 3-4(b-c), Figure 3-5, and Figure 3-6. The derivative of capacitance was estimated using the linear approximation of $\frac{C_{Max}-C_{Min}}{\theta_{Max}-\theta_{Min}}$. Figure 3-9 shows the summary of these 24 simulations. The results for a=3 and a=2 (10 μm gap size) are in agreement with the previous method (less than 5% error). As expected, the torque of the machine increases by more than a factor of 2 when the gap is decreased from 10 to 5 μm. Fabrication imperfections will limit the implementation of a small gap. In contrast, the torque is reduced when the gap is increased from 10 to 15 μm. Fabrication of a machine with the gap of 15 μm is more feasible than 5 μm. The values shown in Figure 3-9 will be increased by a factor of 2.25 if the excitation voltage is increased from 100 to 150 V. The maximum excitation voltage is limited by the instrumentation and the dielectric breakdown voltage.

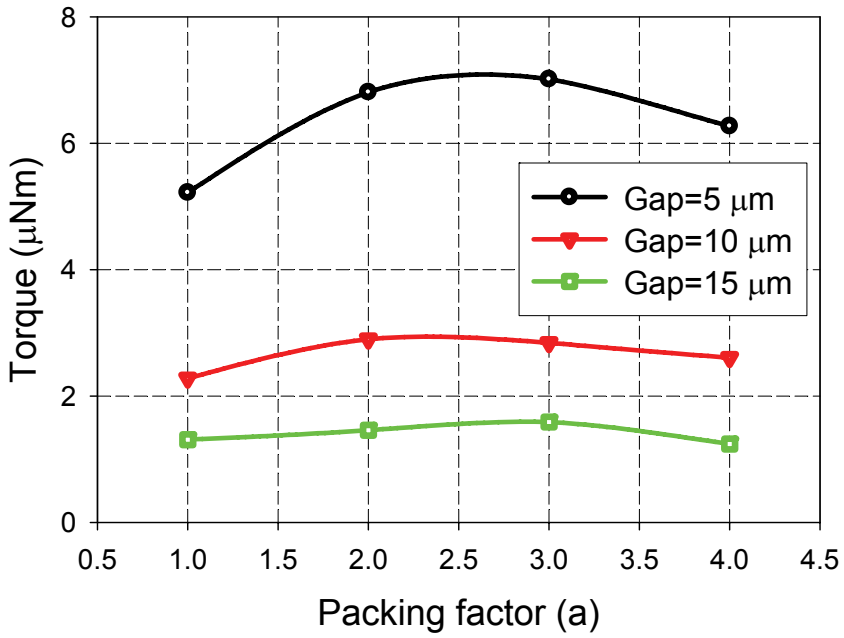

Figure 3-9: Estimated torque as a function of the geometry and the gap for four different designs at V=100 V. With the gap of 10 μm, the torque is about 3 μN·m for the two primary designs i.e. a=2 and a=3.

Simulation results for the torque of the machine (with a=3) as a function of the gap size is shown in Figure 3-10. The gap size is changed from 1.5 μm to 15 μm in each simulation step. The data points are fitted to a *1/gap* function illustrating a good agreement between the data and the projected trend (R^2=*0.9828*). As mentioned earlier achieving a small gap size has enormous fabrication challenges. The results obtained through the series of simulations presented here are used as a guideline for designing four different geometries for the micromotor.

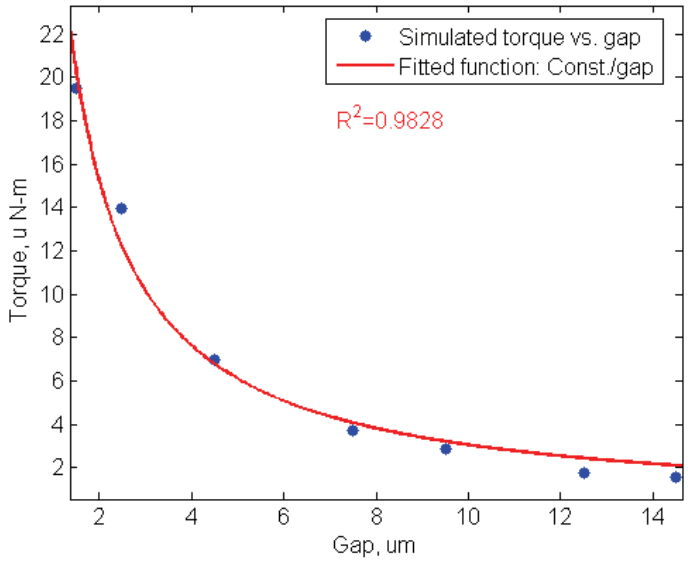

Figure 3-10: Simulation results for the torque of the machine as a function of the air gap.

3.3.5 Normal Force

The torque, calculated in the previous section, is the result of the tangential force on the rotor produced by the electric field and determines the performance of the machine in driving loads. As discussed in Chapter 2, the electric field also produces a normal force on the rotor which helps with stability and holding the rotor on the stator. The normal force, however, does not produce any work because there is no movement associated with the z direction. This force affects the frictional torque on the rotor and needs to be calculated. Similar to the tangential force, the normal force can be written as

$$F_Z = -\frac{1}{2}V^2\frac{dC(z)}{dz} \qquad \textbf{Eq. 3-9}$$

Since the capacitance is now a function of gap as well as angular position of the rotor, the simulation is not trivial. In contrast, previous simulations were all performed at a

constant gap. Nevertheless, two assumptions can be made to calculate F_z. First, the minimum capacitance is zero i.e. C_{Min}=0. Second, the normal force is estimated by

$$F_Z = -\frac{1}{2} V^2 \frac{dC_{Max}(z)}{dz} \qquad \textbf{Eq. 3-10}$$

Figure 3-11 illustrates the maximum capacitance as a function of the gap for 5<G<15 μm. As expected, the capacitance increases by decreasing the gap. This simulation is performed with values listed in Table 3-2. Parallel plate approximation suggests that the C_{Max} and z are inversely proportional. Therefore, the simulation data is fitted to a function in a form of

$$C_{Max}(z) = \frac{k_1 k_2}{k_2 + z} \qquad \textbf{Eq. 3-11}$$

Where k_1 and k_2 are a constant and can be extracted from the curve fit.

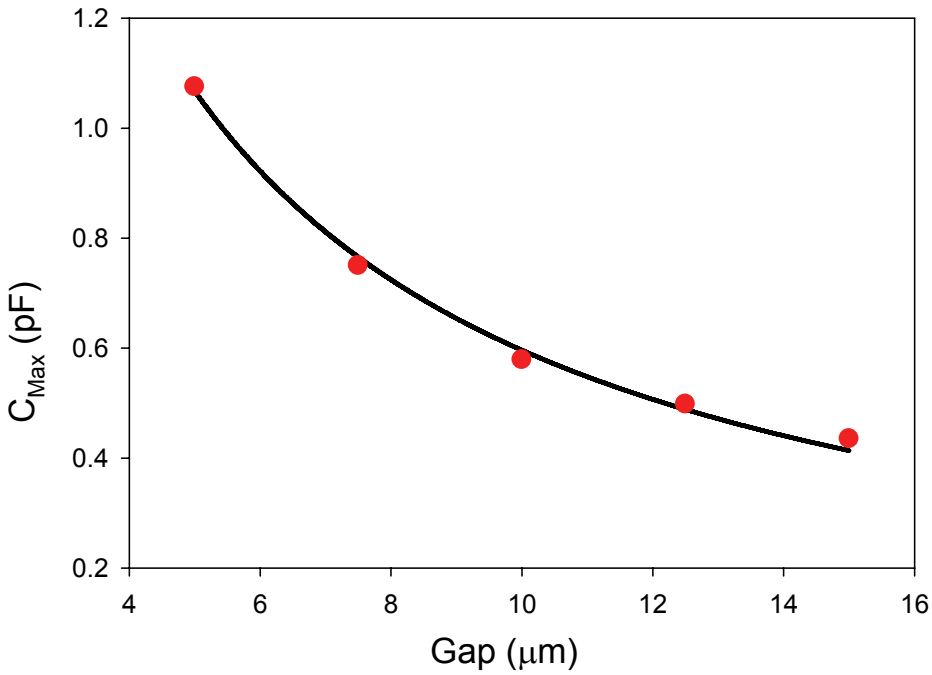

Figure 3-11: 3D simulation results for the maximum capacitance as a function of the gap size and the fitted curve (a=3).

Using SigmaPlot, the standard coefficient of determination (R^2), k_1, and k_2 were calculated to be R^2=0.9995, 5.06, and 1.33, respectively. The first derivative of the function is calculated after the fit curve and is shown in Figure 3-12. The derivative, in conjunction with the force equation, is used to calculate the normal force on the rotor. Figure 3-13 shows the absolute value of the normal force versus the gap for micromotor with a=3, N_e=156, and V=100 and 150 V. The results show that the electrostatic force is at least one order of magnitude larger than gravitational force on the rotor. Therefore, the frictional force depends mainly on the geometry of the machine and the amplitude of the applied voltage.

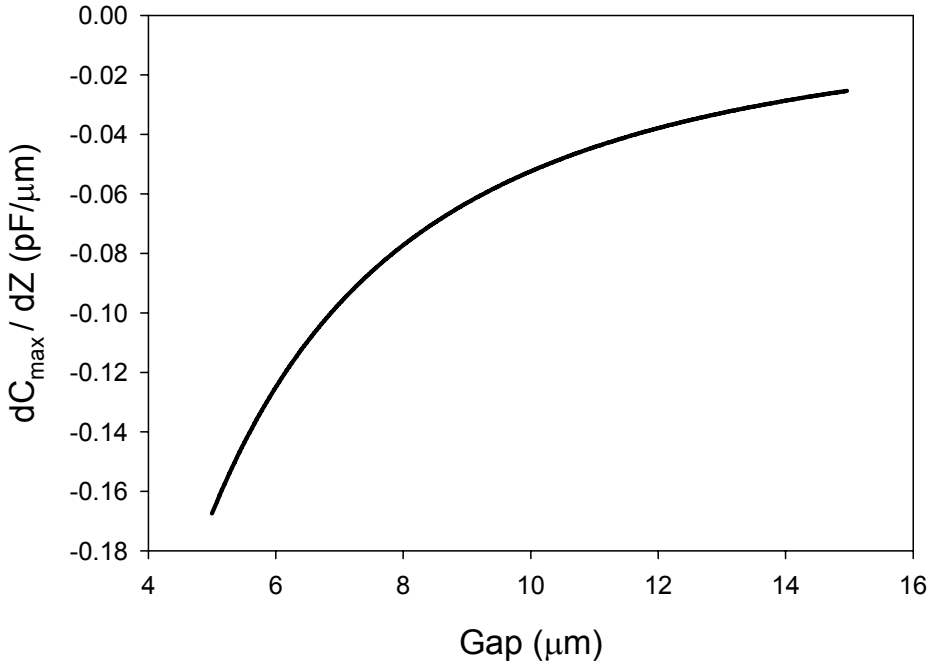

Figure 3-12: Derivative of capacitance as a function of the gap size is derived from calculating the first derivative of capacitance from the previous figure.

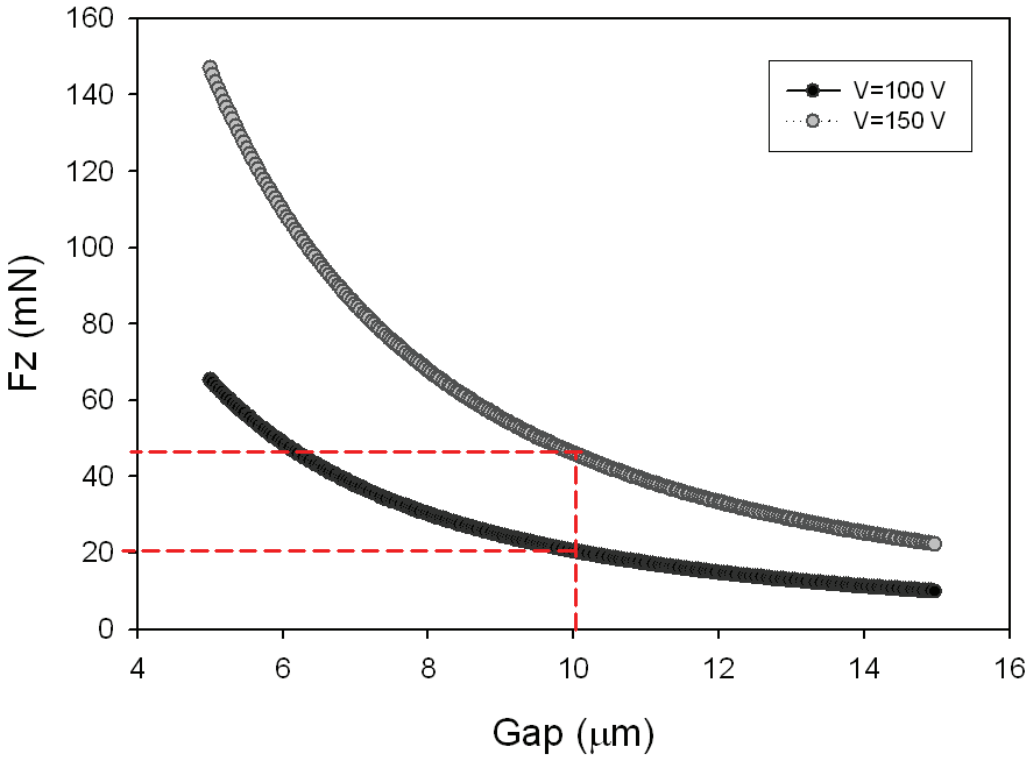

Figure 3-13: Absolute value of the normal force as a function of the gap size. The estimated normal force of the motor with *G*= 10 μm and V=100V is 20.5 mN.

3.3.6 Rotor Deflection

The normal force, discussed in the previous section, deflects the rotor towards the substrate and could potentially change the gap. The deflection in the *z* direction is quantified using FEM. A silicon disc, similar to the geometry of the rotor was simulated using Comsol Multiphysics. The disc is 550 μm thick with an inner and outer radius of 1 and 6 mm, respectively. Circular microball housing 250 μm wide and 150 μm deep was also included in the structure. While the bottom of the housing was fixed, the bottom surface of the rotor was pulled with a force of F_N. The rest of the structure was free to move. Figure 3-14 shows the displacement (deflection) of the rotor with a constant force of 30 mN. The maximum deflection in the *z* direction at

the radius of 1 mm is less than 3 nm. A series of simulations for $0 < F_N < 100$ mN were performed; the results are shown in Figure 3-15. The maximum displacement even at load conditions as high as 100 mN is less than 10 nm and is negligible compared to the gap size of a few microns. Therefore, the displacement of the rotor due to the normal force does not have any impact on the gap, torque, or operation of the machine.

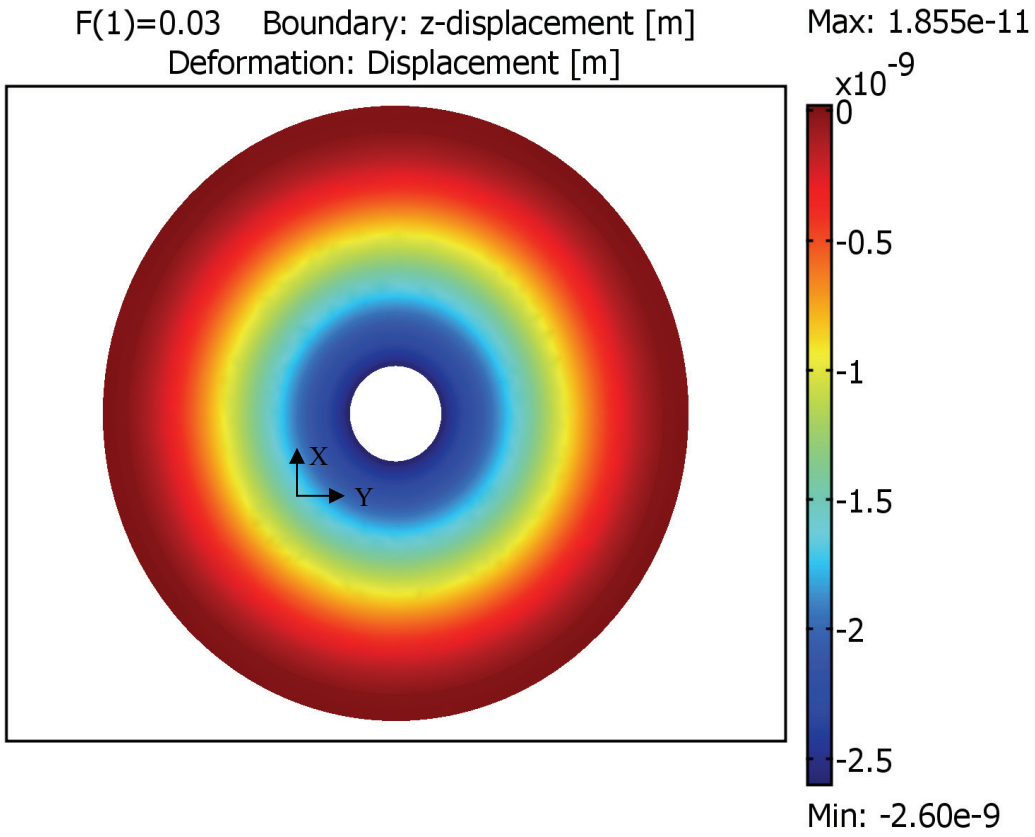

Figure 3-14: Simulation results showing maximum rotor deflection of 2.6 nm in the *z* direction with the applied force of 30 mN.

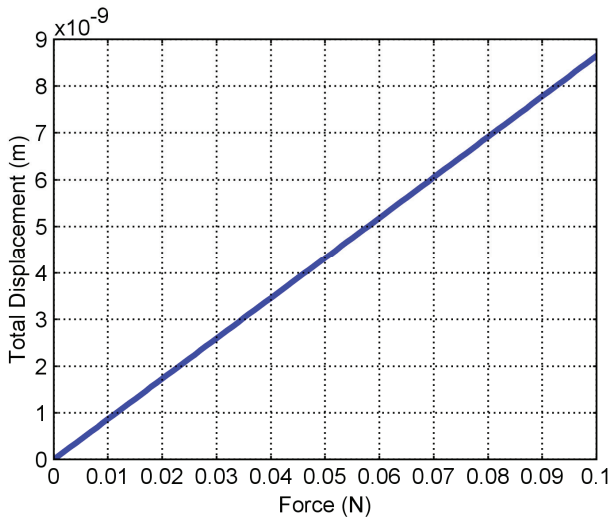

Figure 3-15: Simulation results of the total rotor displacement in the *z* direction as a function of the force applied to the rotor. The deflection is measured at R=1 mm where it is maximum as shown in the previous figure.

3.3.7 Effect of the Dielectric at the Gap

As mentioned earlier in Chapter 1, the torque of the machine can be increased by replacing the machine's air gap with a material of higher relative permittivity (ε_R) than air. As shown in Chapter 2, the torque is proportional to $dC(\theta)/d\theta$, therefore, by replacing air with a material of higher relative permittivity at the gap, the capacitance value, $dC(\theta)/d\theta$, and torque are all increased by approximately a factor of ε_R.

Implementation of a high-k dielectric in the variable capacitance micromotor has a few practical obstacles. Liquid lubricants like silicone would increase the torque but introduce large viscous drag losses. Lower net torques and speeds were previously reported for such machines [45]. Implementation of a gas as a dielectric material is possible but does not improve the performance of the machine because most of the noble gases have a relative permittivity of around 1. Solid dielectrics such as polymers can be used, however, from the practical point of view there need to be

clearance between the moving parts i.e. rotor and stator. That would result into a partial filling of the gap with a high-k material.

A series of simulations were performed on the micromotor structure to determine the high-k effect. Figure 3-16(a) shows the simplified cross section of a micromotor with 90 μm wide, 0.5 μm thick, and 5 mm long electrodes and the air gap of 10 μm. Figure 3-16(b) shows the similar structure when 5 μm of the gap is filled with a high-k material ($1 < \varepsilon_R < 30$). The 5 μm value was chosen based on 50% filling of the gap just for demonstration purposes. Figure 3-17 shows the minimum and maximum capacitance of a single electrode-pole pair obtained from 3D simulation (Comsol Multiphysics) for such a structure. The difference between the maximum and minimum capacitance, which is an apt representation for torque, is also shown in this figure. Since the net capacitance of the machine in Figure 3-16(b) is made of two capacitors in series, the smaller capacitor (air) is dominant. Results from Figure 3-17 verify that *partial* gap filling method with a high-k material has little or no effect on the performance of the machine. For this method to be effective, almost the entire gap needs to be filled with a high-k material. For the same reason, the effect of the 3 μm thick BCB film (passivation layer) on the performance of the machine was neglected in the previous simulation.

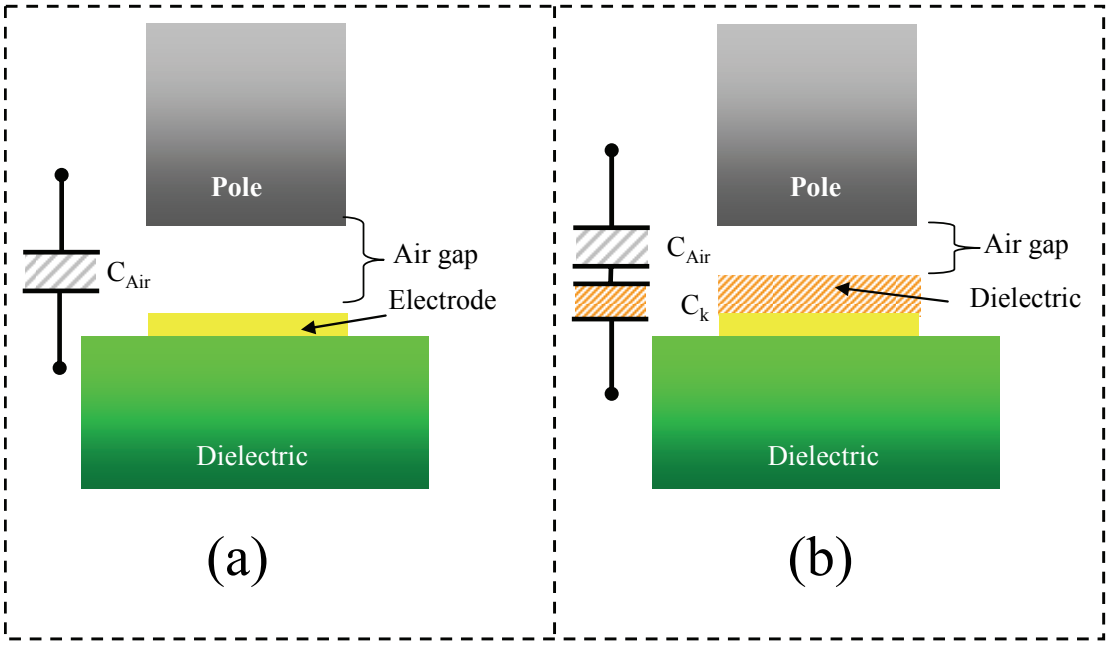

Figure 3-16: Schematic cross section of the micromotor with (a) 10 μm air gap, and (b) 5 μm thick dielectric and 5 μm air at the gap. The latter forms two capacitors in series.

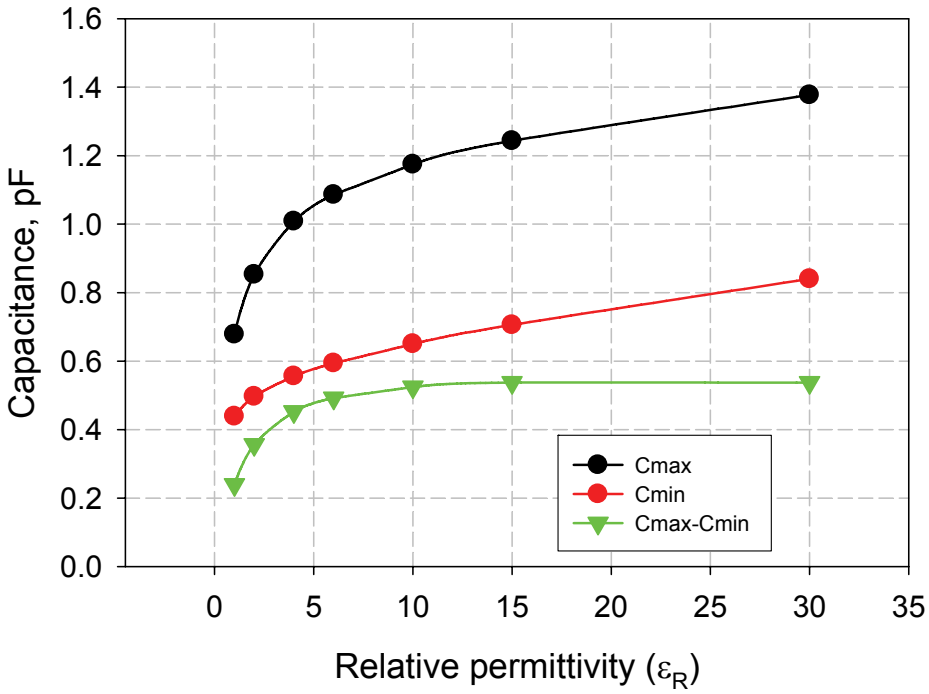

Figure 3-17: Maximum and minimum capacitance (C_{Max}, C_{Min}), as well as $C_{Max} - C_{Min}$ as a function of the relative permittivity of the dielectric material at the gap of the micromotor. The simulation is performed using 3D Comsol Multiphysics for the structure shown in the previous figure.

3.3.8 Simulation Summary

In Section 3.3, the FE simulation results were reported. The change in the capacitance with respect to the angular position of the rotor was simulated. The resulting capacitance was differentiated after a sine-squared curve fit, and the torque of the machine was estimated. The effect of the packing factor on the torque was studied for a=1, 2, 3, and 4. Additionally, the role of the gap size on the torque was investigated through similar FE simulations. The torque of a motor with the outer radius of 5 mm at 100 V was calculated to be 3 μN·m nearly 2-3 orders of magnitude higher than side-drive machines. The normal force on the rotor and the elastic deformation of the silicon substrate were simulated and found to be 30 mN and 3 nm, respectively (G=10 μm, V=100 V). The results show that the normal force is at least one order of magnitude larger than gravitational force and plays a significant role in the friction of system; however, its effect on the gap size is insignificant. The role of the dielectric material with $1 < \varepsilon_R$ in the gap was investigated. The analysis shows that partial filling of the gap even with high-k materials have insignificant effect on the capacitance variation and torque of the device.

3.4 Design Variations

3.4.1 Electromechanical Design

Based on the FE simulation results four different geometries were designed for the rotary micromotor. The active area in all devices were chosen to be 75 mm^2 (R_1=1, and R_2=5 mm). The difference between these devices is mainly the width of the electrodes or their spacing. Figure 3-18 shows the isosceles trapezoid shapes of D1, D3, and D4 electrodes. Table 3-4 summarizes the electrode geometric factors. D1 and

D2 are designed based on the gap size of 10 μm. D4 is designed to have electrodes with half the width of D1 for the gap of 5 μm. Finally, D3 is designed to have a high synchronous speed i.e. small number of electrodes. Theoretically, the smallest number of electrode is 6; however, such a machine does not produce significant torque. Consequently 30 electrodes were chosen for D3.

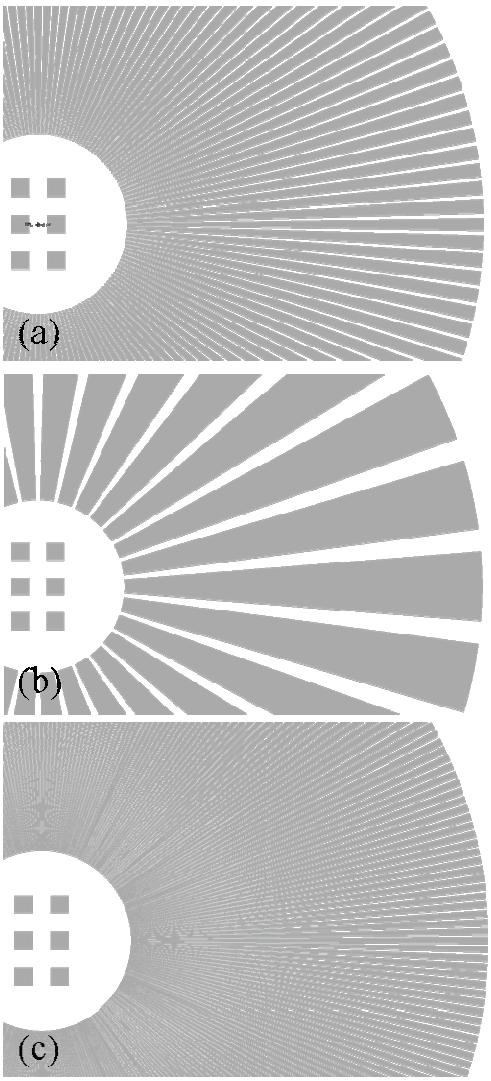

Figure 3-18: Electrode geometry for design (a) D1, (b) D3, and (c) D4.

Table 3-4: Trapezoid side lengths for each device.

Device	With of parallel side 1 (μm)	With of parallel side 2 (μm)	Height between parallels (mm)
D1	30	150	4
D2	30	150	4
D3	155	800	4
D4	15	75	4

3.4.2 Mechanical Support

The designed micromotor is the first demonstration of the rotary machine using microball bearing technology. Therefore, the effect of microball housing on the performance of the machine is unknown. To study the role of the housing on the performance of the machine four primitive designs were chosen for the machine that are shown in Figure 3-19. The primary design is a continuous trench, however, segmented trench and double trench are also considered. The fourth design is for a device with interconnection pads positioned outside of the regular device area.

3.5 Mask Layout

Due to the fabrication complexity of the stator, it is desired to have maximum number of micromotors on each wafer. Considering the radius of each device, a total number of 17 dies were designed on the wafer. Each die lies in a symmetric grid to ease the subsequent wafer dicing step if needed. Figure 3-20 shows the layout of the stator. The specifications of each device on the stator and rotor wafers are listed in Table 3-5. The detail of the first 6 layers of the stator is shown in Figure 3-21. The first layer shown in this figure is for etching permanent alignment marks on silicon. The other layers are respectively for the formation of BCB island, interconnection (first metal), interlayer dielectric and vias, electrodes (second metal), and passivation

layers that are all shown in Figure 3-21 for D1. The microball housing design was previously shown in Figure 3-19.

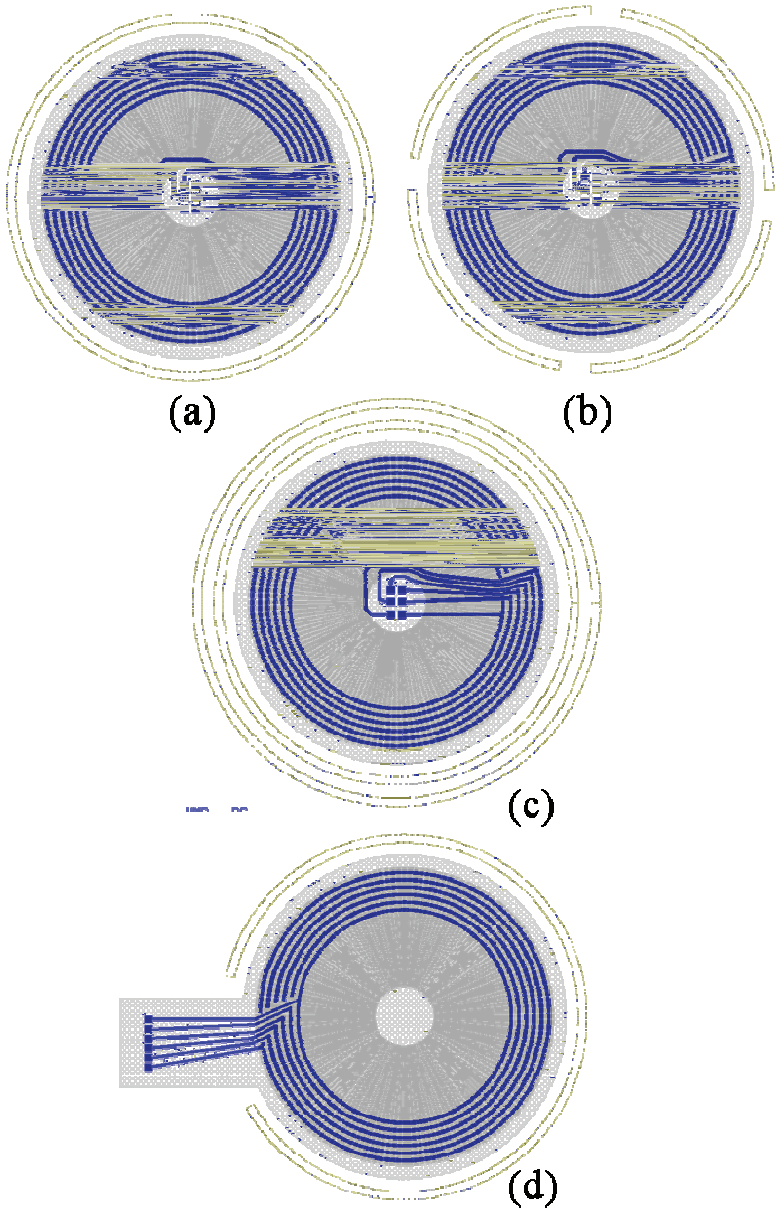

Figure 3-19: Four different bearing designs showing a machine with (a) one continuous trench, (b) four separate trenches each 80 degree long, (c) two continuous trenches, and (d) one discontinuous trench 317 degree long.

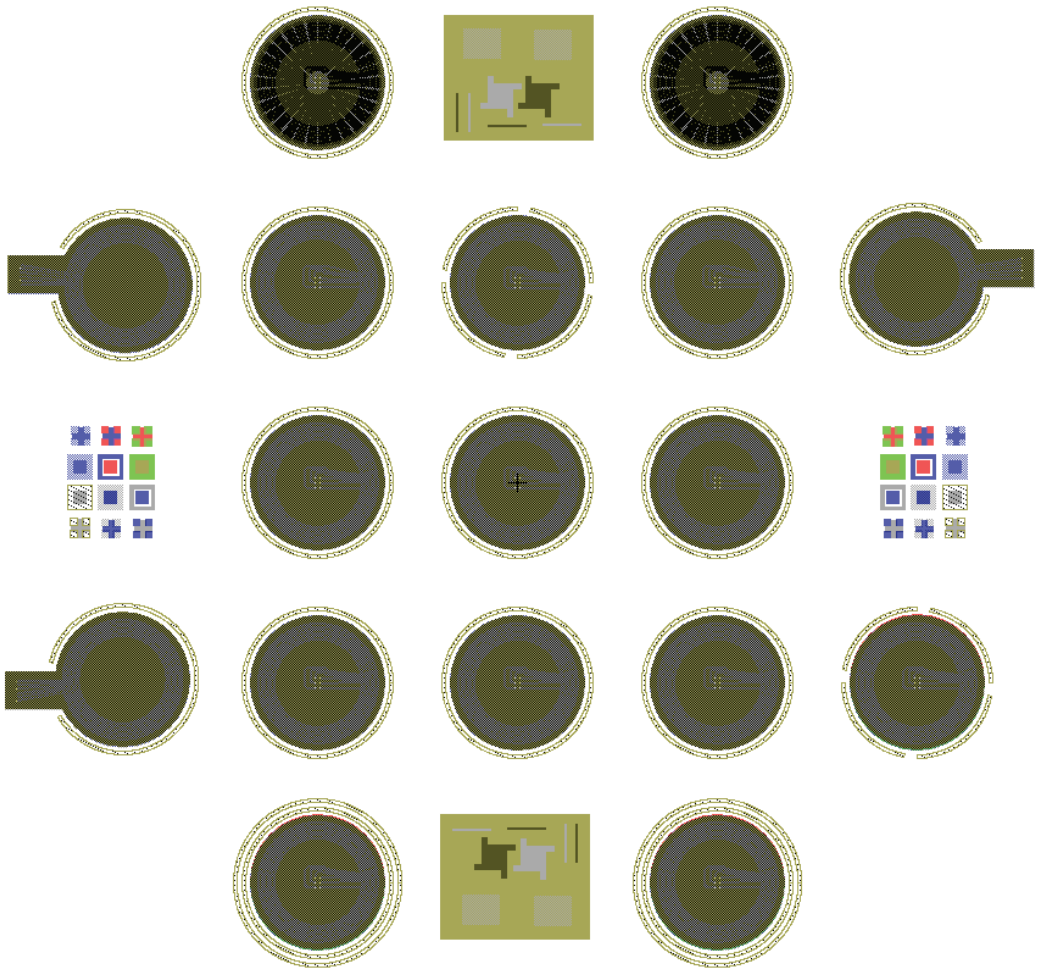

Figure 3-20: Stator layout is composed of 17 devices, test structures, and alignment marks.

.

Table 3-5: Summary of wafer layout for the stator and the rotor.

Device name	Purpose	Specs	Number of devices on stator	Number of devices on rotor
D1	Base 1	Ne=156, a=3	3	1
D2	Base 2	Ne=138, a=2	3	1
D3	High speed	Ne=30	2	1
D4	High torque	Ne=312	2	1
D5	Double trench	Ne=156, a=3	1	1
D6	Double trench	Ne=138, a=2	1	1
D7	Segmented trench	Ne=156, a=3	1	0
D8	Segmented trench	Ne=138, a=2	1	0
D9	Pad outside device	Ne=156, a=3	2	0
D10	Pad outside device	Ne=138, a=2	1	0

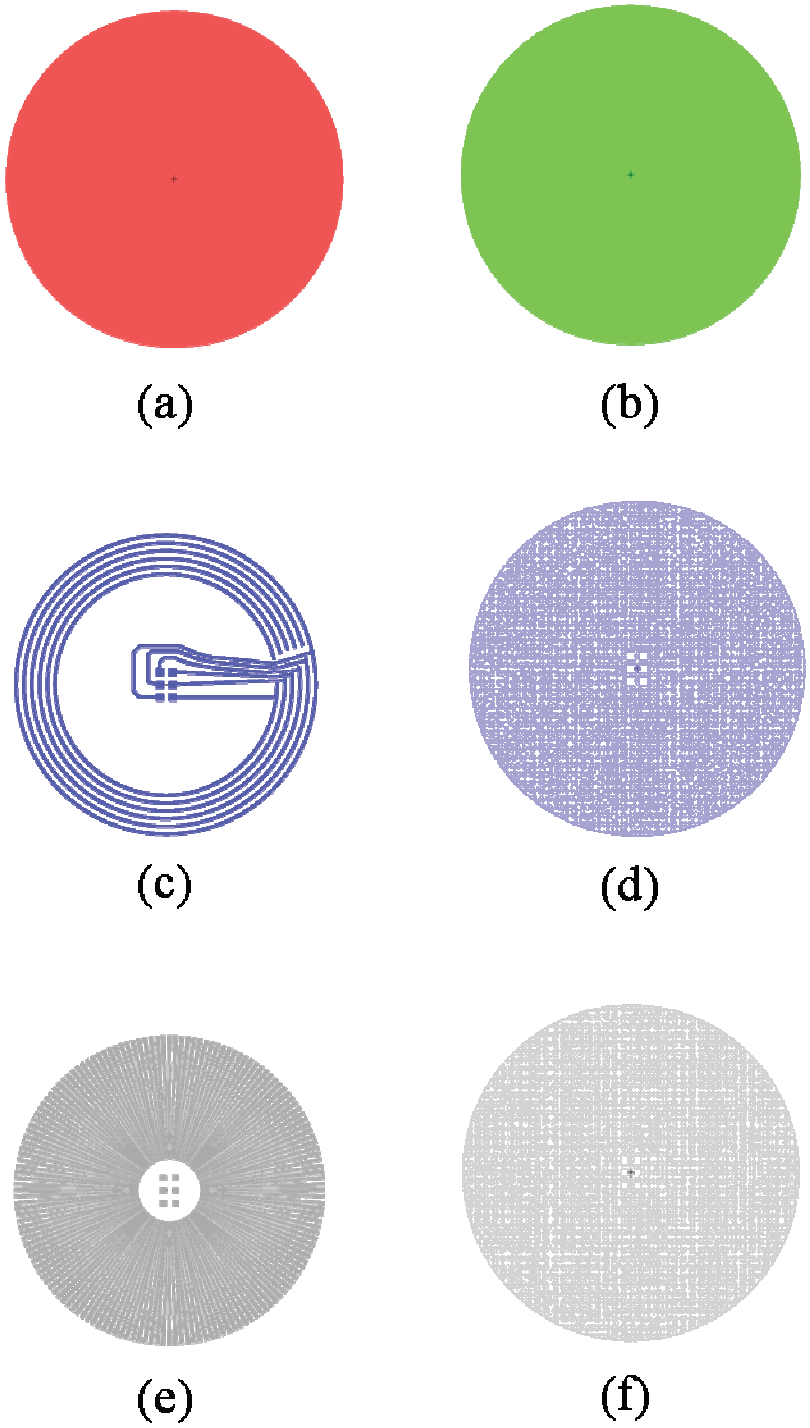

Figure 3-21: First 6 layers on the stator composed of (a) silicon pit, (b) BCB island, (c) interconnection, (d) interlayer dielectric, (e) electrodes, and (f) passivation.

Unlike the stator, the rotor layout is composed of only six devices. This is to reduce the loading in the DRIE steps which is explained in Chapter 4. Since the

fabrication of the rotor is fairly straightforward, there is no significant advantage in increasing the number of devices on a single wafer. Figure 3-22 shows the rotor layout on the wafer. Details of each layer are show in Figure 3-23. The expected theoretical angular velocities for D1-D4 are shown in Figure 3-24. As it is shown, D1, D2, and D4 are designed to operate at high-torque regimes while D3 is designed for high-speed applications. Key design parameters for each device are shown in Table 3-6. A complete fabrication process using the masks presented here is reported in Chapter 4.

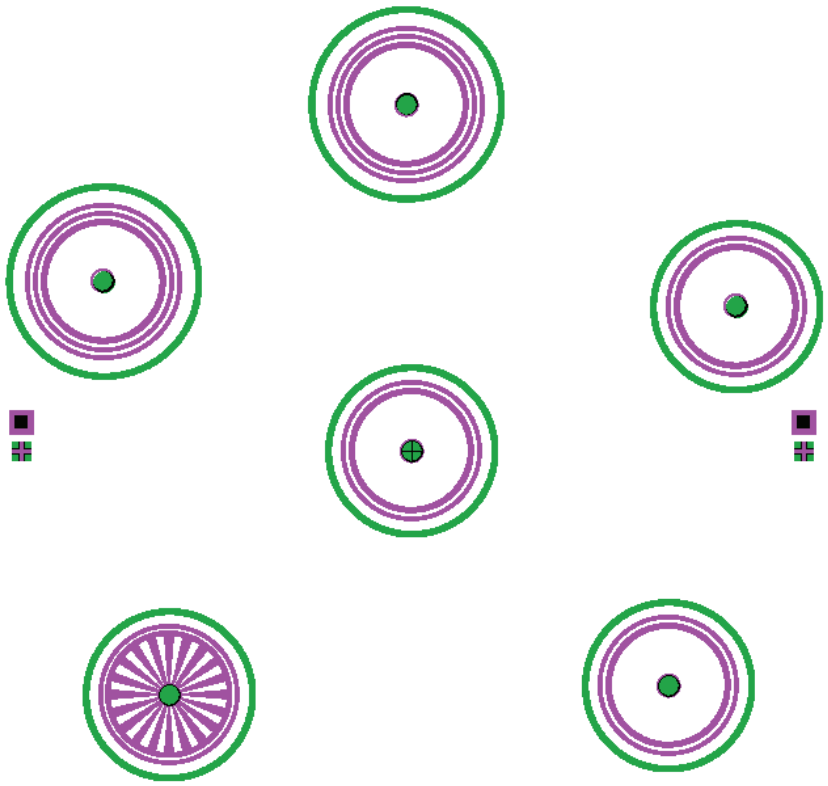

Figure 3-22: Rotor layout composed of 6 devices. The salient poles are only shown in one device.

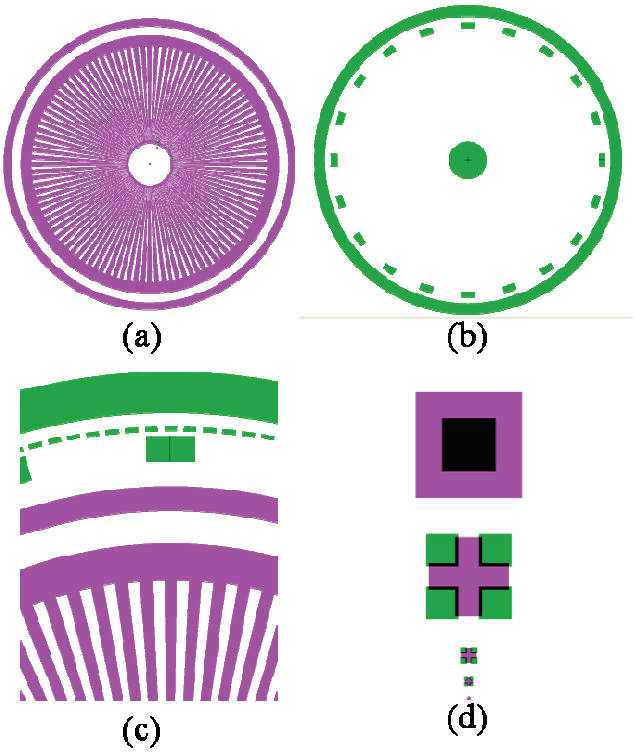

Figure 3-23: Rotor layers showing (a) trench and poles, (b) release and marks, (c) close up view of the marks, and (d) front-to-back alignment marks.

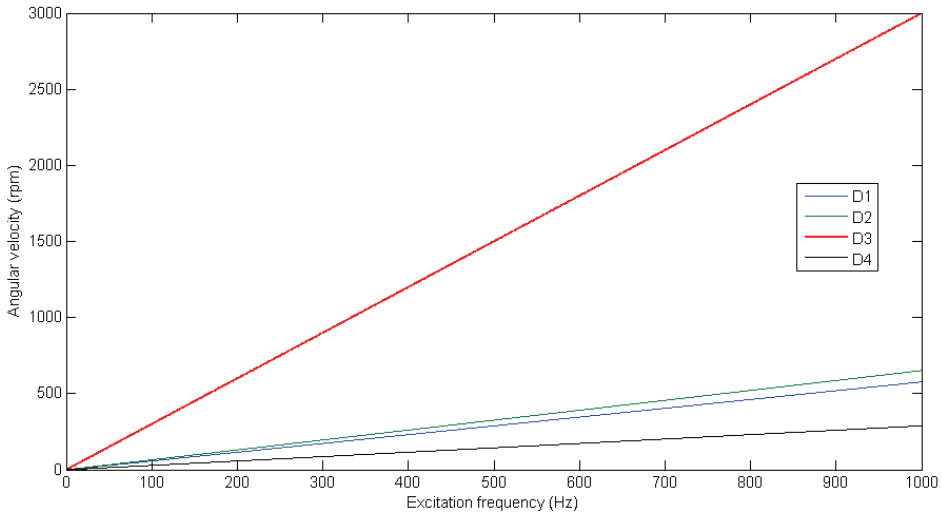

Figure 3-24: Angular velocity of the machine versus excitation frequency for D1-D4. D1, D2 and D4 are designed to achieve a highest possible torque, whereas D3 is designed for the highest velocity.

Table 3-6: Specification for key device features (D1).

Mask #	Feature	Value (μm)
2	Silicon pit etch window	Radius: 5400
3	Dielectric island	Radius: 5405
4	Interconnection (×6)	Width: 100 Center to center: 250 Radius: 3500-4850
4	Pads (×6)	240 × 240
5	ILD	Radius: 5390
5	Via	80 × 80
5	Opening for pads	200 × 200
6	Electrodes	Inner radius: 1000 Outer radius: 4957 Width: 30, 90, 150
7	Dielectric passivation	5415
7	Opening for pads	180 × 180
8	Microball housing	Width: 290 Radius: 5800-6090
R1	Microball housing	Width: 290 Radius: 5800-6090
R1	Poles	Inner radius: 1000 Outer radius: 4957 Width: 30, 90, 150
R1	Dummy etch 1	Radius: 900-1000
R1	Dummy etch 1	Radius: 4958-5400
R2	Rotor release hole (inside)	Radius: 905
R2	Rotor release hole (outside)	Radius: 7000-7500
R2	Large velocity detection pits	300 × 150
R2	Small velocity detection pits	150 × 50

3.6 Alignment

The design of the alignment marks used in the fabrication of 7 different layers on the stator is challenging. The fabrication process of each layer should be considered in designing the alignment marks. If inappropriate alignment sequence is chosen, misalignment tolerances during each step could add up to deteriorate the accuracy of the final geometry. The designed alignment marks are shown in Figure 3-25 where 7 different colors represent 7 different layers. The alignment marks used are basically crosses and squares. The alignment sequence for the stator and rotor are shown in Table 3-7 and Table 3-8, respectively.

For both dark field and clear field marks, the marks that are already on the wafer should be visible through the marks on the mask. Therefore, if the second mask is dark field a set of squares are used and if the second mark is clear field, a set of crosses are used on the mask. The relative size of the marks is chosen based on the same analogy. The most critical alignment step in the fabrication of the machine is the electrode layer and microball housing layer. Tight alignment between these layers is required to have a unified center of rotation for the bearing and the electrodes; otherwise, the behavior of the rotor would be unpredictable.

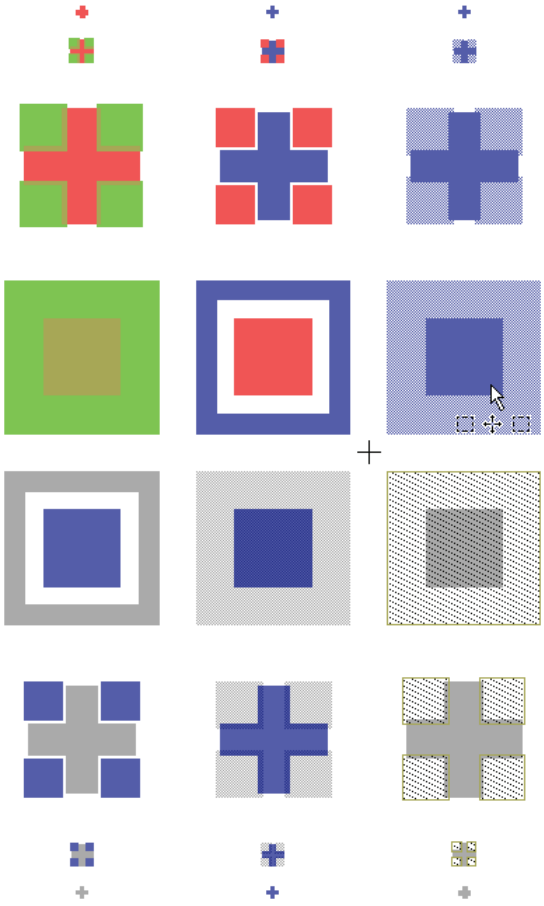

Figure 3-25: Stator alignment marks where each color represents the following layers-red: silicon pit, green: island, dark blue: interconnection, light blue: interlayer dielectric, dark gray: electrodes, light gray: passivation, and dotted green: microball housing.

Table 3-7: Mask alignment sequence for the stator.

Mask #	L-Edit layer name	Physical layer	Make tone	Aligned to
2	Poly	Silicon Pits	Negative (Dark field)	Wafer Flat
3	Active	BCB Islands	Negative (Dark field)	Mask#2
4	Metal1	Interconnects	Positive (Clear field)	Mask#2
5	Metal1-tight	Vias	Negative (Dark field)	Mask#4
6	Metal 2	Electrodes	Positive (Clear field)	Mask#4
7	Metal2-tight	Passivation/Pads	Negative (Dark field)	Mask#4
8	N Well	Trench	Negative (Dark field)	Mask#7

.

Table 3-8: Mask alignment sequence for the rotor.

Mask #	L-Edit layer name	Physical layer	Make tone	Aligned to
R1	N Select	Trenches/poles	Negative (Dark field)	Wafer flat
R2	P Select	Release and marks	Positive (Clear field)	Mask#R1

4 Fabrication

4.1 Introduction

One of the major challenges in the development of the micromotor has been the fabrication of the device. The micromachine, as discussed in chapters 2 and 3, is made of a micro fabricated stator and rotor. The stator is composed of five layers of thin films (dielectric or conductor) on the silicon substrate and bulk micromachined silicon structures for microball housing. The large number of layers, together with the use of a low-k polymer in the structure of the stator, has made the fabrication process extremely complex. The stator fabrication process consists of 7 major steps each composed of a few sub steps. The rotor process is less complicated and has three major steps. Both processes are detailed in the next section.

4.2 Process Flow Design

Four-inch, <100>, p-type, 1-10 Ω·cm, 525 ±25 μm thick, double-polished silicon substrates were used as starting material for the fabrication of the stator and the rotor. The choice of substrate properties was discussed in Chapter 3. The wafers were selected to be double polished to make infrared imaging of the balls possible[28]. The schematic cross section of the stator fabrication process is shown in Figure 4-1. The process consists of surface micromachining (thin film deposition and patterning) and bulk micromachining (deep etching) steps. To keep all photolithography processes planar, the bulk micromachining is performed at the last step.

[28] Infra red imaging was not pursued at the final characterization step.

The stator fabrication starts with etching alignment marks in silicon (not shown in Figure 4-1). The marks are used in subsequent alignment steps as discussed in Chapter 3. The mask that contains the marks has silicon pit structures to allow fabrication of the machine using an embedded BCB island in silicon (EBiS). The EBiS process is discussed in Chapter 6 and was not used here.

A thin layer of BCB layer is deposited next to isolate any conductor used in the machine's structure from the substrate. A thin metal layer is then deposited to form the interconnection layer. This layer is isolated from the second metal layer with a thin BCB layer (ILD). Vias are formed in the ILD so that the second metal layer would be electrically connected to the first layer at the selected areas. The second metal layer is then deposited to form electrodes. The electrodes are then passivated by a thin BCB film. The last step in the fabrication of the stator is to etch silicon using deep anisotropic dry etching. All the steps are shown in Figure 4-1.

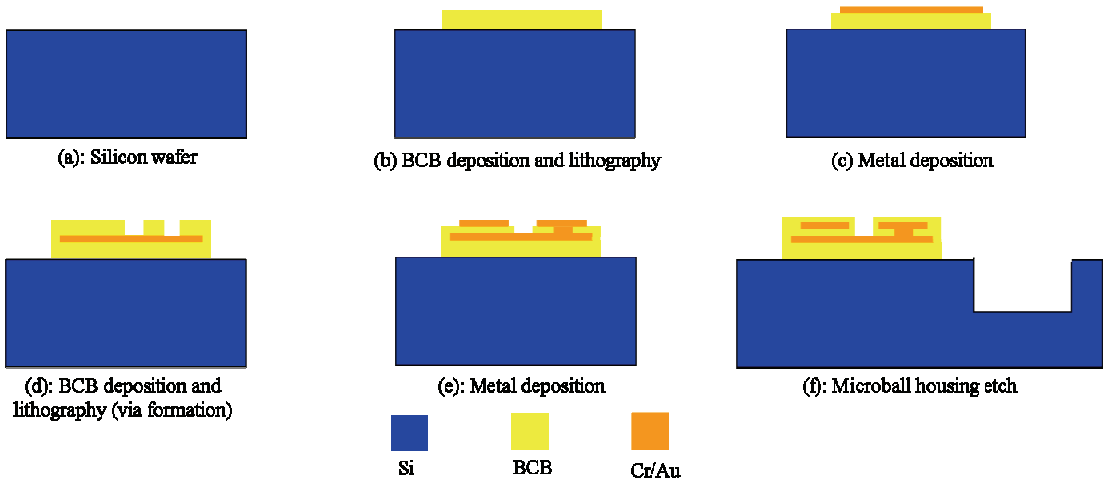

Figure 4-1: Cross section schematics showing the stator fabrication process from start (a) to finish (f).

The rotor fabrication process, shown in Figure 4-2, starts with the anisotropic etching of silicon on one side of the wafer to form microball housing and poles. The

second dry etching step from the other side of the wafer is then used to release the rotor. Furthermore, several position detection marks and the center cavity of the rotor are etched thoroughly in this step. Position sensing marks shown in Figure 4-2 as shallow etch are actually through wafer etch. Once the rotor dies are released, a thin film of silicon carbide is deposited to reduce the friction of the microballs in the silicon housing.

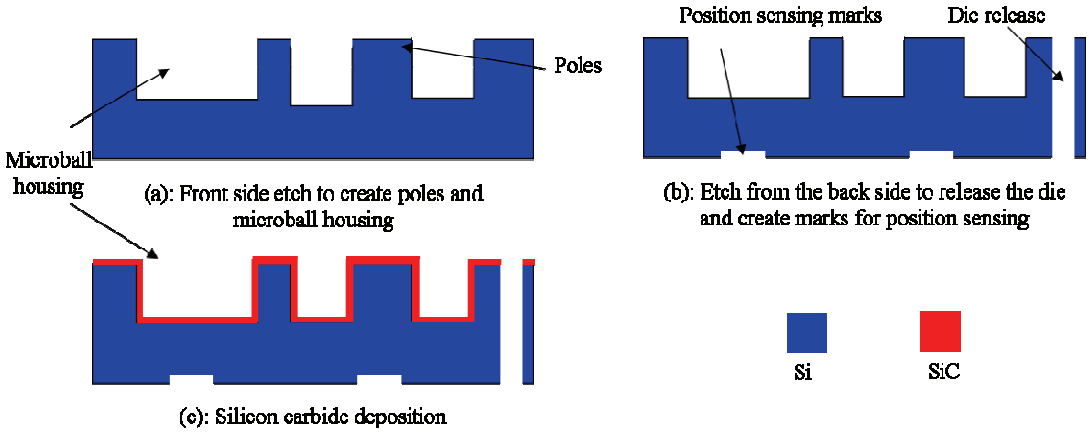

Figure 4-2: Cross section schematics showing three steps of the rotor fabrication process.

4.3 Stator Fabrication Steps

4.3.1 Alignment Marks

The first step in the fabrication process is to etch permanent alignment marks into the silicon. Figure 4-3 shows the process flow of this step. Photoresist is used as a masking layer during the reactive ion etching of silicon. A 5 μm thick resist is deposited and patterned using a contact mask aligner (Q4000 from Quintel) with the process parameters shown in Table 4-1. Before any photolithography step, wafers are dehydrated on hotplate at 130 °C for 15-30 min. Thick films of photoresist (> 5 μm) are also used throughout the fabrication process with the parameters shown in the table.

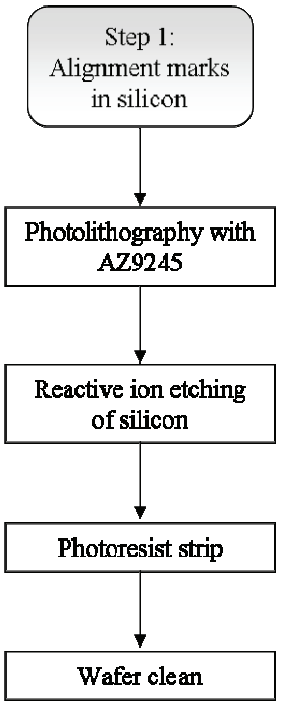

Figure 4-3: Fabrication steps for creating alignment marks in silicon.

Table 4-1: Fabrication process details for AZ9245 photoresist.

	Step/Material	Details	5 μm thick	6 μm thick	10 μm thick
1	Adhesion promoter (HMDS)	Cover wafer	Wait for 1 min	Wait for 1 min	Wait for 1 min
		Spin	3000 rpm, 30 s	3000 rpm, 30 s	3000 rpm, 30 s
2	AZ9245	Spin	1750 rpm, 5 s 3500 rpm, 40 s	1750 rpm, 5 s 3000 rpm, 40 s	300 rpm, 5 s 1000 rpm, 40 s
	Edge bead removal (AZ EBR Solvent)	Spin	-	-	600 rpm, 8 s 900 rpm, 30 s
3	Soft bake	Hotplate	110 °C, 90 s	110 °C, 90 s	110 °C, 120 s
4	Exposure	Contact	300 mJ/cm^2 @ 405 nm	300 mJ/cm^2 @ 405 nm	720 mJ/cm^2 @ 405 nm
5	Development (AZ400K)	Diluted 1:3	120 s	120 s	180 s

A plasma etcher (Trion Technology) is then used and 5.8 μm of silicon is etched in 6 min. The process parameters used for silicon etch as well as photoresist and BCB films (used in the succeeding steps) are shown in Table 4-2. The resist is then stripped in acetone for 5 min followed by acetone, methanol, isopropyl alcohol (IPA), and deionized (DI) water rinse. The last step in cleaning is to dip wafer in 5:1 mixture of H_2SO_4:H_2O_2 for 10 min followed by DI rinse, 30 s dip in 49% HF, DI rinse, and nitrogen dry.

Table 4-2: Process parameters for the plasma etching of silicon etching, photresist descum, and BCB descum.

Material	Power (W)	Pressure (mTorr)	Gas, flow (sccm)	Gas, flow (sccm)
Silicon	100	200	SF_6, 40	O_2, 20
Photoresist	50	200	O_2, 50	-
BCB	100	250	O_2, 90	CF_4, 10

4.3.2 BCB Island

Figure 4-4 shows the process flow for the deposition of the first BCB layer. The first step is to deposit and pattern 3.2 μm thick photosensitive BCB film. Process parameters for BCB photolithography are shown in Table 4-3 for three different film thicknesses. The thickness is given based on 100% polymerization (hard cure). After the film deposition, the film is partially cured at 210 °C for 40 min in the nitrogen environment. The temperature of the wafer tube during the softcure was measured to be 212 °C using a thermocouple. The last step is to remove the BCB residues using a 30 s long oxygen plasma (descum) step. The process parameters are shown in Table 4-2. Figure 4-5 and Figure 4-6 show the alignment marks and the BCB island after the completion of this step.

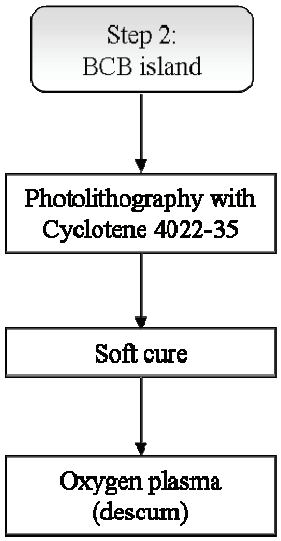

Figure 4-4: Fabrication steps for BCB island deposition.

Table 4-3: Process parameters for photosensitive BCB.

	Step/Material	Details	3.2 µm thick	2.8 µm thick	2.0 µm thick
1	Adhesion promoter (AP3000)	Spin	3000 rpm, 30 s	3000 rpm, 30 s	3000 rpm, 30 s
2	Cyclotene 4022-35	Spin	500 rpm, 8 s 2500 rpm, 30 s	500 rpm, 8 s 3200 rpm, 30 s	500 rpm, 8 s 5000 rpm, 30 s
3	Edge bead removal (T100)	Dispense (spin)	800 rpm, 8 s	800 rpm, 8 s	800 rpm, 8 s
		Dry (spin)	2000 rpm, 30 s	3000 rpm, 30 s	3000 rpm, 30 s
4	Soft bake	Hotplate	65 °C, 90 s	65 °C, 90 s	65 °C, 90 s
5	Exposure	Contact	75 mJ/cm^2 @ 365 nm	75 mJ/cm^2 @ 365 nm	75 mJ/cm^2 @ 365 nm
6	Pre develop bake	Hotplate	55 °C, 30 s	55 °C, 30 s	55 °C, 30 s
7	Puddle develop (DS2100)	Dispense	0 s	0 s	0 s
		Rinse	500 rpm, 7s	500 rpm, 7s	500 rpm, 7s
		Spin dry	2000 rpm, 30 s	3000 rpm, 30 s	3000 rpm, 30 s
8	Post develop bake	Hotplate	65 °C, 60 s	65 °C, 60 s	65 °C, 60 s

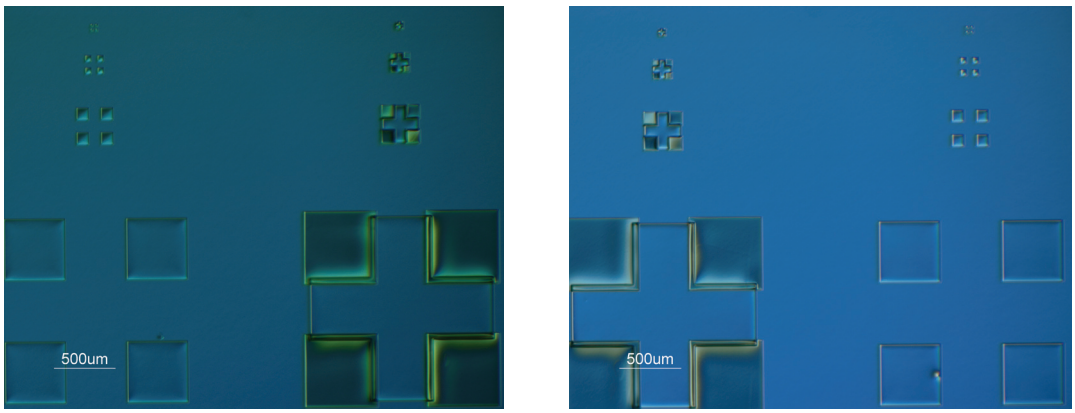

(a) (b)

Figure 4-5: Optical micrographs of the alignment marks on the left (a) and right (b) side of the 4 inch wafer showing etched silicon and patterned BCB.

Figure 4-6: Optical micrograph of the circular BCB film on the silicon substrate.

The residual stress of the BCB film is an important mechanical property that causes wafer bow, and thus affects the gap uniformity and stability of the micromotor. The stress of thick (> 9 μm) BCB films was measured using stylus profiler (Dektak D6 from Veeco Instruments). The stress calculation is based on the two-step measurement of the radius of curvature of a silicon substrate with and without the BCB film. The radius-of-curvature measurement is performed by measuring the height of the substrate, smoothing the scanned height data by fitting a 5th order polynomial, followed by calculating the radius of curvature using the first and second derivative of the fitted curve. The residual stress of the film (∑) can then be calculated using Stoney's equation of

$$\Sigma = \frac{E_s t_s^2}{6(1-\upsilon_s)t_f}\left(\frac{1}{R_1}-\frac{1}{R_2}\right) \qquad \textbf{Eq. 4-1}$$

where E_s and υ_s are the Young's modulus and Poisson's ratio of the substrate, respectively, t_s and t_f are the thickness of the substrate and the film, respectively, and

R_1 and R_2 are the radius of the curvature after and before film deposition, respectively. By measuring R_1 and R_2 and knowing the other 4 parameters (E_s, υ_s, t_s, and t_f) the stress of the film is calculated. The curvature of the wafer is measured using a contact profiler. The thickness of the BCB film was measured using an optical profiler (NT1100 from Veeco Instruments). The thickness of the substrate was measured using a micrometer (from Mitutoyo) with 0.001 mm resolution to be 469 μm. Due to uncertainty in E_s, υ_s, t_s, and t_f, the calculated stress is only an approximation. The Young's modulus was assumed to be 180.5 GPa for a <100> silicon substrate. Figure 4-7 shows a typical 30 mm long scan profiles that were performed before and after film deposition. Figure 4-8 shows the average and maximum stress measured with different scans on two wafers. These values are directly calculated by the software. The average stress is calculated from above equation, while the maximum stress illustrates the local stress estimated by the software. The average stress calculated for a 9.6 μm and 23.5 μm thick samples were 28.1 and 29.0 MPa-tensile, respectively. These values are in good agreement with reported data in the literature [97]. Considering a stress of 28.1 MPa for a 9.6 μm thick film, the maximum bow after the film deposition on a flat silicon substrate is 29 μm across a 100 mm diameter wafer[29]. The bow across a smaller die would be appreciably smaller e.g. 0.29 μm across a 10 mm die. Small bow allows the gap to be uniform across the device.

[29] t_s= 525 μm, E_s = 180 GPa, υ_s = 0.27.

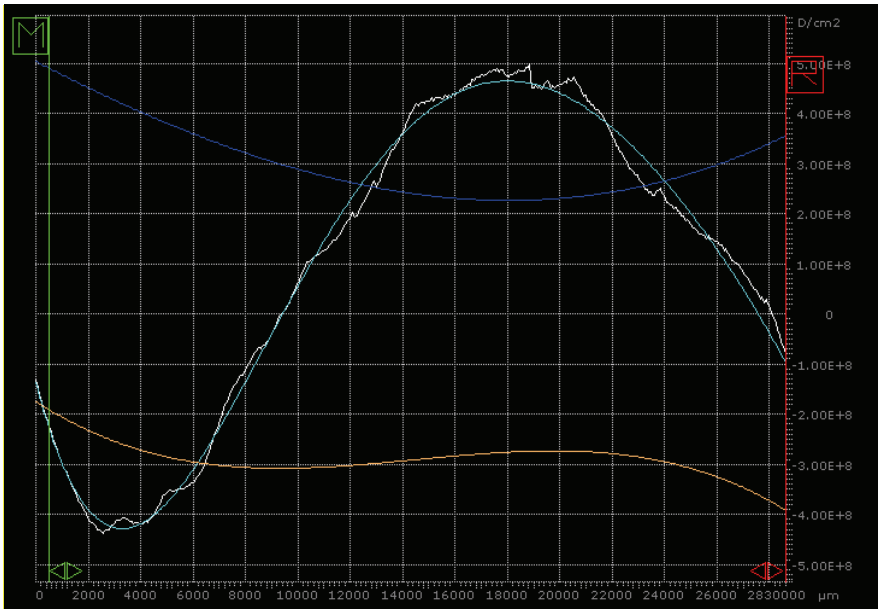

Figure 4-7: Typical substrate scan profiles without (brown) and with (blue) the BCB film. The difference in the profiles (white) is also shown together with a 5th order polynomial fit (cyan).

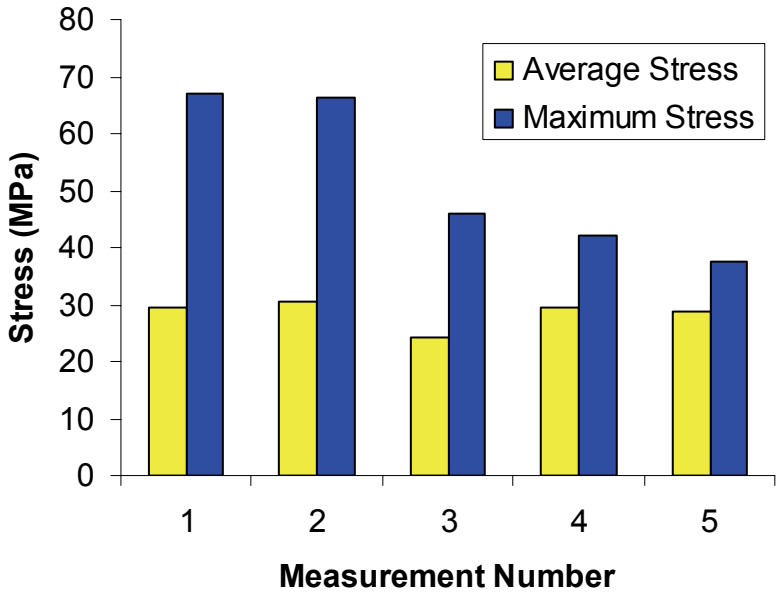

Figure 4-8: Average and maximum measured stress on a 4 inch diameter wafer.

4.3.3 Interconnections

The first layer of metal forms an interconnection layer that connects electrodes in groups of six. The fabrication process is shown in Figure 4-9. After wafer dehydration, a 20 nm thick chromium film and 250 nm thick gold film are deposited using a DC magnetron sputtering (AJA International). Process parameters are shown in Table 4-4. Low deposition power (50 W) is chosen to reduce the penetration of the metal ions into the polymer. The chromium and gold depositions are performed for 8 and 20 min, respectively. To reduce the contamination effects, the sputtering targets are conditioned for a few minutes before each deposition.

The metal layers are then patterned with a 5 μm thick photoresist (AZ9245). The process parameters are summarized in Table 4-1; however, no adhesion promoter (HMDS) is used here. This ensures a good electrical connection between the interconnection and electrode layers. Figure 4-10 shows the lithography results. The gold and chromium layers are then etched using commercial wet etchants (Transene Company Inc). The gold film is etched for 90 s using TFA etchant at room temperature, and the chromium is etched for 40 s using TFD etchant at 40 °C.

After inspection, the photoresist is removed using CLK888 photoresist/residue remover (JT Baker). This step is performed at 60 °C for 5 min. CLK888 is chosen over other stripers for two reasons. First, the solution is compatible with a number of low-k dielectrics such as BCB. Second, the solution acts both as a bulk resist striper and as a residue remover. The latter is important because low ohmic resistance is required between the two metal layers. Wafers are rinsed with DI, blow dried, and dehydrated next. The fabrication results are shown in Figure 4-11.

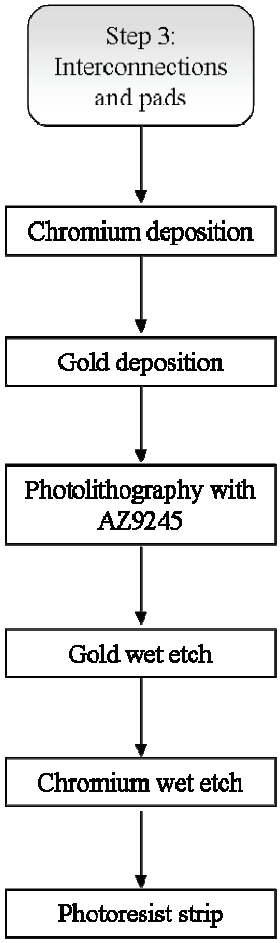

Figure 4-9: Fabrication steps for the metal deposition.

Table 4-4: Sputtering deposition parameters.

Target	Power supply	Pressure (mTorr)	Carrier gas, flow (sccm)	Power (W)	Deposition rate (nm/min)
Chromium	DC	5	Ar, 20	50	2.5
Gold	DC	5	Ar, 200	50	12.5

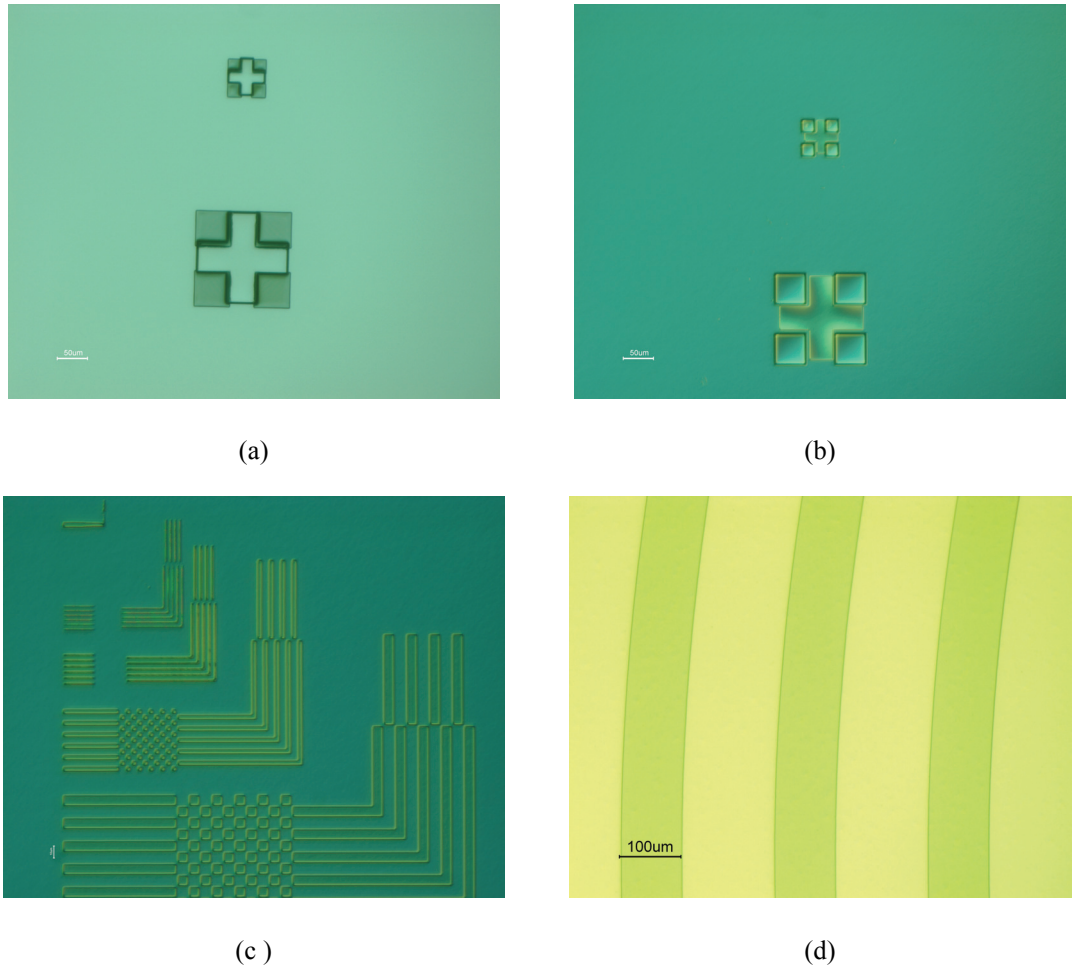

(a) (b)

(c) (d)

Figure 4-10: Optical micrographs of the (a-b) alignment marks on the two sides, (c) test structures in photoresist, and (d) interconnections after the lithography and before the wet etching steps.

4.3.4 Interlayer Dielectric

The deposition of the interlayer dielectric (ILD) is very similar to the deposition of the first metal layer; however, no adhesion promoter is used (Figure 4-12). Process parameters for 2.8 μm thick film are summarized in Table 4-3. After photolithography the polymer is cured at 210 °C for 40 min (soft cure). The last step is 30 s long O_2/CF_4 plasma with the process parameters summarized in Table 4-2. The fabrication results are shown in Figure 4-13.

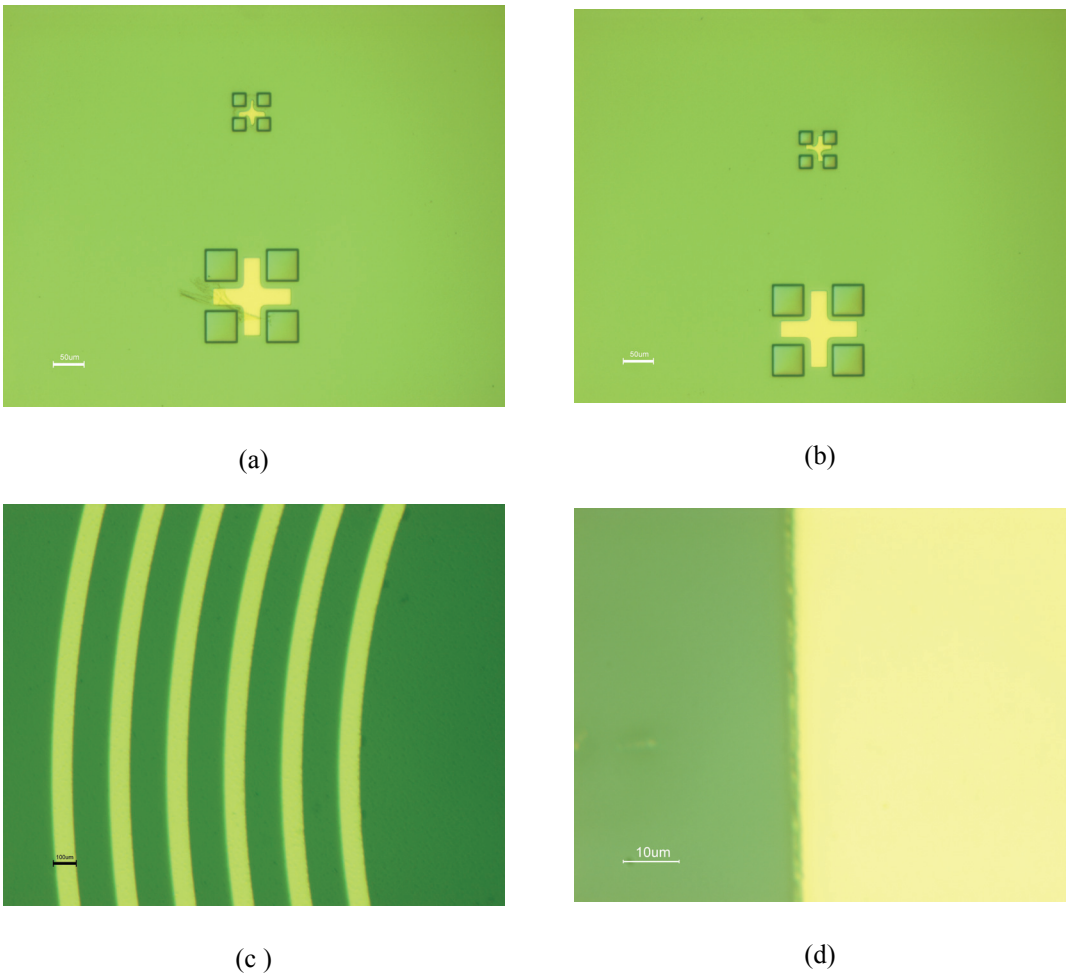

Figure 4-11: Optical micrographs of the alignment (a-b) marks and interconnection lines (c-d) after the metal etching and photoresist stripping.

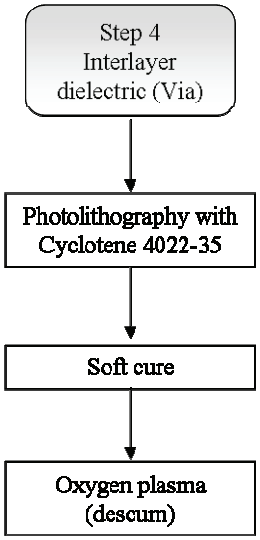

Figure 4-12: Fabrication steps for the ILD deposition.

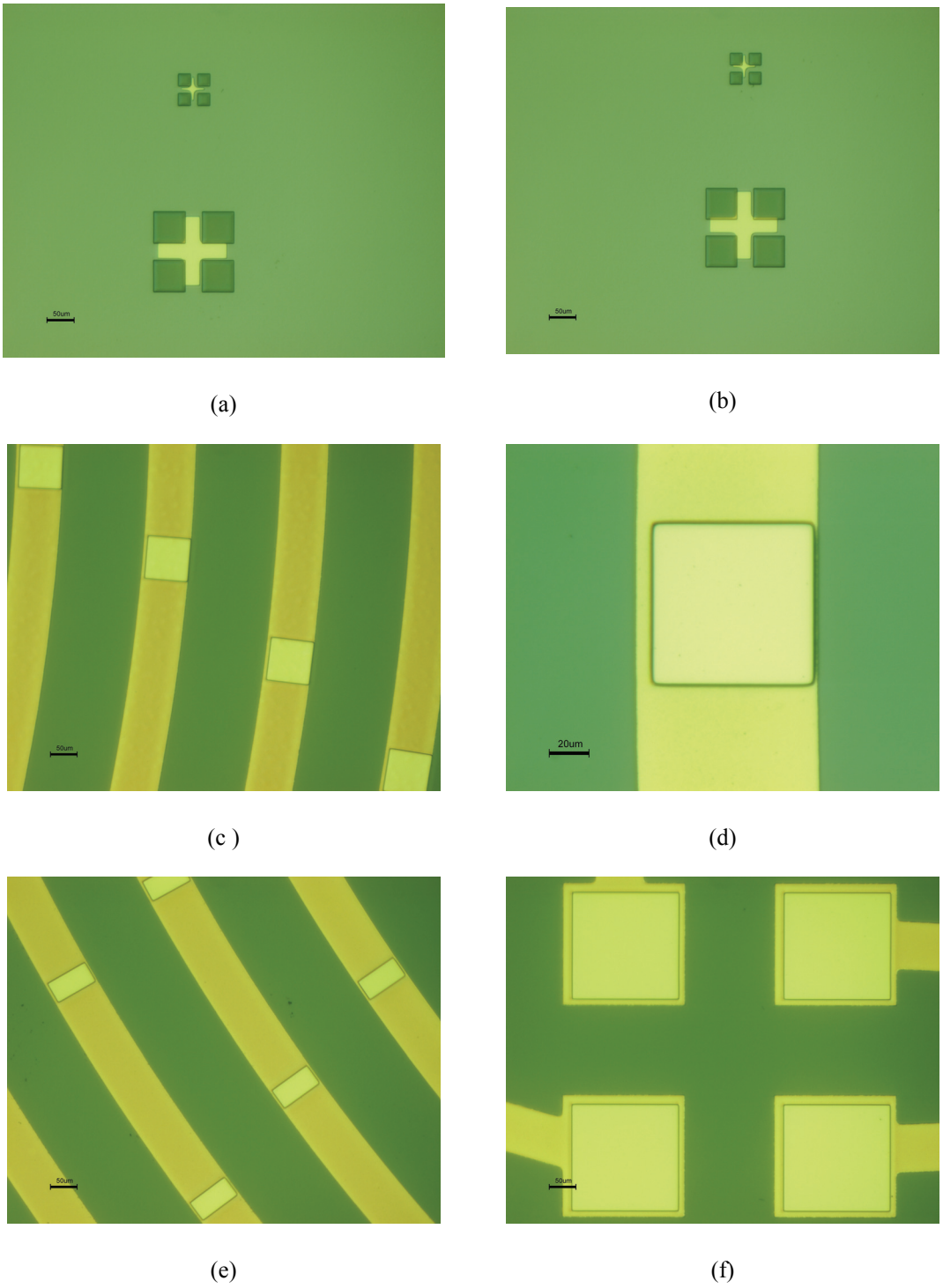

Figure 4-13: Optical micrographs of the alignment marks (a-b), interconnections (c-e), and pads (f) after the deposition of the via layer.

4.3.5 Electrodes

The fabrication process of the electrode layer is different from the interconnection layer. The lift-off process summarized in Figure 4-14 is used instead of the "etch process". Etch process was used for the interconnection layer because the exact geometry of the lines is not important. However, if a single line is lost due to the imperfections in the fabrication process, the machine has no longer six phases. The adhesion loss of the metal film to the BCB layer is highly probable in the lift-off process[30]. Therefore, the etch process was used for the first metal layer. For the electrode layer, however, the precision in the geometry is extremely important. Therefore, the lift-off process is used.

The fist step is creating a photoresist layer with lift-off profile (angled sidewalls). This photolithography step is detailed in Table 4-5. Figure 4-15 shows the fabrication results after photolithography.

Short oxygen plasma is used before metal deposition to remove any photoresist residues from the via opening areas. This ensures good electrical connection between the two metal layers. The photoresist etching parameters are summarized in Table 4-2. Similar to the first metal layer, chromium and gold films are sputtered next. The wafer is then placed inside an acetone solution in an ultrasonic bath (from Bronson) for 15 min. The acetone solution is renewed followed by another 15 min of ultrason. Finally, the wafer is rinsed with DI for 30 min in the ultrasonic bath. The purpose of the latter is to remove any metal residues from the surface. Figure 4-16 shows a micrograph of the device after the completion of this step.

[30] If lift-off process were used for the first metal, eventually the first metal line would go through acetone ultrasonic bath twice (once for each metal layer).

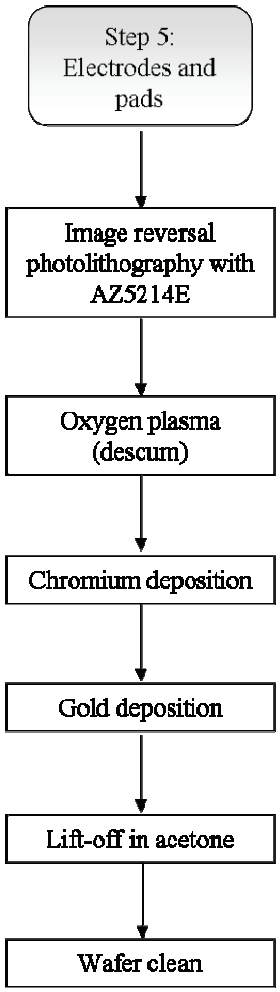

Figure 4-14: Fabrication steps for electrode deposition.

Table 4-5: Fabrication process details for AZ5214E lithography (lift-off profile).

	Step/Material	Details	Notes
1	AZ5214E	Spin	3000 rpm, 30 s
2	Edge bead removal with AZ EBR Solvent if needed	Spin	600 rpm, 8 s 2000 rpm, 30 s
3	Soft bake	Hotplate	100 °C, 60 s
4	First exposure (with mask)	Contact	40 mJ/cm^2 @ 405 nm
5	Post exposure bake	Hotplate	120 °C, 45 s
6	Second exposure (flood)	Contact	1200 mJ/cm^2 @ 405 nm
7	Development (AZ400K)	Diluted 1:6	120 s

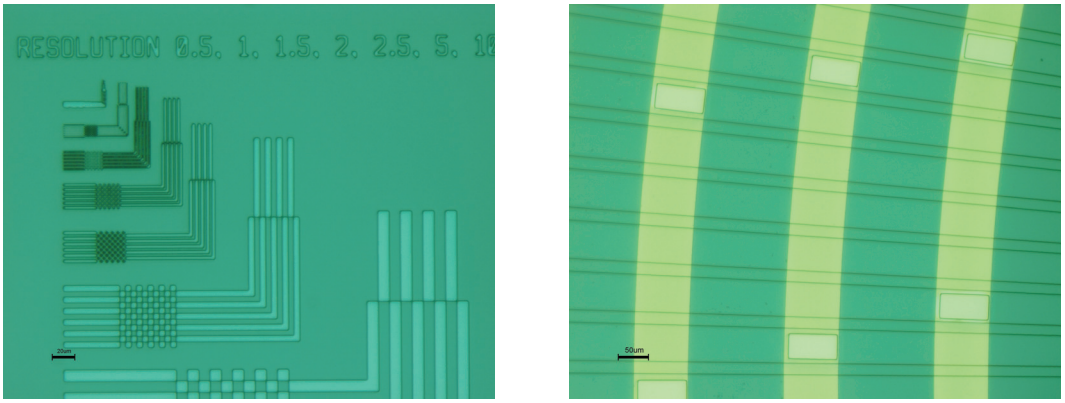

(a) (b)

Figure 4-15: Optical micrographs of the photoresist after image reversal process.

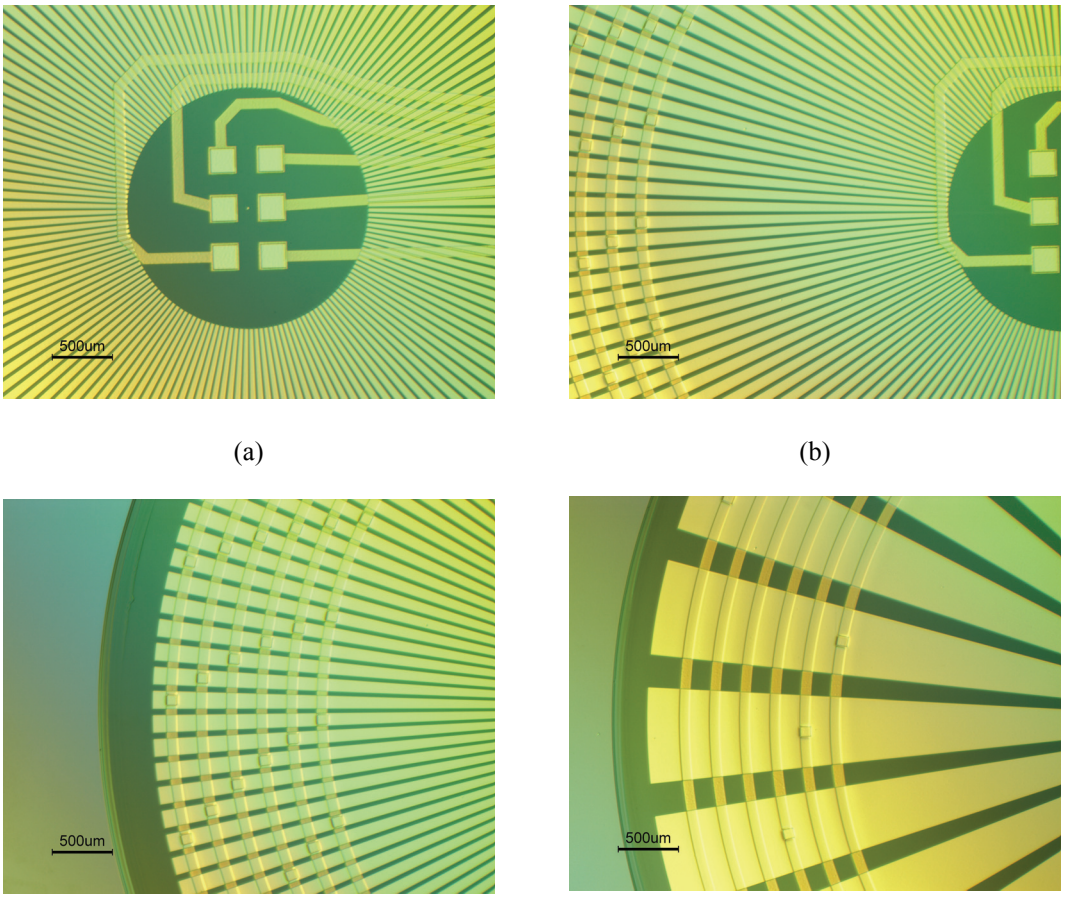

(a) (b)

(c) (d)

Figure 4-16: Optical micrographs of the (a) D4, (b) D4, (c) D4, and (d) D3 designs after electrode deposition.

4.3.6 Passivation Layer

The deposition of the passivation layer is similar to the two previous BCB deposition steps with the exception of the thickness. The process steps and the results are shown in Figure 4-17 and Figure 4-18, respectively. The smallest thickness achievable with Cyclotene 4022-35 series is 2 μm and is used here. Table 4-3 summarizes the details of the process. Similar to the previous BCB deposition step, the adhesion promoter is not used here. After photolithography the polymer is cured at 210 °C for 40 min (soft cure). The last step is a 30 s long O_2/CF_4 plasma with the process parameters summarized in Table 4-2. The process steps and the results are shown in Figure 4-17 and Figure 4-18, respectively.

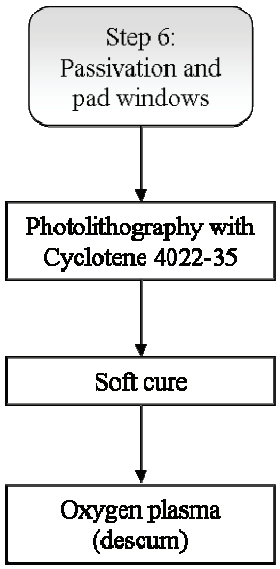

Figure 4-17: Fabrication steps for passivation layer deposition.

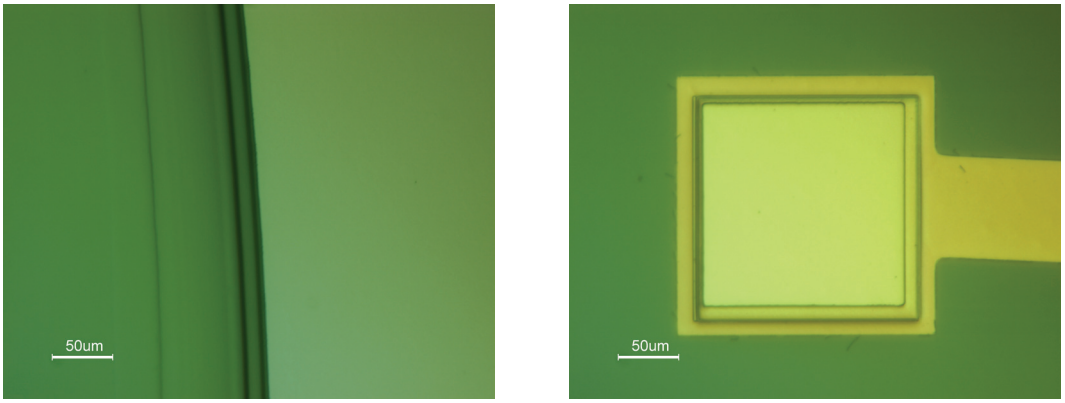

(a) (b)

Figure 4-18: Optical micrographs of the device after third BCB deposition showing (a) the edge of where the passivation layer is extended 10 μm on top of the island layer, and (b) opening in the pad are.

4.3.7 Microball Housing

Figure 4-19 shows the steps involved in the fabrication of the deep rectangular trenches in silicon. A 10 μm thick resist is patterned with parameters listed in Table 4-1; however, adhesion promoter (HMDS) is not used. As mentioned in Chapter 3, the alignment accuracy of the microball housing with the electrodes is crucial. Since a contact mask aligner (EV620 from EVG Group) is used for exposing thick photoresist, the edge bead removal of the photoresist after spin becomes important. The misalignment, as shown in Figure 4-20, is less than 2 μm.

Deep reactive ion etching is performed for 48 min using the process parameters listed in Table 4-6 and a Bosch plasma etcher (Surface Technology Systems). A 30 s long isotropic oxygen plasma etch is performed inside the DRIE tool to remove the teflon-like polymer from the sidewalls. Photoresist is stripped in CLK888 bath for 10 min at 65 °C. The polymer is fully cured at 250 °C for 1 h. The last step in the fabrication of the stator is to perform a 30 s long O_2/CF_4 plasma etch to remove any

residue from the contact pads. Figure 4-21 shows the fabricated device before and after the DRIE step.

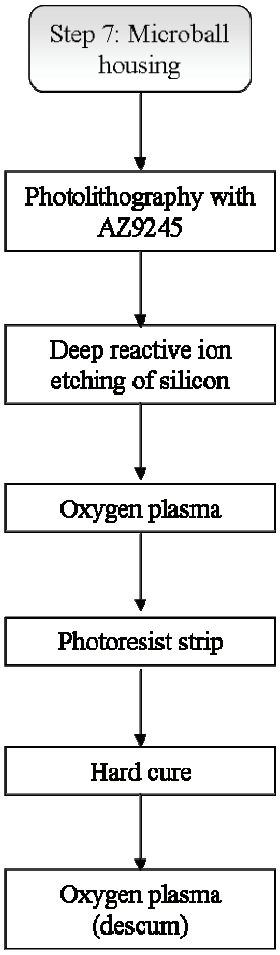

Figure 4-19: Fabrication steps for microball housing.

Table 4-6: Fabrication process details for microball housing etch in silicon.

	Parameter		Etch Cycle	Passivation Cycle
1	Cycle length (s)		10	6.5
2	Pressure control		Fixed APC 80%	Fixed APC 80%
3	Gas flow (sccm)	C_4F_8	0	85
		SF_6	130	0
		O_2	13	0
4	Coil power (w)		600	600
5	Platern power (w)		17	0
6	Helium pressure (mTorr)		800	

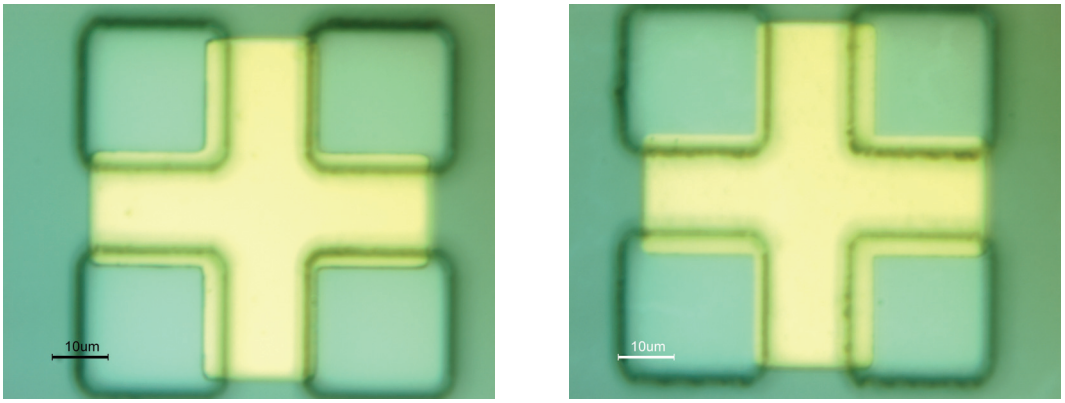

(a) (b)

Figure 4-20: Optical micrographs of the alignment marks on the two sides of the wafer. The golden crosses are electrode layer and transparent squares are microball housing in photoresist. Alignment accuracy is better than 2 μm.

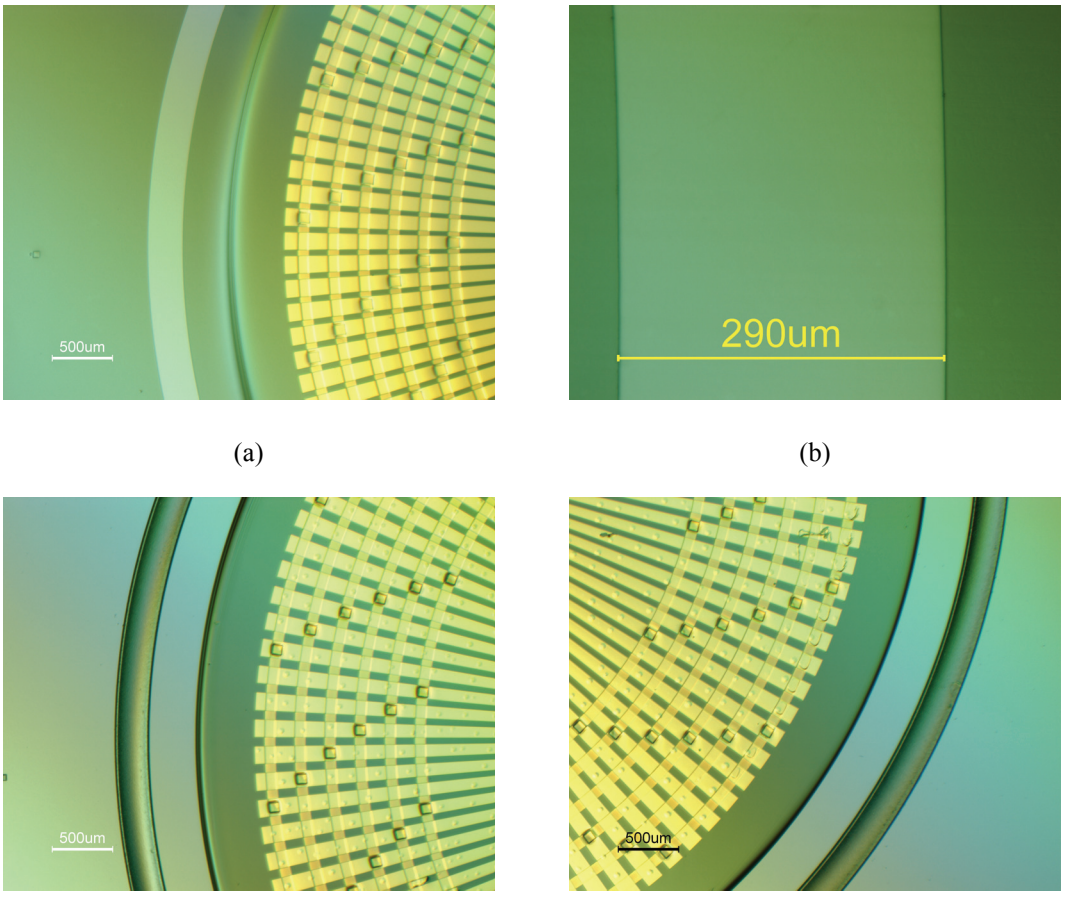

(a) (b)

(c) (d)

Figure 4-21: Optical micrographs of the device after photolithography (a-b) and after DRIE (c-d).

4.4 Rotor Fabrication

4.4.1 Poles and Microball Housing

The first step in fabrication of the rotor is to etch poles and microball housing on one side of the wafer. Figure 4-22 shows the details of this step. A 10 μm thick photoresist is used as a mask for the DRIE process. The process parameters for the thick resist are listed in Table 4-1. A short oxygen plasma etch is performed to ensure that there is no photoresist residue in the developed areas. The DRIE step is identical to the previous DRIE. The etch rate was measured to be 2.86 μm/min. The photoresist is then removed in acetone; the wafer is rinsed with acetone, methanol, IPA, and DI water. The wafer is dried and dehydrated to be ready for the next step. Figure 4-23 shows optical micrograph of four different designs.

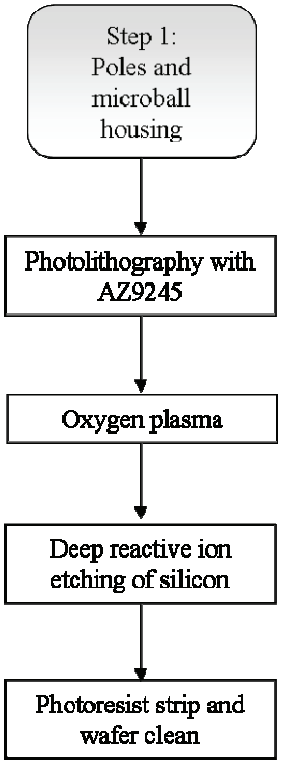

Figure 4-22: Fabrication steps for rotor poles and microball housing.

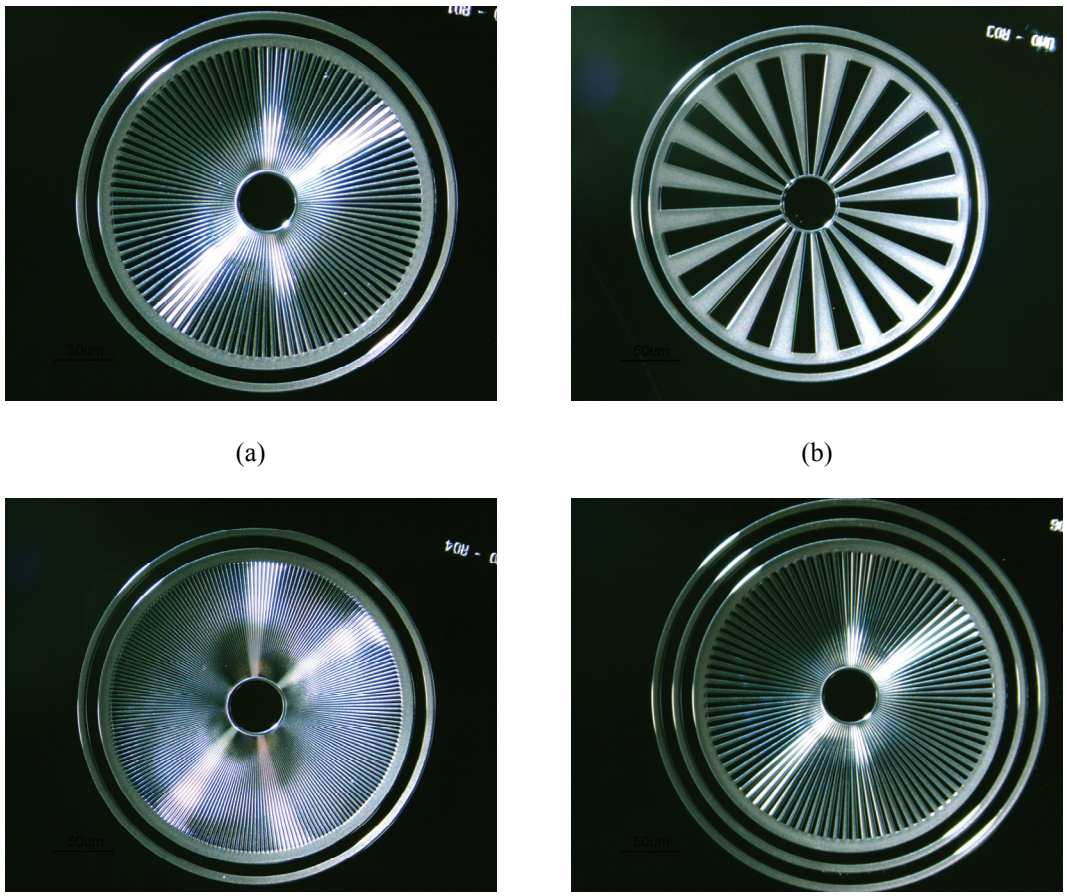

(a) (b)

(c) (d)

Figure 4-23: Optical micrographs of the rotor (ϕ=14 mm)showing (a) RD1, (b) RD3, (c) RD4, and (d) RD6.

4.4.2 Rotor Release and Cavity Etch

The second step in the fabrication of the rotor is shown in Figure 4-24. The photolithography step is similar to the previous lithography. The wafer is bonded to a carrier wafer using a Shipley 1813 photoresist as an adhesive layer. The process involves spinning the resist at 3000 rpm for 30 s to achieve 1.6 μm thick film. The two wafers are pressed against each other and baked on a hotplate at 50 °C for 5 min. The wafer is then kept at room temperature for 30 min under a few Newton force. A high-selectivity recipe is used for through wafer etch using the DRIE tool. The etch parameters are listed in Table 4-7. The etch time was 2 h and 40 min and the etch rate

was measured to be 2.72 μm/min. Wafers are de-bonded in acetone bath, cleaned in piranha for 10 min, rinsed, and dried. Figure 4-25 shows the scanning electron micrographs of the released die.

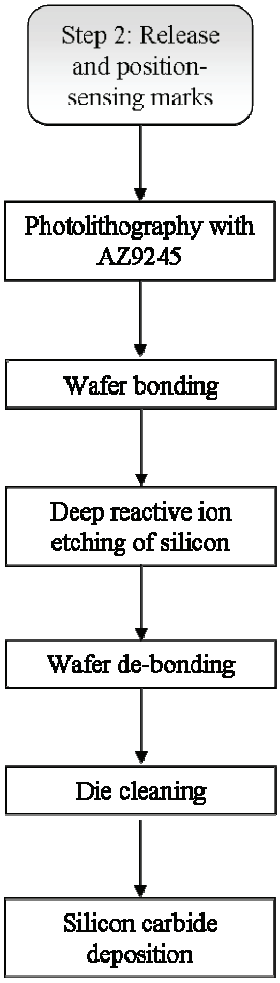

Figure 4-24: Fabrication steps for rotor release.

Table 4-7: Fabrication process details for DRIE release.

	Parameter		**Etch Cycle**	**Passivation Cycle**
1	Cycle length (s)		10	3
2	Pressure control		Fixed APC 85%	Fixed APC 85%
3	Gas flow (sccm)	C_4F_8	0	100
		SF_6	130	0
		O_2	0	0
4	Coil power (w)		600	600
5	Platern power (w)		10	0
6	Helium pressure (mTorr)		800	

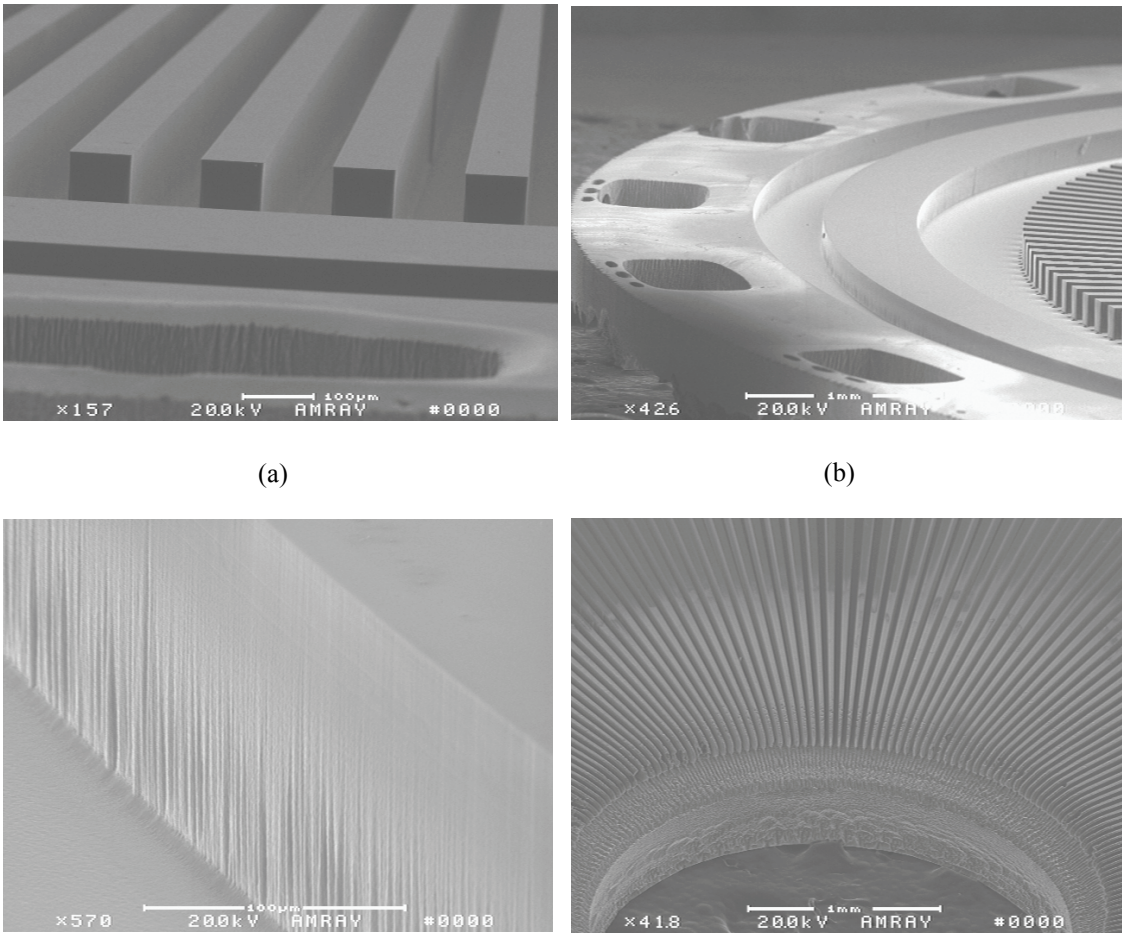

Figure 4-25: Scanning electron micrographs of the rotor (RD1) after release showing (a) poles, (b) microball housing and position sensing pits, (c) sidewall of the trench, and (d) center cavity.

4.4.3 Silicon Carbide Film as a lubricant

After initial testing of the micromotor, it was concluded that the friction force between stainless steel microballs and silicon trenches is too high and the rotor can not spin. Therefore, a solid lubricant film of silicon carbide is deposited on the rotor. RF magnetron sputtering is used for the silicon carbide deposition at the room temperature. A few possible process conditions are listed in Table 4-8. The deposition process is generally slow. The process with highest deposition rate (7.5 mTorr pressure) results in deposition of impurities and large grains; therefore, the process

with the second highest rate (2.5 mTorr pressure) is used. With the total deposition time of 1 h the estimated silicon carbide thickness is 173 nm.

Table 4-8: Silicon carbide sputtering conditions.

Target	Power supply	Pressure (mTorr)	Carrier gas, flow (sccm)	Power (W)	Bias (W)	Deposition rate (A/min per watt)
Silicon carbide	RF	2.5	Ar, 20	300	300	5.7
Silicon carbide	RF	5	Ar, 20	200	200	4
Silicon carbide	RF	7.5	Ar, 20	300	300	6.3

4.5 Micromachine Assembly

After the fabrication of the stator and rotor, the stator is clamped (fixed) on an aluminum chuck. The stainless steel microballs are then manually positioned inside the stator trench using fine-tip tweezers. The rotor is then manually aligned and positioned on top of the rotor using tweezers. If the rotor is aligned and positioned properly, it rotates freely with little resistance.

4.6 Fabrication Summary

The thickness of each layer is measured using a contact or optical profilometer. A summary of the layer thickness or etch depth for all steps is listed in Table 4-9. The scanned profiles for the stator and rotor are shown in Figure 4-26 and Figure 4-27, respectively. Figure 4-26(a) shows the profile of the island after softcure and descum. The final thickness of the film is given in Table 4-9 which is 10 % smaller due to film shrinkage during hard cure step. Figure (b) and (d) the interconnection and electrode layer profiles, respectively, with the thickness of 0.26 μm. Figure (c) and (e) show the profile of the second and third BCB layers, respectively. The thickness of the first BCB layers before hard cure were measured to be 3.6, 3.1, and 2.2 μm, respectively.

Figure (f) shows the final profile of the island edge made out of three BCB layers with the thickness of 8 μm.

The depths of the silicon trenches on the stator and rotor measured with both contact and optical profilometer were in agreement. Multiple rotor wafers were fabricated to achieve the desired depth of 135 μm, which corresponds to the air gap of 10-12 μm. The profile of the rotor is shown in Figure 4-27. The results show etch depth nonuniformity of 0.7% across each die.

Table 4-9: Summary of layer thicknesses.

Layer	Substrate	Material	Thickness/depth (μm)
Alignment marks	Stator	Silicon	5.8
Island	Stator	BCB	3.2
Interconnection	Stator	Chromium/gold	0.020/0.26
ILD	Stator	BCB	2.8
Electrode	Stator	Chromium/gold	0.020/0.25
Passivation	Stator	BCB	2.0
Microball housing	Stator	Silicon	132.4±0.4
Microball housing/poles	Rotor	Silicon	135.5±0.4
Rotor release	Rotor	Silicon	~525

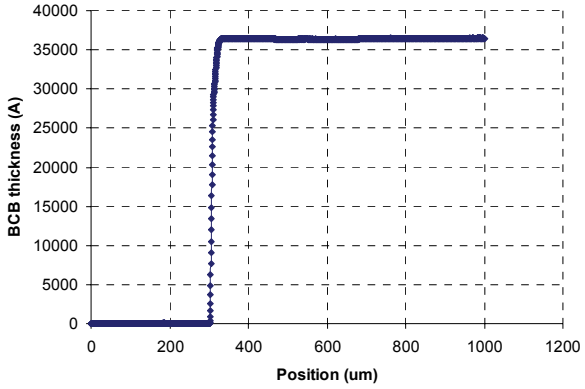

(a)

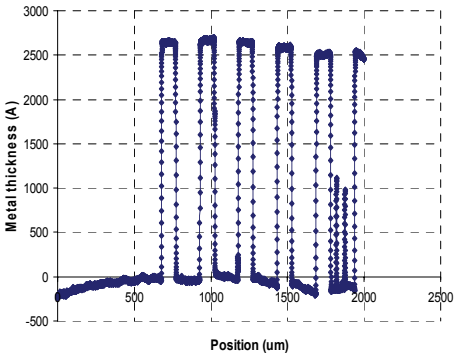

(b)

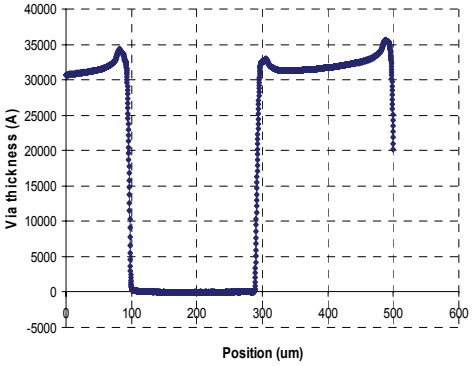

(c)

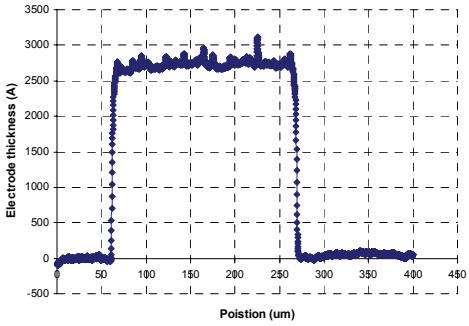

(d)

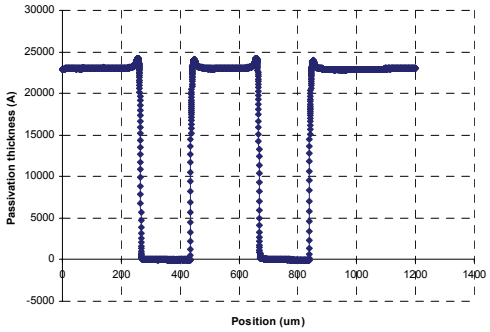

(e)

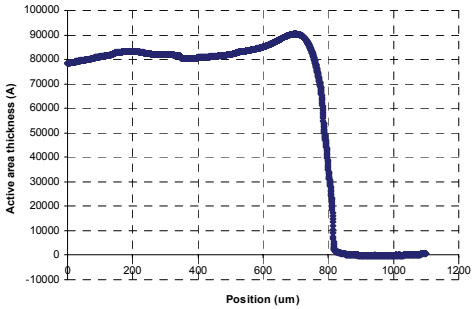

(f)

Figure 4-26: Contact profilometery results of the stator after the completion of each step: (a) BCB island, (b) interconnection (c) ILD, (d) electrodes, (e) passivation, and (f) The distance between silicon substrate and the third BCB layer.

.

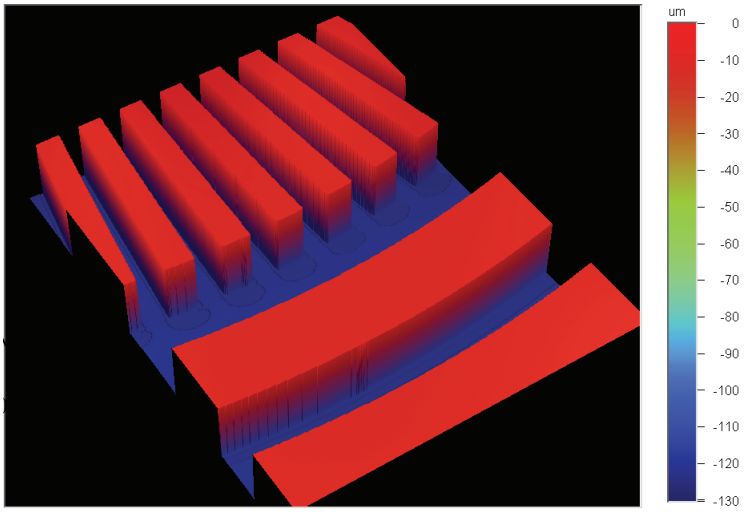

(a)

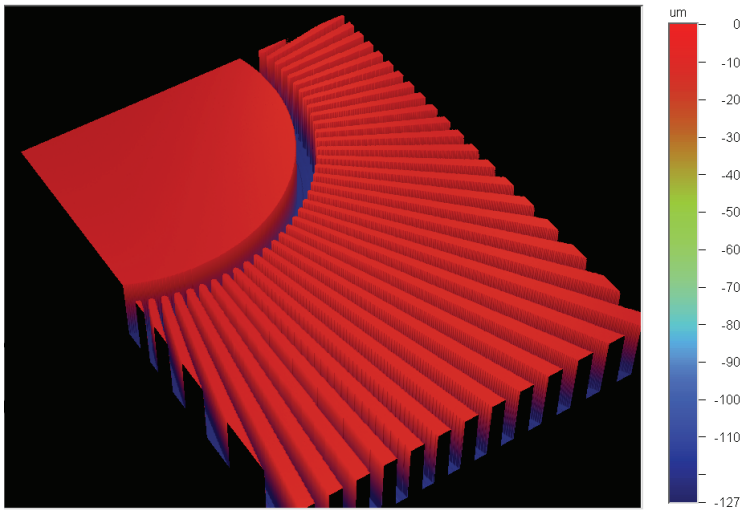

(b)

Figure 4-27: 3D optical profiles of the rotor obtained using vertical scanning interferometer (Veeco NT1100) showing (a) outer part and (b) inner part of the rotor.

The fabrication results reported in this chapter were the product of extensive unit process development. To avoid confusion, the discussions on the development of these unit steps were not covered in this manuscript. The successful fabrication of the micromotor has enabled the testing of multiple devices. From 17 devices on a single

stator wafer, 15 are testable. The characterization of the fabricated devices is discussed in Chapter 5.

5 Characterization

The development of the rotary micromotor is based on the previous work on the design, fabrication, and testing of the linear micromotors. The rotary micromotor was extensively discussed in Chapter 1 through 4. In Section 5.1, however, the work preceding the development of the rotary device is reported. This work has been an essential backbone for the evolution of the rotary machine. The characterization results for the linear device are discussed first. In the second part of this chapter (Section 5.2), the characterization results for the rotary device are reported.

5.1 Linear Micromotor Characterization

5.1.1 Introduction

The primary application of the bottom-drive linear variable-capacitance micromotor (B-LVCM) is long-range, high-speed, linear micropositioning. In addition, this device provides a platform to investigate the mechanical properties of roller bearings in MEMS and learn how to design, fabricate, and test the rotary micromotor. The detailed design and fabrication, as well as initial test results for the first-generation 6-phase B-LVCM, were previously reported [130, 131].

The fabrication of the second-generation B-LVCM together with the dynamic characterization is reported in this chapter. The design and fabrication are described first, and the test setup used for the characterization is introduced next. The dynamic characterization including the measurement results of position, instantaneous velocity, acceleration, and the net force on the slider [132], are presented. The device is modeled as a simple mass-dashpot-spring system. The model parameters were

extracted from the measured data. Test and modeling results are compared and discussed in Section 5.1.2.

5.1.2 Development of the Second-Generation Linear Micromotor

Figure 5-1 shows a 3D exploded view of the linear micromotor supported on microball bearings. B-LVCM is comprised of three major components: stator, slider, and microballs. The slider is the linear counterpart of the rotor. Two new technologies were implemented in the development of the linear micromachine: (1) microball bearing in silicon as a support mechanism and (2) BCB low-k polymer as an insulating layer [130, 133]. The geometry specifications of the tested B-LVCM are shown in Table 5-1. The micromotor has an electrode-to-pole ratio of 6:4 with identical electrode and pole width of 90 μm[31].

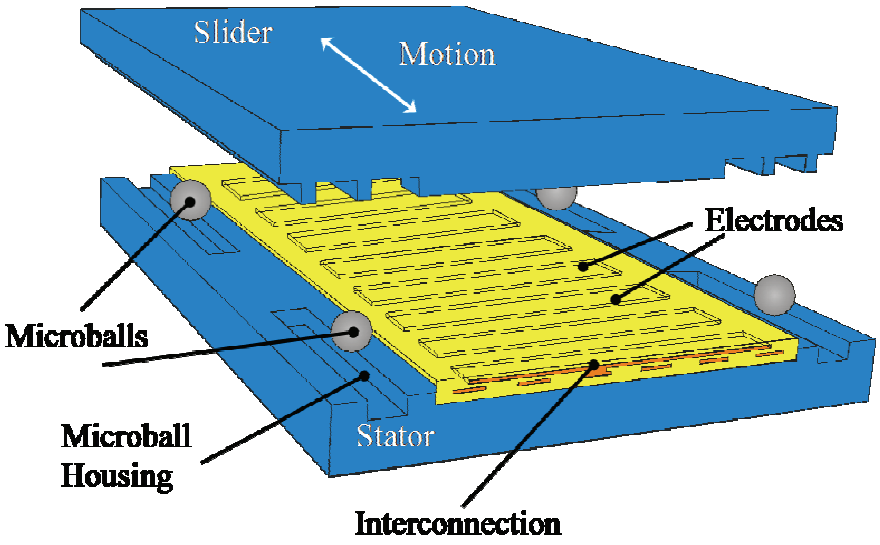

Figure 5-1: Schematic 3D view of the bottom-drive, linear, variable-capacitance micromotor.

[31] The design of the B-LVCM is performed by Mr. Alireza Modafe, University of Maryland, 2003.

Table 5-1: Linear micromotor geometry specifications.

Parameter	Value
Electrode/pole width (μm)	90/90
Electrode/pole spacing (μm)	30/90
Electrode/pole number	84/36
Air gap (μm)	26-34
Microball housing width (μm)	290
Microball housing length (mm)	3.6
Stator length/width (mm)	14/10
Slider length/width (mm)	12/10

The second-generation B-LVCM was fabricated with major modifications to the process of the first-generation [131] device. The fabrication process of the stator uses 7 mask levels and involves the deposition and patterning of three BCB layers, two metal layers, and etching of microball housings in silicon. The schematic cross section of the stator is similar to that of the rotary micromotor as shown in Figure 5-2. The first BCB layer isolates the substrate from the active part of the device. The first metal layer forms the interconnection level that connects every other sixth electrode of the 6-phase micromachine, whereas, the second metal layer forms the electrode level. Similar to the rotary micromotor, the second and third BCB layers are for interlayer dielectric and passivation purposes, respectively.

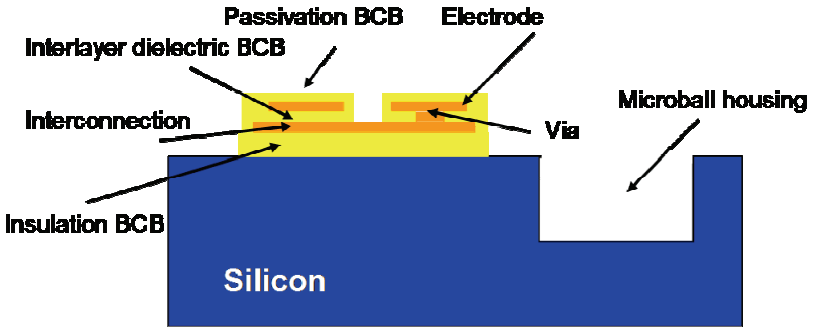

Figure 5-2: Schematic cross section of the B-LVCM stator with three dielectric and two metal layers (Dimensions are not to scale).

First, a 3 μm thick photosensitive BCB (Cyclotene 4024-40 from Dow Chemical) is spun, patterned, and partially cured (at 210 °C for 50 min). In the first-generation device [131] this step included a silicon etch step (30 μm deep) using DRIE and multiple photolithography and chemical mechanical planarization (CMP) steps. For simplicity, those steps were replaced by a 3 μm thick BCB deposition. The drawback of this process is smaller thickness for the isolation layer. Consequently, a higher parasitic capacitance and lower efficiency device is attained. The advantage of this process is less fabrication complexity, higher yield, and shorter process time.

A 20/250 nm thick Cr/Au metal layer (interconnection) is then sputtered and patterned using a positive photoresist (Shipley 1813) and wet etching. The yield of the Cr/Au metallization process was increased by replacing the original lift-off process, in the first-generation device, with an etch process. The original lift-off process resulted in the partial loss of interconnection layer. This phenomenon reduces the number of active phases of the machine.

A dielectric layer (Cyclotene 4024-40) with a thickness of 3.2 μm is then spun, patterned, and partially cured (at 210 °C for 50 min) to form an interlayer dielectric (ILD) with open vias for electrical connection between the two metal layers. The partial cure of the BCB results in 75 % polymerization and a better adhesion to the metal layers [93]. The thickness of this layer was increased from 2 μm in the first-generation device to 3.2 μm to provide more uniform step coverage and higher breakdown voltage.

The second metal layer (electrode) with 20/250 nm thick Cr/Au layer is patterned using photolithography with an image reversal photoresist (AZ5214E), sputtering, and lift-off in acetone. A 2.1 μm thick passivation layer (Cyclotene 4022-35) is then spun, patterned, and fully cured (at 250 °C for 1 h). This is followed by the patterning and etching of silicon (130 μm deep) using a 9 μm thick positive photoresist (AZ9245) and DRIE to form the microball housings. The process details for each step are similar to ones reported in Chapter 4 for the rotary device. Figure 5-3 shows the optical micrograph of the stator at different fabrication steps.

The slider fabrication process is comprised of a lithography step and a DRIE step to etch microball housing and poles simultaneously. Figure 5-4 and Figure 5-5 show the fabricated stator and slider of the 6-phase micromotor, respectively. The assembly of the micromotor requires the manual placement of the microballs in the stator trenches using a pair of tweezers. The slider is then aligned with the stator and positioned on top of the microballs.

5.1.3 Test Setup

A test-bed for the characterization of the micromotor was developed. Figure 5-6 shows the block diagram of the test station consisting of a 6-channel, high-voltage actuation system, a high-speed camera, and an image processing unit. Initially, the motion of the motor was captured using a 30-frame-per-second (fps) camera (Model DCR-HC42 from Sony) and a microscopic lens (35 mm, 24×).

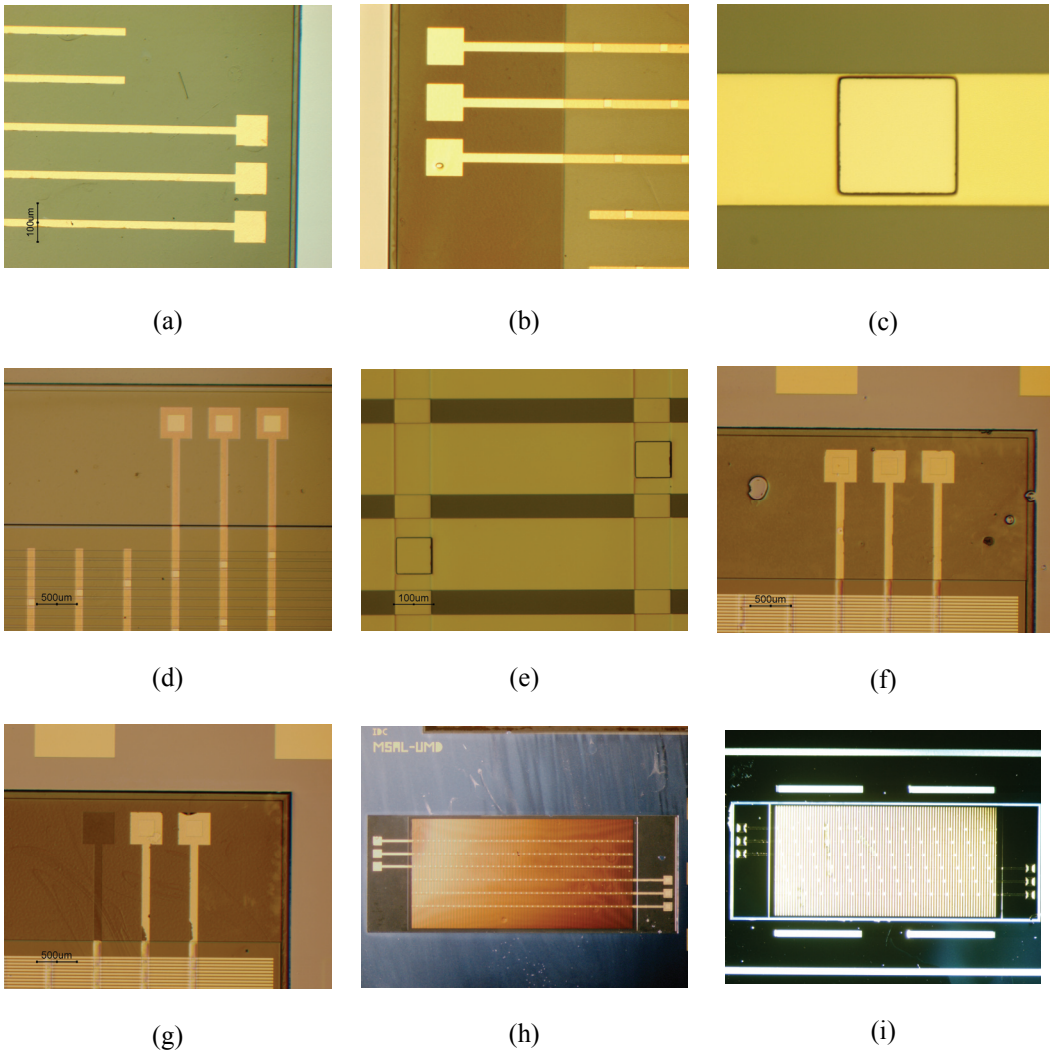

Figure 5-3: Optical micrographs of the second-generation linear micromotor at the following fabrication stages: (a) first level of metal (interconnects) on the BCB island, (b) second layer of BCB forming vias, (c) close-up of a via, (d) image-reversal lithography for the second level of metal (electrodes), (e) electrode deposition, (f) passivation layer deposition, (g) same as (f), however, fabrication imperfection caused one interconnect phase peel-off during lift-off process of the second metal layer, (h) complete micromotor with 30-µm-wide electrode before trench fabrication, and (i) complete machine with after trench fabrication.

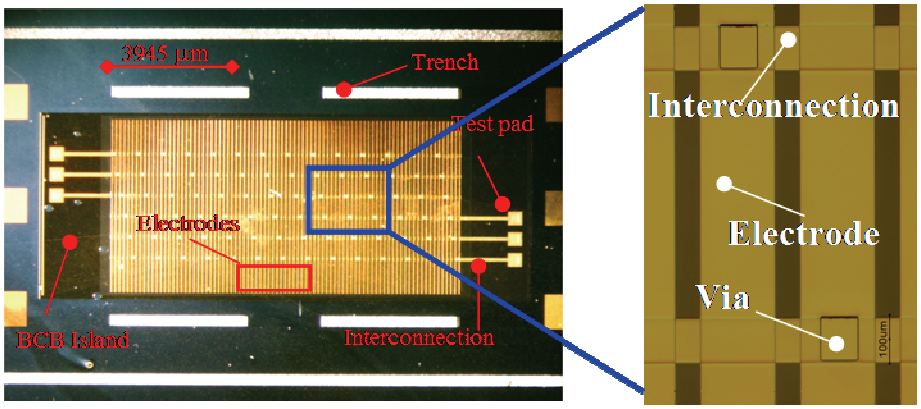

Figure 5-4: Optical micrographs (top view) of the 6-phase stator comprises three BCB layers, two metal layers, and four trenches for housing microballs.

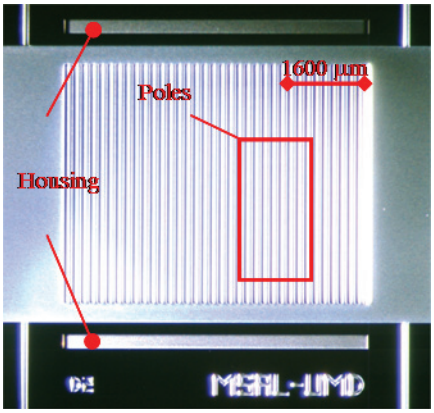

Figure 5-5: Optical micrograph (top view) of the slider showing poles and microball housing etched into silicon substrate using DRIE.

The speed of a standard 30-fps camera was found to be too slow for capturing the transient response of the micromotor. Therefore, a more accurate measurement was performed using a low-noise, monochromatic, high-speed (635-1000 fps) video camera with 1280×1024 pixels (MotionPro HS-3 from Redlake) and a long-distance, microscopic lens system (Model KV from Infinity Photo-Optical). This measurement method was preferred over conventional stroboscopic dynamometry techniques previously used for side-drive micromotors [80] because of the greater displacement and temporal accuracy.

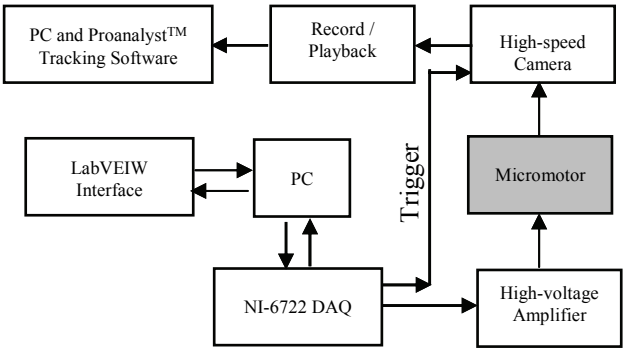

Figure 5-6: Block diagram of the micromotor test station.

5.1.4 Characterization Results

The micromotor is excited with six square-wave signals. The first three phases are 120° out of phase. The remaining three phases are the inverse of the first three. As mentioned in Chapter 2, the excitation configuration with equal number of positive and negative potentials prevents charge build-up on the slider. Figure 5-7 and Figure 5-8 show the displacement of the slider measured for excitation frequencies (f_e) of 10 and 20 Hz, respectively, at a capture rate of 30-fps. Since the range of motion in this design is limited to 3.6 mm, the direction of motion is changed (forward and backward) at a frequency of f_d =1.5 Hz. This is accomplished by switching the sequence of the phases. The value of f_d is chosen such that the direction of the slider motion is changed before it reaches the end of the microball housing. The saw-tooth profile, observed in figures, is a result of the change in the direction of the motion.

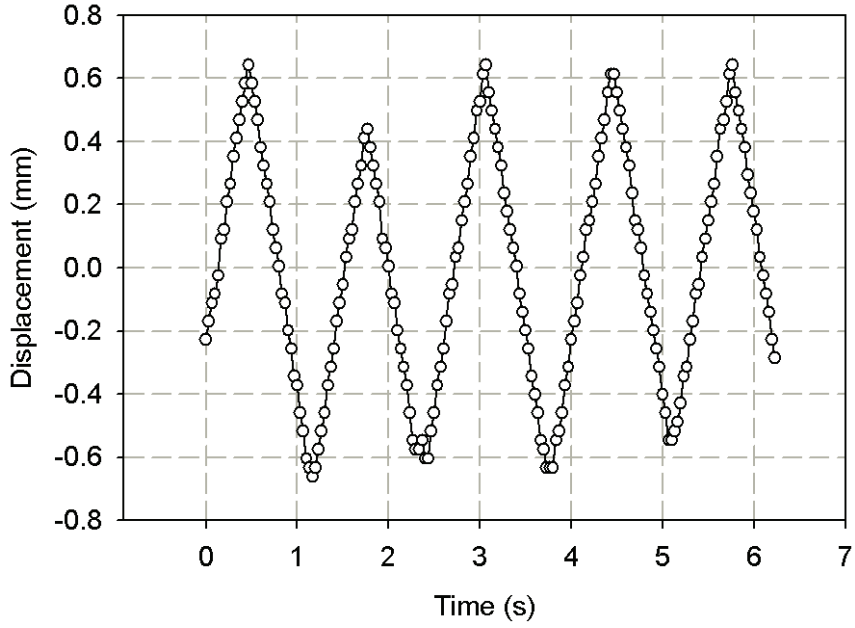

Figure 5-7: Displacement of the slider when excited with 120 V, 10 Hz, 6-phase, square pulses and measured using a 30-fps camera. The direction of the motion alternates with f_d=1.5 Hz.

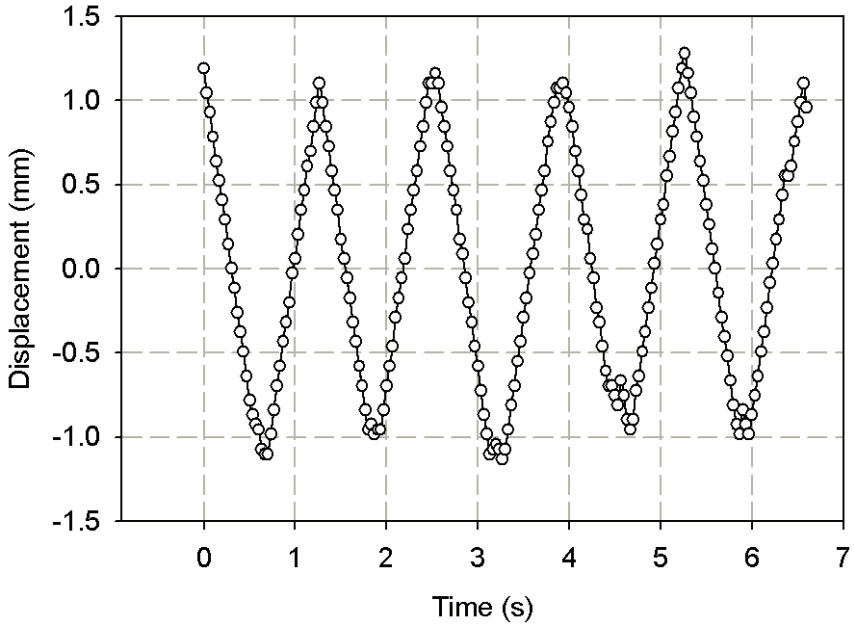

Figure 5-8: Displacement of the slider when excited by 120V, 20 Hz, 6-phase, square pulses and measured using a 30-fps camera (f_d=1.5 Hz).

The theoretical average velocity (V_{avg}) of the slider is given by

$$V_{avg} = 2Wf_e \qquad \textbf{Eq. 5-1}$$

where W is the width of an electrode or pole and f_e is the frequency of excitation voltage [131]. The average velocity can be experimentally determined from the slopes of the ramps in the last two graphs. Similar measurements were performed at 40 Hz and 80 Hz excitation frequencies. The results, summarized in Table 5-2, show a good agreement between predicted (from Eq. 6-1) and measured values of V_{avg} for $f_e \leq 60$ Hz.

The transient response of the micromotor to 120-V square pulses and excitation frequency of f_e =10 Hz was measured at 1000 fps while the camera's capture sequence was triggered with the excitation voltage. Figure 5-9 shows the acceleration of the slider from rest position to a quasi-steady-state in approximately 20 ms (first region). After this period the machine continues with an average velocity of V_{avg} (second region); however, the instantaneous acceleration is not zero and the velocity changes around the average.

Table 5-2: Comparison of predicted and measured average velocity of the micromotor.

Excitation frequency (Hz)	Predicted average velocity (mm/s)	Measured average velocity (mm/s)
10	1.80	1.94±0.02
20	3.60	3.98±0.02
40	7.20	7.37±0.12
80	14.40	7.21-11.10

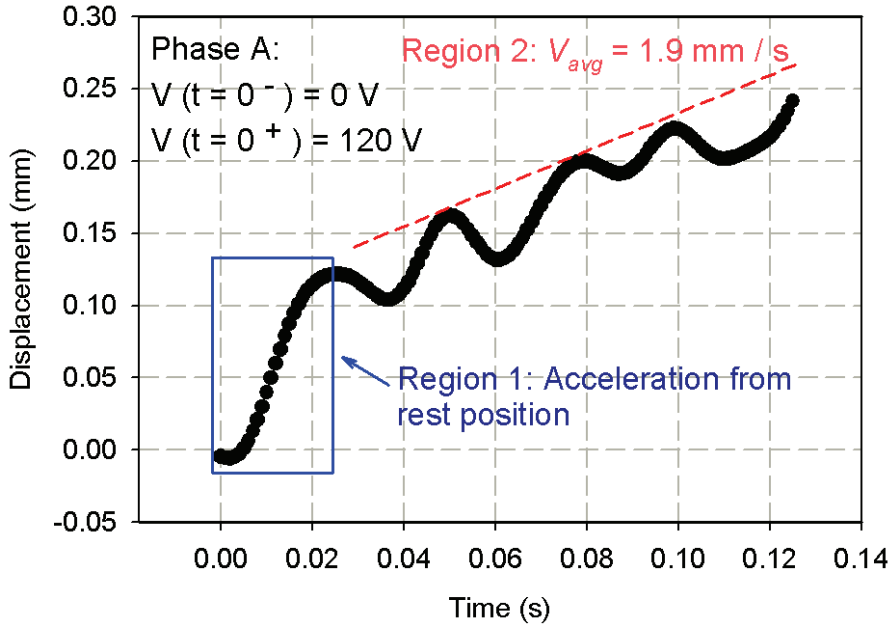

Figure 5-9: Startup of the micromotor from rest position captured with a 1000-fps camera showing two regions of operation: (1) acceleration from rest position and (2) quasi-steady-state operation with an average velocity of V_{avg} and local oscillations.

Figure 5-10 shows the oscillation of the slider position, *X(t)*, in a 130-ms window captured at 635 fps (V=120 V, f_e =10 Hz). This is similar to Figure 5-9, except that the lower capture rate was used to facilitate faster image and data processing. Figure 5-10 shows a time window that was arbitrary chosen from the operation phase of the machine. In order to study the transient response of the machine, the linear component of the displacement signal, $V_{avg} \times t$, was filtered out from the graph in Figure 5-10 and the remaining component, $x(t) = X(t) - (V_{avg} \times t)$, which shows the local oscillation of the displacement, was plotted in Figure 5-11. A damped sinusoidal transient response of the slider motion can be seen in this figure. The instantaneous velocity and acceleration were computed from the first and second derivatives of the fitted curve (red curve in Figure 5-11) and are shown in Figure 5-12 and Figure 5-13

respectively. The average velocity of 1.9 mm/s observed in Figure 5-12 is similar to the low-speed measurement results from a 30-fps camera. Furthermore, Figure 5-13 demonstrates the instantaneous net force on a 0.1-gram slider (plotted on the right axis). This net force is the difference between electrostatic and frictional forces that are discussed in the next section. Similarly, Figure 5-14 shows the acceleration and the net force measured with the applied voltage of 150 V. As expected, the net force at 150 V is increased by a ratio of $\left(\frac{150}{120}\right)^2 = 1.56$ from the force measured at 120 V. The results show an excellent agreement between the measured and predicted values.

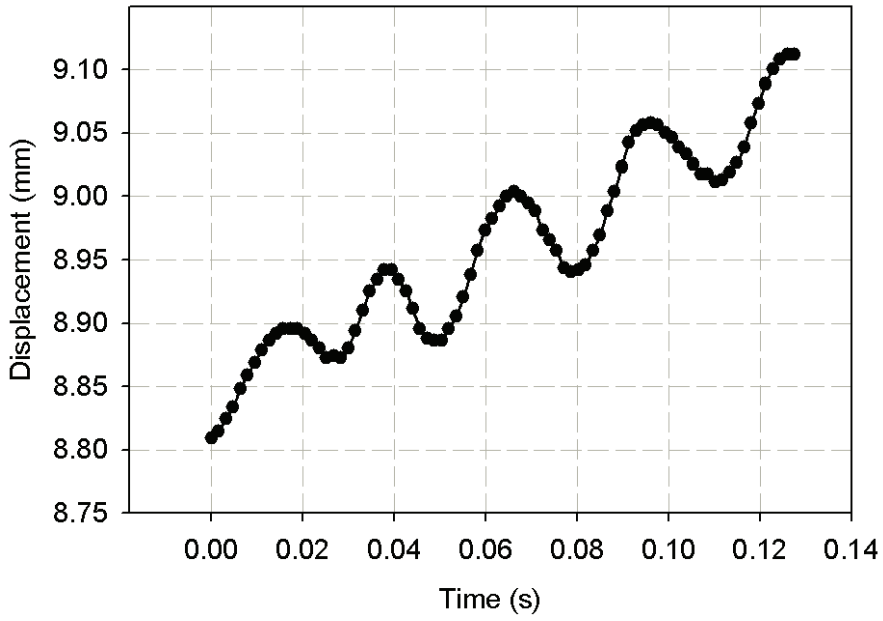

Figure 5-10: Position of the slider, *X(t)*, in a 130-ms time window captured at 635 fps shows an average speed of 1.9 mm/s at 10 Hz excitation, as well as a sinusoidal oscillation.

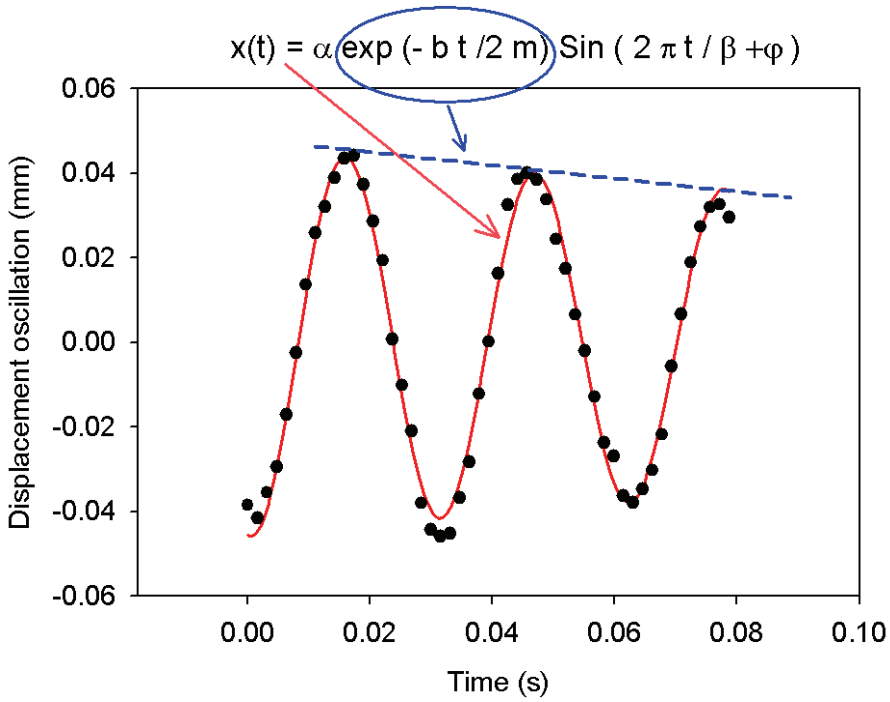

Figure 5-11: Local slider displacement, $x(t)=X(t) - (V_{avg} \times t)$, measured at 635 fps shows damped sinusoidal transient response. The standard coefficient of determination (R^2) was calculated to be 0.9876 (V=120 V).

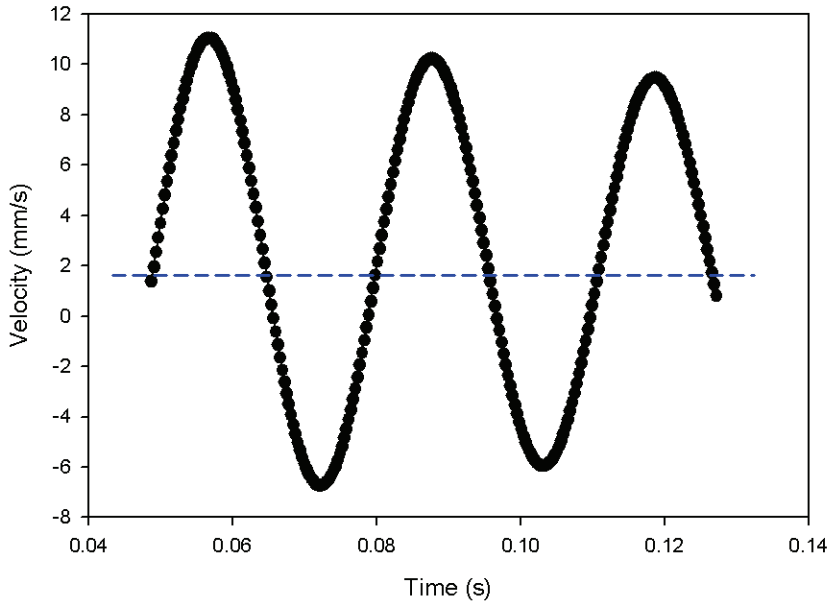

Figure 5-12: Instantaneous velocity of the slider at V=120 V with damped sinusoidal form was computed from the curve fit to the position data. The average velocity is 1.9 mm/s.

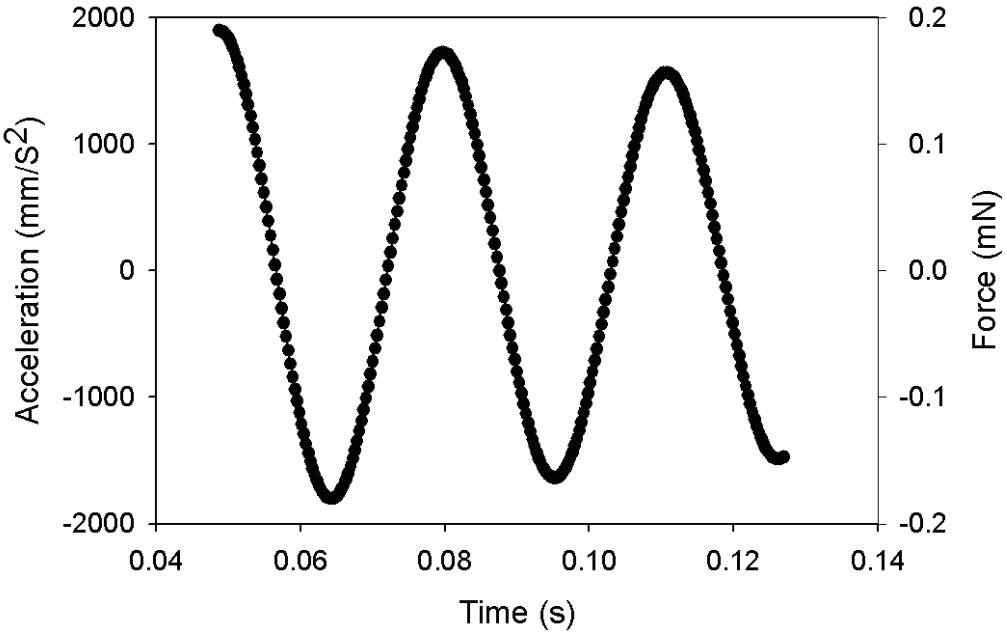

Figure 5-13: Measured instantaneous acceleration (left axis) and the net force (right axis) of the 0.1 gram slider with excitation voltage of V=120 V were computed from the velocity data shown in the previous graph.

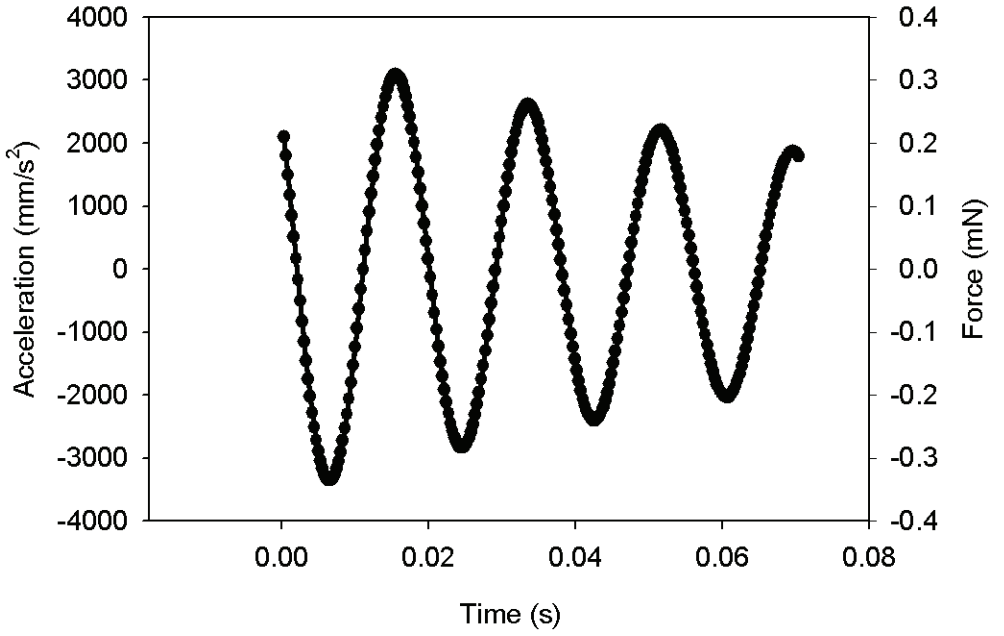

Figure 5-14: Measured instantaneous acceleration (left axis) and the net force (right axis) of the slider with excitation voltage of *V*=150 V shows a 1.57 fold increase in the net force compared to *V*=120 V excitation.

5.1.5 Modeling

The force measurement results, discussed earlier, can be compared to the force of a lossless system obtained from finite element simulations. The aligning force of the slider can be written as

$$F_{Ph} = \frac{1}{2} V_{Ph}^{2} \frac{\partial C_{Ph}}{\partial x} \qquad \textbf{Eq. 5-2}$$

where F_{Ph} is the aligning force generated by each phase, V_{Ph} is the amplitude of the applied voltage, C_{Ph} is the capacitance of each phase, and x is the position of the slider [131]. Therefore, the aligning force at a given voltage can be derived from the capacitance variations. This data was obtained from finite element simulation using Comsol Multiphysics (FEMLAB). Figure 5-15 shows the simulation results of the machine capacitance with the electrode width and the air gap of 90 and 10 μm, respectively[32]. The capacitance of the first three phases, shown in Figure 5-15, can be differentiated to obtain the total aligning force of the 6-phase micromotor. The differentiation is performed after curve fitting to a sine-squared function. The remaining three phases (not shown in Figure 5-15) have identical capacitance profiles.

Figure 5-16 shows the numerical differentiation of the capacitance of the first three phases versus slider displacement. Figure 5-17 illustrates the extracted aligning force versus position *(x)* and its average value with a 120 V excitation calculated from Figure 5-16 and Eq. 6-2. This aligning force, which represents the total electrostatic force (without considering any electrical or mechanical losses), is comparable to (but slightly larger than) the net force obtained in our experiment.

[32] Simulation data is provided by Mr. Alireza Modafe, University of Maryland, 2006.

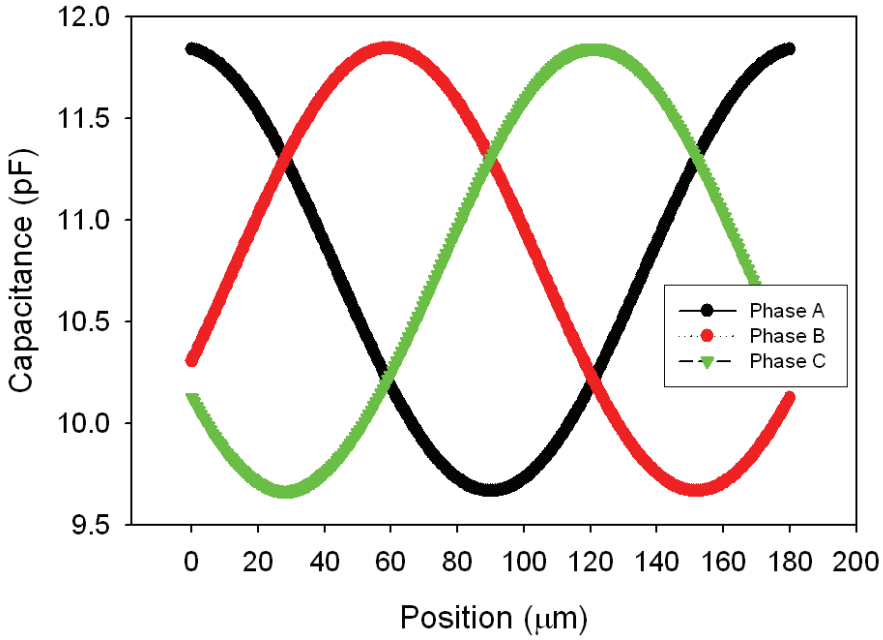

Figure 5-15: Finite element simulation results of the B-LVCM capacitance versus position for the first three phases.

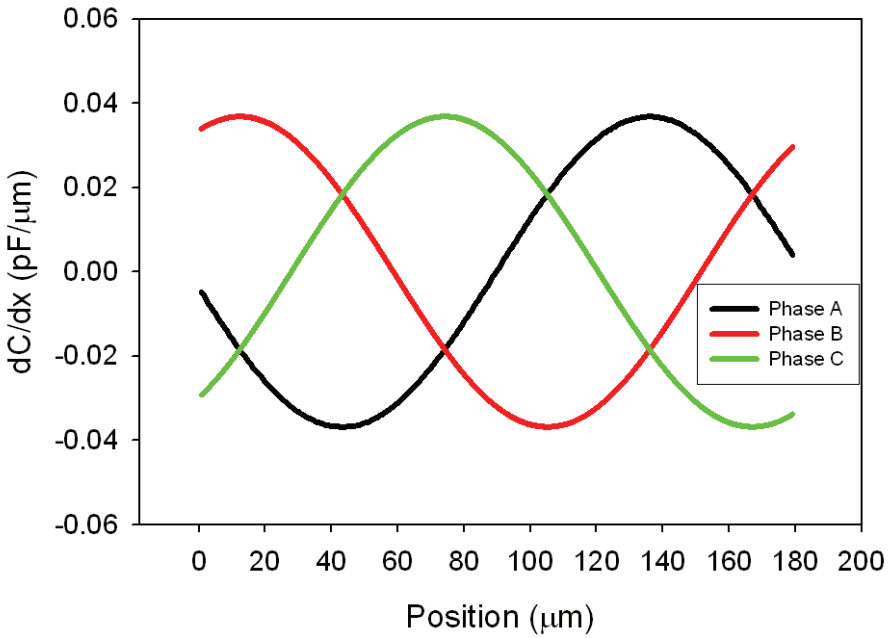

Figure 5-16: Numerical differentiation results of capacitance versus slider displacement.

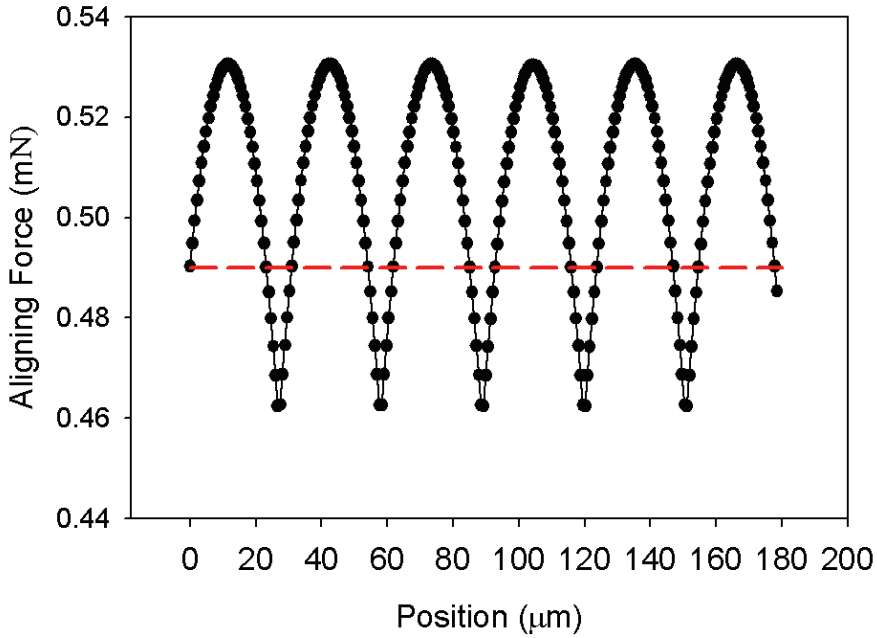

Figure 5-17: Total aligning force of the 6-phase micromotor at *V*=120 V extracted from the simulation data

The measurement results shown in Figure 5-11 are used to model the dynamics of the system and extract the model parameters of the micromotor. The B-LVCM was modeled with a simple mass-dashpot-spring system as shown in Figure 5-18. A mass-dashpot-spring system was used because of its simplicity and relevance to the measured data. Such a system is described by the 2nd order differential equation:

$$m\frac{d^2x}{dt^2} + b\frac{dx}{dt} + k_s x = 0 \qquad \textbf{Eq. 5-3}$$

where m is the mass of the slider, b is a dashpot coefficient representing the friction of microballs and silicon housing, and k_s represents the (electrostatic) spring constant of the electrode-pole variable capacitors. More complicated systems that include nonlinear spring(s) or higher order term(s) will likely represent the behavior of the system more accurately; however, finding the solution to the differential equation will likely be difficult or impossible.

The above equation describes the dynamic response of the B-LVCM in absence of any external force. The underdamped solution for such a system is

$$x(t) = A\exp\left(\frac{-b}{2m}t\right)Sin\left(\omega_d t + \phi\right) \qquad \textbf{Eq. 5-4}$$

where A and ϕ are constant values and

$$\omega_d = \sqrt{\frac{k_s}{m} - \frac{b^2}{4m^2}} \qquad \textbf{Eq. 5-5}$$

The values for b and k_s can be extracted from the measurement of the displacement decay $\left(\exp\left(\frac{-b}{2m}\right)t\right)$ and displacement period $\left(T_d = \frac{2\pi}{\omega_d}\right)$ shown in Figure 5-11. The dashpot coefficient values *(b)* were found to be 6.25×10^{-4} and 2.0×10^{-3} kg/s at *V=120* and *150 V*, respectively. Furthermore, the (electrostatic) spring constant values *(k_s)*, extracted from the period of displacement data, were found to be 4.3 and 30.4 N/m at *V=120* and *150 V*, respectively.

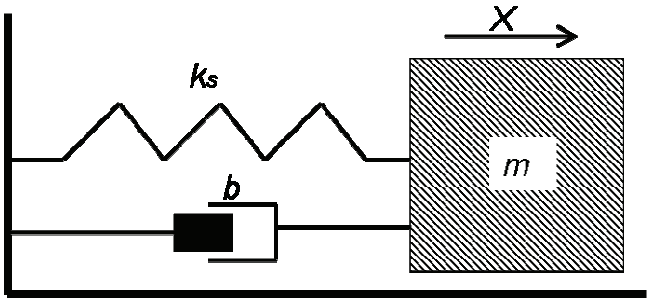

Figure 5-18: Simplified model of the micromotor represented by a mass-dashpot-spring system.

In another approach, the frictional force *($F_{Friction}$)* of the micromotor can be modeled as

$$F_{Friction} = Bv \qquad \textbf{Eq. 5-6}$$

where B and v are the dashpot coefficient and velocity of the slider, respectively. In this model, B is also a function of time or velocity. The frictional force can be written in terms of a theoretical aligning force and net measured force.

$$F_{Friction} = F_{Align} - F_{Measured} \quad \textbf{Eq. 5-7}$$

Therefore, the dashpot coefficient, B, can be found using

$$B = \frac{F_{Align} - F_{Measured}}{v} \quad \textbf{Eq. 5-8}$$

The value of F_{Align} and $F_{Measured}$ are extracted from Figure 5-13 and Figure 5-17, respectively. It is observed from the above equation that the limit of $B(t)$ as $v(t)$ goes towards 0 approaches infinity. $B(t)$ as $v(t)$ are shown in Figure 5-19(a); $B(t)$ and $a(t)$ are shown in Figure 5-19(b). It is observed that for a short range of time the average value of B is ±0.1 kg/s. Consequently, as shown in Figure 5-19(b), whenever the maximum or minimum of acceleration is achieved the value of $B(t)$ approaches infinity. In order to study the effect of velocity on friction, B is plotted as a function of v in Figure 5-20. The coefficient of friction shows a hysteresis behavior with respect to velocity. It is believed that this behavior is originated from the damped sinusoidal nature of the velocity function and force. The extracted coefficient (B) is one order of magnitude larger than the value extracted for a mass-spring-dashpot system (b) due to neglecting the spring effect in this analysis. The precision of the results directly depends on the exactness of the simple model used for the analysis (Eq. 6-6).

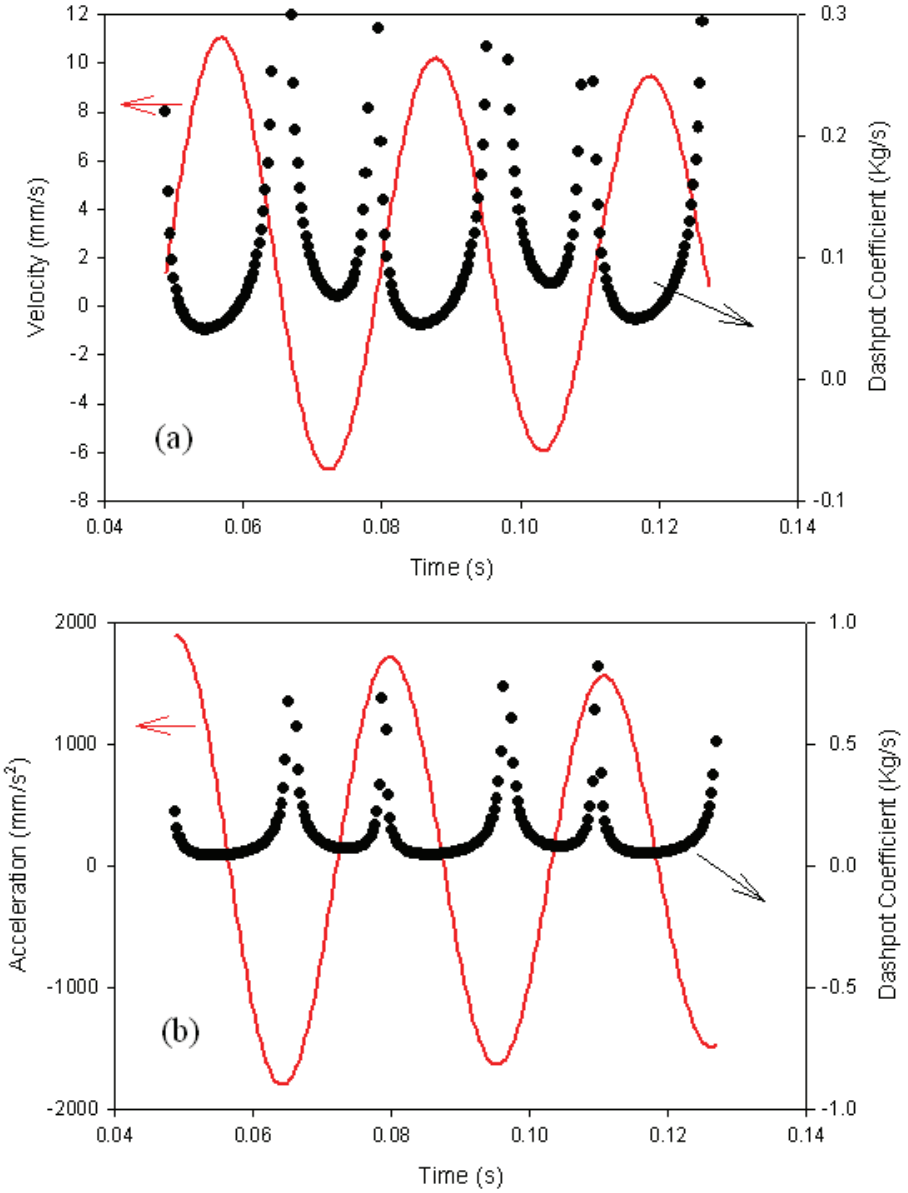

Figure 5-19: Time dependent dashpot coefficient together with slider (a) velocity and (b) acceleration.

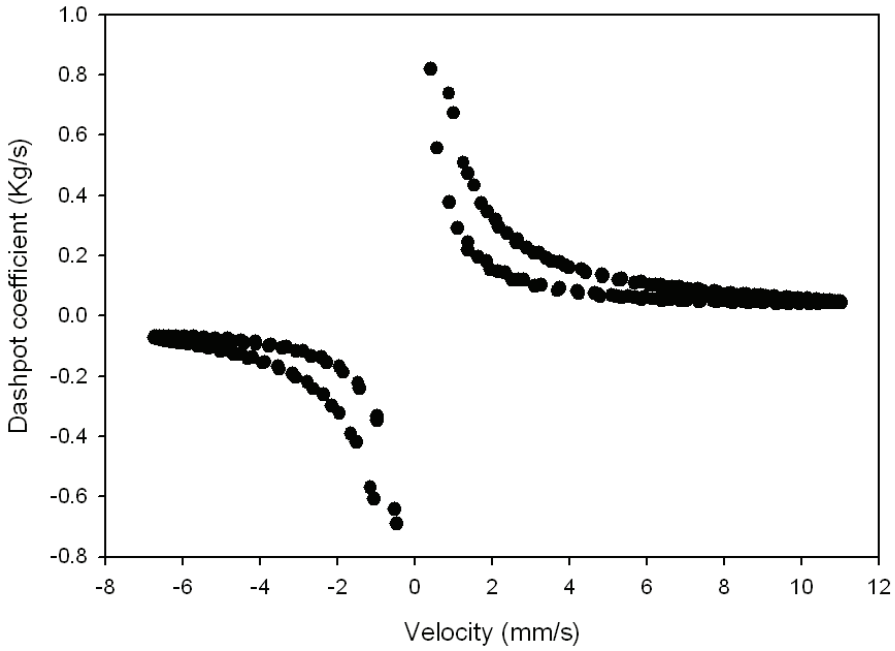

Figure 5-20: Dashpot coefficient, representing the coefficient of friction, as a function of velocity.

The presented analysis can be used to derive the coefficient of friction (μ). The coefficient of friction can be calculated using

$$\mu = \frac{b\,v}{F_N} \qquad \textbf{Eq. 5-9}$$

Assuming 20 mN of normal force on the slider, time varying $\mu(t)$ and its average are plotted in Figure 5-21. The average μ is calculated to be 0.024 which is in good agreement with the extracted value from tribology experiments for the linear bearings as well as the rotary micromotor.

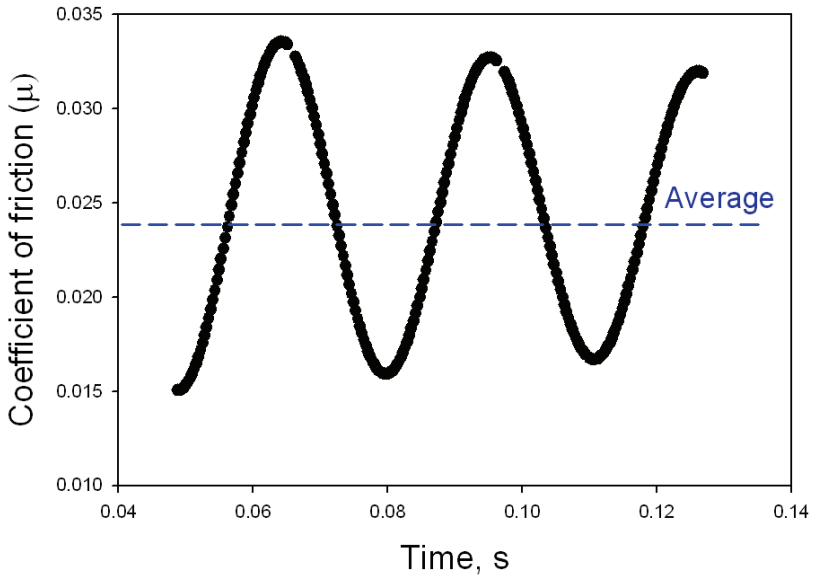

Figure 5-21: Time dependent coefficient of friction (μ) is plotted based on the 10 mN normal force. The μ has an average of 0.021.

5.1.6 Discussion

The results from the position measurement using a 30-fps camera, summarized in Table 5-2, show a good agreement between predicted and measured values of the average velocity for the excitation frequency of $f_e \leq 60$ Hz. However, the motor does not pull into synchronization at 80 Hz or higher. This phenomenon is partially due to the limited range of the motion (3.6 mm) and the change in the direction. The lack of synchronization at higher excitation frequencies is also due solely to the open-loop excitation of the micromotor and is expected to be improved with a closed-loop excitation configuration which is out of the scope of this dissertation.

The period of the oscillations in the transient response measurements (Figure 5-9 through 13) was found to be independent of the frequency of excitation voltage. It is believed that this period is determined mainly by the system characteristics such as

slider mass, friction, and electrostatic spring constant of a variable-capacitance structure. The mass-dashpot-spring system presented earlier explains this behavior.

The mass of the slider was calculated from the volume of the slider and density of silicon to be 0.1 gram. The measured net force, shown in Figure 5-13 and Figure 5-14, is the result of the electrostatic force produced by the micromachine and the frictional force between microball bearings and the silicon housing. This force was verified to be proportional to the square of voltage. It can be seen that the measured net force (Figure 5-13) is less than the average aligning force obtained from simulation (Figure 5-17). The friction force is calculated from the difference between measured and simulated forces. The friction force is a function of the normal force on the slider and, therefore, changes with slider position. Assuming a constant normal force of 20 mN the coefficient of friction is calculated to be on average 0.02.

The presented mass-spring-dashpot model is a valuable tool to understand the dynamics of the micromotor including electrostatic and frictional behavior. The increase in the dashpot coefficient *(b)* with increase in the excitation voltage is due to the increase in the normal force. As mentioned earlier, *b* is a coefficient which represents the frictional force on the slider. This force is proportional to the normal force on the slider and is increased with the increase in the applied voltage. Another extracted parameter is the electrostatic spring constant *(k_s)*. For simplicity, k_s was chosen to be independent of the slider position *(x)*. Furthermore, the spring constant value, which increases with the increase in the applied voltage, is also a function of device capacitance and slider position. The mass-dashpot-spring model was proven to be a simple and suitable tool for extracting device parameters. Non-linear effects,

such as position dependency of the electrostatic spring, velocity dependency of the friction force, and the microscale tribological effects (adhesion and hysteresis) were considered to be negligible. The modeling results show that the micromotor is well represented with a second-order linear system.

5.1.7 Summary

The fabrication and dynamic characterization of a 6-phase, bottom-drive, linear, variable-capacitance micromotor (B-LVCM) supported on microball bearings was reported in this section. The second-generation device is a 6-phase machine; whereas, the first-generation device was tested in a 3-phase configuration. The improvements in the fabrication process were the main reasons for this achievement. The second-generation device showed more reliable and smoother motion. Top velocity of 7.2 mm/s was measured compared to 3.5 mm/s for the first generation device.

The slider position of the B-LVCM was measured using low- and high-speed video cameras; the instantaneous and average velocity, acceleration, and net force were extracted from the position measurement. Considering the effect of frictional force in the operation of the micromotor, the measured force (0.2 mN peak) is in good agreement with the simulated force (0.53 mN peak). The transient response of the micromotor to square-pulse excitation was analyzed.

The B-LVCM was modeled with a mass-spring-dashpot system; the dashpot coefficient and electrostatic spring constant were extracted from measurement results at two different actuation voltages. The evaluation of these two values (b and k_s), for different micromotors with distinct electrical or mechanical designs, enables us to determine the optimum design for a given application. The characterization

methodology presented in this chapter is applicable to a wide range of micromachines and provides useful information for design, control, and understanding the dynamic behavior of micromachines.

5.2 Rotary Micromotor Characterization

The fabrication of the micromotor was reported in Chapter 4. The output variables determining the performance of the micromotor were discussed in chapters 2 and 3. In this chapter the angular displacement, velocity, acceleration, torque, power, and frictional losses of the fabricated devices are measured through non-contact techniques. The test setup developed for the characterization of the micromotors is discussed first. The non-contact steady-state and transient response measurement methodology is discussed second. The results obtained after testing different designs together with comparison between measured and theoretical values are reported at the end of this chapter.

5.2.1 Test Setup

The characterization of the micromotor requires development of a test setup that is capable of 6-phase voltage excitation and angular displacement measurement. The block diagram of the setup is shown in Figure 5-22. The micromotor is excited with a 6-channel high-voltage pulse generator (shown in yellow). A LabVIEW interface and a personal computer are used to program a data acquisition card (DAQ). The DAQ card (model PCI-6722 from National Instruments) provides 6 analog output channels

required for the motor excitation. Using the LabVIEW interface[33], the waveform shape (e.g. square, sine, and triangular), amplitude, frequency, duty cycle, phase difference, and rotation direction are programmed. Figure 5-23 shows the the LabVIEW interface console. The output of the high-voltage amplifier is connected to the contact pads on the stator using 6 probes (Cascade Microtech). Each probe has a tungsten needle with an angle of 45 ° and a tip radius of 25 μm.

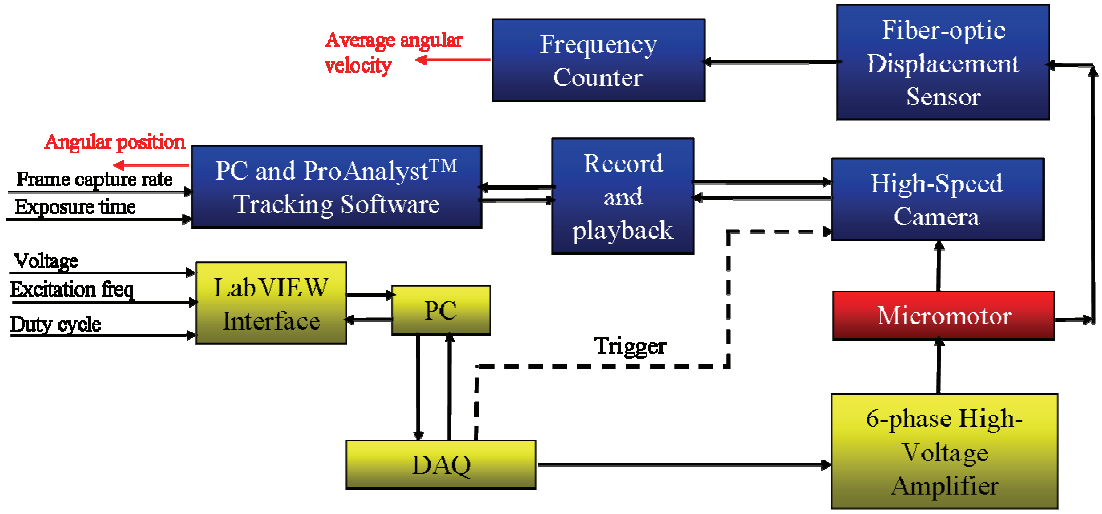

Figure 5-22: Block diagram of the micromotor characterization setup.

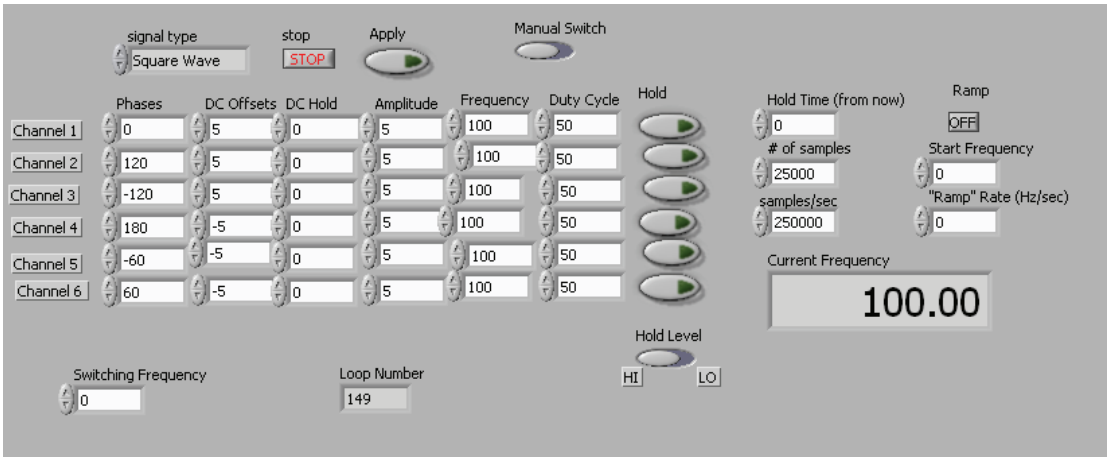

Figure 5-23: Snapshot of the micromotor excitation console.

[33] The LabVIEW interface was developed by Mr. Alex Frey at the MEMS Sensors and Actuators Lab, University of Maryland (2005-2006) under the guidance of Nima Ghalichechian.

The other unit in the test setup, shown in blue in Figure 5-22, is the angular displacement measurement section. Two methods were implemented for the measuring the displacement of the rotor. The first method is using optical displacement sensors (Model D6 from Philtech) to detect the silicon pits etched in the rotor. The displacement sensor has a light source that illuminates the silicon surface. The intensity of the reflected light is then measured and converted to an analog voltage signal. A total of 20 square pulses are generated when 20 silicon pits pass under the sensor in one revolution. The output signal from the sensor is monitored on an oscilloscope. Using this technique, the position is measured with the angular resolution of $2\pi/20$ rad. The sensor used in this experiment has a spot size of 155 μm and an optimal working distance (from rotor) of about 0.25 mm. Therefore, the sensor is mounted on an XZ micropositioner (Model UltraAlign 561D from Newport Corporation).

The second method used in the displacement measurement utilizes a high-speed, high-resolution CCD camera (Model HS-3 from Redlake) together with a microscopic lens tube (Model KV from Infinity Photo-Optical Company with CFV-3 objectives) and an infrared-filtered light source (Model Intralux 5100 from Volpi USA)[34]. Table 5-3 summarizes a list of key features for the high-speed camera system. The images are taken at the frame rate of 1000 frames per second, saved in the camera's built-in memory during capture, and later downloaded on a computer with USB-2 connection. The memory size dictates the maximum image capture time.

[34] Infrared wavelengths are filtered to prevent the test setup from heating up when lighted with a 150 W halogen bulb. High light intensity is required especially at very short exposure times.

If required, the capture sequence is triggered with external pulses supplied from the data acquisition card. With this method, it is possible to characterize the acceleration from or deceleration to the rest position.

Table 5-3: Summary of high-speed measurement system.

Camera model	Speed at full resolution	Full resolution	Exposure time	Built-in memory	Synchronization	Trigger
MotionPro HS-3	1000 frames per second	1280×1024 pixels	970 ms	4 GB	Internal	External pulse(3.3V)

After downloading the images from the camera to the computer, an image tracking software (ProAnalys from Xcitex Inc.) is used for processing. The images are first calibrated to convert units from pixels to micrometers. Several features are defined for 2D tracking. The marks are automatically tracked and the results are exported to an Excel file. The data is converted from Cartesian coordinates to the polar coordinates and the angular position versus time is computed and plotted. Figure 5-25 shows an image of the center part of the micromotor that is used for tracking. The center part is chosen to include the center of the stator/rotor in the field of view. A 10 μm radius circle is included in the design of the interconnection layer to mark the machine's center. This mark improves the precision of Cartesian to polar conversion. Figure 5-26 shows an example of 2D tracking of a point (etching residue) on the backside of the rotor. The field of view in these measurements is 5.8 mm × 4.7 mm and each pixel equals 4.6 μm. Therefore, the theoretical resolution of the system in the XY plane is 4.6 μm. Nonetheless, in practice the resolution is also limited by the size of the tracking mark, quality of the captured image (e.g. brightness, contrast,

gamma, file compression), and errors in the image processing which depends on pixel threshold tolerance, sub pixel accuracy, trajectory prediction algorithms, and image processing filters. As a result the actual resolution (numerical value) of the system is expected to be much larger than 4.6 μm.

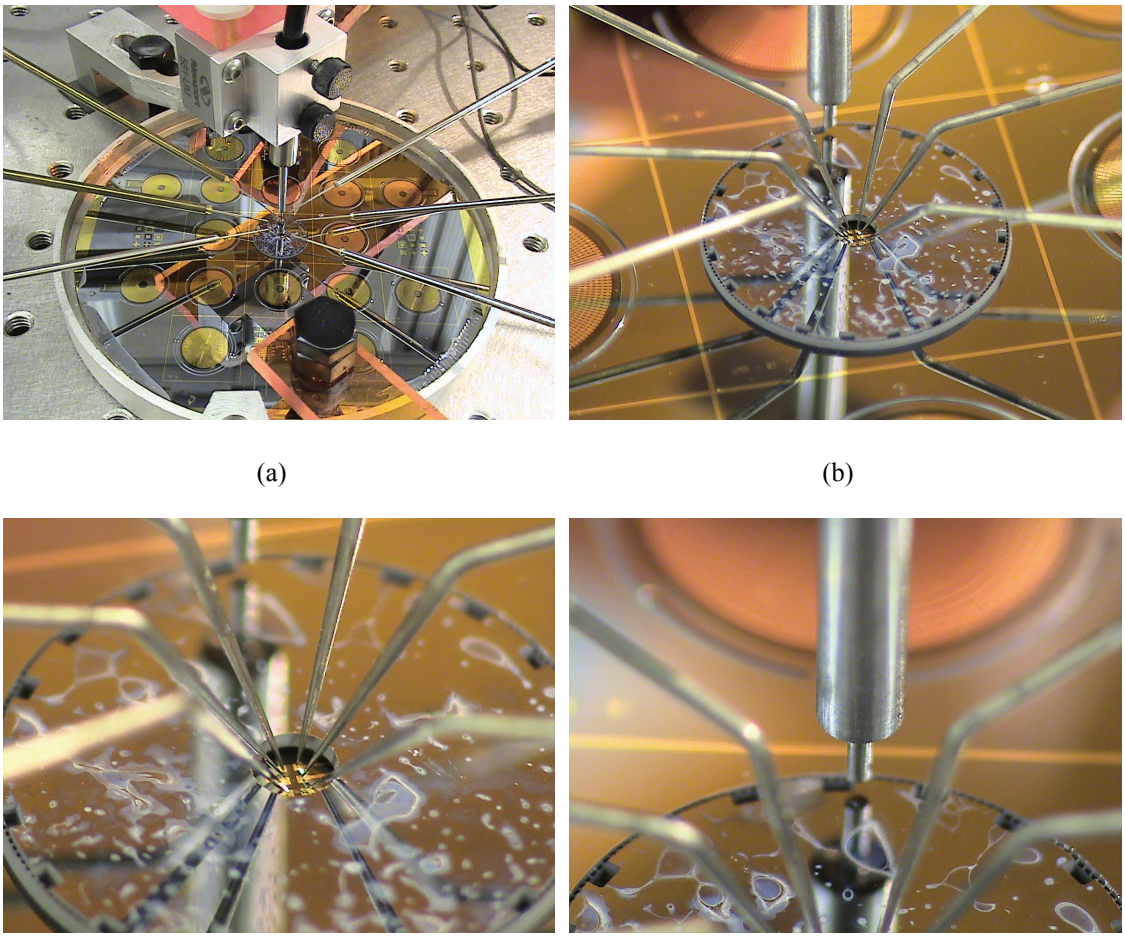

(a) (b)

(c) (d)

Figure 5-24: Photographs of the micromotor and the test setup illustrating (a) 4 inch stator substrate clamped on an aluminum chuck, (b) a single device under test, (c) six probes passing by the rotor cavity and making electrical connection with the pads on the stator, and (d) optical displacement sensor positioned above and at the edge of the rotor.

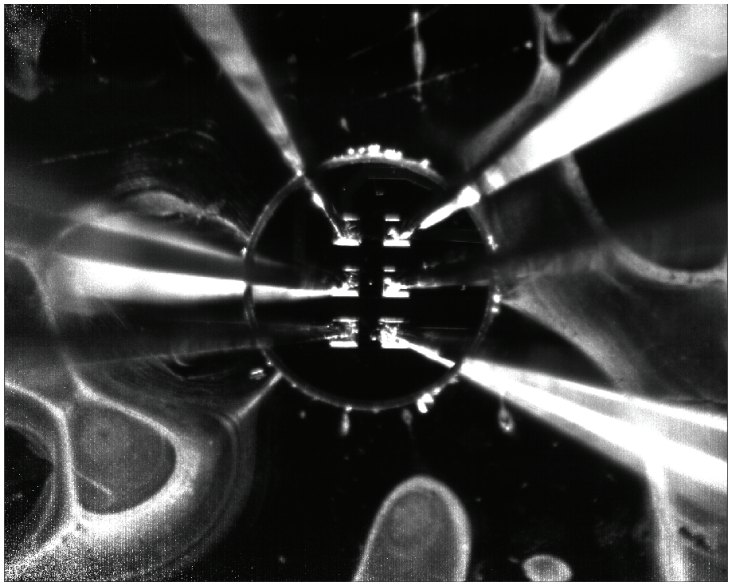

Figure 5-25: Image of a single frame captured during the operation of the micromotor. The field of view is 5.8 mm ×4.7 mm.

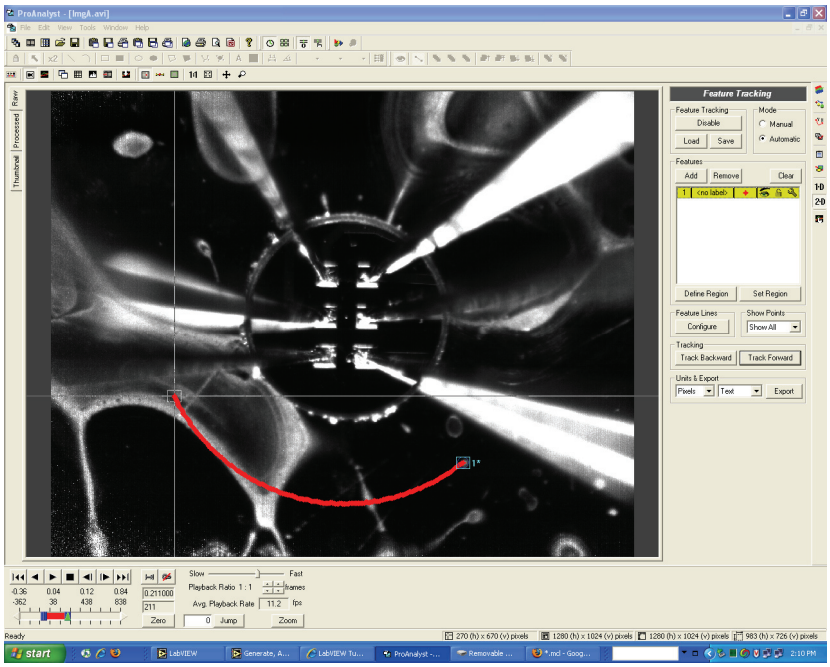

Figure 5-26: Example of 2D image tracking.

5.2.2 Steady-State Response

As mentioned in Chapter 2, one of the characteristics of any synchronous motor is the synchronization of the mechanical motion of the rotor with the electrical excitation of the stator. A series of experiments are performed to test the angular

velocity of the rotor versus the excitation frequency for D1 and D2. The velocity of the rotor is measured using the optical displacement sensor as described previously. Figure 5-27 and Figure 5-28 show the experimental results together with the theoretical values for D1 and D2, respectively. Top velocity of 517 rpm, corresponding to the linear tip velocity of 324 mm/s is measured for D2. The achieved velocity is about 44 times higher than the maximum velocity measured for the second generation linear device. As shown in these figures, there is an excellent agreement between measured and predicted angular velocities. More discussion is provided in Section 5.2.4.

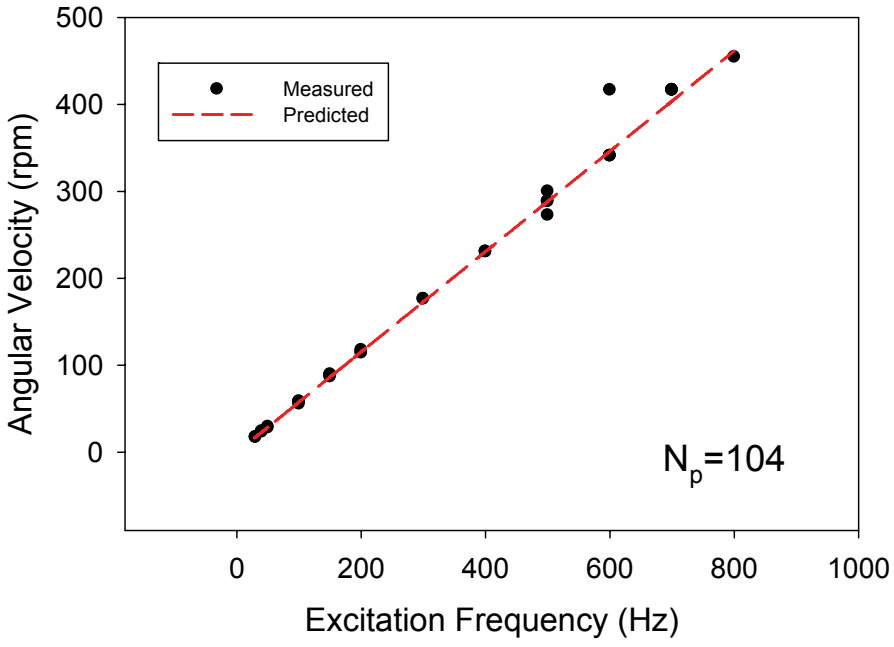

Figure 5-27: Angular velocity of the rotor versus the excitation frequency for D1 with 104 poles and 156 electrodes shows a good agreement between measured and predicted velocities.

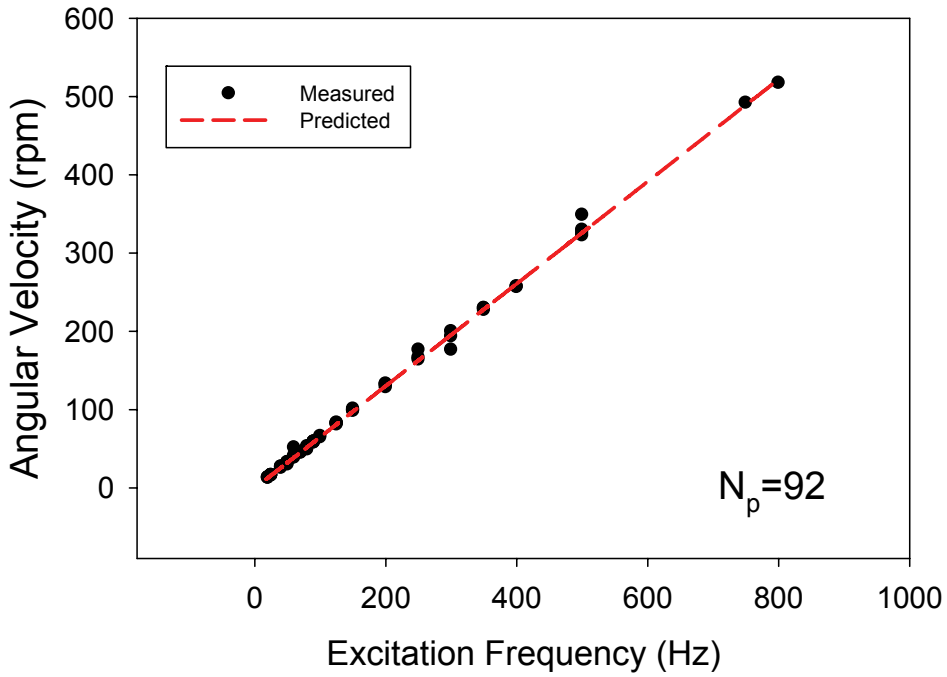

Figure 5-28: Angular velocity of the rotor versus the excitation frequency for D2 with 92 poles and 138 electrodes shows a good agreement between measured and predicted velocities.

It is also possible to measure the displacement of the rotor as a function of time and examine if the velocity of the rotor is constant over small time periods. This measurement is performed when the micromotor is excited at a constant frequency. The high-speed camera system described earlier is used for this study (no triggering is necessary). Figure 5-29 through Figure 5-32 show the angular displacement of the rotor as a function of time at the excitation frequency of 30, 50, 70, and 100 Hz, respectively. The slope of the graph determines the average angular velocity of the rotor and can be determined by fitting a line to the graph. The calculated velocities with this method match with the previous results; however, interesting behavior is observed. The measurement results show ripples in the motion of the machine especially at lower excitation frequencies (*fe* < 70 Hz). This behavior is believed to be due to two reasons. First, the microball housing is 5 μm wider than the ball

diameter; therefore, the rotor has a lateral movement of about 5 μm. The lateral movement has also been observed on the raw images. As shown in the last four figures, this motion is more pronounced at lower frequencies because the absolute displacement is less.

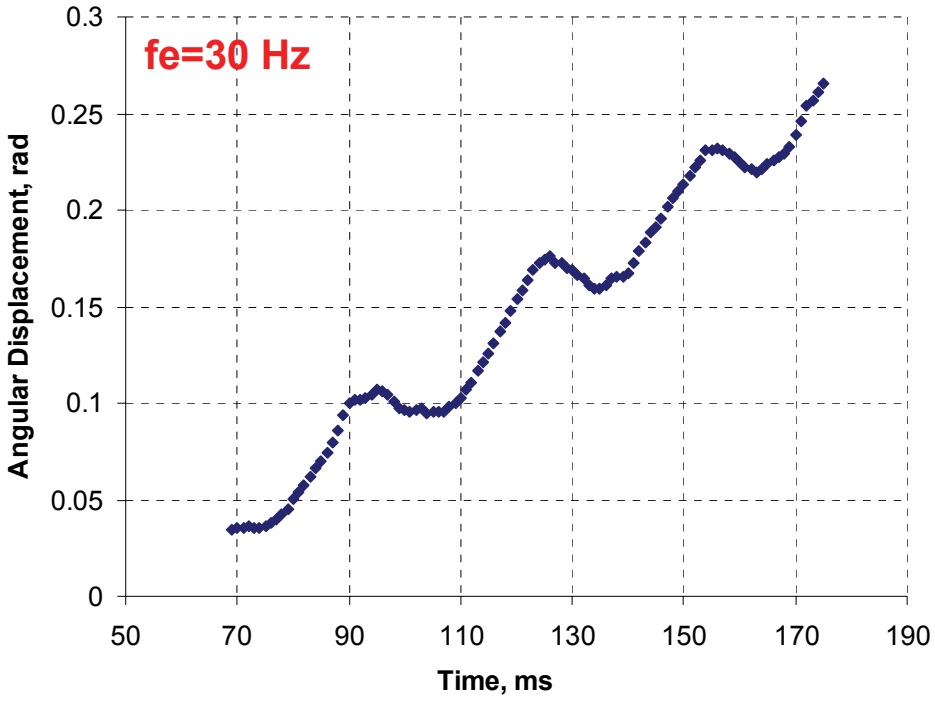

Figure 5-29: Angular displacement of the rotor as a function of time at the excitation frequency of 30 Hz measured with the high-speed camera system showing ripple in the motion caused by the low excitation frequency.

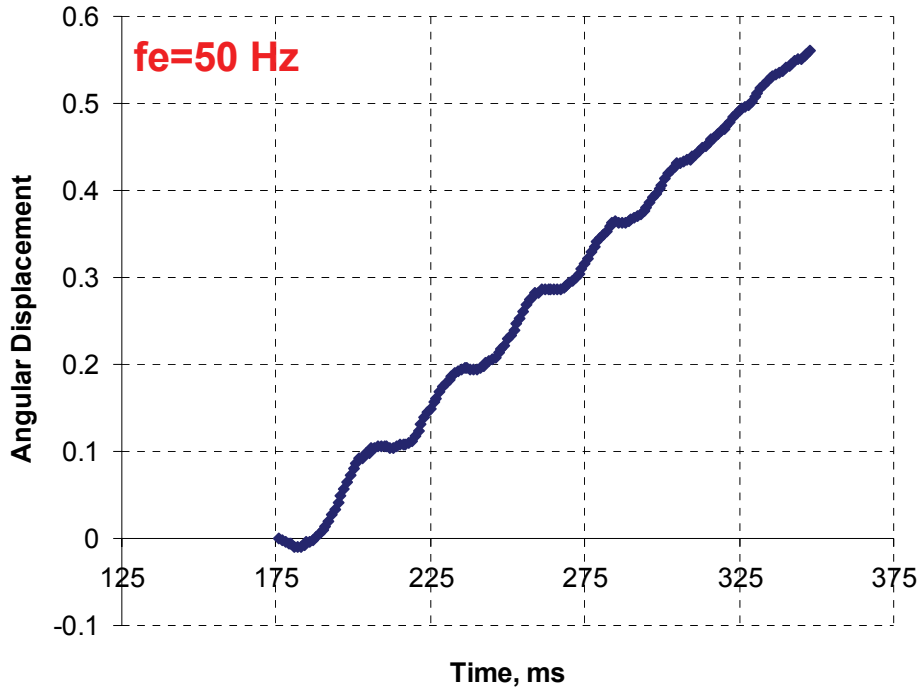

Figure 5-30: Angular displacement of the rotor as a function of time at the excitation frequency of 50 Hz measured using the high-speed camera system.

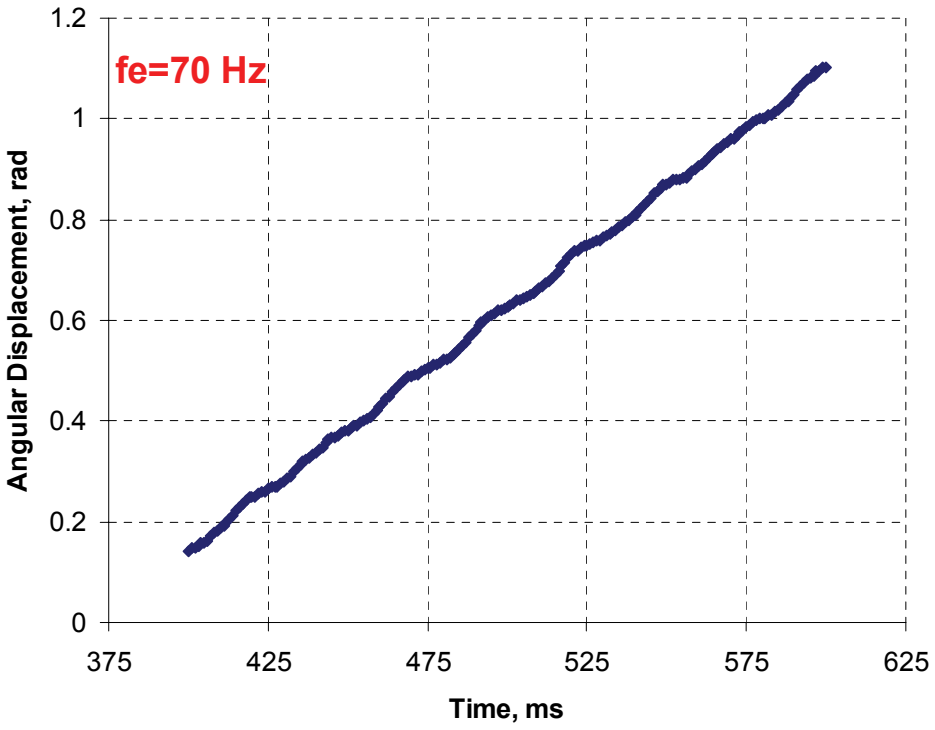

Figure 5-31: Angular displacement of the rotor as a function of time at the excitation frequency of 70 Hz measured using the high-speed camera system.

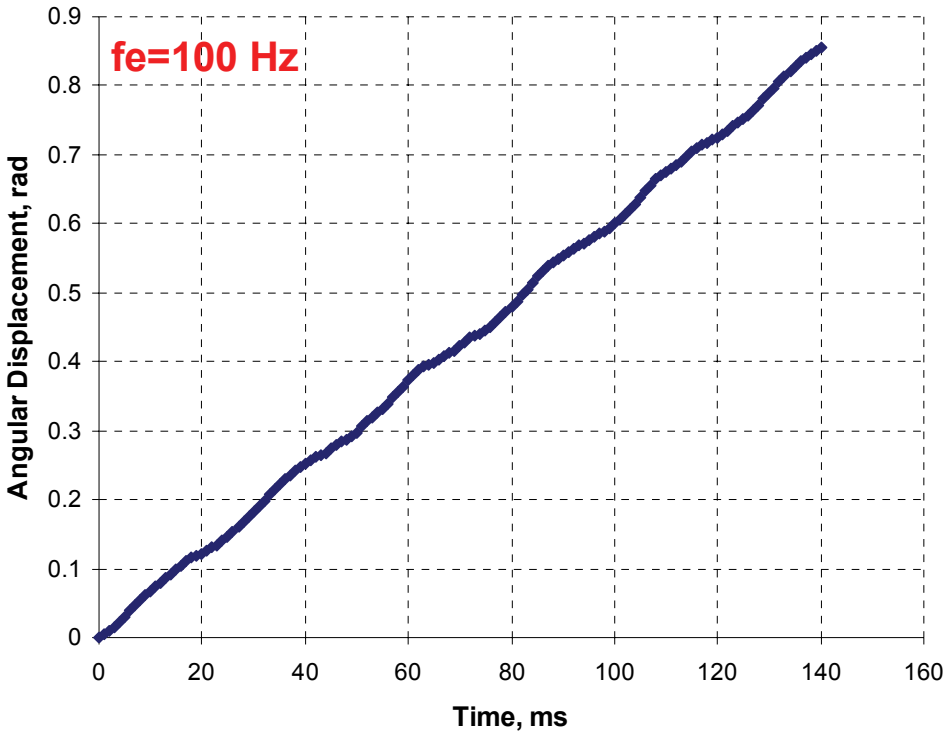

Figure 5-32: Angular displacement of the rotor as a function of time at the excitation frequency of 100 Hz measured using the high-speed camera system.

5.2.3 Transient Response

5.2.3.1 Characterization Methodology

For a point mass one can write the moment of inertia along the rotation center to be

$$I = M\, r^2 \qquad \textbf{Eq. 5-10}$$

where I is the moment of inertia, M is the mass, and r is the rotation arm or the perpendicular distance from the axis of rotation. Similarly, for a rigid mass consisting of many points the moment of inertia is

$$I = \int_0^M r^2 dm \qquad \textbf{Eq. 5-11}$$

The mass is replaced by the volume and the density. Therefore,

$$I = \int r^2 \rho \, dV \qquad \textbf{Eq. 5-12}$$

where ρ and V are the density and volume of the mass system, respectively. A 3D schematic of the rotor structure being a hollow cylinder with inner and outer radius of R_1 and R_2 and height of h is shown in Figure 5-33. For this geometry, the moment of inertia is calculated using cylindrical coordinates to be

$$I = \iiint_V r^2 \rho \, d\theta \, r dr \, dz$$

$$I = 2\pi\rho \int_{-\frac{h}{2}}^{\frac{h}{2}} \int_{R_1}^{R_2} r^2 r dr dz \qquad \textbf{Eq. 5-13}$$

$$I = 2\pi\rho \int_{-\frac{h}{2}}^{\frac{h}{2}} \frac{\left(R_2^4 - R_1^4\right)}{4} dz$$

$$I = \frac{1}{2} M \left(R_1^2 + R_2^2\right)$$

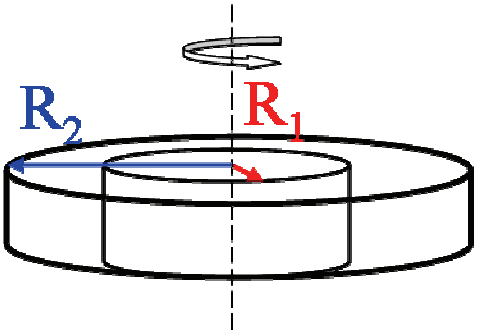

Figure 5-33: 3D schematic of the rotor with inner and outer radius of R_1 and R_1 rotating along the z axis.

The electromechanical torque produced by the micromotor works against the frictional losses to maintain a constant rotor velocity. At the equilibrium, one can write

$$T_{EM} + T_{Load} + T_{Loss} = 0 \qquad \textbf{Eq. 5-14}$$

where T_{EM} is the electromechanical torque of the machine, T_{Loss} is the loss torque composed of frictional, viscous drag and other losses, and T_{Load} is the load torque which is the result of moment of inertia of the rotor and angular acceleration. T_{Load} at any time can be written as

$$T_{Load} = \alpha\, I \qquad \textbf{Eq. 5-15}$$

where α and I are the angular acceleration and moment of inertia of the rotor, respectively. One of the characteristics of a variable-capacitance machine is that the velocity of the rotor is proportional to the excitation frequency and stays constant for a fixed frequency. At the constant velocity regime

$$\alpha = \frac{d\omega}{dt} = 0 \qquad \textbf{Eq. 5-16}$$

Therefore the T_{Load} term is zero and we can write

$$T_{EM} + T_{Loss} = 0 \qquad \textbf{Eq. 5-17}$$

By measuring T_{Loss} the electromechanical torque of the machine can be calculated to be

$$T_{EM} = -T_{Loss} \qquad \textbf{Eq. 5-18}$$

T_{Loss} can be extracted from transient analysis measurement. In this method, the motor is spun at a constant velocity, then at $t=0$ the applied voltage to all 6 phases is set to $V=0$ V. Therefore,

$$T_{EM}\big|_{V=0} = 0 \qquad \textbf{Eq. 5-19}$$

The main torque equation can now be written as

$$T_{Load} + T_{Loss} = 0 \qquad \textbf{Eq. 5-20}$$

$$T_{Loss} = -T_{Load} = -\alpha\, I \qquad \textbf{Eq. 5-21}$$

Therefore, by measuring the rotor deceleration (α) at t>0 the loss torque with no applied voltage can be calculated. Assuming that the frictional losses are the dominant loss mechanism for a micromotor rotating at relatively low speeds, the frictional torque is

$$T_{Friction} = T_{Loss} = -\alpha\, I \qquad \textbf{Eq. 5-22}$$

The frictional force can be modeled at the product of the normal force and the coefficient of friction. Therefore,

$$T_{Friction} = \mu \times Mg \times R_0 \qquad \textbf{Eq. 5-23}$$

where μ is the coefficient of friction (COF), Mg is the weight of the rotor, and R_0 is the radius of the bearing. The coefficient of friction can be calculated from

$$\mu = \frac{T_{Friction}}{MgR_0} = \frac{\alpha I}{MgR_0} = \frac{\alpha \frac{1}{2} M\left(R_1^2 + R_2^2\right)}{MgR_0} = \underbrace{\frac{R_1^2 + R_2^2}{2gR_0}}_{Const.} \alpha \qquad \textbf{Eq. 5-24}$$

After the rotor deceleration is measured, the COF is extracted from above equation.

The electromechanical torque of the machine at $V=V_0$ can also be extracted from the same measurement. Assuming that the COF is not a function of the normal force (F_N), the electromechanical torque is equal to the frictional torque at a constant velocity.

$$T_{EM}\Big|_{V=V_0} = \mu \times F_N \times R \qquad \textbf{Eq. 5-25}$$

$$T_{EM}\Big|_{V=V_0} = \underbrace{\frac{F_N\left(V_0\right)\left(R_1^2 + R_2^2\right)}{2g}}_{const.} \alpha \qquad \textbf{Eq. 5-26}$$

The above equation is used for the torque extraction after the measurement of deceleration. Experiments have shown that the machine does not operate at excitation

amplitudes lower than 150V. The change in the power angle of the machine to balance the load and electromechanical torque was discussed in Chapter 2. If the applied voltage, V_0, is the onset of operation i.e. the spinning motor would stop if lower voltage is applied, the power angle of the machine is at the critical value[35]. The $F_N(V_0)$ value is obtained from the 3D finite element simulations reported in Chapter 3.

5.2.3.2 Angular Velocity and Acceleration

It was described in Section 5.2.3.1 that the transient response of the micromotor is used to extract the electromechanical torque, frictional torque, and coefficient of friction. In this type of measurement, the micromotor is excited with square pulses with constant amplitude, frequency, and duty cycle. At $t=0$ s, the applied voltage is set to be zero; however, the rotor does not stop immediately since it has a finite angular momentum of $I\omega$. Because the motion detection system has a high temporal resolution (1 ms) and is triggered at $t=0$ s, it is possible to measure the angular displacement of the rotor with high precision at the time period of $t<0$ and $t=t_s$ where t_s is the time when rotor completely stops.

The angular velocity, $\omega(t)$, and angular acceleration, $\alpha(t)$, can be obtained by taking the first and second numerical derivative of position ($\theta(t)$). However, numerical differentiation amplifies noise. Therefore, it is necessary to filter the position data (e.g. smoothing) or fit the position data to a function. The current methodology uses the curve fitting method. The first step is to find a function that fits well to the data and has a rational correspondence with the physics of the problem. In order to find an appropriate $\theta(t)$ function a differential equation of

[35] For more information please refer to the power angle discussion in Chapter 2.

$$\ddot{\theta} = A\dot{\theta} + B \qquad \textbf{Eq. 5-27}$$

is defined to express the angular acceleration of the system as a linear function of the angular velocity, where $\ddot{\theta}$ and $\dot{\theta}$ are the second and first derivatives of the angular displacement with respect to time. The above equation is written based on the assumption that the coefficient of friction is constant plus some linear dependence on the angular velocity. This approach allows velocity dependant COF and is justified after comparison to the measured data. One solution of such differential equation is[36]

$$\theta = ae^{bt} + ct + d \qquad \textbf{Eq. 5-28}$$

where $A = b$ and $B = -bc$. The first and second derivatives of the displacement are respectively

$$\dot{\theta} = abe^{bt} + c \qquad \textbf{Eq. 5-29}$$

$$\ddot{\theta} = ab^2e^{bt} \qquad \textbf{Eq. 5-30}$$

Figure 5-34 shows the angular displacement of the rotor together with the fitted curve with R^2 value of 0.9999. The fitting is performed using the MATLAB Curve Fitting Toolbox. After the curve fit a, b, c, and d constants are obtained with 95% confidence bound. A good agreement between assumed model and measured data is shown in the figure. Table 5-4 lists the summary of the fitting parameters. $\ddot{\theta}$ and $\dot{\theta}$ are then calculated using the constants and the last two equations. The angular position, velocity and acceleration results for $0<t<1$ s are shown in Figure 5-35, Figure 5-36, and Figure 5-37, respectively. The excitation frequency of 300 Hz corresponds to the initial rotor velocity of 20.5 rad/s. From Figure 5-36, the initial

[36] Final solution is only reported.

value for the angular velocity, $\omega(t=0)$, is measured to be 23 rad/s that matches well with the theoretical value of 20.5 rad/s.

It is possible to plot $\ddot{\theta}$ as a function of $\dot{\theta}$ to test the model. The result, shown in Figure 5-38, illustrates the linear dependence between acceleration and velocity. The obtained results are used next to determine electromechanical torque, friction torque, and coefficient of friction.

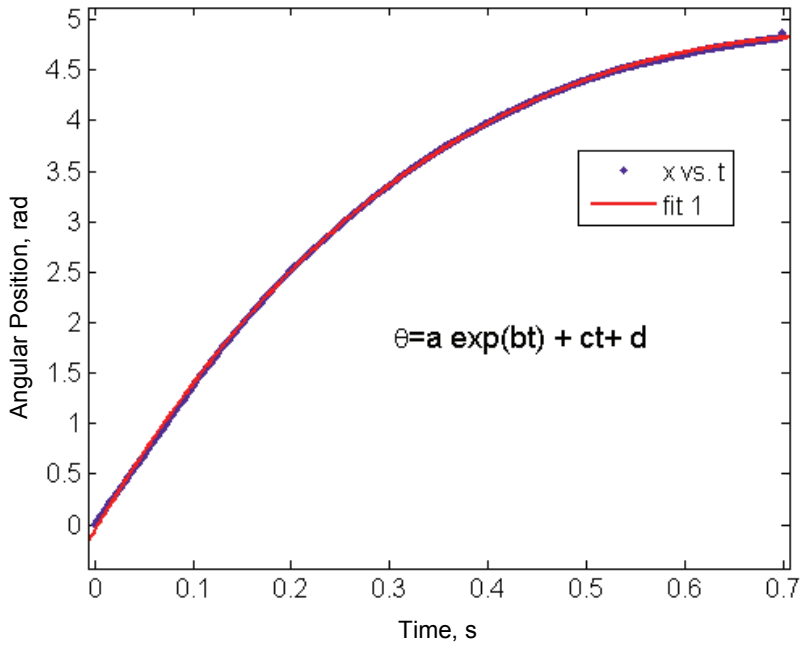

Figure 5-34: Angular position of the rotor versus time and the fitted exponential function.

Table 5-4: Summary of fitting parameters.

t, s	a	b	c	d
0-0.7	-21.15	-1.48	-7.95	21.09

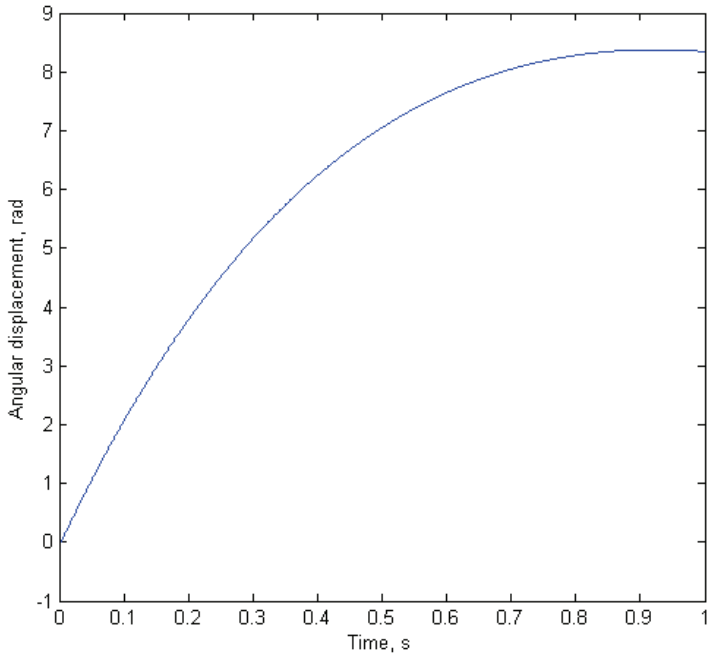

Figure 5-35: Angular displacement of the rotor as a function of time was obtained from measuring the rotor position using the high-speed camera system and fitting the data to the function obtained from solving the differential equation.

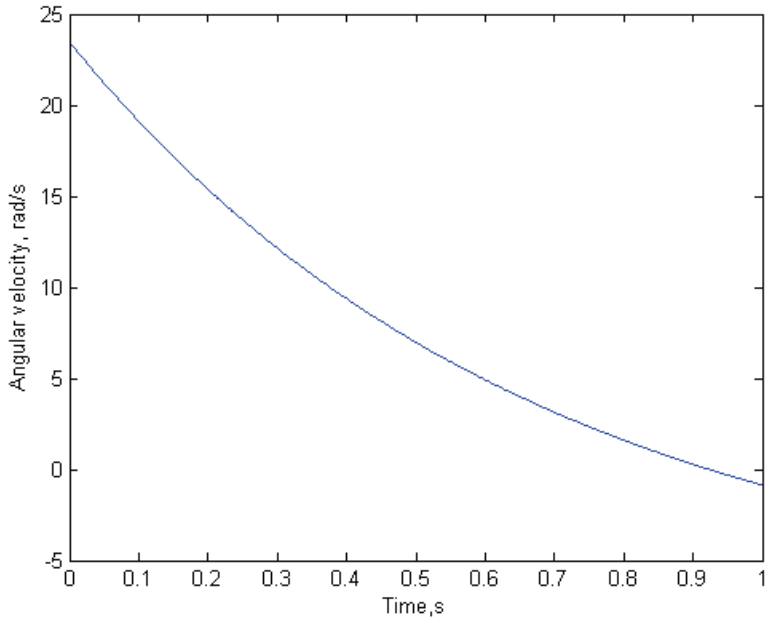

Figure 5-36: Angular velocity of the rotor as a function of time is derived from time differentiation of the angular displacement function.

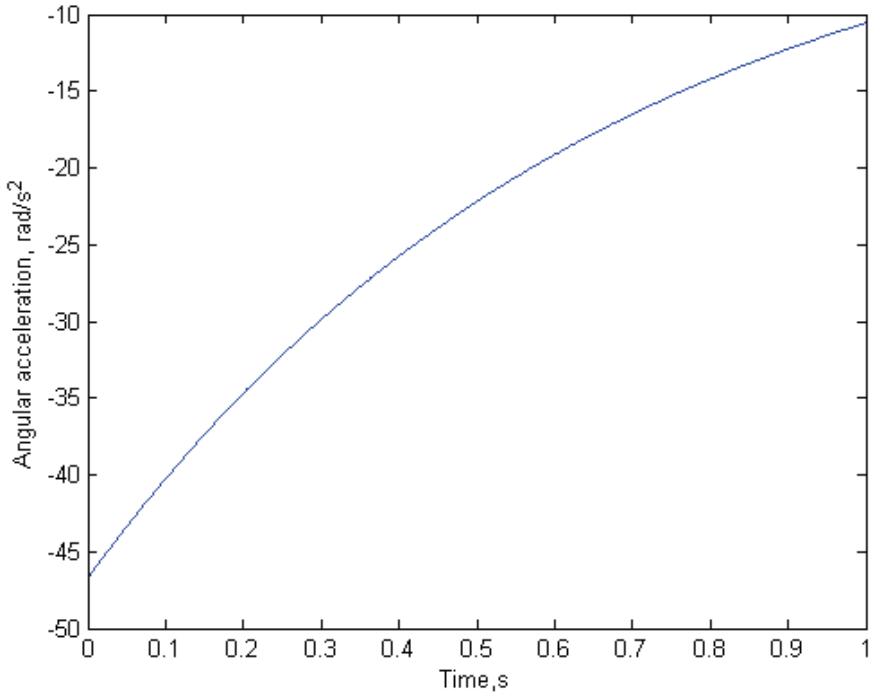

Figure 5-37: Angular acceleration of the rotor as a function of time is derived from time differentiation of the angular velocity function.

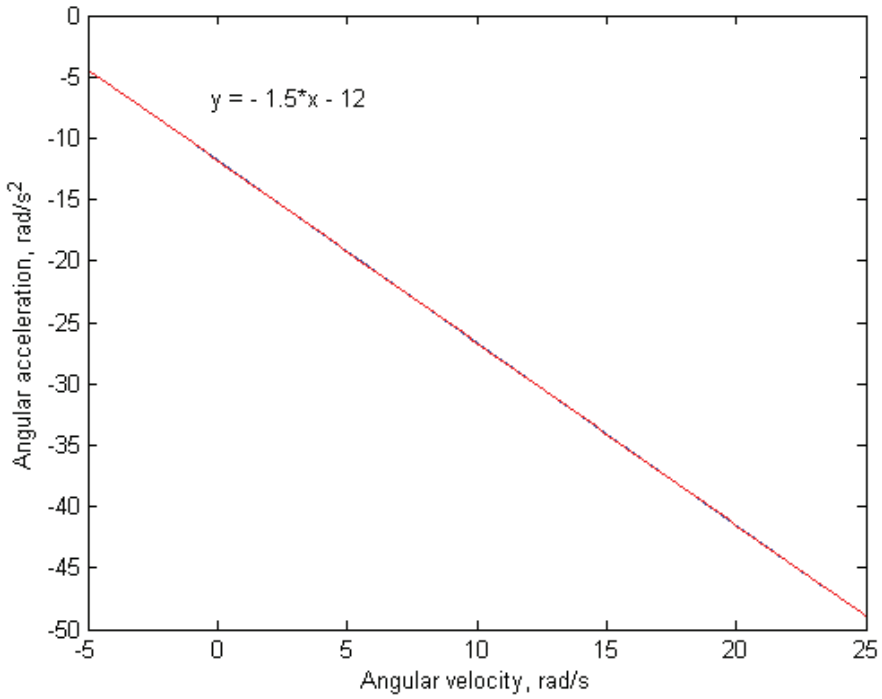

Figure 5-38: Angular acceleration of the rotor as a function of angular velocity shows the $\ddot{\theta} = A\dot{\theta} + B$ relationship.

5.2.3.3 Torque, Power, and Friction

Based on the derivation of Section 5.2.3.1, the coefficient of friction and torque of the machine are calculated using $\mu = \underbrace{\frac{R_1^2 + R_2^2}{2gR_0}}_{Const.} \alpha$ and $T_{EM}\big|_{V=V_0} = \underbrace{\frac{F_N(V_0)(R_1^2 + R_2^2)}{2g}}_{Const.} \alpha$.

The angular acceleration at *t=0* s was extracted to be -46 rad/s^2 from Figure 5-37. The acceleration value at *t=0* was selected to represent the status of the system at the onset of turn off. Table 5-5 shows the results as well as constants used in the calculations. As shown in the table, the electromechanical torque of the machine with the gap of 10 μm at 150 V is indirectly measured to be -5.62 μN·m. This value is in agreement with the simulation result of -6.75 μN·m reported in Chapter 3 (V=150 V). The mechanical power is proportional to be angular velocity and is calculated using

$$p_{Mech.} = T_{EM}\ \omega \qquad \textbf{Eq. 5-31}$$

The motor's maximum output mechanical power (D2) at the excitation frequency of 800 Hz ($\omega_{Mech.}$*=54.6* rad/s) is calculated to be 307 μW. The frictional torque, force, and coefficient of friction are also listed in the table.

The extraction of torque and coefficient of friction from deceleration of the machine relies on the correct and repeatable measurement of the acceleration (α). Figure 5-39 shows the extracted acceleration for three different measurements. As shown, the error between the three measurements is about 10 %. This implies that the torque and friction measurements have an error on the order of 10%. These correction factors are added to Table 5-5. Torque also relies on the accurate estimation of the normal force.

Table 5-5: Summary of the electromechanical torque of the machine at 150 V, coefficient of friction, frictional torque at no voltage and the constants used in the calculation. Rotor moment of inertia and mass are also included though not used in the calculations.

R_1 (mm)	R_2 (mm)	R_0 (mm)	g (m/s^2)	F_N @ 150V (mN)	α (rad/s^2)
1	7	6	9.8	48	-46
I (kg m^2)	M (kg)	T_{EM} @ 150 V (μN·m)	$T_{Friction}$ @ 0V (μN·m)	$F_{Friction}$ @ 0V (μN)	μ
4.70 ×10^{-9}	1.88×10^{-4}	-5.62 ± 0.5	0.22 ± 0.02	36.0 ± 3	0.0196 ± 0.002

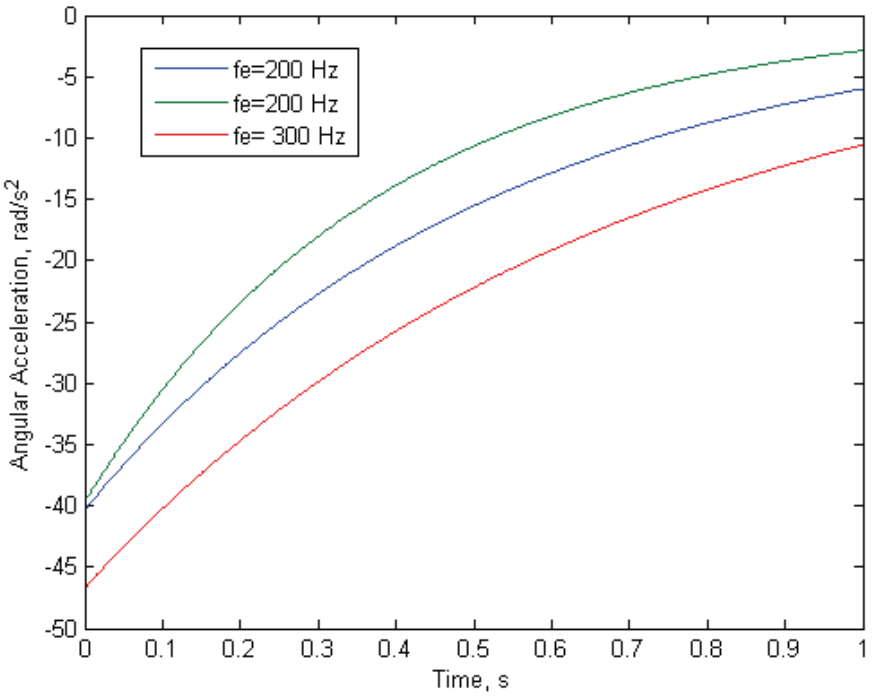

Figure 5-39: Angular acceleration versus time measured with different initial velocities.

5.2.3.4 Acceleration Tests

Using the high-speed camera system, it is possible to measure the time it takes for the micromotor to start from the rest position and reach the steady state velocity. At *t=0* s, the excitation voltage is applied to the micromotor. Figure 5-40 shows the angular position of the rotor versus time at the excitation frequency of 30 Hz. Each data point on the graph represents the position of the tracking mark in a single frame. The micromotor starts the synchronous motion in about 30 ms. It was found that in the frequency range of 10 to 300 Hz the startup time is not a strong function of excitation frequency. Figure 5-41 shows a similar graph for the excitation frequency of 70 Hz. More advanced excitation schemes can be used for faster acceleration of the rotor e.g. open loop variable frequency excitation or closed loop control.

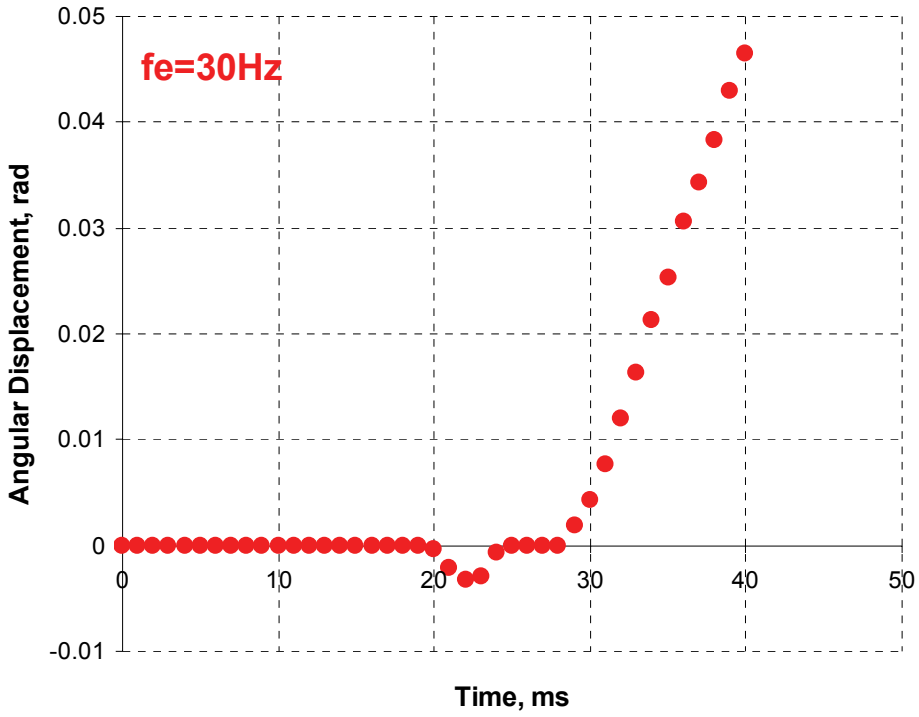

Figure 5-40: Angular displacement of the rotor versus time when the stator is excited at t=0 s showing the startup time less than 30 ms (f_e=30 Hz).

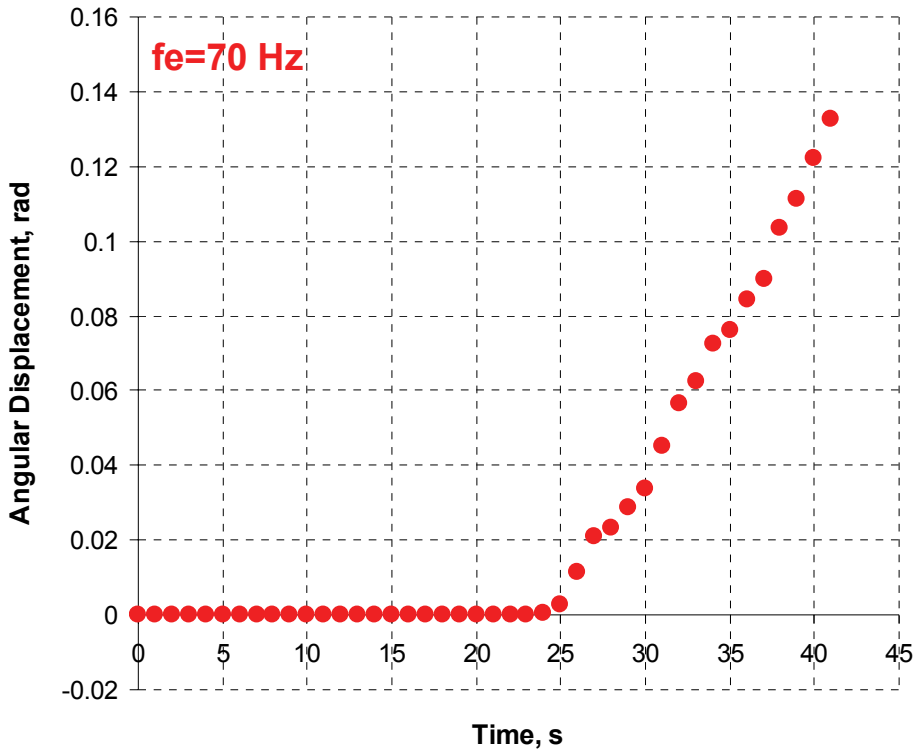

Figure 5-41: Angular displacement of the rotor versus time when the stator is excited at t=0 s showing the startup time less than 30 ms (f_e=70 Hz).

5.2.4 Discussion

The characterization results reported in this chapter are the first demonstration of a rotary micromotor supported on microball bearings. Based on these results, the machine has the potential to be used in a wide verity of applications such as micropumps and micropositioners. It was shown that the primary designs of D1 and D2 are both operational. The angular displacement, velocity, and acceleration are measured for these devices. Top speed of 517 rpm which corresponds to the linear tip speed of 324 mm/s was demonstrated for D2. The measured speed for the rotary machine is 44 times higher than the top speed measured for the linear device. The higher achieved velocity for the rotary micromotor is credited to two reasons. First, due to the nature of the rotary motion, the rotor has continuous momentum and

unlimited range of motion. In contrast, the motion of the linear device is limited to 4 mm. Once the slider reaches the end of the trench, the rotor direction is reversed.

The second reason is attributed to the improvements made to the design and fabrication of the micromotor including the use of SiC film as a *lubricant*[37]. The characterization results of the rotary micromotor with no SiC film demonstrated that the friction torque exceeds the maximum sustainable torque of the machine at 150 V. Therefore, a solid *lubricant* film was deposited on the rotor substrate to reduce the rolling friction. The use of SiC helps the machine stay in the synchronous regime, especially at higher velocities.

It is possible to maintain higher angular velocities with the current design. One necessary modification is using a closed loop control instead of open loop control. The feedback system can potentially sense the position of the rotor and apply appropriate excitation signal to each of the 6 phases. Conversely, with the open loop system, the rotor may go through a short period of sudden change in speed due to the random behavior of the microballs that could ultimately cause the machine to come out of synchronization.

Another method to increase the maximum velocity of the machine is to use more advanced bearing designs. Encapsulated bearings are currently under development and will be used in future generation of micromachines. One major challenge in any bearing design is separation of the microballs. Figure 5-42 shows the ball colocation phenomenon. Balls tend to colocate after a few minutes of operation. Continuous operation of up to 45 minutes is occasionally observed. The higher the velocity of the

[37] Conventionally a hard film can not be called lubricant; however, recently this word is used in the literature to describe the function of some solid films that reduce friction.

rotor, the higher the chance of the ball colocation is. The ball colocation results in non uniform gap and stopping of the rotor. Therefore, it is necessary to implement separation schemes in future designs. The time of operation for the micromotors tested was generally between 1-60 min.

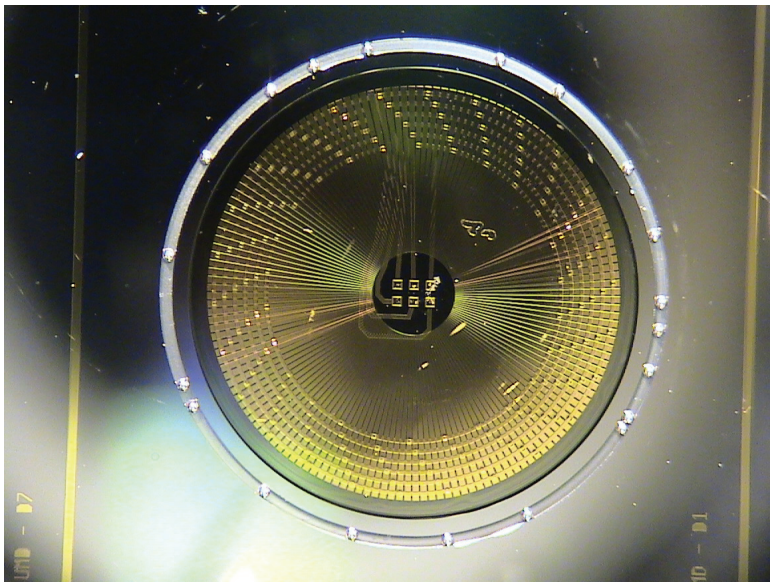

(a)

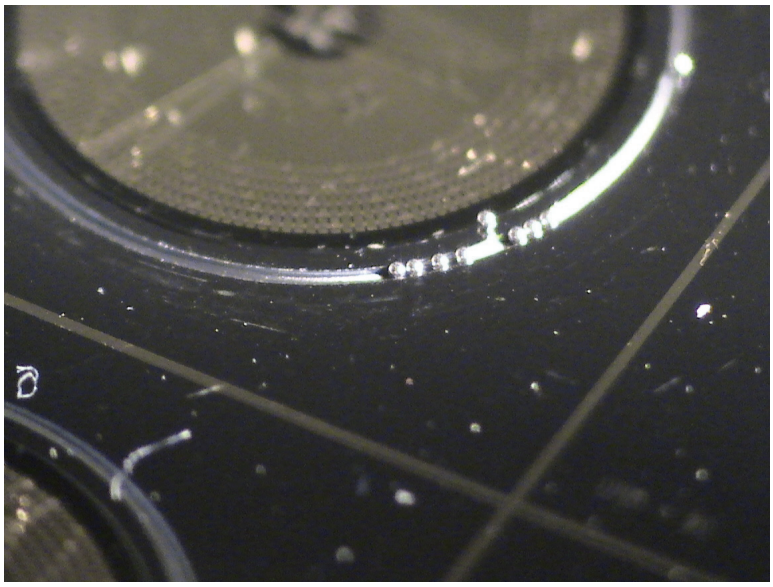

(b)

Figure 5-42: Picture of the microballs in the stator housing (a) before, and (b) after testing showing ball colocation after testing.

Other micromotor designs (D3-6) were also tested in a similar manner. It was observed that the high-torque design (D4) is operational; however, the machine's operation is neither continuous nor reliable. D4 was originally designed for a 5 μm gap size; however, such a small gap has not been achieved in this study. Further improvements to the fabrication process are necessary to maintain a small uniform gap. Unreliable operation of the machine is not necessarily due to the electrode geometry design. The behavior can also be attributed to the high normal force compared to D1 and D2 and therefore, higher friction torque.

Among the other designs, D3, D5, and D6 were never successfully tested. It is believed that D3's theoretical maximum torque is not sufficient to overcome the friction for the current bearing design. D5 and D6 have both double-trench bearings that are believed to result in higher friction or less stability due to the imperfections in the fabrication process of the two trenches.

The measurement results of the machine's angular velocity shows an excellent agreement between theory and experiment (Figure 5-27 and Figure 5-28). It was discussed in Chapter 2 that the angular velocity of these types of machines is formulated by $n_r=60\ f_e\ /\ N_p$. Three methods for the derivation of velocity were reported in Chapter 2 that all differ from the commonly used formulation in the literature ($n_r=120\ f_e\ /\ N_p$). The theoretical derivation supported by the experimental results show that direct adaptation of the magnetic machine's equation for the electrostatic machines results in overestimation of the angular velocity. If such adaptations are pursued, the difference in the nature of the two should be taken into consideration. The most important disparity is concealed in the definition of the *poles*.

In an electromagnetic machine, poles are defined by the stator circuitry. Each S-N pair makes a single pole. For a variable-capacitance machine, however, the definition of poles has to be altered because a capacitor is formed by two conductors, one physically located on the stator and one on the rotor. Without the existence of the capacitor, the operation of the machine is not possible. Therefore, the numbers of stator and rotor saliencies are both taken into consideration. This subject was discussed in Chapter 2. The experimental results reported in this chapter support the developed theory for these types of machines. The theory and the experimental results, contradicting the literature, are both presented for the first time in this dissertation.

The electromechanical torque is indirectly measured for the excitation voltage of ±150 V to be -5.62 μN·m. This value is in agreement with the simulation result of -6.75 μN·m. It is desirable to measure the torque at different excitation voltages; however, with the current test setup the maximum applied voltage is limited to ±150 V. Micromotor operation below 150 V was not achieved. The maximum output mechanical power was calculated to be 307 μW (at ±150 V).

One of the advantages of the developed characterization methodology is the ability to extract frictional torque and COF from the measurements. The accuracy of the calculated COF solely depends on the geometrical factors and the measured acceleration. The COF was measured to be around 0.02 which corresponds to the interaction between stainless steel microballs, silicon housing on the stator, and SiC-coated silicon housing on the rotor. The loading and the number of the microballs are also a factor. In all the experiments discussed in Section 5.2, 10 microballs are used;

therefore, the average load on each contact point is about 20 mg. The extracted COF is in good agreement with the previously reported COF of 0.04 for the v-grooves etched by potassium hydroxide (10 g per ball loading conditions). The COF of v-groove trenches are expected to be higher; however, higher loading conditions are believed to reduce the COF. Recent tribology experiments suggest that [134]

$$\mu \propto (contact\ force)^{\frac{-1}{3}} \qquad \textbf{Eq. 5-32}$$

Currently a series of tribology experiments is underway by colleagues at the MEMS Sensors and Actuators Lab to further analyze the effect of ball housing shape, coating, ball number, and loading on the COF.

Measurements showed that the machine requires about 30 ms to start from zero velocity and reach steady state condition. This is basically the time that takes the machine to overcome static friction and get into synchronization. This time is identical to the startup time of the linear micromotors. When the micromotor is used as a positioner, it is necessary to change the direction of rotation. It was shown that the direction of the rotation is changed without interruption in the operation of the machine. This is performed by changing the sequence of the phases. For example, *ABCABC* and *ACBACB* sequences result in the counterclockwise and clockwise rotations, respectively. Change-of-direction experiments revealed that a time on the order of 30 ms is required for the machine to change its direction.

6 Summary and Conclusion

6.1 Summary

The successful development of the first rotary micromotor supported on microball bearings was demonstrated in this dissertation. The micromotor is a six-phase variable-capacitance machine composed of stator, rotor, and microballs. Compared to their magnetic counterparts, variable-capacitance machines are voltage driven, have a comparable energy density at small gaps, and have a simpler fabrication process. Furthermore, they are more efficient, have a lighter rotor, and can potentially be operated at higher temperatures. Nevertheless, one of the major challenges in the development of electric micromachines has been the robustness of the rotor mechanical support. Previous designs utilize gas-lubricated bearings in turbomachinery or center-pin bearings in early surface-micromachined devices. The fabrication of the gas-lubricated bearings is extremely complex. The micromotors based on center-pin bearings are highly inefficient and unreliable. The microball-bearings technology in silicon provides a reliable support with less friction and wear compared to center-pin bearings and less fabrication complexity compared to gas-lubricated bearings. Another advantage is the ability to sustain uniform air gap, which is critical for the operation of the micromachine. Furthermore, this technology enables higher torques due to the implementation of a bottom-drive design.

The theory of the machine's operation, including derivation of angular velocity and torque, are fully discussed in Chapter 2. The machine's geometry is designed based on finite element simulation results. The effect of the electrodes packing factor as well as the gap size on the torque of the machine was studied through a series of

finite element simulations using Comsol Multiphysics. It was found that for the gap size of 10 μm and electrode width of 90 μm, the optimal lateral distance between electrodes is 30 μm or 45 μm. Both designs were calculated to produce 3 μN·m of torque at 100 V for a machine with an active area of 75 mm^2. This torque is about 2 orders of magnitude higher than that of conventional side-drive micromotors.

The designed micromotors were fabricated using a complex 9 level mask process. The stator and rotor are fabricated separately on silicon substrates and assembled with the microballs. The electrode and interconnection layers are fabricated with two layers of gold films. The interconnection layer connects every sixth electrode to form a six-phase machine. Low dielectric constant benzocyclobutene (BCB) polymer is used as a dielectric layer in the structure of the stator providing electrical isolation between the metal lines, substrate, and environment. The integration of this polymer in the structure of the micromachine has several momentous benefits. The electrical efficiency of the BCB-based micromotor, compared to silicon dioxide-based devices, is increased due to the low relative permittivity ($k=2.6$) and large achievable thickness (1-30 μm) of the film. Furthermore, the air gap across the device is more uniform due to the low residual stress ($\Sigma=28$ MPa-tensile) of the film. The microball housings on both rotor and stator are fabricated using dry anisotropic etching. The rotor structure also includes salient poles etched deep in silicon. A thin film of silicon carbide is deposited after die release and before testing. The silicon carbide film was found to reduce the friction.

The fabricated device is the first demonstration of a rotary micromachine supported on microball bearings. The process reported in this dissertation is unique

and extremely complicated; this work is the result of careful process development carried out to address the adhesion of metal-polymer films, process yield, eccentricity due to misalignment of electrodes to microball housing, interconnection resistance, and small gap size. The rotary device significantly benefited from the process characterization performed throughout the development of the second-generation linear device, which by itself, was a major improvement to the first-generation.

The test setup originally developed for the characterization of the second-generation linear micromotor was modified to accommodate the steady state and transient response measurement. A top angular velocity of 517 rpm was measured corresponding to a linear tip velocity of 324 mm/s; this is 44 times higher than the top velocity measured for the linear device (7.2 mm/s). The electromechanical torque was indirectly measured for the excitation voltage of ±150 V to be -5.62±0.5 μN·m. This value is in agreement with the simulation result of -6.75 μN·m. The maximum output mechanical power at ±150 V and 517 rpm was calculated to be 307 μW.

One of the benefits of the characterization methodology discussed in this dissertation is the capability to extract COF from the transient measurements. The COF was measured to be 0.02 which is in good agreement with our previous tribology experiments and literature.

6.2 Contributions

Major contributions of this research dissertation are:

- Development of the first rotary micromotor supported on microball bearings with top measured velocity of 517 rpm and torque of 5.6 μN·m.

- Development of the second-generation linear micromotors supported on microball bearings with top speed of 7.3 mm/s.
- Optimization of the fabrication process for linear machines.
- Dynamic characterization of the linear micromotors to indirectly obtain the net slider force.
- Modeling of the linear micromotors and extraction of model parameters from experiments.
- Feasibility demonstration of a microball bearing technology as a support mechanism for rotary machines.
- Design and 3D finite element simulation of a rotary variable-capacitance micromachine.
- Development of complex fabrication process using a 9-level-mask process.
- Integration of the benzocyclobutene polymer (as a low permittivity dielectric material) with thin film deposition and silicon bulk micromachining.
- Implementation of a solid silicon carbide layer as a lubricant film.
- Development of a new characterization methodology for indirect measurement of torque and coefficient of friction.

6.3 Future Work

The evolution of future microsystems that are capable of microsurgery, micropropulsion, micropumping, and microassembly functions requires the development of reliable, low-power, and efficient micromotors. Previous micromotors suffer from friction, wear, stability, and fabrication complexities. A major challenge in developing instrumental micromotors is to design and fabricate a

reliable support mechanism for the rotor; a challenge that has not been successfully addressed in conventional designs. Another important area is the development of micromotors capable of providing the necessary torque and speed with a high energy efficiency.

The rotary micromotor reported in this dissertation is a driving platform for highly-desirable microsystems such as micropumps. Micropumps can be used for drug delivery, fuel delivery, cooling, and vacuum applications. The motor can also be used as an actuator. A micropositioner can be used for fiber-to-fiber alignment, optical switching, and interferometry. Other applications include microrobotics, micropropulsion, microsurgery, microassembly, and electric power generation. Figure 6-1 shows a few areas where the developed micromotor can be utilized.

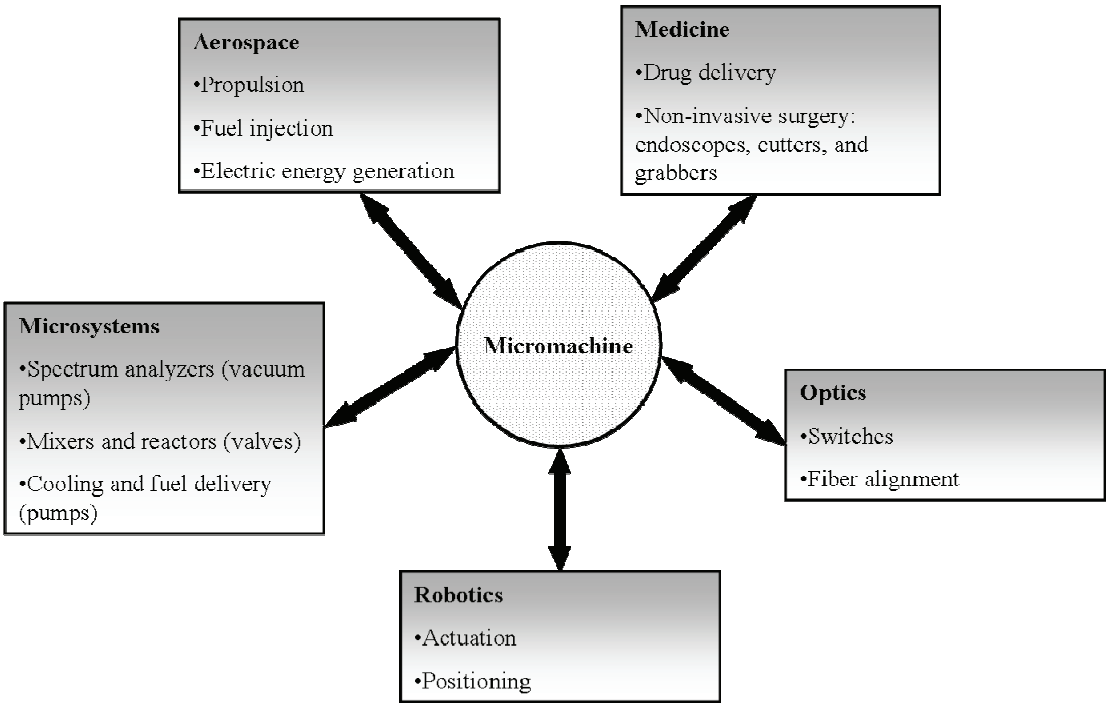

Figure 6-1: Block diagram of the micromachine's potential applications

The implementation of the current design in the above applications requires additional improvements to the electrical and mechanical designs. In the electrical domain, a closed-loop excitation system is required for position, speed, and torque control. A feedback control system will improve the reliability, stability, and functionality of this synchronous machine. Furthermore, the performance of the machine is improved with small gap size and large number of electrodes. There are number of fabrication challenges including gap uniformity that need to be addressed to achieve gap sizes smaller than 10 μm.

Improvements to the mechanical design are also necessary. Currently, encapsulated bearings are under development at UMD for centrifugal micropumps (without a motor) using wafer bonding steps. In these designs, the balls are encapsulated in housings etched in rotor and stator. The encapsulated bearing can potentially be used at speeds up to a few hundred thousands of rpm. Moreover, one of the drawbacks of the current bearing design reported in this dissertation is ball colocation. Therefore, it is necessary to design and fabricate ball retainer rings to eliminate microball collisions. Finally, the friction and wear of the microballs and the housing need to be reduced using dry lubricant films. The geometry of the ball housing, as well as the coating, needs to be optimized. Tribology experiments are currently underway in our research group to study the effect of hard coatings such as silicon carbide and diamond-like-carbon on the friction and wear.

References

[1] X. Wang, S. Cui, and S. Cheng, "Advantages of electrostatic micromotor and its application to medical instruments," presented at Conference Record of the 2002 IEEE Industry Applications, Pittsburgh, PA, USA, 2002.

[2] D. Polla, A. Erdman, D. Peichel, R. Rizq, Y. Gao, and D. Markus, "Precision micromotor for surgery," presented at Proceedings of 1st Annual International IEEE-EMBS Special Topic Conference on Microtechnologies in Medicine and Biology, Lyon, France, 12-14 Oct. 2000.

[3] L. M. Gao, Y. Chen, L. M. Lin, and G. Z. Yan, "Micro motor based new type of endoscope," presented at Proceedings of the 20th Engineering in Medicine and Biology Society, Hong Kong, China, 1998.

[4] D. J. Laser and J. G. Santiago, "A review of micropumps," *Journal of Micromechanics and Microengineering*, vol. 14, pp. R35, 2004.

[5] T. Weisener, G. Vogele, M. Widmann, C. Bark, R. D. Schraft, A. Bertholds, and A. Braunschweiler, "Development and fabrication of a rotary micropump and its industrial and medical applications," presented at Proceedings of the SPIE, Austin, TX, USA, 1996.

[6] C. H. Ahn and M. G. Allen, "Fluid micropumps based on rotary magnetic actuators," presented at IEEE Microelectromechanical Systems (MEMS '95), Amsterdam, Netherlands, 1995.

[7] B. Mladen, J. M. Jack, P. G. Andrew, and S. Schultz, "Electromagnetic micromotor for microfluidics applications," *Applied Physics Letters*, vol. 79, pp. 1399-1401, 2001.

[8] S. Fatikow, A. Falzullin, and J. Seyfried, "Planning of a microassembly task in a flexible microrobot cell," presented at Proceedings of the IEEE International Conference on Robotics and Automation (ICRA), San Francisco, CA, USA, 24-28 April, 2000.

[9] R. Yeh, S. Hollar, and K. S. J. Pister, "Design of low-power silicon articulated microrobots," *Journal of Micromechatronics*, vol. 1, pp. 191, 2002.

[10] R. Yeh, E. J. J. Kruglick, and K. S. J. Pister, "Surface-micromachined components for articulated microrobots," *Journal of Microelectromechanical Systems*, vol. 5, pp. 10, 1996.

[11] W. S. N. Trimmer and K. J. Gabriel, "Design Consideration for a Practical Electrostatic Micro-motor," *Sensors and Actuators*, vol. 11, pp. 189-206, 1987.

[12] O. D. Jefimenko and D. K. Walker, *Electrostatic motors: their history, types, and principles of operation*. Star City, West Virginia: Electret Scientific Company, 1973.

[13] B. Bollee, "Electrostatic Motors," *Philips technical review*, pp. 178-194, 1969.

[14] J. G. Trump, "Eloctrostatic Sources of Electric Power," *Electrical Engineering*, vol. 66, pp. 525-534, 1947.

[15] J. G. Trump, "Vaccum Electrostatic Engineering." Cambridge, MA, USA: Massachusetts Institute of Technology, 1933.

[16] M. J. Mulcahy and W. R. Bell, "Electrostatic Generators," in *Electrostatic and its application, Chapter 8*, 1973, pp. 148-179.

[17] P. L. Chapman and P. T. Krein, "Micromotor technology: Electric drive designer's perspective," presented at Industry application conference annual meeting, Chicago, IL, USA, 2001.

[18] D. P. Arnold, F. Cros, I. Zana, M. G. Allen, S. Das, and J. H. Lang, "Magnetic induction machines embedded in fusion-bonded silicon," presented at Solid-State Sensors, Actuators and Microsystems Workshop, Hilton Head Island, SC, USA, 2004.

[19] S. Das, D. P. Arnold, and M. G. Allen, "Multi-watt electric power from a fabricated permanent-magnet generator," presented at IEEE Micro Electro Mechanical Systems (MEMS '05), Miami, FL, USA, 2005.

[20] K. Dutta, P. Dev, R. Dewilde, B. Sharma, and R. W. Newcomb, "Integrated Micromotor Concepts," Stanford University AFOSR70-1682TR, 1970.

[21] P. L. Chapman and P. T. Krein, "Smaller is better? Micromotors and electric drives," *IEEE Industry Applications Magazine*, vol. 9, pp. 62, 2003.

[22] J. Boland, Y.-H. Chao, Y. Suzuki, and Y. C. Tai, "Micro electret power generator," presented at IEEE Sixteenth Annual International Conference on Micro Electro Mechanical Systems, MEMS-03, Kyoto, Japan, 2003.

[23] J. Boland, H. W. Messenger, H. W. Lo, and Y. C. Tai, "Arrayed liquid rotor electret power generator systems," presented at IEEE Micro Electro Mechanical Systems (MEMS '05), Miami, FL, USA, 2005.

[24] T. Sterken, P. Fiorini, K. Baert, R. Puers, and G. Borghs, "An electret-based electrostatic μ-generator," presented at 12th International Conference on, TRANSDUCERS, Solid-State Sensors, Actuators and Microsystems, Boston, MA, USA, 2003.

[25] S. Tanaka, T. Genda, and M. Esashi, "High power electrostatic motor and generator using electrets," presented at 12th International Conference on,TRANSDUCERS, Solid-State Sensors, Actuators and Microsystems, Boston, MA, USA, 2003.

[26] Y. B. Jeon, R. Sood, J. H. Jeong, and S. G. Kim, "MEMS power generator with transverse mode thin film PZT," *Sensors and Actuators*, vol. in press, 2005.

[27] R. Sood and S. G. Kim, "Piezoelectric micro power generation for energy harvesting," presented at Solid-State Sensors, Actuators and Microsystems Workshop, Hilton Head Island, SC, USA, 2004.

[28] S. Cagatay, B. Koc, P. Moses, and K. Uchino, "A piezoelectric micromotor with a stator of phi =1.6mm and l=4 mm using bulk PZT," *Japanese Journal of Applied Physics, Part 1*, vol. 43, pp. 1429-1433, 2004.

[29] J. Friend, K. Nakamura, and S. Ueha, "A piezoelectric micromotor using in-plane shearing of PZT elements," *IEEE/ASME Transactions on Mechatronics*, vol. 9, pp. 467-473, 2004.

[30] S. Dong, S. P. Lim, K. H. Lee, J. Zhang, L. C. Lim, and K. Uchino, "Piezoelectric ultrasonic micromotor with 1.5 mm diameter," *IEEE Transactions on Ultrasonics, Ferroelectrics and Frequency Control*, vol. 50, pp. 361-367, 2003.

[31] J. T. Leinvuo, S. A. Wilson, H. J. A. Almond, and R. W. Whatmore, "Experimental design and construction of a flextensional ultrasonic piezoelectric micro-motor," presented at Tenth European Meeting on Ferroelectricity, Cambridge, UK, 2004.

[32] L. S. Fan, Y. C. Tai, and R. S. Muller, "IC-processed electrostatic micro-motors," presented at Technical Digest of International Electron Devices Meeting, San Francisco, CA, USA, 1988.

[33] Y. C. Tai, L. S. Fan, and R. S. Muller, "IC processed micro-motors: design, technology, and testing," presented at Proceedings of Micro Electro Mechanical Systems, Salt Lake City, UT, 1989.

[34] M. Mehregany, S. F. Bart, L. S. Tavrow, J. H. Lang, and S. D. Senturia, "Principles in design and microfabrication of variable-capacitance side-drive motors," *Journal of Vacuum Science & Technology A*, vol. 8, pp. 3614-3624, 1990.

[35] J. M. Bustillo, R. T. Howe, and R. S. Muller, "Surface micromachining for microelectromechanical systems," *Proceedings of the IEEE*, vol. 86, pp. 1552-1574, 1998.

[36] H. C. Nathanson, W. E. Newell, R. A. Wickstrom, and J. R. Davis, Jr., "The resonant gate transistor," *Electron Devices, IEEE Transactions on*, vol. 14, pp. 117, 1967.

[37] T. A. Lober, "A microfabricated electrostatic motor design and process." Cambridge, MA: Massachusetts Institute of Technology, 1988.

[38] L. S. Fan, Y. C. Tai, and R. S. Muller, "Integrated movable micromechanical structures for sensors and actuators," *IEEE Transactions on Electron Devices*, vol. 35, pp. 724, 1988.

[39] M. Mehregany, K. J. Gabriel, and W. S. N. Trimmer, "Integrated fabrication of polysilicon mechanisms," *IEEE Transactions on Electron Devices*, vol. 35, pp. 719, 1988.

[40] M. Mehregany, S. F. Bart, L. S. Tavrow, J. H. Lang, and S. D. Senturia, "Principles in design and microfabrication of variable-capacitance side-drive motors," *Journal of Vacuum Science & Technology A: Vacuum, Surfaces, and Films*, vol. 8, pp. 3614-3624, 1990.

[41] M. Mehregany, S. D. Senturia, J. H. Lang, and P. Nagarkar, "Micromotor fabrication," *IEEE Transactions on Electron Devices*, vol. 39, pp. 2060, 1992.

[42] F. Long-Sheng, T. Yu-Chong, and R. S. Muller, "IC-processed electrostatic micro-motors," presented at Technical Digest of International Electron Devices Meeting, San Francisco, CA, USA, 1988.

[43] M. Mehregany, S. D. Senturia, and J. H. Lang, "Measurement of wear in polysilicon micromotors," *IEEE Transactions on Electron Devices*, vol. 39, pp. 1136, 1992.

[44] M. Mehregany, S. D. Senturia, and J. H. Lang, "Friction and wear in microfabricated harmonic side-drive motors," presented at IEEE Solid-State Sensor and Actuator Workshop Technical Digest, Hilton Head Island, SC, USA, 1990.

[45] V. R. Dhuler, M. Mehregany, and S. M. Phillips, "Micromotor operation in a liquid environment," presented at IEEE Solid-State Sensor and Actuator Workshop Technical Digest, Hilton Head Island, SC, USA, 1992.

[46] A. Azzam Yasseen, J. N. Mitchell, D. A. Smith, and M. Mehregany, "High-aspect-ratio rotary polygon micromotor scanners," *Sensors and Actuators A: Physical*, vol. 77, pp. 73-79, 1999.

[47] A. Azzam Yasseen, J. N. Mitchell, J. F. Klemic, D. A. Smith, and M. Mehregany, "A rotary electrostatic micromotor 1 times 8 optical switch," *Journal of Selected Topics in Quantum Electronics*, vol. 5, pp. 26-32, 1999.

[48] V. D. Samper, A. J. Sangster, R. L. Reuben, and U. Wallrabe, "Multistator LIGA-fabricated electrostatic wobble motors with integrated synchronous control," *Journal of Microelectromechanical Systems*, vol. 7, pp. 214, 1998.

[49] A. Azzam Yasseen, W. Chien Hung, C. A. Zorman, and M. Mehregany, "Fabrication and testing of surface micromachined polycrystalline SiC micromotors," *Electron Device Letters, IEEE*, vol. 21, pp. 164, 2000.

[50] A. Azzam Yasseen, W. Chien-Hung, C. A. Zorman, and M. Mehregany, "Fabrication and testing of surface micromachined silicon carbide micromotors," presented at Proceedings of 12th International Workshop on Micro Electro Mechanical Systems (MEMS'99), Orlando, FL, USA, 17-21 Jan,1999.

[51] W. Zhang, G. Meng, and H. Li, "Electrostatic micromotor and its reliability," *Microelectronics Reliability*, vol. 45, pp. 1230, 2005.

[52] R. Agrawal, Q. Hasan, N. Ashraf, K. B. Sundaram, L. C. Chow, J. S. Kapat, and J. Vaidya, "Design and fabrication of meso-scale variable capacitance motor for miniature heat pumps," *Journal of Microemechanics and Microengineering*, vol. 13, pp. 1-7, 2002.

[53] K. Noguchi, H. Fujita, M. Suzuki, and N. Yoshimura, "The measurements of friction on micromechatronics elements," presented at IEEE Micro Electro Mechanical Systems (MEMS'91), Nara, Japan, 1991.

[54] K. Deng, W. H. Ko, and G. M. Michal, "A preliminary study on friction measurements in MEMS," presented at International Conference on Solid-State Sensors and Actuators, Digest of Technical Papers (TRANSDUCERS '91), San Francisco, CA, USA, 1991.

[55] J. U. Jeon, S. J. Woo, and T. Higuchi, "Variable-capacitance motors with electrostatic suspension," *Sensors and Actuators A: Physical*, vol. 75, pp. 289, 1999.

[56] C. B. Williams, C. Shearwood, P. H. Mellor, and R. B. Yates, "Modelling and testing of a frictionless levitated micromotor," *Sensors and Actuators A: Physical*, vol. 61, pp. 469, 1997.

[57] C. Shearwood, K. Y. Ho, C. B. Williams, and H. Gong, "Development of a levitated micromotor for application as a gyroscope," *Sensors and Actuators A: Physical*, vol. 83, pp. 85, 2000.

[58] X. S. Wu, W. Y. Chen, X. L. Zhao, and W. P. Zhang, "Micromotor with electromagnetically levitated rotor using separated coils," *Electronics Letters*, vol. 40, pp. 996.

[59] C. Ruffert, R. Gehrking, B. Ponick, and H. H. Gatzen, "Magnetic Levitation Assisted Guide for a Linear Micro-Actuator," *Magnetics, IEEE Transactions on*, vol. 42, pp. 3785, 2006.

[60] W. Chien-Chang, Y. Yeong-Der, L. Chien-Sheng, and C. Lung-Yu, "Micro-magnetic suspension motor design for miniature optical drive," *Japanese Journal of Applied Physics, Part 1 (Regular Papers, Short Notes & Review Papers)*, vol. 45, pp. 5801.

[61] C. Livermore, A. R. Forte, T. Lyszczarz, S. D. Umans, A. A. Ayon, and J. H. Lang, "A high-power MEMS electric induction motor," *Journal of Microelectromechanical Systems*, vol. 13, pp. 465-471, 2004.

[62] J. L. Steyn and J. H. Lang, "Generating electric power with a MEMS electroquasistatic induction turbine-generator," presented at IEEE Microel ectro mechanical systems (MEMS '05), Miami, FL, USA, 2005.

[63] C. H. Ahn, Y. J. Kim, and M. G. Allen, "A planar variable reluctance magnetic micromotor with fully integrated stator and coils," *Journal of Microelectromechanical Systems*, vol. 2, pp. 165-173, 1993.

[64] C. H. Ahn, Y. J. Kim, and M. G. Allen, "A planar variable reluctance magnetic micromotor with fully integrated stator and wrapped coils," presented at IEEE micro electro mechanical systems (MEMS '93), Fort Lauderdale, FL, USA, 1993.

[65] D. P. Arnold, F. Cros, I. Zana, D. R. Veazie, and M. G. Allen, "Electroplated metal microstructures embedded in fusion-bonded silicon: conductors and magnetic materials," *Journal of Microelectromechanical Systems*, vol. 13, pp. 791, 2004.

[66] H. Koser and J. H. Lang, "Magnetic induction micromachine-part I: Design and analysis," *Microelectromechanical Systems, Journal of*, vol. 15, pp. 415, 2006.

[67] F. Cros, H. Koser, M. G. Allen, and J. H. Lang, "Magnetic induction micromachine-part II: fabrication and testing," *Microelectromechanical Systems, Journal of*, vol. 15, pp. 427, 2006.

[68] H. Koser and J. H. Lang, "Magnetic induction micromachine-part III:Eddy currents and nonlinear effects," *Microelectromechanical Systems, Journal of*, vol. 15, pp. 440, 2006.

[69] T. W. Krygowski, M. S. Rodgers, J. Sniegowski, S. M. Miller, and J. Jakubczak, "A low-voltage rotary actuator fabricated using a five-level polysilicon surface micromachining technology," presented at International Electron Devices Meeting (IEDM), Washington, DC, 1999.

[70] B. C. Yen and J. H. Lang, "A Variable-Capacitance Vibration-to-electric Energy Harvester," *Submitted to IEEE Transactions on Circuits and Systems I*, 2005.

[71] M. Miyazaki, H. Tanaka, G. Ono, T. Nagano, N. Ohkubo, and T. Kawahara, "Electric-energy generation through variable-capacitive resonator for power-free LSI," *IEICE Transactions on Electronics*, vol. E87-C, pp. 549-555, 2004.

[72] P. Glynne-Jones, M. J. Tudor, S. P. Beeby, and N. M. White, "An electromagnetic, vibration-powered generator for intelligent sensor systems," *Sensors and Actuators A: Physical*, vol. 110, pp. 344-349, 2004.

[73] D. P. Arnold, H. Florian, Z. Iulica, G. Preston, P. Jin-Woo, D. Sauparna, H. L. Jeffrey, and G. A. Mark, "Design optimization of an 8 W, microscale, axial-flux, permanent-magnet generator," *Journal of Micromechanics and Microengineering*, vol. 16, pp. S290, 2006.

[74] D. P. Arnold, S. Das, J. W. Park, I. Zana, J. H. Lang, and M. G. Allen, "Microfabricated High-Speed Axial-Flux Multiwatt Permanent-Magnet Generators; Part II: Design, Fabrication, and Testing," *Microelectromechanical Systems, Journal of*, vol. 15, pp. 1351, 2006.

[75] S. Das, D. P. Arnold, I. Zana, J. W. Park, M. G. Allen, and J. H. L. Lang, "Microfabricated High-Speed Axial-Flux Multiwatt Permanent-Magnet Generators; Part I: Modeling," *Microelectromechanical Systems, Journal of*, vol. 15, pp. 1330, 2006.

[76] T. C. Neugebauer, D. J. Perreault, J. H. Lang, and C. Livermore, "A six-phase multilevel inverter for MEMS electrostatic induction micromotors," *IEEE Transactions on Circuits and Systems II: Express Briefs*, vol. 51, pp. 49, 2004.

[77] S. L. Garverick, M. L. Nagy, N. K. Rao, D. K. Hartsfield, and A. Purushotham, "A capacitive sensing integrated circuit for detection of micromotor critical angles," *IEEE Journal of Solid-State Circuits*, vol. 32, pp. 23, 1997.

[78] J. T. Horstmann and K. F. Goser, "Monolithic integration of a silicon micromotor in combination with the CMOS drive circuit on one chip," *Microelectronic Engineering*, vol. 67-68, pp. 390, 2003.

[79] S. F. Bart, "Modeling and design of electroquasistatic microactuators.," in *Dept. of Electrical Engineering and Computer Science*. Cambridge, MA, USA: Massachusetts Institute of Technology, 1990.

[80] S. F. Bart, M. Mehregany, L. S. Tavrow, J. H. Lang, and S. D. Senturia, "Electric micromotor dynamics," *IEEE Transactions on Electron Devices*, vol. 39, pp. 566, 1992.

[81] K. C. Stark, M. Mehregany, and S. M. Phillips, "Mechanical coupling and direct torque measurement of outer-rotor polysilicon micromotors," presented at Proceedings IEEE, The Tenth Annual International Workshop on Micro Electro Mechanical Systems., An Investigation of Micro Structures, Sensors, Actuators, Machines and Robots, New York, NY, USA, 1997.

[82] K. C. Stark, A. Azzam Yasseen, S. M. Phillips, and M. Mehregany, "Micro torque measurement using outer-rotor polysilicon micromotors," presented at Proceedings of IEEE Sensors, Orlando, FL, USA, 2002.

[83] A. Modafe, N. Ghalichechian, J. H. Lang, and R. Ghodssi, "A Microball-Bearing-Supported Linear Electrostatic Micromotor with Benzocyclobutene Polymer Insulating Layers," presented at The 13th International Conference

on Solid-State Sensors, Actuators, and Microsystems (Transducers '05), Seoul, Korea, 2005.

[84] A. Modafe, "Benzocyclobutene-Based Electric Micromachines Supported on Microball Bearings: Design, Fabrication, and Characterization," in *Deprtment of Electrical and Computer Engineering*. Collge Park, MD, USA: University of Maryland, 2007.

[85] L. G. Frechette, S. A. Jacobson, K. S. Breuer, F. F. Ehrich, R. Ghodssi, R. Khanna, W. Chee Wei, Z. Xin, M. A. Schmidt, and A. H. Epstein, "High-speed microfabricated silicon turbomachinery and fluid film bearings," *Journal of Microelectromechanical Systems*, vol. 14, pp. 141, 2005.

[86] A. Modafe, N. Ghalichechian, M. Powers, M. Khbeis, and R. Ghodssi, "Embedded benzocyclobutene in silicon: An integrated fabrication process for electrical and thermal isolation in MEMS," *Microelectronic Engineering*, vol. 82, pp. 154, 2005.

[87] A. Modafe, "Benzocyclobutene-Based Electric Micromachines Supported on Microball Bearings: Design, Fabrication, and Characterization," in *Deaprtment of Electrical and Computer Engineering*. Collge Park, MD, USA: University of Maryland, 2006.

[88] L. Ta-Wei, A. Modafe, B. Shapiro, and R. Ghodssi, "Characterization of dynamic friction in MEMS-based microball bearings," *Instrumentation and Measurement, IEEE Transactions on*, vol. 53, pp. 839, 2004.

[89] A. Modafe, N. Ghalichechian, B. Kleber, and R. Ghodssi, "Electrical characterization of Benzocyclobutene polymers for electric micro machines," *IEEE Transactions on Device and Materials Reliability*, vol. 4, pp. 495-508, 2004.

[90] N. Ghalichechian, A. Modafe, P. Lazzeri, V. Micheli, M. Anderle, and R. Ghodssi, "Characterization of Benzocyclobutene and Chromium-gold Film Interface for Application in Silicon Micromachining," presented at Material Research Society 2005 Spring Meeting, San Francisco, CA, USA, 28-April 1, 2005.

[91] N. Ghalichechian, A. Modafe, and R. Ghodssi, "Integration of Silicon Anisotropic Wet Etching and BCB Processes," presented at AVS 50th International Symposium, Baltimore, MD, USA, November 2-7, 2003.

[92] N. Ghalichechian, "Integration of Benzocyclobutene Polymers and Silicon Micromachines Structures Fabricated with Anisotropic Wet Etching," in

Department of Electrical and Computer Engineering. College Park, MD, USA: University of Maryland, 2004.

[93] N. Ghalichechian, A. Modafe, R. Ghodssi, P. Lazzeri, V. Micheli, and M. Anderle, "Integration of Benzocyclobutene Polymers and Silicon Micromachined Structures Using Anisotropic Wet Etching," *Journal of Vacuum Science & Technology B*, vol. 22, pp. 2439-244, 2004.

[94] M. J. Madou, *Fundamentals of microfabrication the science of miniaturization*, 2nd ed. Boca Raton: CRC Press, 2002.

[95] R. A. Kirchhoff and K. J. Bruza, "Benzocyclobutenes in polymer synthesis," *Progress in Polymer Science*, vol. 18, pp. 85-185, 1993.

[96] M. F. Farona, "Benzocyclobutenes in polymer chemistry," *Progress in Polymer Science*, vol. 21, pp. 505-555, 1996.

[97] M. E. Mills, P. Townsend, D. Casrillo, S. Martin, and A. Achen, "Benzocyclobutene (DVS-BCB) polymer as an interlayer dielectric (ILD) material," *Microelectronic Engineering*, vol. 33, pp. 327-334, 1997.

[98] "Processing procedures for dry-etch CYCLOTENE advance electronics resins (dry-etch BCB)," Dow Chemical, 2004.

[99] P. B. Chinoy and J. Tajadod, "Processing and microwave characterization of multilevel interconnects using benzocyclobutene dielectric," *IEEE Transactions on Components, Hybrids, and Manufacturing Technology*, vol. 16, pp. 714-719, 1993.

[100] A. J. G. Strandjord, R. H. Heistand, P. Garrou, and T. G. Tessier, "A photosensitive-BCB on laminate technology (MCM-LD)," presented at 44th Electronic Components and Technology Conference, Washington DC, USA, 1994.

[101] D. C. Burdeaux, P. H. Townsend, J. N. Carr, and P. Garrou, "Benzocyclobutene (BCB) dielectrics for the fabrication of high density, thin film multichip modules," *Journal of Electronic Materials*, vol. 19, pp. 1357-1366, 1990.

[102] M. J. Berry, T. G. Tessier, I. Turlik, G. M. Adema, D. C. Burdeaux, J. N. Carr, and P. Garrou, "Benzocyclobutene as a dielectric for multichip module fabrication," presented at 40th Electronic Components and Technology Conference, 1990.

[103] R. D. Sandell, G. Akerling, and A. D. Smith, "Multi-chip packaging for high speed superconducting circuits," presented at Applied Superconductivity Conference, Boston, MA, USA, 1995.

[104] T. Miyagi, Y. Iseki, K. Higuchi, Y. Shizuki, T. Hanawa, E. Takagi, M. Saito, K. Yoshihara, and M. Konno, "MCM-D/L using copper/photosensitive-BCB multilayer for upper microwave band systems," presented at 46th Electronic Components and Technology Conference, Orlando, FL, USA, 1996.

[105] Y. Ida, P. E. Garrou, A. J. G. Strandjord, S. L. Cummings, W. B. Rogers, M. J. Berry, and S. R. Kisting, "Processing, transfer solder bumping, chip attachment and testing of a thin film Cu/photo-BCB MCM-D," presented at 8th IEEE/CPMT Int. Electronic Manufacturing Technology Symp., Japan, 1995.

[106] L. A. Keser, R. Bajaj, and T. Fang, "Redistribution and bumping of a high I/O device for flip chip assembly," *IEEE Transactions on Advanced Packaging*, vol. 23, pp. 3-8, 2000.

[107] D. T. Price, R. J. Gutmann, and S. P. Murarka, "Damascene copper interconnects with polymer ILDs," presented at 24th International Conference on Metallurgical Coatings and Thin Films, Switzerland San Diego, CA, USA, 1997.

[108] A. J. G. Strandjord, W. B. Rogers, Y. Ida, R. R. De Vellis, S. Shiau, E. S. Moyer, D. M. Scheck, and P. E. Garrou, "Photosensitive benzocyclobutene for stress-buffer and passivation applications (one mask manufacturing process)," presented at 47th Electronic Components and Technology Conference, San Jose, CA, 1997.

[109] X. Huo, K. J. Chen, and P. C. H. Chan, "High-Q copper inductors on standard silicon substrate with a low-k BCB dielectric layer," presented at Proceedings of 2002 International Microwave Symposium, Seattle, WA, USA, 2002.

[110] C. F. Kane and R. R. Krchnavek, "Benzocyclobutene optical waveguides," *IEEE Photonics Technology Letters*, vol. 7, pp. 535-537, 1995.

[111] S. Wolff, A. R. Giehl, M. Renno, and H. Fouckhardt, "Metallic waveguide mirrors in polymer film waveguides," presented at 10th European Conference on Integrated Optics, Paderborn, Germany, 2001.

[112] C. Laville, C. Pellet, and G. N'Kaoua, "Interdigitated humidity sensors for a portable clinical microsystem," presented at 1st Ann. Int. IEEE-EMBS Special Topic Conf. Microtechnologies in Medicine and Biology, Lyon, France, 2000.

[113] H. H. Gatzen, E. Obermeier, T. Kohlmeier, T. Budde, H. D. Ngo, B. Mukhopadhya, and M. Farr, "An electromagnetically actuated bi-stable mems optical microswitch," presented at 12th International Conference on TRANSDUCERS, Solid-State Sensors, Actuators and Microsystems, Boston, MA, USA, 2003.

[114] P. Turmezei, A. Polyakov, J. R. Mollinger, M. Bartek, A. Bossche, and J. N. Burghartz, "Low-cost microfilter for red blood cell membrane stiffness measurement using photosensitive bcb," presented at 12th Innational Conference on Solid-State Sensors, Actuators and Microsystems, Boston, MA, USA, 2003.

[115] A. Jourdain, X. Rottenberg, G. Carchon, and H. A. C. Tilmans, "Optimization of 0-level packaging for RF-MEMS devices," presented at 12th Innational Conference on TRANSDUCERS, Solid-State Sensors, Actuators and Microsystems, Boston, MA, USA, 2003.

[116] F. Niklaus, H. Andersson, P. Enoksson, and G. Stemme, "Low temperature full wafer adhesive bonding of structured wafers," presented at Proceedings of EUROSENSORS, Switzerland Copenhagen, Denmark, 2001.

[117] T.-K. A. Chou and K. Najafi, "3D MEMS fabrication using low-temperature wafer bonding with benzocyclobutene (BCB)," presented at Solid-State Sensors and Actuators 11th International Conference, Munich, Germany, 2001.

[118] J. Oberhammer and G. Stemme, "Incrementally etched electrical feedthroughs for wafer-level transfer of glass lid packages," presented at Solid-State Sensors, Actuators and Microsystems 12th Innational Conference, Boston, MA, USA, 2003.

[119] J. M. Snodgrass and R. H. Dauskardt, "The effect of fatigue on the adhesion and subcritical debonding of benzocyclobutene/silicon dioxide interfaces," presented at Materials, Technology and Reliability for Advanced Interconnects and Low-k Dielectrics Symposium, San Francisco, CA, USA, 2001.

[120] J. M. Snodgrass, D. Pantelidis, M. L. Jenkins, J. C. Bravman, and R. H. Dauskardt, "Subcritical debonding of polymer/silica interfaces under monotonic and cyclic loading," *Acta Materialia*, vol. 50, pp. 2395-2411, 2002.

[121] J. Im, E. O. Shaffer, R. Peters, T. Rey, C. Murlick, and R. L. Sammler, "Physical and mechanical properties determination of photo-BCB-based thin films," presented at International Symposium on Microelectronics, 1996.

[122] J.-h. Im, E. O. Shaffer, II, T. Stokich, Jr, A. Strandjord, J. Hetzner, J. Curphy, C. Karas, G. Meyers, D. Hawn, A. Chakrabarti, and S. Froelicher, "On the mechanical reliability of photo-BCB-based thin film dielectric polymer for electronic packaging applications," *Transactions of the ASME. Journal of Electronic Packaging*, vol. 122, pp. 28-33, 2000.

[123] J. T. Beechinor, E. McGlynn, M. O'Reilly, and G. M. Crean, "Optical characterisation of thin film benzocyclobutene (BCB) based polymers," presented at Advanced Materials for Interconnections Symposium, E-MRS Spring Meeting Conference, Netherlands Strasbourg, France, 1997.

[124] S. Guo, "Cyclotene(R) diaphragm for MEMS-based IR detectors," presented at Proceedings of the SPIE - The International Society for Optical Engineering, Micromachining and Microfabrication Process Technology VII, USA San Jose, CA, USA, 2003.

[125] C. L. Borst, D. G. Thakurta, W. N. Gill, and R. J. Gutmann, "Chemical-mechanical planarization of low-k polymers for advanced IC structures," *Transactions of the ASME, Journal of Electronic Packaging*, vol. 124, pp. 362-366, 2002.

[126] F. Kuchenmeister, Z. Stavreva, U. Schubert, K. Richter, C. Wenzel, and M. Simmonds, "A comparative CMP study of BCB and SiLK for copper damascene technologies," presented at Advanced Metallization Conference, Colorado Springs, CO, USA, 1998.

[127] A. Modafe, N. Ghalichechian, A. Frey, J. H. Lang, and R. Ghodssi, "Microball-Bearing-Supported Electrostatic Micromachines with Polymer Dielectric Films for Electromechanical Power Conversion," *Journal of Micromechanics and Microengineering*, vol. 16, pp. S182-S190, 2006.

[128] S. D. Senturia, *Microsystem design*. Boston: Kluwer Academic Publishers, 2001.

[129] J. D. Jackson, *Classical Electrodynamics*, 3rd ed. New York: John Wiley and Sons, 1998.

[130] A. Modafe, N. Ghalichechian, A. Frey, J. H. Lang, and R. Ghodssi, "Microball-Bearing-Supported Electrostatic Micromachines with Polymer Dielectric Films for Electromechanical Power Conversion," presented at The fifth International Workshop on Micro NanoTechnology for Power Generation and Energy Conversion Applications (Power MEMS '05), Tokyo, Japan, 2005.

[131] A. Modafe, N. Ghalichechian, A. Frey, J. H. Lang, and R. Ghodssi, "Microball-Bearing-Supported Electrostatic Micromachines with Polymer Dielectric Films for Electromechanical Power Conversion," *Journal of Micromechanics and Microengineering*, In Press, 2006.

[132] N. Ghalichechian, A. Modafe, A. Frey, J. H. Lang, and R. Ghodssi, "Dynamic Characterization of a Linear Variable-Capacitance Micromotor," presented at Solid-State Sensor, Actuator, and Microsystems Workshop, Hilton Head Island, SC, USA, June 4-8, 2006.

[133] A. Modafe, N. Ghalichechian, J. H. Lang, and R. Ghodssi, "A Microball-Bearing-Supported Linear Electrostatic Micromotor with Benzocyclobutene Polymer Insulating Layers," presented at The 13th International Conference on Solid-State Sensors, Actuators, and Microsystems (Transducers '05), Seoul, Korea, 2005.

[134] M. McCarthy, B. Hanrahan, C. Zorman, and R. Ghodssi, "Rolling Friction in MEMS Ball Bearings: The Effects of Loading and Solid Film Lubrication," presented at ASME/STLE International Joint Tribology Conference, San Diego, CA, USA, 2007.